

**ACTIVATED CARBON FROM LONGAN SEED:  
ITS ACTIVATION MODEL AND ADSORPTION  
OF WATER VAPOR AND BENZENE**

**Supunnee Junpirom**

**A Thesis Submitted in Partial Fulfillment of the Requirements for the  
Degree of Doctor of Philosophy in Chemical Engineering  
Suranaree University of Technology  
Academic Year 2006**

ถ่านกัมมันต์จากเม็ดลำไย: แบบจำลองการกระตุ้น  
และการดูดซับไอน้ำและเบนซีน

นางสาวสุพรรณิ จันทร์ภิรมณ์

วิทยานิพนธ์นี้เป็นส่วนหนึ่งของการศึกษาตามหลักสูตรปริญญาวิศวกรรมศาสตรดุษฎีบัณฑิต  
สาขาวิชาวิศวกรรมเคมี  
มหาวิทยาลัยเทคโนโลยีสุรนารี  
ปีการศึกษา 2549

**ACTIVATED CARBON FROM LONGAN SEED:  
ITS ACTIVATION MODEL AND ADSORPTION  
OF WATER VAPOR AND BENZENE**

Suranaree University of Technology has approved this thesis submitted in partial fulfillment of the requirements for the Degree of Doctor of Philosophy.

Thesis Examining Committee

Terasut Sookkumnerd  
(Dr. Terasut Sookkumnerd)

Chairperson

Chaiyot Tangsathitkulchai  
(Assoc. Prof. Dr. Chaiyot Tangsathitkulchai)

Member (Thesis Advisor)

M. Tangsathitkulchai  
(Assoc. Prof. Dr. Malee Tangsathitkulchai)

Member

Deacha Chatsiriwech  
(Assoc. Prof. Dr. Deacha Chatsiriwech)

Member

Ratanawan Kiattikomol  
(Asst. Prof. Dr. Ratanawan Kiattikomol)

Member

S. Rattanaphi  
(Assoc. Prof. Dr. Saowanee Rattanaphani)

Vice Rector for Academic Affairs

V. Khompit  
(Assoc. Prof. Dr. Vorapot Khompis)

Dean of Institute of Engineering

สุพรรณิ จันทร์ภิรมณ์ : ถ่านกัมมันต์จากเมล็ดลำไย: แบบจำลองการกระตุ้นและการดูดซับ  
ไอน้ำและเบนซีน (ACTIVATED CARBON FROM LONGAN SEED: ITS  
ACTIVATION MODEL AND ADSORPTION OF WATER VAPOR AND BENZENE)  
อาจารย์ที่ปรึกษา : รศ. ดร.ชัยยศ ตั้งสถิตย์กุลชัย, 220 หน้า

งานวิจัยนี้มีวัตถุประสงค์เพื่อศึกษาหัวข้อต่าง ๆ เกี่ยวกับถ่านกัมมันต์ ได้แก่ การเตรียม  
การวิเคราะห์สมบัติ และ กระบวนการดูดซับ โดยใช้เมล็ดลำไย ซึ่งคาดว่าจะเป็นวัตถุคิชนิดใหม่ที่มี  
มีศักยภาพ สำหรับผลิตถ่านกัมมันต์ที่มีคุณภาพดี ขอบเขตของงานวิจัยนี้ได้ครอบคลุมถึงการ  
วิเคราะห์ทางความร้อนของเมล็ดลำไย การเตรียม และ วิเคราะห์สมบัติความพรุนถ่านกัมมันต์  
การศึกษาสมดุล และ จลนพลศาสตร์การดูดซับ นอกจากนี้ ยังได้พัฒนาแบบจำลองการกระตุ้น  
เพื่ออธิบาย และ ทำนายการพัฒนาารุพรุนของถ่านกัมมันต์ในกระบวนการแก๊สซีพีเคชัน

การสลายตัวทางความร้อนของเมล็ดลำไย ในกระบวนการไพโรไลซิสแบบอุณหภูมิไม่คงที่  
เกิดขึ้นส่วนใหญ่ในช่วงอุณหภูมิระหว่าง 210-330 องศาเซลเซียส ซึ่งสามารถอธิบายได้ด้วยแบบ  
จำลองสองปฏิกิริยาคู่ขนาน จากการเตรียมถ่านกัมมันต์โดยวิธีกระตุ้นทางกายภาพแบบสองขั้นตอน  
คือ การคาร์บอนเซชัน และ การกระตุ้นด้วยแก๊สคาร์บอนไดออกไซด์ พบว่าเมื่อคาร์บอนน้ำหนัก  
ที่หายไปในช่วงขั้นตอนการกระตุ้น มีค่าเพิ่มมากขึ้นจนถึงร้อยละ 70 ค่าพื้นที่ผิว ปริมาตรรูพรุนรวม  
และ ปริมาตรรูพรุนขนาดเล็ก มีค่าเพิ่มมากขึ้น แต่ที่ร้อยละน้ำหนักที่หายไปสูงมากกว่านี้ สมบัติ  
ดังกล่าวมีค่าลดลง งานวิจัยนี้ได้เสนอแบบจำลอง เพื่ออธิบายกระบวนการเกิดรูพรุนในขั้นตอนการ  
กระตุ้น และ ใช้ทดสอบกับผลการทดลอง ซึ่งสามารถอธิบายการพัฒนาของ พื้นที่ผิว และ  
ปริมาตรรูพรุน ที่มีความสัมพันธ์กับร้อยละน้ำหนักที่หายไปในช่วงขั้นตอนการกระตุ้นได้ การศึกษาผล  
ของอุณหภูมิในขั้นตอนการคาร์บอนเซชัน พบว่าตัวแปรนี้ มีผลต่อสมบัติความว่องไวในการ  
เกิดปฏิกิริยาของถ่านชาร์ในขั้นตอนการกระตุ้น ซึ่งส่งผลต่อเนื่องถึงสมบัติของถ่านกัมมันต์ จากการ  
ทดลองเตรียมถ่านกัมมันต์โดยวิธีการกระตุ้นแบบขั้นตอนเดียว ด้วยแก๊สคาร์บอนไดออกไซด์  
ได้ถ่านกัมมันต์ที่มีสมบัติความพรุน ใกล้เคียงกับการเตรียมโดยใช้วิธีธรรมดาแบบสองขั้นตอน  
ถ่านกัมมันต์ที่เตรียมโดยวิธีการกระตุ้นทางเคมีด้วยกรดฟอสฟอริก จะเกิดรูพรุนขนาดเล็ก  
เป็นส่วนใหญ่

การศึกษาสมดุลการดูดซับไอน้ำ พบว่าสมบัติถ่านกัมมันต์ที่สำคัญต่อกระบวนการนี้ คือ  
สมบัติการกระจายขนาดรูพรุน และ หมู่ฟังก์ชันกรดบนพื้นผิว แบบจำลองการดูดซับไอน้ำแบบ  
กลุ่มโมเลกุล (cluster) ที่เสนอโดย Do และ Do ได้ถูกนำมาใช้ เพื่ออธิบายพฤติกรรมดูดซับ  
ไอน้ำ ในงานวิจัยนี้ได้เสนอให้มีการปรับขนาดของกลุ่มโมเลกุลในแบบจำลอง เพื่อสามารถอธิบาย

การดูดซับไอน้ำในรูปอนุภาคใหญ่ ผลไอโซเทิร์มการดูดซับเอทานอล แสดงลักษณะแตกต่างจากการดูดซับไอน้ำ และสามารถอธิบายได้ด้วยสมการแลงเมียร์แบบคู่

การศึกษาจลนพลศาสตร์การดูดซับเบนซีน โดยใช้เทคนิคการไหลแบบคงที่ (constant molar flow rate) พบว่าค่าสัมประสิทธิ์การแพร่กระจายบนพื้นผิว มีค่าอยู่ในช่วง  $1 \times 10^{-10}$  ตารางเมตรต่อวินาที ค่าสัมประสิทธิ์การแพร่กระจายบนพื้นผิวนี้อ มีความสัมพันธ์กับอุณหภูมิ เป็นไปตามสมการอาร์เรเนียส โดยมีค่าพลังงานกระตุ้นเท่ากับหนึ่งในสามของค่าความร้อนการดูดซับ ที่ภาวะการดูดซับเป็นศูนย์

สาขาวิชาวิศวกรรมเคมี

ปีการศึกษา 2549

ลายมือชื่อนักศึกษา สุพรรณ จันทร์ภิรมณ์

ลายมือชื่ออาจารย์ที่ปรึกษา ดร. ธีรภัทร

ลายมือชื่ออาจารย์ที่ปรึกษาร่วม ดร. วิวัฒน์

SUPUNNEE JUNPIROM : ACTIVATED CARBON FROM LONGAN SEED: ITS ACTIVATION MODEL AND ADSORPTION OF WATER VAPOR AND BENZENE. THESIS ADVISOR : ASSOC. PROF. CHAIYOT TANGSATHITKULCHAI, Ph.D. 220 PP.

#### ACTIVATED CARBON/ADSORPTION/LONGAN SEED

The overall objective of this thesis research was to perform an extensive study on the preparation, characterization and adsorption of activated carbon from longan seed, considered to be a new highly potential precursor. The scope of research work covers the thermal analysis of the raw material, the preparation of activated carbon under different conditions, and the studies of equilibrium and kinetics of adsorption. The breakthrough from this work was the development of a structural model that can predict the evolution of activated carbon during char gasification.

The non-isothermal pyrolysis process showed the main devolatilization to be in the temperature range of 210-330°C. Thermal decomposition behavior could be well described by the two-parallel reactions model. On the preparation processes, the conventional two-step CO<sub>2</sub> activation revealed that the porous properties of activated carbon such as BET surface area, total pore volume, and micropore volume increased with an increase in the burn-off up to 70%, beyond which these properties tended to decrease. A new structural model for char activation was developed to predict the evolution of pore volume, pore surface area and pore size distribution of prepared activated carbons with respect to the extent of gasification of char. For the two-step physical preparation, the carbonization temperature was found to be the factor

controlling the char reactivity which had a subsequent effect on the property of activated carbon in the activation step. One-step CO<sub>2</sub> activation produced the activated carbon with approximately the same porous properties as compared to the conventional two-step preparation. The chemically activated carbon by H<sub>3</sub>PO<sub>4</sub> activation was found to consist dominantly with microporosity.

Water adsorption behavior was found to depend significantly on the pore size distribution through the role of inherent acidic functional groups. Cluster model of Do and Do was used to describe the water adsorption isotherms and further modification on the cluster size in the larger pores was required to give correct predictive results. The shape of ethanol adsorption isotherm showed a significant difference from that of water adsorption and was found to be fitted well with the dual-Langmuir equation.

The kinetics of benzene adsorption was conducted by the technique of constant molar flow rate. Surface diffusivity was determined to be in the order of  $1 \times 10^{-10}$  m<sup>2</sup>/s. This surface diffusivity followed an Arrhenius relationship with respect to temperature, giving the activation energy to be one third of the heat of adsorption at zero loading.

School of Chemical Engineering

Academic Year 2006

Student's Signature Supumee J.

Advisor's Signature Chaiyot J.

Co-advisor's Signature M. T. Suthithani

## ACKNOWLEDGEMENTS

With the achievement of this degree, I am grateful to all the people that have contributed to this dissertation. First and foremost, I would like to express my special thanks to Assoc. Prof. Dr. Chaiyot Tangsathitkulchai, my thesis advisor, for his providing me with the opportunity to undertake a Ph.D. My special thanks are also extended to my co-advisor, Assoc. Prof. Dr. Malee Tangsathitkulchai. They are wonderful supervisors, without their patience, encouragement and insightful suggestion, I would not have achieved this far and this thesis would not have been completed. Also, my deep appreciation goes to Prof. Dr. Doung D. Do, a great supervisor during my research time at the University of Queensland. More importantly, they taught me to have tremendous enthusiasm and confidence in science research, which I know is priceless.

I would like to express my gratitude to Dr. Terasut Sookkumnerd, Assoc. Prof. Dr. Deacha Chatsiriwech, Asst. Prof. Dr. Ratanawan Kiattikomol, for their kind agreement to serve on my committee and also for their many important comments and suggestions.

Also, I would like to sincerely thank to all of the academic members in the School of Chemical Engineering, for their teaching, support and encouragement. Especially, Assoc. Prof. Dr. Kasem Prabripataloong, Assoc. Prof. Dr. Chaiyot Tangsathitkulchai, Asst. Prof. Dr. Chalongsri Flood and Assoc. Prof. Dr. Adrian E. Flood, for whom firstly led me to the world of Chemical Engineering.

The assistances from the technical staff in the Center for Scientific and Technology Equipment, SUT and in the Division of Chemical Engineering, UQ, are appreciated, especially, Mr. Saran and Ms. Rungruang, the technical staff in Chemical Engineering's laboratory, SUT. My thanks also go to Mrs. Amporn, for her skillful secretarial work of our school.

Thanks also are due to Naparat, Natthaya, Dr. Sukanya, Piyamaporn, Yodkwan, and Areeya for their invaluable assistance and a great company. The present colleagues in carbon and adsorption research group, Porntep, Yuvarat, Piyarat, and Chaturaporn, thanks for their assistance and research contribution and also to solving the problems in our laboratory. Thanks to all of the graduate students in School of Chemical Engineering, for making a good atmosphere in our research rooms. The colleagues in adsorption group at UQ, Dr. Jun-Seok Bae, Atichat and Greg also deserve my thanks for their invaluable assistance and conversations to make my memorable time. My great senior friends, Dr. Peerapong and Dr. Monthippa are paid of my thanks for their unforgettable assistance.

Financial support from the Thailand Research Fund (TRF) through the Royal Golden Jubilee Ph.D. Program (RGJ-Ph.D.), grant number PHD/0087/2543 is gratefully acknowledged. My sincere thanks also send to all members and staff in RGJ-Ph.D. program for their assistance.

Finally, I would like to dedicate this work to my parents, for their dedication to me has never wavered. Many thanks also pass to my brother and my relatives, it is really great to have them around.

Supunnee Junpirom

# TABLE OF CONTENTS

	<b>Page</b>
ABSTRACT (THAI).....	I
ABSTRACT (ENGLISH) .....	III
ACKNOWLEDGEMENTS .....	V
TABLE OF CONTENTS .....	VII
LIST OF TABLES .....	XV
LIST OF FIGURES.....	XVIII
SYMBOLS AND ABBREVIATIONS .....	XXVI
<b>CHAPTER</b>	
<b>I INTRODUCTION.....</b>	<b>1</b>
1.1 Rationale of the Study .....	1
1.2 Research Objectives .....	3
1.3 Scope and Limitations.....	4
1.4 Research Development.....	5
1.5 Expected Results from the Study .....	6
1.6 References .....	6
<b>II LITERATURE REVIEW.....</b>	<b>8</b>
2.1 Activated Carbon .....	8
2.1.1 Structure and Surface Chemistry.....	9

## TABLE OF CONTENTS (Continued)

	<b>Page</b>
2.1.2	Manufacture ..... 11
2.1.3	Carbonization ..... 12
2.1.4	Activation ..... 13
2.1.4.1	Physical Activation..... 14
2.1.4.2	Chemical Activation..... 15
2.1.5	Porosity and Pore Size Distribution ..... 17
2.1.6	Applications ..... 19
2.2	Gas and Vapor Adsorption..... 21
2.3	Adsorption Equilibrium ..... 22
2.3.1	Adsorption Isotherms ..... 23
2.3.2	Adsorption Isotherm Equations..... 26
2.3.2.1	Langmuir Equation..... 26
2.3.2.2	Brunauer-Emmett-Teller (BET) Equation... 29
2.3.2.3	Dubinin-Radushkevich (DR) Equation ..... 32
2.3.2.4	Dubinin-Astakhov (DA) Equation ..... 33
2.3.3	Surface Area and Pore Volume Determination..... 34
2.3.3.1	Langmuir Equation..... 34
2.3.3.2	BET Equation..... 35
2.3.4	Heat of Adsorption..... 35
2.3.5	Pore Size Distribution by DFT..... 36

## TABLE OF CONTENTS (Continued)

	<b>Page</b>
2.4 Adsorption Kinetics .....	40
2.4.1 Modes of Diffusion in Porous Medium .....	40
2.4.1.1 Knudsen Flow.....	40
2.4.1.2 Viscous Flow .....	40
2.4.1.3 Continuum Diffusion.....	41
2.4.1.4 Surface Diffusion .....	41
2.4.2 Measurement Methods for Adsorption Kinetics .....	41
2.5 References .....	43
<b>III THERMOGRAVIMETRIC ANALYSIS</b>	
<b>OF LONGAN SEED .....</b>	<b>47</b>
3.1 Abstract .....	47
3.2 Introduction .....	48
3.2.1 Biomass Pyrolysis Kinetic Model.....	51
3.2.1.1 One-Step Global Model.....	53
3.2.1.2 Two-Parallel Reactions Model.....	54
3.2.2 Objectives of the Study .....	58
3.3 Materials and Methods .....	58
3.3.1 Pyrolysis of Longan Seed.....	58
3.3.2 Proximate Analysis .....	59
3.4 Results and Discussion.....	60

## TABLE OF CONTENTS (Continued)

	<b>Page</b>
3.4.1 Proximate and Ultimate Analyses of Longan Seed.....	60
3.4.2 Typical Results of Non-Isothermal Pyrolysis of Longan Seed .....	61
3.4.3 Initial Sample Weight Effect.....	64
3.4.4 Particle Size Effect .....	65
3.4.5 Heating Rate Effect .....	68
3.4.6 Model Fitting of Pyrolysis Data.....	71
3.4.7 Sensitivity Analysis of the Two-Parallel Reactions Model.....	80
3.5 Conclusions .....	83
3.6 References .....	83
<b>IV ACTIVATED CARBON FROM LONGAN SEED .....</b>	<b>87</b>
4.1 Abstract .....	87
4.2 Introduction .....	88
4.2.1 Carbon Activation Model.....	90
4.2.1.1 Algorithm of Carbon Activation Model.....	92
4.2.2 Objectives of the Study .....	97
4.3 Materials and Methods .....	97
4.3.1 Conventional Two-Step Physical Activation by CO <sub>2</sub> .....	97

## TABLE OF CONTENTS (Continued)

	<b>Page</b>
4.3.1.1	Carbonization ..... 97
4.3.1.2	Activation ..... 98
4.3.2	Carbonization Temperature Effect ..... 98
4.3.3	One-Step Activation ..... 99
4.3.4	Chemical Activation by H <sub>3</sub> PO <sub>4</sub> ..... 100
4.3.5	Activated Carbon Characterization ..... 100
4.4	Results and Discussion ..... 101
4.4.1	Conventional Two-Step Physical Activation by CO <sub>2</sub> ..... 101
4.4.1.1	Characterization of Char ..... 101
4.4.1.2	Activation of Char ..... 102
4.4.1.3	Porous Properties of Activated Carbons ... 104
4.4.2	Carbon Activation Model ..... 111
4.4.3	Carbonization Temperature Effect ..... 119
4.4.3.1	Char Properties ..... 119
4.4.3.2	Activation of Chars ..... 123
4.4.3.3	Porous Properties of Activated Carbons ... 124
4.4.4	One-Step Activation ..... 127
4.4.4.1	Total Weight Loss in Activation ..... 127
4.4.4.2	Porous Properties of Activated Carbon ..... 128

## TABLE OF CONTENTS (Continued)

	<b>Page</b>
4.4.5 Chemical Activation by $H_3PO_4$ .....	132
4.4.5.1 Yield of Chemically Activated Carbon.....	132
4.4.5.2 Porous Properties of Chemically Activated Carbon.....	134
4.5 Conclusions .....	138
4.6 References .....	141
<b>V EQUILIBRIA STUDY OF LONGAN SEED</b>	
<b>ACTIVATED CARBON .....</b>	<b>147</b>
5.1 Abstract .....	147
5.2 Introduction .....	148
5.2.1 Water Adsorption .....	148
5.2.2 Model of Water Adsorption in Activated Carbon.....	151
5.2.2.1 Dubinin-Serpinsky (DS) Equation .....	151
5.2.2.2 Do and Do Equation.....	152
5.2.3 Ethanol Adsorption .....	152
5.2.3.1 Dual-Langmuir Equation.....	153
5.2.5 Objectives of the Study .....	153
5.3 Materials and Methods .....	154
5.3.1 Materials .....	154
5.3.2 Material Characterization.....	155

## TABLE OF CONTENTS (Continued)

	<b>Page</b>
5.3.3 Water Adsorption Experiment .....	155
5.3.4 Ethanol Adsorption Experiment.....	156
5.4 Results and Discussion.....	156
5.4.1 Water Vapor Adsorption .....	156
5.4.1.1 Porous Characteristics of Activated Carbons.....	156
5.4.1.2 Water Adsorption Isotherms .....	161
5.4.1.3 Simulation of Water Adsorption Isotherms .....	168
5.4.2 Ethanol Adsorption .....	174
5.5 Conclusions .....	179
5.6 References .....	180
<b>VI KINETICS OF BENZENE ADSORPTION</b>	
<b>IN ACTIVATED CARBON.....</b>	<b>184</b>
6.1 Abstract .....	184
6.2 Introduction .....	185
6.2.1 The Formulation of Equations for CMF Analysis.....	186
6.2.2 Objectives of the Study .....	191
6.3 Materials and Methods.....	191

## TABLE OF CONTENTS (Continued)

	<b>Page</b>
6.3.1 Materials .....	191
6.3.2 Benzene Adsorption Isotherm.....	192
6.3.3 Constant Molar Flow Rate Experiment.....	192
6.4 Results and Discussion.....	194
6.4.1 Porous Properties of Test Activated Carbons .....	194
6.4.2 Benzene Adsorption Isotherm.....	196
6.4.3 Benzene Adsorption Kinetics.....	201
6.5 Conclusions .....	207
6.6 References .....	208
<b>VII CONCLUSIONS AND RECOMMENDATIONS.....</b>	<b>210</b>
7.1 Conclusions .....	210
7.2 Recommendations .....	214
7.2.1 Gasification Studying in a Thermogravimetric Analyzer .....	214
7.2.2 Refinement of a Carbon Activation Model.....	215
7.2.3 The Surface Functional Group Influence on Water Adsorption .....	215
7.2.4 Kinetic Parameters at Loading Variation.....	215
<b>APPENDIX LIST OF PUBLICATIONS.....</b>	<b>217</b>
<b>BIOGRAPHY .....</b>	<b>220</b>

## LIST OF TABLES

Table	Page
2.1 Gasification reactions of carbon by three oxidizing gases .....	15
2.2 Methodologies of direct and indirect analyses of porosity .....	17
2.3 Examples of commercial adsorption processes using activated carbon .....	20
2.4 General characteristics of physical and chemical adsorption .....	22
2.5 Advantages and disadvantages of various kinetic techniques .....	42
3.1 Proximate analyses of longan seed and some biomasses used for activated carbon preparation.....	60
3.2 Ultimate analyses of longan seed and some biomasses.....	61
3.3 The kinetic parameters obtained from the two-parallel reactions model of longan seed with different particle sizes under the nitrogen atmosphere and a heating rate 5°C/min .....	75
3.4 The kinetic parameters obtained from the two-parallel reactions model of longan seed at different heating rates with a particle size of 1.0 mm .....	77
3.5 The values of Max. Error derived from the changing of kinetic parameters for sensitivity analysis, for a particle size of 1.0 mm at heating rate of 100°C/min.....	82
4.1 Typical generated reactivities of carbon layers of some graphitic crystallites .....	96

## LIST OF TABLES (Continued)

<b>Table</b>	<b>Page</b>
4.2 Proximate analyses of longan seed, char and activated carbon .....	102
4.3 Porous properties of activated carbons prepared from different activation conditions .....	107
4.4 Model-generated pore evolution data .....	117
4.5 Porous properties of chars and the char-derived activated carbon .....	126
4.6 Porous properties of activated carbons prepared from different activation conditions by one-step CO <sub>2</sub> activation.....	130
4.7 Porous properties of activated carbons prepared from different activation conditions by chemical activation.....	136
5.1 Porous properties derived from N <sub>2</sub> adsorption of activated carbons .....	158
5.2 The average pore width in each pore size range from DFT calculation.....	160
5.3 Surface chemistry property obtained from Boehm titration .....	161
5.4 Pore volume derived from the DFT analysis of N <sub>2</sub> (-196°C) data and the adsorbed water amount .....	165
5.5 Estimated relative pressure from water isotherms for volume adsorbed corresponding to ultramicropore volume .....	166
5.6 The optimized parameters derived from the water adsorption model of Do and Do .....	170
5.7 The optimized parameters derived from the modified isotherm model of Do and Do .....	172

**LIST OF TABLES (Continued)**

<b>Table</b>	<b>Page</b>
5.8 The optimized parameters from dual-Langmuir equation fitting with the ethanol adsorption isotherm at several temperatures.....	179
6.1 Porous and physical properties of test activated carbon.....	195
6.2 The optimized parameters from dual-Langmuir equation fitting with the benzene adsorption isotherms at different temperatures .....	201
6.3 Parameters for CMF calculation.....	204
6.4 Effect of temperature on Henry constant of benzene adsorption in test activated carbons.....	205
6.5 Kinetic parameters of benzene adsorption in test activated carbons for zero loading.....	206

## LIST OF FIGURES

Figure	Page
2.1	Examples of surface functional groups on carbon surface ..... 10
2.2	A hierarchical view of the molecular structure of an activated carbon ..... 11
2.3	The five types of adsorption isotherm, I to V, in the classification of Brunauer, Deming, Deming and Teller (BDDT), together with Type VI, the stepped isotherm..... 25
3.1	Representative structures of biomass components ..... 50
3.2	Schematic diagram of a thermogravimetric system..... 51
3.3	The typical residual weight fraction (TG) and weight loss rate (DTG) for the non-isothermal pyrolysis of longan seed, particle size 2.1 mm and a heating rate 5°C/min ..... 62
3.4	The weight loss rate curves (DTG) for the non-isothermal pyrolysis of longan seed under the inert (nitrogen) and the oxidizing (air) atmosphere, particle size 2.1 mm and a heating rate 5°C/min ..... 63
3.5	The TG for the non-isothermal pyrolysis of longan seed with different of the sample weight, at heating rate of 5 and 100°C/min for a particle size of 1.0 mm ..... 65

**LIST OF FIGURES (Continued)**

<b>Figure</b>	<b>Page</b>
3.6 The TG curves for the non-isothermal pyrolysis of longan seed with different particle sizes under the nitrogen atmosphere and a heating rate at 5°C/min.....	66
3.7 The DTG for the non-isothermal pyrolysis of longan seed with different particle sizes under the nitrogen atmosphere and a heating rate 5°C/min.....	67
3.8 The TG for the non-isothermal pyrolysis of longan seed with different particle sizes under the nitrogen atmosphere and a high heating rate 100°C/min.....	68
3.9 TG curves for the non-isothermal pyrolysis of longan seed at different heating rates of a particle size 1.0 mm, (a) versus the temperature and (b) versus the time .....	69
3.10 The DTG for the non-isothermal pyrolysis of longan seed at different heating rates of a particle size 1.0 mm .....	70
3.11 The comparison of the TG for the non-isothermal pyrolysis of longan seed at heating rate 5 and 100°C/min in different particle sizes.....	71
3.12 The TG curves for the effect of (a) particle size and (b) heating rate; from the experiment (symbols) and the one-step global model fitting (lines) .....	72

## LIST OF FIGURES (Continued)

Figure	Page
3.13	The TG and DTG curves with different particle sizes at a heating rate 5°C/min for experimental data, the lines denote for the fitted data from two-parallel reactions model ..... 74
3.14	The TG and DTG curves for different heating rates with a particle size of 1.0 mm from the experiment and the two-parallel reactions model fitting ..... 76
3.15	The variation of kinetic parameters depend on the effects of (a) particle size and (b) heating rate ..... 78
3.16	The relative weight fraction ( $\alpha$ ) derived from the reaction schemes for a particle size of 1.0 mm at heating rate of 100°C/min ..... 80
3.17	The sensitivity analysis of kinetic parameters on the weight fraction..... 81
4.1	Schematic diagram of a graphitic crystallite (a) before activation (b) after activation..... 95
4.2	The variation of char burn-off with activation condition ..... 103
4.3	N <sub>2</sub> adsorption isotherms at -196°C for activated carbons prepared at activation temperatures of 800, 850, and 900°C with different activation times ..... 105
4.4	BET surface area, total pore volume and micropore volume of longan seed activated carbons at different extent burn off ..... 109
4.5	Pore volume of activated carbons prepared with different char burn-offs ..... 110

## LIST OF FIGURES (Continued)

<b>Figure</b>	<b>Page</b>
4.6	Pore size distribution of activated carbons derived from different degrees of char burn-offs ..... 110
4.7	Surface area and total pore volume of experimental and simulated data ..... 113
4.8	Total pore and micropore volumes of experimental and simulated results with different interlayer spacing ..... 114
4.9	The pore size distribution of simulated data at different degrees of char burn-offs ..... 116
4.10	Comparison of experimental and computed pore size distributions of activated carbon at two degrees of char burn-offs ..... 118
4.11	Yield of chars and weight loss prepared at different carbonization temperatures..... 119
4.12	Proximate analysis of chars prepared at different carbonization temperatures..... 120
4.13	True density of chars prepared at different carbonization temperatures ..... 121
4.14	CO <sub>2</sub> adsorption isotherms at 0°C of chars prepared at different carbonization temperatures ..... 122
4.15	Micropore volumes calculated from CO <sub>2</sub> adsorption isotherm at 0°C of chars prepared at different carbonization temperatures ..... 122

**LIST OF FIGURES (Continued)**

<b>Figure</b>	<b>Page</b>
4.16 Burn-off during activation process and the total weight loss of longan seed for the chars prepared at different carbonization temperatures, activation temperature of 850°C and for 2 h.....	124
4.17 N <sub>2</sub> adsorption at -196°C isotherms on activated carbons prepared from the chars derived at different carbonization temperature.....	125
4.18 BET surface area and total pore volume of activated carbons prepared from the chars derived at different carbonization temperatures .....	127
4.19 The total weight loss in one-step and two-step activation versus the activation time at different activation temperatures .....	128
4.20 N <sub>2</sub> adsorption at -196°C isotherms on activated carbons prepared by one-step activation at different activation times and temperatures (the numbers in figure represent for activation condition of temperature-time).....	129
4.21 BET surface area and pore volumes of one- and two-step activated carbons as a function of total weight loss.....	132
4.22 The total yield of chemically activated carbons and the yield of char prepared without pre-impregnation .....	134
4.23 N <sub>2</sub> adsorption isotherms at -196°C of chemically activated carbon prepared at different carbonization temperatures .....	135

## LIST OF FIGURES (Continued)

Figure	Page
4.24	BET surface area and total pore volume of chemically activated carbons prepared at different carbonization temperatures..... 137
4.25	The pore volumes of chemically activated carbons prepared at different carbonization temperatures ..... 138
5.1	Typical N <sub>2</sub> adsorption isotherms at –196°C of test activated carbons; solid symbols denote adsorption, open symbols denote desorption ..... 157
5.2	Pore size distribution of activated carbons derived from DFT model..... 159
5.3	Typical water adsorption isotherms at 30°C for different activated carbons; (a) adsorption–desorption branches, (b) adsorption branch..... 162
5.4	The incremental of water adsorbed amount versus relative pressure ..... 163
5.5	Water adsorption isotherms for different activated carbons at various temperatures..... 167
5.6	Isosteric heat of water adsorption for different activated carbons..... 168
5.7	Fitting of the Dubinin–Serpinsky (DS) model to the experimental water isotherms of activated carbon series: symbols denote experimental data, lines denote fitted results..... 169
5.8	Fitting of the original Do and Do model to the experimental water isotherms of activated carbon series; symbols denote experimental data, lines denote fitted result ..... 170

## LIST OF FIGURES (Continued)

Figure	Page
5.9	Fitting of the modified isotherm model of $D_0$ and $D_0$ to the experimental water isotherms of carbon series..... 172
5.10	Typical adsorption isotherm of ethanol at 30°C for test activated carbons. Filled symbols are for adsorption and empty symbols are for desorption..... 175
5.11	Ethanol adsorption isotherms in test activated carbons at various temperatures..... 176
5.12	Heat of adsorption of ethanol adsorption in LAC3 and CAC carbons..... 177
5.13	Fitting of the dual-Langmuir model to the experimental ethanol isotherms at 30°C in carbon samples; symbols denote experimental data and lines denote fitted results..... 178
6.1	Schematic diagram of diffusion mechanisms in activated carbon..... 187
6.2	Schematic diagram of a constant molar flow (CMF) adsorption test rig ..... 193
6.3	$N_2$ adsorption isotherms at -196°C for test activated carbons. Filled symbols are for adsorption and empty symbols are for desorption..... 195
6.4	Typical benzene adsorption isotherms at 50°C for test activated carbons. Filled symbols are for adsorption and empty symbols are for desorption..... 196

## LIST OF FIGURES (Continued)

Figure	Page
6.5	Benzene adsorption isotherms in test activated carbon at different temperatures..... 197
6.6	The isosteric heat of adsorption for benzene adsorption in test activated carbons ..... 198
6.7	Benzene adsorption isotherms at 50°C of test activated carbons obtained from experiment and dual-Langmuir fitting ..... 200
6.8	The benzene amount adsorbed data from dual-Langmuir fitting at temperature 50°C of test activated carbons ..... 200
6.9	Approximation of the Henry's law region of benzene adsorption isotherm ..... 202
6.10	The kinetic data of pressure responses of benzene adsorption in longan seed based-activated carbon (LACW) (a)-(c) at different temperatures and in a commercial activated carbon (CGC) (d) at 50°C, with the adsorbate flow rate of $6.60 \times 10^{-9}$ mol/sec ..... 203
6.11	Temperature dependence of surface diffusivity ( $D_{\mu}$ ) for benzene adsorption in longan seed activated carbon..... 207

## SYMBOLS AND ABBREVIATIONS

$a$	=	carbon layer reactivity
	=	initial weight fraction of component 1
$A$	=	frequency or pre-exponential factor [ $\text{min}^{-1}$ ]
$A_m$	=	average area occupied by one molecule of adsorbate [ $\text{m}^2/\text{molecule}$ ]
$b$	=	affinity constant or Langmuir constant
	=	initial weight fraction of component 2
BO	=	burn-off [%]
BET	=	Brunauer-Emmett-Teller equation
$c$	=	ratio of the rate constant
$C$	=	BET equation constant
	=	adsorbate concentration in the space inside particle [ $\text{mol}/\text{cm}^3$ of solid]
$C_b$	=	adsorbate concentration in vessel [ $\text{mol}/\text{cm}^3$ ]
$C_\mu$	=	adsorbed concentration [ $\text{mmol}/\text{g}$ ]
$C_{\mu m}$	=	saturation adsorbed concentration [ $\text{mmol}/\text{g}$ ]
$C_{\mu s}$	=	saturation concentration of water in micropore [ $\text{mmol}/\text{g}$ ]
$C_{\mu 0}$	=	concentration of the primary sites [ $\text{mmol}/\text{g}$ ]
CMF	=	constant molar flow
$D_{app}$	=	apparent diffusivity [ $\text{m}^2/\text{s}$ ]
$D_K$	=	Knudsen diffusivity [ $\text{m}^2/\text{s}$ ]
$D_p$	=	pore diffusivity [ $\text{m}^2/\text{s}$ ]

## SYMBOLS AND ABBREVIATIONS (Continued)

$D_{\mu}$	=	surface diffusivity [ $\text{m}^2/\text{s}$ ]
DA	=	Dubinin-Astakhov equation
DFT	=	density functional theory
DR	=	Dubinin-Radushkevich equation
DS	=	Dubinin-Serpinsky equation
$E$	=	activation energy [ $\text{kJ/mol}$ ]
	=	characteristic energy in Dubinin equation [ $\text{kJ/mol}$ ]
$E_{D\mu}$	=	activation energy of surface diffusion [ $\text{kJ/mol}$ ]
$i$	=	$i^{\text{th}}$ of data points
IGA	=	intelligent gravimetric analyzer
$k$	=	rate constant of pyrolysis process [ $\text{min}^{-1}$ ]
	=	rate of loss the secondary sites
$k_B$	=	Boltzmann's constant [ $1.38 \times 10^{-23}$ J/molecule-K]
$k_d$	=	rate constant for desorption if the surface are fully covered
$k_{d\infty}$	=	rate constant for desorption at infinite temperature
$K$	=	Henry's law constant
$K_f$	=	chemisorption equilibrium constant
$K_{\mu}$	=	micropore adsorption equilibrium constant
$K_0$	=	Knudsen flow parameter [cm]
$L_i$	=	initial length of carbon layer [ $\text{\AA}$ ]
$L_t$	=	length of carbon layer at a theoretical time $t$ [ $\text{\AA}$ ]

## SYMBOLS AND ABBREVIATIONS (Continued)

$m_f$	=	final mass fraction
$m_p$	=	mass of solid particle [g]
$M$	=	molecular weight [mol/g]
	=	residual weight fraction
$M_{ac}$	=	weight of activated carbon [g]
$M_c$	=	initial weight of raw char [g]
$M_i$	=	initial weight of raw material [g]
$n$	=	adsorbed amount [mmol/g]
	=	parameter associated with the distribution function in Dubinin equation
	=	reaction order of pyrolysis process
	=	number of water molecules in a cluster
$\dot{N}$	=	molar supply rate of adsorbate [mol/s]
$P$	=	pressure [kPa]
$P^o$	=	vapor pressure [kPa]
PSD	=	pore size distribution
$Q_{st}$	=	isosteric heat of adsorption [kJ/mol]
$r$	=	radius of particle [cm]
$r_G$	=	rate of gasification [ $\text{min}^{-1}$ ]
$R$	=	particle radius [cm]
$R_a$	=	rate of adsorption [ $\text{mol/m}^2\text{-s}$ ]
$R_d$	=	rate of desorption [ $\text{mol/m}^2\text{-s}$ ]

## SYMBOLS AND ABBREVIATIONS (Continued)

$R_g$	=	gas constant [8.314×10 <sup>3</sup> kPa-cm <sup>3</sup> /mol-K]
$s$	=	particle shape factor
$s_i$	=	surface area covered by $i^{\text{th}}$ layer [m <sup>2</sup> ]
$S$	=	total area of all individual area in each layer [m <sup>2</sup> ]
$S_{\text{BET}}$	=	BET surface area [m <sup>2</sup> /g]
$S_0$	=	functional group concentration [mmol/g]
$t$	=	time [s or min]
	=	theoretical time
$T$	=	temperature [°C or K]
TGA	=	thermogravimetric analyzer
$u$	=	pairwise adsorbate-adsorbate interaction energy
$V$	=	vessel volume [cm <sup>3</sup> ]
	=	total volume of gas adsorbed [cm <sup>3</sup> /g]
	=	volume of char at theoretical time $t$ [cm <sup>3</sup> ]
$V_i$	=	volume of gas adsorbed by $i$ layers [cm <sup>3</sup> ]
$V_m$	=	volume of gas adsorbed by monolayer coverage [cm <sup>3</sup> ]
$V_{\text{me+ma}}$	=	mesopore and macropore volume [cm <sup>3</sup> /g]
$V_{\text{mic}}$	=	micropore volume [cm <sup>3</sup> /g]
$V_{\text{tot}}$	=	total pore volume [cm <sup>3</sup> /g]
$V_0$	=	initial volume of char [cm <sup>3</sup> ]
$w$	=	actual mass of sample [mg]
$w_f$	=	final mass of sample [mg]

**SYMBOLS AND ABBREVIATIONS (Continued)**

$w_0$	=	initial mass of sample [mg]
$W$	=	micropore volume being filled by the adsorbate [ $\text{cm}^3/\text{g}$ ]
$W_0$	=	total micropore volume [ $\text{cm}^3/\text{g}$ ]
$x$	=	relative pressure
$\Delta\psi$	=	free energy of the hard sphere
$\Lambda$	=	deBroglie wavelength
$\Omega$	=	grand potential function
$\alpha$	=	conversion defined in terms of the reacted mass fraction
$\beta$	=	heating rate [ $^{\circ}\text{C}/\text{min}$ ]
$\varepsilon$	=	particle porosity
$\varepsilon_{ff}$	=	depth of the intermolecular potential
$\mu$	=	bulk chemical potential
$\pi$	=	constant [3.14159...]
$\theta$	=	fractional coverage
$\rho$	=	average density of the fluid [ $\text{cm}^3/\text{g}$ ]
$\rho_p$	=	density of solid particle [ $\text{cm}^3/\text{g}$ ]
$\sigma_{ff}$	=	molecular diameter
$\tau$	=	macropore tortuosity

# CHAPTER I

## INTRODUCTION

### 1.1 Rationale of the Study

Activated carbon is a versatile adsorbent being used in many separation and purification processes in both liquid and gas phases. Activated carbon is a porous carbon material with high internal surface area and hence high adsorption capacity. It can be prepared by a two-step physical activation with oxidizing gases such as carbon dioxide or steam, or by a one-step chemical activation with inorganic chemicals such as zinc chloride, potassium hydroxide and phosphoric acid. Activated carbon can be commercially produced from a variety of carbonaceous materials, e.g. coconut shell, coal, lignite, wood and some polymers. Due to its industrial significance, the past decade has seen many literatures reporting on the production of activated carbon from agricultural and industrial by-products such as macadamia nut shell (Ahmadpour and Do, 1997), corn-cob (Tseng and Tseng, 2005), apricot stone (Gergova and Eser, 1996), grape seed (Gergova, Petrov and Eser, 1994), almond shell (Gergova et al.; Rodriguez-Reinoso and Molina-Sabio, 1992), olive stone (Rodriguez-Reinoso and Molina-Sabio), peach stone (Rodriguez-Reinoso and Molina-Sabio), cherry stone (Gergova et al.; Lussier, Shull and Miller, 1994), oil-palm shell (Daud, Ali and Sulaiman, 2000), etc. Among these precursors, fruit stone or fruit seed shows good promise for activated carbon production because of its hardness and low ash and heteroatom contents (Lussier et al.).

Because of its abundant availability, longan seed, an inner part of longan fruit, is considered as a potential precursor for activated carbon production in Thailand. Approximately  $7 \times 10^5$  tons of longan fruit was produced in Thailand in the year 2005 (Ministry of Agriculture and Cooperatives, Office of Agricultural Economics, 2006). The harvested fruits are processed and available in the form of fresh-, frozen-, canned-, and dried products. From fruit cannery processes alone, longan seed was discharged as solid waste in the order of 10,000 tons in the year 2005. This waste is generally incinerated or crushed and used as mulch. However, both methods present serious handling problems to the industry. This work was initiated with the aim to convert this waste into useful activated carbon, the process of which is considered to be a more effective means for waste disposal control. If the longan seed based carbon is proved to be a potential adsorbent, it could then be produced on a large scale to supply the increased demand for commercial adsorbents.

The important characteristic of activated carbon is its porosity, which is normally measured in terms of pore size distribution (PSD). The suitable PSD for each desired adsorption application may or may not require the same pattern, but mostly just obey the rule that different molecules need the difference in PSD. Therefore, the tailoring of porosity in produced activated carbon is considered to be one of the challenging tasks. Basically, the main factor used to control the developed porosity is the conditions of preparation, involving the process of carbonization and activation in physical or chemical methods. Therefore, it was decided to study in details the effect of preparation conditions on the porous properties of activated carbon and also to propose a model to predict the pore evolution during the process of physical activation.

Researches on the adsorption in activated carbon have been widely studied and a wealth of information is available in the literature. Adsorption behavior of non-polar molecules has been relatively well understood but not with most of the polar molecules. A good example is water which is considered as one of the most important substance and yet possibly the least well understood on its adsorption behavior. Industrially, the presence of water or humidity in feed stream significantly reduces the selective adsorption capacity in practical operations. Along this line of argument, this work was set up to study the equilibrium of water adsorption in a series of activated carbons prepared under different conditions. These experimental findings should explain the role and effect of porosity on the water adsorption behavior.

Another important aspect in adsorption area is the kinetic study. The difficulties in studying adsorption kinetics in activated carbon are two folds. The first is the complexity of activated carbon surface structure and porous properties leading to difficulty in analyzing the kinetic mechanism. The second is the validity and limitation of the measurement methods. Therefore, there have been less available data in the literature for the kinetic parameters of adsorption in activated carbon. For this reason and the important application of activated carbon in the area of volatile organic compounds (VOC) control in order to prevent the emission of this vapor into the atmosphere, the kinetic adsorption of benzene is therefore included in this research project.

## **1.2 Research Objectives**

The overall objective of this thesis work is to study the preparation and characterization of activated carbon from the longan seed and investigate the

adsorption behavior of derived activated carbon for some representative molecules. The research scheme includes the thermal analysis of longan seed, the preparation of activated carbon, the equilibrium and the kinetic study. The specific objectives of this research are:

**1.2.1** To study thermal analysis of longan seed in a non-isothermal pyrolysis mode by using a thermogravimetric analyzer. The behavior and kinetics of longan seed decomposition in the pyrolysis process is examined.

**1.2.2** To prepare the activated carbons from longan seed by physical and chemical activation and also to characterize the porous structure of derived activated carbons. Evolution of pores is elucidated by developing a model to describe its hierarchical behavior.

**1.2.3** To investigate the equilibrium adsorption of water using a series of longan seed derived-activated carbon with different pore size distributions. The ethanol adsorption is also performed for comparison as another polar adsorbate.

**1.2.4** To elucidate the kinetics of benzene adsorption in longan seed activated carbon by using the constant molar flow rate technique. The kinetics parameters i.e. pore diffusivity and surface diffusivity are determined.

### **1.3 Scope and Limitations**

The porous properties of activated carbon are known to be influenced by the composition and type of precursor. This study is limited to the use of longan seed produced from the fruit factory of Malee Sampran Public Company Limited, Nakhon Pathom, Thailand. The major method in activated carbon preparation is by physical activation because it is more environmentally favorable than chemical activation. Experimental

study of adsorption equilibrium is focused on the water adsorption and ethanol adsorption is additionally performed for comparison. In the kinetic part, the constant molar flow rate (CMF) technique with the combination of pore and surface diffusion controlling is applied for the determination of relevant kinetic parameters by the analysis of asymptote at long time solution.

## 1.4 Research Development

This dissertation is divided into 7 chapters. The introduction in **Chapter I** describes the rationale and the objectives of the research. The scope and limitations in this research are also listed in this part. **Chapter II** provides some background theories that are basically required in the activated carbon field. It includes the details of the structure, manufacture, application, and also the commonly used characterization methods for activated carbon. Reporting on the research results commences by the thermogravimetric analysis of longan seed which is presented in **Chapter III**. The kinetic parameters of longan seed pyrolysis under the non-isothermal are calculated by the optimization technique using the kinetics reaction model of one-step global model and two-parallel reactions model. In **Chapter IV**, the preparation of activated carbon is presented to examine the effect of preparation conditions on the porous properties of activated carbons. The preparation methods include the conventional two-step physical activation, one-step physical activation and chemical activation. In addition, a model of carbon activation is proposed to follow the gasification reaction of the longan seed char. The progressive development of porosity in activated carbon for each stage of burn-off level is elucidated by this model. To explore the use of prepared activated carbon in some applications, the

equilibrium study of water and ethanol adsorption in activated carbon are demonstrated in **Chapter V**. **Chapter VI** presents the kinetic study of benzene adsorption in longan seed activated carbon by using the constant molar flow rate technique. Finally, **Chapter VII** concludes the findings from this dissertation and some recommendations for future study.

### **1.5 Expected Results from the Study**

This work has a major purpose to investigate the porous properties of activated carbon that can be produced from the new precursor, longan seed. The information of this investigation is derived and will provide the useful data for future development of commercial production and applications of activated carbon. A carbon activation model is proposed which is invaluable in predicting the pore evolution of activated carbon and could be further refined to give a generalized model that can be extended to other different precursors. In addition, further studies of the subjects in adsorption equilibria of water and ethanol and information on kinetic study of benzene adsorption should provide a body of knowledge that can be applied to the practical systems.

### **1.6 References**

- Ahmadpour, A. and Do, D. D. (1997). The preparation of activated carbon from macadamia nutshell by chemical activation. **Carbon** 35: 1723-1732.
- Daud, W. M. A. W., Ali, W. S. W. and Sulaiman, M. Z. (2000). The effects of carbonization temperature on pore development in palm-shell-based activated carbon. **Carbon** 38: 1925-1932.

- Gergova, K. and Eser, S. (1996). Effects of activation method on the pore structure of activated carbons from apricot stones. **Carbon** 34: 879-888.
- Gergova, K., Petrov, N. and Eser, S. (1994). Adsorption properties and microstructure of activated carbons produced from agricultural by-products by steam pyrolysis. **Carbon** 32: 693-702.
- Lussier, M. G., Shull, J. C. and Miller, D. J. (1994). Activated carbon from cherry stones. **Carbon** 32: 1493-1498.
- Ministry of Agriculture and Cooperatives, Office of Agricultural Economics. (2006). **Production of the important agricultural products in Thailand** [On-Line]. Available: <http://www.oae.go.th/Prcai/Longan.xls>
- Rodriguez-Reinoso, F. and Molina-Sabio, M. (1992). Activated carbons from lignocellulosic materials by chemical and/or physical activation: an overview. **Carbon** 30: 1111-1118.
- Tseng, R-L. and Tseng, S-K. (2005). Pore structure and adsorption performance of the KOH-activated carbons prepared from corncob. **J. Colloid Interface Sci.** 287: 428-437.

## **CHAPTER II**

### **LITERATURE REVIEW**

#### **2.1 Activated Carbon**

Charcoal or carbonized wood was first used as an adsorbent for medicinal purposes and in the food and drinking purification by Egyptians in around 1500 B.C. (Bansal, Donnet and Stoeckli, 1988). There is an evidence that the ancient Hindus also used charcoal to filter their water. The charcoal was first applied to the refinement of sugar in 1794 (Jankowska, Swiatkowski and Choma, 1991). At present, charcoal was changed the nomenclature to ‘activated carbon’, which is from the fact that the precursors may come from animal, vegetable or mineral origin (Hassler, 1963).

Activated carbon can be produced from various carbonaceous materials such as peat, wood, lignite, coal, fruit pits and shells. The world demand for activated carbon in the year 2005 is 970,000 tons which can be divided for each region as follows: 52% in Asia/Pacific, 26% in North America, 13% in Western Europe and 9% for other regions. It is forecast to expand around 5% per year through 2009 to over 1.2 million tons in 2010 (Freedonia Group, 2006).

There are about 150 companies manufacture activated carbons around the world, with the leading industrial companies including Calgon Carbon, NORIT, MeadWestvaco, PICA, CECA, Kuraray and Takeda. The market of activated carbon in developed nations is growing in the pharmaceutical and medical sector. Nevertheless, in the developing market it is driven by a grater emphasis on environment issues

including water treatment applications, flue gas treatment and hazardous waste remediation. In addition, the using of activated carbon in specialized motor vehicle filtration products, particularly cabin air filters, will have strong growth prospect (Freedonia Group, 2006).

### **2.1.1 Structure and Surface Chemistry**

Activated carbon possesses versatile characteristics in adsorption by its extremely high surface area and pore volume. However, the structure of activated carbon is one of the most complex structures in porous solids. Basically, activated carbon structure consists of the amorphous structure and the graphite-like microcrystalline structure. The graphite-like structure is dominant for the contribution of the porosity to accommodate the adsorbate molecules. This porosity originates from the free interstices between the graphene layers that are arranged in a disordered structure. This disorganized structure makes the pores to cover the broad range of pore sizes. The pore of activated carbon is normally assumed as the slit shape with the pore size being reported as the pore half width. Among the graphene layers, there are some defect and the presence of built-in heteroatoms such as hydrogen, oxygen, nitrogen and sulphur, as well as inorganic material such as metal oxides and metal particles. These atoms may present in form of the surface functional groups such as carboxyl, lactones, phenol, carbonyl, ether, pyrone and chromene. These surface groups are shown diagrammatically in Figure 2.1. The heteroatoms or the groups present are dependent upon the precursor including the conditions during manufacture.

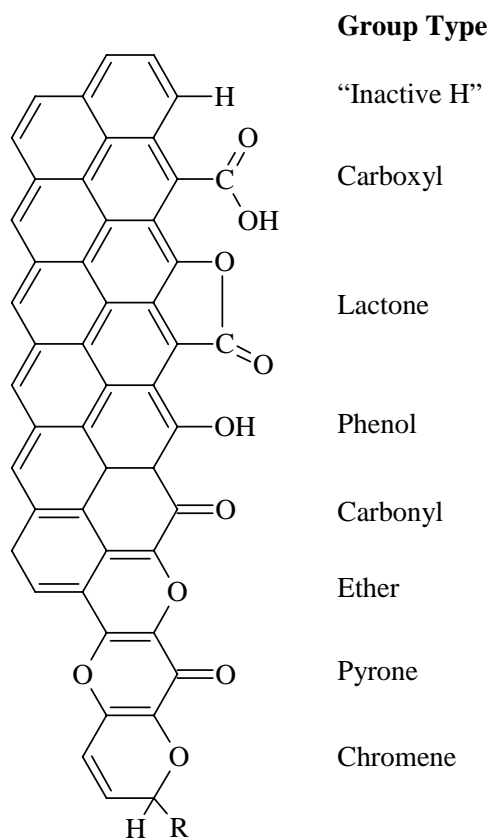


**Figure 2.1** Examples of surface functional groups on carbon surface (Leon y Leon D and Radovic, 1994).

The widely used image to represent the molecular structure of activated carbon is exhibited as a hierarchical structure in Figure 2.2 (Bandosz et al., 2003). The fundamental building block is called the basic structural unit (BSU). This BSU is composed of the layers of the polyaromatic-like molecules. Some functional groups may present at the edge of these layers as stated above. Therefore, the layering of these aromatic layers differs from the graphite-like order structure. Generally, the interlayer spacing is greater than that of graphite structure. The turbostratic is seen in the disorder in the c direction in Figure 2.2. The BSUs are assembled to be the region of local molecular orientation (LMO). The end of this hierarchy is the assembling of

the LMOs to yield the complex structure which constitute the porosity in its structure as seen in the figure.

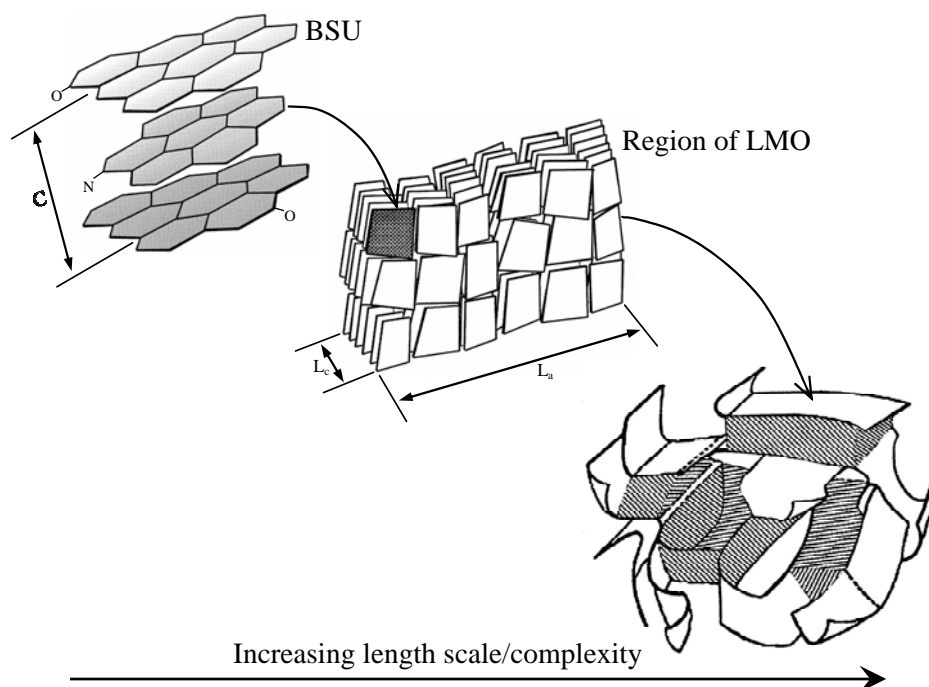


**Figure 2.2** A hierarchical view of the molecular structure of an activated carbon (Bandosz et al., 2003).

### 2.1.2 Manufacture

The commercial production of activated carbon is strongly dependent on many factors such as economics, including collection, transportation, sustainable supply and price. Based on these limitations the favorable precursors in industrial production are softwood, hard wood, peat, lignin, coal, and coconut shell. Some special activated carbons are produced from carbon fibers and synthetic non-fusing polymer such as PAN and SARAN. In industrial production, activated carbon is normally manufactured by two distinct methods, physical activation which involves

carbonization at relatively low temperature followed by activation at high temperature with steam or carbon dioxide at elevated temperature. The second method is chemical activation which involves the addition of chemicals such as zinc chloride or phosphoric acid before carbonization. Activated carbon product is generally produced in the forms of granular, powder or extruded. The requiring form depends on the application; in gas phase likely to be the granular or extruded, whereas the powder is preferred in liquid phase system.

### **2.1.3 Carbonization**

Carbonization is the process to remove the volatile matters from the carbonaceous material by thermal decomposition under the inert atmosphere. It is normally undertaken at temperature between 600°C and 1000°C. The derived product essentially consists of fixed carbon called char. The purpose of carbonization is to produce the carbon structure and to create an initial porosity in the char. Char properties including chemical and textural structure properties are important to be the imprint effect on the final activated carbon product. Therefore, the requirement of char properties is dependent markedly on the requirement of activated carbon quality.

On carbonization, some small molecules such as water, carbon dioxide, and low molecular weight organics are thermally removed from the precursors. This gives the original solid state lattice to consist dominantly of residual carbon remaining more or less intact. The position vacated by the constituent atoms of the volatiles decomposition products are the created porosity. This new carbon lattice which contains the porosity is quite disorganized but with further heating becomes more structured resembling to the hexagonal array of carbon atoms as found in sheets or graphene layers which constitute single crystal graphite.

As an example, the char formation from coal pyrolysis is revealed that there are many processes in competition (Mastral, Rubio, Membrado and Fananas, 1990). On one hand, there is a progressive depolymerization, leading to gas, water and tars formation and, on the other hand, there is a condensation or repolymerization process leading to char formation. The first is the consequence of thermal breaking of the network component and of the release of the mobile component depending on the conversion conditions. The second process is the consequence of recombination and condensation reactions between thermal fragments.

The affecting parameters to this process are the heating rate, final temperature, holding time at final temperature and the most important is the chemical and physical properties of the precursor. The initial properties of the parent material results in the difference of created carbon lattices, whereas the carbonization conditions influence the amount of the volatiles being released from the raw material and eventually affecting the yield and porosity of the char.

#### **2.1.4 Activation**

The activation is the process to create the porosity of final product, activated carbon, in such a way to satisfy the required application. This activation step is crucial for tailoring the pore size distribution of the carbon. Commonly used activation processes can be divided into two main types: physical activation and chemical activation. Physical activation has a purpose to enhance or develop the porosity in carbonized char. This method is achieved by gasifying the carbon in char with the oxidizing gas such as steam or carbon dioxide in the temperature range 850-1100°C. Chemical activation is carried out in a single step by thermal decomposition

or carbonization of the precursor impregnated with chemical agents such as zinc chloride or phosphoric acid at lower temperatures between 500-900°C.

#### **2.1.4.1 Physical Activation**

The char obtained from carbonization contains only low level of microporosity. Physical activation involves the development of the porosity by removing carbon via reaction of gasification with an oxidizing gas, typically steam or carbon dioxide. Gasification level known as burn-off is dependent on the properties of char carbon and the activation conditions including temperature, activation time, composition and flow rate of oxidizing gases etc. The study of mechanism of such gasification reaction has been attempted for many years so far. However, the exact mechanisms are still debating. The simplest explanation is that gasification proceeds by the progressive removal of carbon atoms by the gas molecules. The reaction also needs to be carried out under conditions where the intrinsic reaction is the rate-controlling step. The relative rates of gasification of graphite by oxidizing gases have been studied at 800°C and 0.1 atm (Yang, 2003), and the corresponding heats of reaction (Bansal et al., 1988) are shown in Table 2.1. The gasification by carbon dioxide requires a higher temperature than with oxygen or steam resulting from a lesser in energetic reaction. Commercial production normally employs the flue gas adding with a certain amount of steam, so that a combination of activation with steam and carbon dioxide can occur. Oxygen is rarely used as oxidizing gas in practice. This results from its exothermic combustion reaction leading to the excessive burning which is difficult to control.

**Table 2.1** Gasification reactions of carbon by three oxidizing gases.

<b>Gasification reaction</b>	<b>Approx. Relative rate (at 800°C and 0.1 atm)</b>	<b>Heat of reaction [kcal]</b>
$C + O_2 \longrightarrow CO_2$	$1 \times 10^5$	+92.4
$C + H_2O \longrightarrow CO + H_2$	3	-29
$C + CO_2 \longrightarrow 2CO$	1	-39

The major target of activation is to tailor the pore size distribution of derived activated carbon to satisfy the required application system. The main factors influencing the control of porosity are the activation conditions which are represented as the degree of burn-off. It has been observed that the major portion of early pore development occurs by burning of single aromatic sheet followed by gasification of walls of layer planes leading to the creation of the larger pores (Kalback, Brown and West, 1970). Dubinin and Zaverina (1949) found in their work that for burn-off higher than 75%, the product resulted from the collapse of the microporous structure and the derived structure was predominantly macroporous. The burn-off lower than 50% produced the carbon with the high contribution of the microporous and for the burn-off range between 50-70% the resulting carbons possess the combination of micro and mesoporous character.

#### **2.1.4.2 Chemical Activation**

The method of chemical activation proceeds by impregnating a precursor with a chemical reagent. This chemical added sample is further carbonized in an inert atmosphere at temperature in the range of 400-800°C. The activating agents

used normally are phosphoric acid ( $\text{H}_3\text{PO}_4$ ), zinc chloride ( $\text{ZnCl}_2$ ), and sulfuric acid ( $\text{H}_2\text{SO}_4$ ). The other types of chemical that have also been suggested are potassium sulfide ( $\text{K}_2\text{S}$ ), potassium hydroxide ( $\text{KOH}$ ) and carbonates of alkali metals, chlorides of calcium, magnesium and ferric iron (Bansal et al., 1988). These inorganic chemicals serve to degrade and dehydrate the lignocellulosic materials and, simultaneously, to prevent the shrinkage during carbonization, whereby reducing the amount of volatile matters released, and so increasing the carbon yield. The cross-linking and aromatization in the carbon structure occurring during carbonization further enhances the pore development. Therefore, the chemical activation is carried out without further need for activation in oxidizing gases.

The mechanism associated with pore generation depends on the chemical types, giving activated carbon with different pore structures. For example in the preparation of chemically activated carbon from macadamia nutshell, the micropores were predominantly created when the low range chemical ratio of  $\text{ZnCl}_2$  and  $\text{KOH}$  were used. Pore widening is a predominant mechanism for  $\text{ZnCl}_2$  series with increasing in chemical ratio, while in the case of  $\text{KOH}$  the micropore still plays an important role (Ahmadpour and Do, 1997). The chemically activated carbon could be produced with high surface area over  $3,000 \text{ m}^2/\text{g}$  where this value was calculated by BET equation with the  $\text{N}_2$  adsorption isotherm (Otowa, Tanibata and Itoh, 1993). This type of carbon is made from the mixing of petroleum coke and the excess amount of  $\text{KOH}$  by carbonizing at about  $700^\circ\text{C}$  and the product is commercially available. The suggested mechanism was that at the temperature approximately  $700^\circ\text{C}$  the potassium metal is considered to be generated by the reduction reactions and then

these metallic molecules moves to intercalate in the carbon matrix, leading to the widening of the carbon layers and the forming of pore structure.

### 2.1.5 Porosity and Pore Size Distribution

Activated carbon possesses the pores in various sizes. However, based on the experiences in adsorption, all porosity is classified into three groups. These three groups are classified by IUPAC (1972) as follows:

- Micropore: pore width of less than 2 nm
- Mesopore: pore width between 2 and 50 nm
- Macropore: pore width of greater than 50 nm

The definitions are based on adsorption behavior and are not strictly absolute. Generally, pore size distribution in activated carbon is polymodal and there are various methods available for porosity measurement as listed in Table 2.2. These methodologies are based on the wide range of techniques and the range of expertise needed to interpret the data.

**Table 2.2** Methodologies of direct and indirect analyses of porosity (Marsh, 2001).

Methodology	Value
1) Adsorption isotherms.	
– Effective surface area based on nitrogen adsorption at $-196^{\circ}\text{C}$ [ $\text{m}^2/\text{g}$ ]	500-2,500
– Surface areas using other adsorbates [ $\text{m}^2/\text{g}$ ]	
– Volumes in micro-, meso- and macroporosity [ $\text{cm}^3/\text{g}$ ]	0.5-2.5
– Isotherm constants (energetics) ‘b’ of the Langmuir equation and ‘C’ of the BET equation	

**Table 2.2** Methodologies of direct and indirect analyses of porosity (Continued).

Methodology	Value
<ul style="list-style-type: none"> <li>– Gradient of plot of <math>\log n_a</math> versus <math>\log^2 P/P^0</math> (DR equation) as an indicator of pore (energy) size distribution and mean pore diameter.</li> <li>– Use of the Dubinin-Astakhov, Dubinin-Izotova and Dubinin-Stoeckli equations</li> <li>– Distributions of characteristic energies of adsorption</li> </ul> <ol style="list-style-type: none"> <li>2) Fractal dimension calculations</li> <li>3) Transmission Electron Microscopy</li> <li>4) Phase-contrast, lattice-imaging, High-Resolution Transmission Electron Microscopy (HRTEM) to reveal structure</li> <li>5) Dark-field TEM, indicating stacking order of lamellar constituent molecules (LCM) or graphene layers.</li> <li>6) Small angle X-ray scattering (SAXS) and Small angle neutron scattering (SANS).</li> <li>7) Molecular sieve experiments.</li> <li>8) Pre-adsorption of n-nonane.</li> <li>9) Scanning tunneling microscopy and atomic force microscopy to reveal atomic surface features.</li> <li>10) Calorimetry to measure the energetics and dynamics of adsorption and desorption.</li> <li>11) <math>^{13}\text{C}</math> Nuclear Magnetic Resonance.</li> <li>12) X-ray photoelectron spectroscopy (XPS).</li> <li>13) Computer molecular modeling to simulate structures using minimum energy considerations.</li> </ol>	

**Table 2.2** Methodologies of direct and indirect analyses of porosity (Continued).

Methodology	Value
14) Dynamic breakthrough curves.	
15) Particle size [mm or sieve sizes]	
16) Apparent density [g/cm <sup>3</sup> ]	
17) Particle density [g/cm <sup>3</sup> ]	
18) Hardness number	50-100
19) Abrasion number	
20) Ash content [wt%]	1-20
21) CCl <sub>4</sub> activity	35-125
22) Butane working capacity [g/100cm <sup>3</sup> ]	4-14
23) Iodine number	500-1,200
24) Decolorizing index (Westvaco)	15-25
25) Molasses number (Calgon)	50-250
26) Molasses number (Norit)	300-1,500
27) Heat capacity at 100°C [J/g-K]	0.84-1.3
28) Thermal conductivity [W/m-K]	0.05-0.10

### 2.1.6 Applications

Activated carbon is a dominant adsorbent in the group of the generic adsorbents using in industrial adsorption processes. The estimation of worldwide sales of these adsorbents are, \$ 1 billion for activated carbon, \$ 100 million for zeolites, \$ 27 million for silica gel and \$ 26 million for activated alumina (Humphrey and Keller, 1997). Activated carbon has a broad range of applications. Principal applications of it include gas separation, gas purification, solvent recovery, water

treatment, food and beverage processing, chemical and pharmaceutical processing, sewage treatment, catalyst supports and gold recovery. Examples of the use of activated carbon in commercial adsorption processes are listed in Table 2.3.

**Table 2.3** Examples of commercial adsorption processes using activated carbon  
(Yang, 2003).

Process	System
Gas bulk separations	<ul style="list-style-type: none"> <li>• CO, CH<sub>4</sub>, CO<sub>2</sub>, N<sub>2</sub>, Ar, NH<sub>3</sub>/H<sub>2</sub></li> <li>• Hydrocarbons/vent streams</li> </ul>
Gas purification	<ul style="list-style-type: none"> <li>• Hydrocarbons, halogenated organics, solvents/vent streams</li> <li>• SO<sub>2</sub>/vent stream</li> <li>• Indoor air pollutants-VOCs</li> <li>• Tank-vent emissions/air or nitrogen</li> </ul>
Liquid purification	<ul style="list-style-type: none"> <li>• Organics, halogenated organics, oxygenated organics etc. /H<sub>2</sub>O-water purification</li> <li>• Inorganics (As, Cd, Cr, Cu, Se, Pb, F, Cl, radionuclides, etc.) /H<sub>2</sub>O-water purification</li> <li>• Odor and taste bodies/H<sub>2</sub>O</li> <li>• Decolorizing petroleum fractions, syrups, vegetable oils, etc.</li> <li>• Various fermentation products/fermentor effluent</li> <li>• Drug detoxification in the body</li> </ul>

## 2.2 Gas and Vapor Adsorption

The term 'sorption' was proposed by McBain in 1909 to describe the phenomenon of adsorption on the surface, absorption by penetration into the lattice of the solid, and capillary condensation within the pores. The process of adsorption is to separate the selective component from the bulk stream by a porous solid. Therefore, the porous solid is the heart of adsorption process. Typically, the fluid molecules (gas or liquid) to be removed is called adsorbate, whereas the porous material is referred to as adsorbent.

Adsorption could be divided into two main categories, physical adsorption (physisorption), and chemical adsorption (chemisorption). In physisorption, there is no direct bonding between adsorbate molecules and adsorbent surface. Their interactions result from the formation of relatively weak intermolecular forces such as London dispersion forces, or van der Waals forces from induced dipole-dipole interactions. On the other hand, chemisorption involves the transfer of electron between the adsorbate and the surface leading to direct chemical bonding between these two species. The general characteristics of physical and chemical adsorption are listed in Table 2.4. However, the clear distinction between physisorption and chemisorption is somewhat arbitrary.

**Table 2.4** General characteristics of physical and chemical adsorption.

	<b>Physical Adsorption</b>	<b>Chemical Adsorption</b>
<b>Heat of adsorption</b> [kJ mol <sup>-1</sup> ]	20-40 c.f. heats of liquefaction	> 80 c.f. bulk-phase chemical reaction
<b>Rate of adsorption</b> (at -196°C)	Fast	Slow
<b>Adsorbed amount with increasing temperature</b>	Decrease	Increase
<b>Desorption</b>	Easy By reducing pressure or increasing temperature	Difficult High temperature required to break bonds
<b>Desorbed species</b>	Adsorbate unchanged	May be different to original adsorptive
<b>Specificity</b>	Non-specific	Very specific
<b>Adsorbate layer coverage</b>	Mono or multilayers depending on conditions	Monolayer

### 2.3 Adsorption Equilibrium

Among the information in adsorption, equilibrium is the most important piece of information necessary for the understanding of adsorption process. Basically, the adsorption equilibrium of a single component is the essential data for subsequent analysis of the adsorption kinetics of a single component, adsorption equilibrium of

multicomponent system, and the adsorption kinetics of multicomponent system (Do, 1998).

### 2.3.1 Adsorption Isotherms

In gas systems, the relation between the extent of adsorption (mmol/g of adsorbent) and the equilibrium partial pressure ( $P/P^0$ ) at constant temperature is conventionally called the adsorption isotherm. Adsorption data may alternatively be interpreted in terms of an isobar, the variation in adsorbed amount with temperature at constant pressure, or an isostere, the temperature variation with pressure at a constant surface coverage. The adsorption isotherm provides some useful information about the adsorbent characteristic and the interaction between adsorbate and adsorbent, including:

- Estimates of surface area, pore volume and pore size distribution;
- Assessment of the surface chemistry of adsorbent and fundamental of adsorption processes;
- Assessment of the adsorption capacity and the efficiency of adsorbent.

The adsorbed amount is usually denoted by  $n$ , expressed in mmol per gram of solid, Generally,  $n$  depends on temperature  $T$ , pressure  $P$  of the vapor, and the nature of both adsorbate and the adsorbent, as can be expressed by the following equation:

$$n = f(P, T, \text{adsorbate}, \text{adsorbent}) \quad (2.1)$$

For a particular system of adsorbate and adsorbent at a constant temperature, this equation simplifies to

$$n = f(P)_{T, \text{ adsorbate, adsorbent}} \quad (2.2)$$

By working below the saturation vapor pressure ( $P^o$ ), the pressure may be expressed in terms of relative pressure ( $P/P^o$ );

$$n = f(P/P^o)_{T, \text{ adsorbate, adsorbent}} \quad (2.3)$$

The majorities of adsorption isotherms in physical adsorption may typically be grouped into six classes, from which the five types of I to V was originally classified by Brunauer, Deming, Deming and Teller (1940). The additional classification is the type VI implying the stepped isotherm. Their typical shapes of isotherms are shown in Figure 2.3.

All adsorption isotherms should be categorized by one or a combination of two or more of these isotherms. The detail of each isotherm is outlined below.

**Type I isotherm:** This isotherm is the Langmuir type, showing a monolayer coverage adsorption. The adsorbents are dominated by microporous structure. The majority adsorption occurs at relative pressures below 0.1 and usually complete at the relative pressure approximately 0.5. Examples include the  $N_2$  adsorption at  $-196^\circ\text{C}$  on microporous activated carbons.

**Type II isotherm:** It involves the BET adsorption mechanism, monolayer coverage is followed by multilayering at high relative pressures. The  $N_2$

adsorption at  $-196^{\circ}\text{C}$  on activated carbons having the distribution of pores produces the type II isotherm.

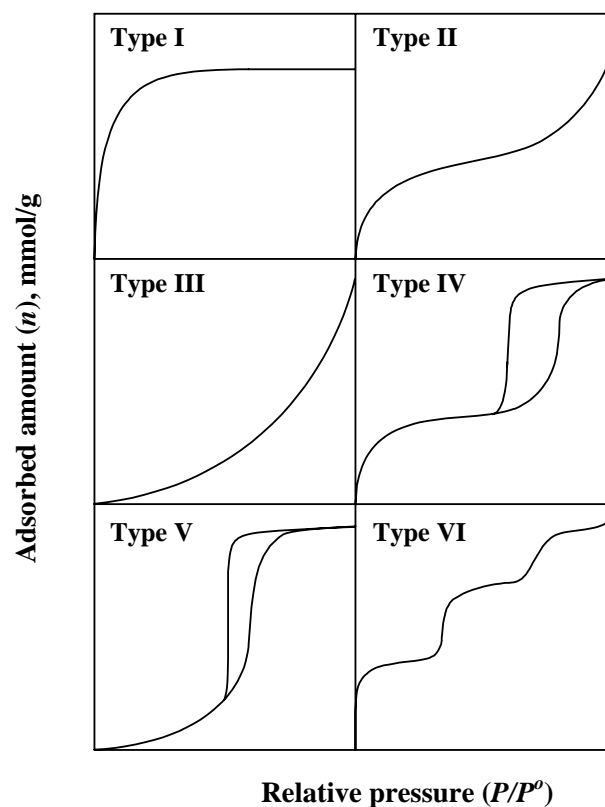


**Figure 2.3** The five types of adsorption isotherm, I to V, in the classification of Brunauer, Deming, Deming and Teller (BDDT), together with Type VI, the stepped isotherm (Gregg and Sing, 1982).

Type III isotherm: This class of isotherm exhibits a characteristic of weak adsorbate–adsorbent interactions, leading to a low capacity of the uptake at low relative pressure. This behavior usually occurs in the adsorption of water on activated carbon because of the non-polar nature of the carbon surface. However, the presence of the oxygenated surface functional groups of activated carbon may act as the

primary sites for water to adsorb on, and then this adsorbed molecule further acts as the secondary site for the other water molecules to adsorb on by hydrogen bonding. The growing of the water cluster around the oxygenated group leads to rapid uptake at higher relative pressures.

Type IV isotherm: The general behavior of this isotherm is the same as type II isotherm, but this type exhibits a limit uptake when the pressure approaches the saturation pressure. The hysteresis loop is generally associated with the presence of mesoporosity.

Type V isotherm: This isotherm type is the same as the type III, the differences are the limit uptake and the presence of hysteresis loop. The water adsorption isotherm on activated carbon may be classified as type V.

Type VI isotherm: This isotherm shape is due to the complete formation of monolayer before the progression to a subsequent layer. Halsey (1948) proposed this isotherm occurs for the adsorption on extremely homogeneous, non-porous surfaces where the monolayer capacity corresponds to the step height. The example is the krypton adsorption at 77.2 K on graphitized carbon black (Kratochvíl, Rathousky and Zukal, 1999).

### **2.3.2 Adsorption Isotherm Equations**

There are various equations developed to describe the adsorption equilibrium. This section will present only some basic examples of those equations that are restricted to the ones related to this work.

#### **2.3.2.1 Langmuir Equation**

The most basic theory in adsorption is due to Langmuir (1918). He first developed the equation for the vapor adsorption on a plane surface of mica.

The Langmuir equation is based on three major assumptions:

1. The surface of adsorbent exhibits constant adsorption energy over all the surface sites.
2. Only one molecule can be adsorbed on any one site and the saturation of adsorption occurs at the monolayer coverage.
3. There are no interactions between any of the adsorbed molecules.

The Langmuir equation was originated from the basis of dynamic equilibrium meaning that the rate of molecules being adsorbed onto the surface equal the rate of removing of the adsorbed molecules from the surface.

The rate of gas molecule striking a surface, defined with the unit of mole per unit time and unit area, is given by

$$R_s = \frac{P}{\sqrt{2\pi MR_g T}} \quad (2.4)$$

Langmuir (1918) defined the coefficient to account for the non perfect sticking of molecule striking the surface, which is called sticking coefficient ( $\alpha$ ).

So the rate of adsorption in mole adsorbed per unit bare surface area per unit time is

$$R_a = \frac{\alpha P}{\sqrt{2\pi MR_g T}} \quad (2.5)$$

The rate of adsorption on an occupied surface is equal to the rate on bare surface multiplied by the fraction of empty sites,

$$R_a = \frac{\alpha P}{\sqrt{2\pi MR_g T}}(1-\theta) \quad (2.6)$$

where  $\theta$  is the fractional coverage. Equation 2.6 represents the number of moles adsorbed per unit area (including covered and uncovered area) per unit time.

The rate of desorption is defined as

$$R_d = k_d \theta \quad (2.7)$$

where  $k_d$  is the rate at which the gas would desorb if the surface are fully covered and

$$k_d = k_{d\infty} \exp\left(\frac{-E_d}{R_g T}\right) \quad (2.8)$$

where  $E_d$  is the activation energy for desorption, which is normally equal to the heat of adsorption for physical adsorption. The  $k_{d\infty}$  is the rate constant for desorption at infinite temperature.

When the gas is in equilibrium with the surface, the rate of adsorption is equal to the rate of desorption:

$$\frac{\alpha P}{\sqrt{2\pi MR_g T}}(1-\theta) = k_d \theta \quad (2.9)$$

Finally, the following famous Langmuir isotherm written in terms of fractional loading reads:

$$\theta = \frac{bP}{1+bP} \quad (2.10)$$

$$b = \frac{\alpha}{k_d \sqrt{2\pi MR_g T}} = \frac{\alpha \exp\left(\frac{E_d}{R_g T}\right)}{k_{d\infty} \sqrt{2\pi MR_g T}} \quad (2.11)$$

The parameter  $b$  is the affinity constant or Langmuir constant. It indicates the strength of an adsorbate molecule to be attracted onto a surface.

### 2.3.2.2 Brunauer-Emmett-Teller (BET) Equation

Brunauer, Emmett and Teller (1938) formulated the theory called BET equation to describe the multiplelayer adsorption on a flat surface. The BET has the following assumptions, basically the same as in the Langmuir theory:

1. The adsorbent surface consists of a regular array of adsorption sites with a constant enthalpy of adsorption in the monolayer,  $\Delta H_A$ .
2. The adsorption is localized to these sites.
3. The neighboring adsorbed molecules do not interact.
4. Multilayer formation is unlimited.
5. The enthalpy of adsorption in the second and subsequent multilayer is equal to the enthalpy of liquefaction,  $\Delta H_L$ .
6. The adsorption or desorption may only occur on or from exposed sites.

Let  $s_0, s_1, s_2, s_n$  be the surface areas covered by no layer, one layer, two layer and  $n$  layers of adsorbate molecules, respectively. The BET equation

used the equilibrium approach as proposed by Langmuir, i.e., the rate of adsorption on any layer is equal to the rate of desorption from that layer. Therefore, the rates of adsorption onto the free surface are equal to the rate of desorption from the first layer,

$$a_1 P s_0 = b_1 s_1 \exp\left(\frac{-E_1}{R_g T}\right) \quad (2.12)$$

where  $a_1$ ,  $b_1$  and  $E_1$  are constant, independent of the amount adsorbed. The  $E_1$  is the interaction energy between the solid and molecule of the first layer and its value is generally higher than the heat of vaporization.

Similarly, the rate of adsorption onto the first layer should be equal to the rate of desorption from the second layer,

$$a_2 P s_1 = b_2 s_2 \exp\left(\frac{-E_2}{R_g T}\right) \quad (2.13)$$

Therefore, for the  $i$ -th layer,

$$a_i P s_{i-1} = b_i s_i \exp\left(\frac{-E_i}{R_g T}\right) \quad (2.14)$$

The sum of all individual area in each layer is the total area, that is

$$S = \sum_{i=0}^{\infty} s_i \quad (2.15)$$

Therefore, the volume of gas adsorbed by one layer of molecules becomes

$$V_1 = V_m \left( \frac{s_1}{S} \right), V_m \text{ is the monolayer coverage} \quad (2.16)$$

The amount adsorbed for two layers of adsorbed molecules,

$$V_2 = V_m \left( \frac{2s_2}{S} \right) \quad (2.17)$$

Similarly, the volume of gas adsorbed by  $i$  layers is,

$$V_i = V_m \left( \frac{i s_i}{S} \right) \quad (2.18)$$

The total volume of gas adsorbed at a given pressure is the total of these volumes.

That is,

$$V = \frac{V_m}{S} \sum_{i=0}^{\infty} i s_i = V_m \frac{\sum_{i=0}^{\infty} i s_i}{\sum_{i=0}^{\infty} s_i} \quad (2.19)$$

Finally, the famous BET equation contains two fitting parameters,  $C$  and  $V_m$  was derived and represented by the equation,

$$\frac{V}{V_m} = \frac{CP}{(P^o - P)[1 + (C - 1)(P / P^o)]} \quad (2.20)$$

### 2.3.2.3 Dubinin-Radushkevich (DR) Equation

The Dubinin-Radushkevich (DR) equation is based on the adsorption potential theory of Polanyi (Do, 1998) and the adsorption process is by micropore volume filling as opposed to layer by layer adsorption on pore walls for adsorption in larger pores.

The Polanyi adsorption potential ( $A$ ) is given by:

$$A = R_g T \ln \left( \frac{P^o}{P} \right) \quad (2.21)$$

The adsorption potential is considered as the differential molar work of adsorption (Do, 1998). The parameter  $P^o$  is the saturation pressure of the free liquid at temperature  $T$ .

The fraction of the micropore volume occupied by the adsorbate  $\theta$  is

$$\theta = \frac{W}{W_0} \quad (2.22)$$

where  $W$  is the micropore volume being filled by the adsorbate and  $W_0$  is the total of micropore volume.

The distribution function of the filling of micropores,  $\theta$ , over the differential molar work of adsorption is

$$\theta = f(A/E, n) \quad (2.23)$$

where  $E$  is the characteristic energy, a measure of the adsorption strength between adsorbate and adsorbent molecules. And  $n$  is the parameter associated with the distribution function.

Dubinin and Radushkevich chose the functional form of the Weibull distribution for the distribution function  $f$  in Equation 2.23, that is

$$f(A/E, n) = \exp\left[-\left(\frac{A}{E}\right)^n\right] \quad (2.24)$$

The parameter  $n$  was first suggested to be equal to 2 by Dubinin and Radushkevich (1947), the following adsorption equation is thus called the DR equation

$$\theta = \exp\left[-\left(\frac{A}{E}\right)^2\right] \quad (2.25)$$

By substituting  $\theta$  and  $A$  into Equation 2.25, the equation is rewritten as

$$W = W_0 \exp\left[-\left(\frac{A}{E}\right)^2\right] = W_0 \exp\left[-\left(\frac{R_g T}{E}\right)^2 \ln^2\left(\frac{P^o}{P}\right)\right] \quad (2.26)$$

#### 2.3.2.4 Dubinin-Astakhov (DA) Equation

The DR equation is not fully applicable to adsorption on porous solids with high degree of surface heterogeneity, for instance, with the carbonaceous solids prepared at high degree of burn-off showing the increasing in the degree of heterogeneity because of the wider pore size distribution (Do, 1998). Therefore, the

DR has been extended by Dubinin and Astakhov (1971) who proposed the more general form of equation to account for this surface heterogeneity as

$$\theta = \exp\left[-\left(\frac{A}{E}\right)^n\right] \text{ or } W = W_0 \exp\left[-\left(\frac{A}{E}\right)^n\right] \quad (2.27)$$

This equation is called DA equation. Dubinin and Astakhov suggested that  $n$  takes values  $1 \leq n \leq 3$ , depending on the porosity of adsorbents. Normally, it is suggested that  $n = 1$  for mesoporous activated carbons,  $n = 2$  for microporous activated carbons and  $n = 3$  for some carbon molecular sieve with a narrow pore size distribution.

### 2.3.3 Surface Area and Pore Volume Determination

#### 2.3.3.1 Langmuir Equation

The surface area can be computed from the Langmuir equation.

The Langmuir equation is (Equation 2.10)

$$\theta = \frac{bP}{1 + bP}$$

Substituting  $\theta = V/V_m$  and rewriting the equation in linear form to obtain

$$\frac{P}{V} = \frac{P}{V_m} + \frac{1}{bV_m} \quad (2.28)$$

where  $V$  is the equilibrium amount adsorbed at pressure  $P$ , and  $V_m$  is the amount of adsorbate required for monolayer coverage on solid surface.

Hence, a plot of  $\frac{P}{V}$  versus  $P$  should yield a linear graph, giving the determination of  $V_m$  from the slope. The specific surface area is then calculated using the relationship,

$$S = V_m A_m L \quad (2.29)$$

where  $S$  is the specific surface area ( $\text{m}^2/\text{g}$ ).  $A_m$  is the average area occupied by one molecule of the adsorbate ( $\text{m}^2/\text{molecule}$ ).  $L$  is the Avogadro's number, being equal to  $6.0221367 \times 10^{23}$  (molecules/mol).

### 2.3.3.2 BET Equation

The BET equation can be rewritten in the linear form as,

$$\frac{P}{V(P^o - P)} = \frac{1}{V_m C} + \frac{(C-1)}{V_m C} \times \frac{P}{P^o} \quad (2.30)$$

The plot of  $\frac{P}{V(P^o - P)}$  against  $\frac{P}{P^o}$  should give a linear relationship which allows the determination of  $C$  and  $V_m$ . The  $V_m$  is used to obtain the specific surface area in the same way as outlined earlier for the Langmuir equation.

### 2.3.4 Heat of Adsorption

The isosteric heat of adsorption ( $Q_{st}$ ) can be calculated from the following thermodynamic van't Hoff equation,

$$\frac{Q_{st}}{R_g T^2} = - \left( \frac{\partial \ln P}{\partial T} \right)_n \quad (2.31)$$

This isosteric heat of adsorption may or may not vary with adsorption loading (Do, 1998).

### **2.3.5 Pore Size Distribution by DFT**

The characterization of porous solids is of great technological interest because of the importance of such materials. The knowing of pore size distribution (PSD) is the goal of this purpose. Attempts to characterize a PSD have been developed by many workers. The most commonly used method is the employing of the data of N<sub>2</sub> adsorption at -196°C and using the Kelvin equation to correlate pore size to the pressure at which condensation in the pore takes place, together with a relation to correct for the thickness of the adsorbed layer at the point of condensation. The method of Barrett, Joyner and Halenda (BJH) is typical (Barrett, Joyner and Halenda, 1951), and the thickness curves of de Boer, Halsey or Harkins and Jura are frequently employed (de Boer, Linsen and Osinga, 1965). However, the Kelvin equation may be regarded to the large pore limit. Its accuracy decreases as the pore dimension become less than a large multiple of molecular size.

The determination of PSD in the micropore region was proposed by many research groups. For example, the method based on the potential theory of the Dubinin school (Dubinin and Radushkevich, 1947), t- or alpha plots (Lippens and de Boer, 1965) or the MP method (Brunauer, Mikhail and Bodor, 1967). Horvath and Kawazoe (1983) recently proposed a quasithermodynamic method akin to the Kelvin method in that it describes a step function mapping of equilibrium relative pressure for pore filling to micropore size modeled as width of slit-like pores.

In the past decade, there have been attempts to provide an understanding of the structure and thermodynamics of inhomogeneous systems of simple molecules,

including surface tension and density profile of the free liquid–vapor interface. These knowledge help to investigate the behaviors of fluids at free solid surfaces and fluids confined by parallel or cylindrical walls. Density functional theory has been especially useful for these investigations, together with the computer simulation which can serve as a definitive reference. Seaton, Walton and Quirke (1989) published the first description of a method by which model isotherms calculated from density functional theory are used to determine a pore size distribution from experimental isotherms. They assumed the pore shape of a slit geometry, and further assumed that the pore size distribution can be described by a bimodal lognormal distribution function.

The evaluation of PSD by the density functional theory (DFT) is briefly described here as reported in the work of Jagiello and Thommes (2004). The methodology is based on the theoretical isotherms calculated for individual pores of a given adsorbate–adsorbent system. These isotherms have the kernel equations which are generated by the approach of DFT. The fundamental molecular parameters of the fluid–fluid and fluid–solid interaction are incorporated in these kernel equations. The theoretical isotherms are fitted with the experimental data to achieve the PSD as the end result. The derived PSD represents the volumetric contribution of pores with the variation of sizes whose the theoretical isotherms best fit the experimental data. The most important factor is the choice of the parameters of the fluid–fluid and fluid–solid interactions, which determines the predicting capability of the model. The Lennard-Jones (LJ) approximation is normally used in the literatures (Neimark, Ravikovitch, Grun, Schuth and Unger, 1998).

The approach of density functional theory to achieve the structure of fluids at a solid interface consists of formulating a grand potential functional  $\Omega$  as a

function of the average density of the fluid at the position  $r$ ,  $\rho(r)$ , and minimizing this with respect to  $\rho(r)$  to obtain the equilibrium density profile and thermodynamic properties. The parameter  $r$  represents a general spatial coordinate. For a single component fluid, a system is specified by the grand canonical ensemble, in which bulk chemical potential  $\mu$ , volume  $V$ , and temperature  $T$  are fixed. The grand potential function for the system can be written as below (Olivier and Conklin, 1992) with this function being derived based on the assumptions explored by Tarazona (1985).

$$\begin{aligned} \Omega = & k_B T \int \rho(r) (\ln(\Lambda^3 \rho(r) - 1)) \, dr + \int \rho(r) \Delta\psi(\bar{\rho}) \, dr \\ & + \frac{1}{2} \int \rho(r) U(r, r') \, dr + \int \rho(r) (V(r) - \mu) \, dr \end{aligned} \quad (2.32)$$

where  $k_B$  is the Boltzmann's constant,  $\Lambda$  is the deBroglie wavelength and  $V(r)$  is the potential acting on a fluid molecule at  $r$  due to the adsorption force of the solid. This potential is also model by a Lennard-Jones expression.

The free energy of the hard-sphere is estimated from the Carnahan and Starling (1969) equation of state

$$\Delta\psi(\rho) = \frac{k_B T \eta (4 - 3\eta)}{(1 - \eta)^2} \quad (2.33)$$

$$\eta = \frac{\rho \pi d^3}{6} \quad (2.34)$$

The  $U(r, r')$  is the summation of the attractive part of the pairwise potential of a molecule at  $r$  with all other fluid molecules in the system. Based on the DFT software used in this work, the  $U(r, r')$  is calculated from the Lennard-Jones 12-6 pairwise relation

$$u(r) = 4\varepsilon_{ff} \left[ \left( \frac{\sigma_{ff}}{r'} \right)^{12} - \left( \frac{\sigma_{ff}}{r'} \right)^6 \right] \quad (2.35)$$

where  $\varepsilon_{ff}$  is the depth of the intermolecular potential well and  $\sigma_{ff}$  is the molecular diameter. And thus

$$U(r, r') = \int u(r) \rho(r') \, dr' \quad (2.36)$$

The solution in Equation 2.32 is obtained by the employing of minimization principle, through the Euler-Lagrange equation. For activated carbon where the pores normally modeled as the slit shape, therefore the  $\rho(r)$  is only a function of  $z$ -coordinate, so the equation can be re-written as

$$\mu = k_B T \ln(\rho(z)) + \Delta\psi(\bar{\rho}(z)) + \int \rho(z) \Delta\psi(\bar{\rho}(z)) \left( \frac{\partial \bar{\rho}}{\partial \rho} \right) dz' + U(z) + V(z) \quad (2.37)$$

which can be solved for the density profile  $\rho(z)$  by an iterative numerical process. Since  $\mu$  is fixed by the pressure of gas phase, the equilibrium density profiles in pores of given width can be calculated as a function of the equilibrium pressure. The net

quantity adsorbed at a pressure is found by integrating the equilibrium density profile from wall to wall and subtracting a quantity equivalent to the non-excluded volume of the pore at the bulk gas density. The result is normalized to one square meter of wall area and expressed as  $\text{cm}^3$  STP for easy comparison with experimental data (Olivier and Conklin, 1992).

## **2.4 Adsorption Kinetics**

The adsorption kinetics information along with the adsorption equilibrium data is prerequisite for the proper design of the adsorber. The important knowledge provided by the kinetic study is the ability of the adsorbate molecule to diffuse into the particle interior of the porous solids.

### **2.4.1 Modes of Diffusion in Porous Medium**

#### **2.4.1.1 Knudsen Flow (Free Molecular Diffusion)**

This diffusion mode was observed by Knudsen (Do, 1998). The flow in this mode occurs when the mean free path of molecules is greater than the pore radius. Therefore, the flow involves the colliding and bouncing of molecules back from the wall of the porous medium. Concentration gradient is the driving force of this transport. The kinetic parameter of this transport mode is the Knudsen diffusivity,  $D_k$ . The transport by Knudsen flow controlling is dependent on the molecular weight of molecule, hence the separation of the mixtures by the kinetics could be readily achieved.

#### **2.4.1.2 Viscous Flow**

The total pressure gradient is the driving force of this flow mode. The flow is for the continuum fluid mixture, so there is no separation of species

due to the viscous flow. This flow behavior inside the pore is assumed to be laminar. The kinetic parameters characterizing the transport for this mode are the mixture viscosity and the viscous flow parameters.

#### **2.4.1.3 Continuum Diffusion**

The continuum diffusion involves the collision among molecules of different types, making a net momentum exchange between the two species. Each species moves relative to each other. The kinetic parameter is the binary diffusion coefficient,  $D_{ij}$ , where  $i$  and  $j$  represent the type of species  $i$  and  $j$ , respectively. This flow occurs when the mean free path is much less than the diameter of pore.

#### **2.4.1.4 Surface Diffusion**

Surface diffusion is the most complicated among these four transport modes. This diffusion involves the movement of the adsorbed species on the surface. The movement of a molecule from one site to the next vacant site is by the hopping mechanism. Therefore, this mobility mechanism is different for different types of molecule, resulting from their different interaction with the surface. This behavior also allows the separation of a binary mixture to be made. The kinetic parameter of this transport mode is surface diffusivity.

### **2.4.2 Measurement Methods for Adsorption Kinetics**

There are several methods that have been used for the kinetic measurement. However, each method has its advantages and disadvantages or limitations. Do (1998) has collected the advantages and disadvantages of several techniques for measuring the adsorption kinetics, as listed in Table 2.5.

**Table 2.5** Advantages and disadvantages of various kinetic techniques (Do, 1998).

Method	Advantages	Disadvantages
Single particle (DAB method)	<ul style="list-style-type: none"> <li>• reliable data</li> <li>• can deal with any type of system</li> <li>• isothermal is ensured</li> </ul>	<ul style="list-style-type: none"> <li>• very time consuming</li> </ul>
TGA	<ul style="list-style-type: none"> <li>• quick collection of data</li> </ul>	<ul style="list-style-type: none"> <li>• flow rate is limited due to the instability of the balance at high flow rate</li> <li>• can not deal with more than one adsorbate unless coupled with other means such as mass spectrometry</li> <li>• non-isothermality if the adsorbate is strongly adsorbing</li> </ul>
Time lag	<ul style="list-style-type: none"> <li>• very easy to collect and analyze data</li> </ul>	<ul style="list-style-type: none"> <li>• difficult in mounting pellet</li> <li>• non-isothermal if high pressure is used</li> <li>• can deal with only pure component</li> </ul>
Diffusion cell	<ul style="list-style-type: none"> <li>• isothermal in steady state operation</li> </ul>	<ul style="list-style-type: none"> <li>• extraction of dead end pore requires the analysis of second moment</li> <li>• heat effect in transient operation</li> </ul>

**Table 2.5** Advantages and disadvantages of various kinetic techniques (Continued).

Method	Advantages	Disadvantages
Chromatography	<ul style="list-style-type: none"> <li>• easy to set up and collection of data</li> <li>• quick if only affinity constant is required</li> </ul>	<ul style="list-style-type: none"> <li>• data analysis is quite cumbersome</li> <li>• non-isothermal operation</li> </ul>
Batch adsorber	<ul style="list-style-type: none"> <li>• easy to set up and collection of data</li> <li>• useful for expensive adsorbate</li> </ul>	<ul style="list-style-type: none"> <li>• non-isothermal operation</li> </ul>

## 2.5 References

- Ahmadpour, A. and Do, D. D. (1997). The preparation of activated carbon from macadamia nutshell by chemical activation. **Carbon** 35: 1723-1732.
- Bandosz, T. J., et al. (2003). Molecular models of porous carbons. In L.R. Radovic. (ed.). **Chemistry and Physics of Carbon** 28: 41-228.
- Bansal, R. C., Donnet, J-B. and Stoeckli, F. (1988). **Active carbon**. New York: Marcel Dekker.
- Barrett, E. P., Joyner, L. G. and Halenda, P. P. (1951). The determination of pore volume and area distributions in porous substances. I. Computations from nitrogen isotherms. **J. Am. Chem. Soc.** 73: 373-380.
- Brunauer, S., Deming, L. S., Deming, W. E. and Teller, E. (1940). On a theory of the van der Waals adsorption of gases. **J. Amer. Chem. Soc.** 62: 1723-1732.

- Brunauer, S., Emmett, P. H. and Teller, E. (1938). Adsorption of gases in multimolecular layers. **J. Amer. Chem. Soc.** 60: 309-319.
- Brunauer, S., Mikhail, R. Sh. and Bodor, E. E. (1967). Pore structure analysis without a pore shape model. **J. Colloid Interface Sci.** 24: 451-463.
- Carnahan, N. F. and Starling, K. E. (1969). Equation of state for nonattracting rigid spheres. **J. Chem. Phys.** 51: 635-636.
- de Boer, J. H., Linsen, B. G. and Osinga, Th. J. (1965). Studies on pore systems in catalysts VI. The universal *t* curve. **J. Catalysis** 4: 643-648.
- Do, D. D. (1998). **Adsorption analysis: Equilibria and kinetics**. New Jersey: Imperial College Press.
- Dubinin, M. M. and Astakhov, V. A. (1971). **Adv. Chem. Ser.** 102: 69.
- Dubinin, M. M. and Radushkevich, L. V. (1947). **Dokl. Akad. Nauk. SSSR.** 55: 327.
- Dubinin, M. M. and Zaverina, E. D. (1949). **Dokl. Akad. Nauk. SSSR.** 68: 91-94.
- Freedonia Group. (2006). New global industry forecasts to 2010 & 2015: World activated carbon [On-line]. Available: [http://freedonia.ecnext.com/coms2/summary\\_0285-335109\\_ITM](http://freedonia.ecnext.com/coms2/summary_0285-335109_ITM)
- Gregg, S. J. and Sing, K. S. W. (1982). **Adsorption, surface area and porosity**. London: Academic Press.
- Halsey, G. (1948). Physical adsorption on non-uniform surfaces. **J. Chem. Phys.** 16: 931-937.
- Hassler, J. W. (1963). **Activated carbon**. New York: Chemical.
- Horvath, G. and Kawazoe, K. (1983). Method for the calculation of effective pore size distribution in molecular sieve carbon. **J. Chem. Eng. Japan** 16: 470-475.

- Humphrey, J. L. and Keller, G. E. (1997). **Separation process technology**. New York: McGraw Hill.
- International Union of Pure and Applied Chemistry. (1972). Manual of symbols and terminology for physicochemical quantities and units. **Pure. Appl. Chem.** 31: 579-638.
- Jagiello, J. and Thommes, M. (2004). Comparison of DFT characterization methods based on N<sub>2</sub>, Ar, CO<sub>2</sub>, and H<sub>2</sub> adsorption applied to carbons with various pore size distributions. **Carbon** 42: 1227-1232.
- Jankowska, H., Swiatkowski, A. and Choma, J. (1991). **Active carbon**. New York: Ellis Harwood.
- Kalback, W. M., Brown, L. F. and West, R. E. (1970). The growth of pores in graphitized carbon reacted with carbon dioxide. **Carbon** 8: 117-124.
- Kratschmer, W., Rathousky J. and Zukal, A. (1999). Adsorption of krypton at 77 K on fullerene C<sub>60</sub>, graphitized carbon black and diamond. **Carbon** 37: 301-305.
- Langmuir, I. (1918). The adsorption of gases on plane surfaces of glass, mica and platinum. **J. Am. Chem. Soc.** 40: 1361-1403.
- Leon y Leon D., C. A. and Radovic, L. R. (1994). Interfacial chemistry and electrochemistry of carbon surfaces. In P. A. Throver (ed.). **Chemistry and Physics of Carbon** 24: 213-310.
- Lippens, B. C. and de Boer, J. H. (1965). Studies on pore systems in catalysts V. The *t* method. **J. Catalysis** 4: 319-323.
- Marsh, H. (2001). **Activated carbon compendium**. Amsterdam: Elsevier Science.
- Mastral, A. M., Rubio, B., Membrado, L. and Fananas, F. J. (1990). Coal conversion into char: a study of the initial steps. **Carbon** 28: 65-69.

- Neimark, A. V., Ravikovitch, P. I., Grun, M., Schuth, F. and Unger, K. K. (1998). Pore size analysis of MCM-41 type adsorbents by means of nitrogen and argon adsorption. **J. Colloid Interface Sci.** 207: 159-169.
- Olivier, J. P. and Conklin, W. B. (1992). Determination of pore size distribution from Density Functional Theoretic models of adsorption and condensation within porous solids. In **International Symposium on the Effects of Surface Heterogeneity in Adsorption and Catalysis on Solids**. Kazimierz Dolny, Poland.
- Otowa, T., Tanibata, R. and Itoh, M. (1993). Production and adsorption characteristics of maxsorb: high-surface-area active carbon. **Gas Sep. Purif.** 7:241-245.
- Seaton, N. A., Walton, J. P. R. B. and Quirke, N. (1989). A new analysis method for the determination of the pore size distribution of porous carbons from nitrogen adsorption measurements. **Carbon** 27: 853-861.
- Tarazona, P. (1985). Free-energy density functional for hard spheres. **Phys. Rev. A** 31: 2672-2679.
- Yang, R. T. (2003). **Adsorbents fundamentals and applications**. New Jersey: John Wiley & Sons.

# **CHAPTER III**

## **THERMOGRAVIMETRIC ANALYSIS**

### **OF LONGAN SEED**

#### **3.1 Abstract**

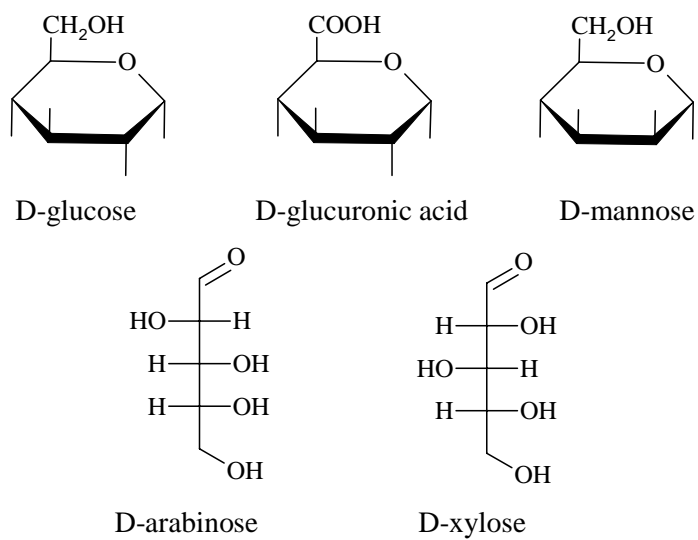
The thermogravimetric analysis of pyrolysis process of longan seed was studied in a thermogravimetric analyzer. All runs of experiment were performed by using the initial sample mass of 15 mg and the final temperature at 650°C under the nitrogen atmosphere. Particle sizes in the range of 0.05-2.1 mm and heating rates at 5-100°C/min were employed to investigate their effects on the thermogram and the kinetic parameters. The TG curves generally showed sigmoid shape and displayed one major peak in DTG curve. The main devolatilization for longan seed occurred in the temperature range of 210-330°C. It was found that the heat transfer resistance in a particle could be reduced either by decreasing the size of particle or increasing the heating rate. The thermal decomposition of longan seed could be well described by the two-parallel reactions kinetic model. This analysis of reaction kinetics gave the values of activation energy for the two fractions of the model close to those for the decomposition of hemicellulose and lignin, respectively.

## 3.2 Introduction

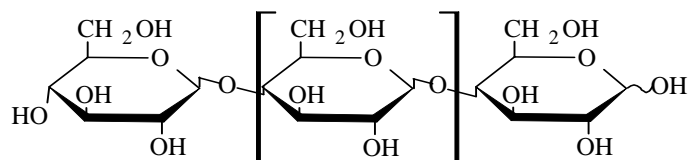
The thermal decomposition of biomass under an inert atmosphere, also called the pyrolysis process, produces valuable products in forms of gases, liquid and solid. The yield and composition of pyrolysis products depend on the operating conditions mainly the temperature and heating rate. These products can be used directly as fuels in liquid, gas and solid forms or as a chemical feedstock for the liquid product. As an example, the released gases with a sufficiently high heating value are sufficient for the total energy requirements of a biomass waste pyrolysis plant, or can be fed into gas turbines in combine cycle technologies (Gonzalez, Encinar, Canito, Sabio and Chacon, 2003). The liquid fraction so called bio-oil is gaining a potential for use as a fuel oil substitute (Oasmaa and Czernik, 1998), or may contain chemicals in economically recoverable concentrations (Balci, Dogu and Yucel, 1993). The solid product is called char; it is a carbon rich solid residue that could be used either for fuel purposes in form of briquette, as char-oil or char-water slurries (Karaosmanoglu, Isigigur-Ergudenler and Sever, 2000), or used as a precursor for activated carbon production (Encinar, Beltran, Bernalte, Ramiro and Gonzalez, 1996; Mackay and Roberts, 1982). Because of the advantages of the biomass pyrolysis, the kinetics of the process has been one of the important research topics in this field. The full understanding of the pyrolysis behavior is thus essential for the proper design of the pyrolysis system. In the present research project, we aim to produce the activated carbon from a new precursor, longan seed. Therefore, the knowledge of thermal analysis of pyrolysis of this biomass is necessary to better understand and optimize the process of carbonization.

It is generally known that the behaviors and the product properties of biomass decomposition are strongly dependent on its compositions (Caballero, Conesa, Font and Marcilla, 1997; Mangut et al., 2006; Orfao, Antunes and Figueiredo, 1999). Biomass normally is composed of three main fractions of hemicellulose, cellulose and lignin. Hemicellulose is a polysaccharide consisting of the variation in composition among species which exhibits a branched molecular structure. It typically contains two to four (and occasionally five to six) different simple sugar units (Nugranad, 1997). Hemicelluloses are soluble in weak alkaline solutions. Cellulose is also a polysaccharide composed of a linear of D-glucose units ( $C_6H_{10}O_5$ ) bonded to each other by ether-type linkage known as glycosidic bonds (Nugranad; Guo and Lua, 2001). Typically, cellulose is the principle of cell wall component in biomass tissue. Lignin is composed of an extremely complex of cross-linked phenolic polymers in which the basic structural unit is the phenylpropane. It fills the spaces in the cell wall between cellulose, hemicellulose and pectin components. It is usually considered the most stable of the biomass compounds (Caballero et al.). Figure 3.1 shows the representative structure of these three major components. There is a critical question whether the pyrolysis of a biomass material can be represented in a simple addition of its components or if these components interact chemically or physically, leading the material to behave in its own unique way during thermal decomposition. Several studies of the kinetic mechanisms of cellulose, hemicellulose and lignin have found that the interactions between these fractions are important. However, in thermogravimetric and its derivative analysis (TG-DTG) of biomass material two or three peaks usually appear, that can be assigned to cellulose, lignin, and hemicellulose, indicating that, although there are interactions between fractions, their

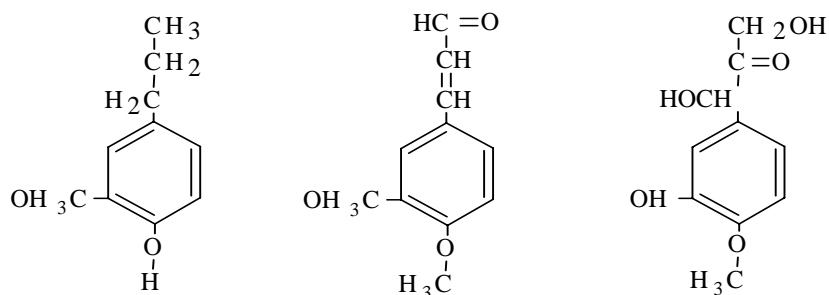
identity is still maintained (Caballero et al.; Garcia-Ibanez, Sanchez and Cabanillas, 2006).



(a) Some monomers of hemicellulose



(b) Structure of cellulose



(c) Some monomers of lignin

**Figure 3.1** Representative structures of biomass components.

Thermogravimetric analysis (TGA) is the most commonly used thermal analysis technique to study the thermal behavior of carbonaceous materials (Freeman and Carroll, 1958). This technique is used to monitor the mass of sample in a specified atmosphere against the time or temperature which is programmed. The instrument used for this measurement is called a thermobalance, or a thermogravimetric analyzer. In general, a thermogravimetric analyzer has four major parts; the electrobalance and its controller, the furnace and temperature sensors, the program or computer and the recorder, plotter or data acquisition device (Haines, 1995). The schematic diagram of the thermogravimetric analyzer is shown in Figure 3.2.

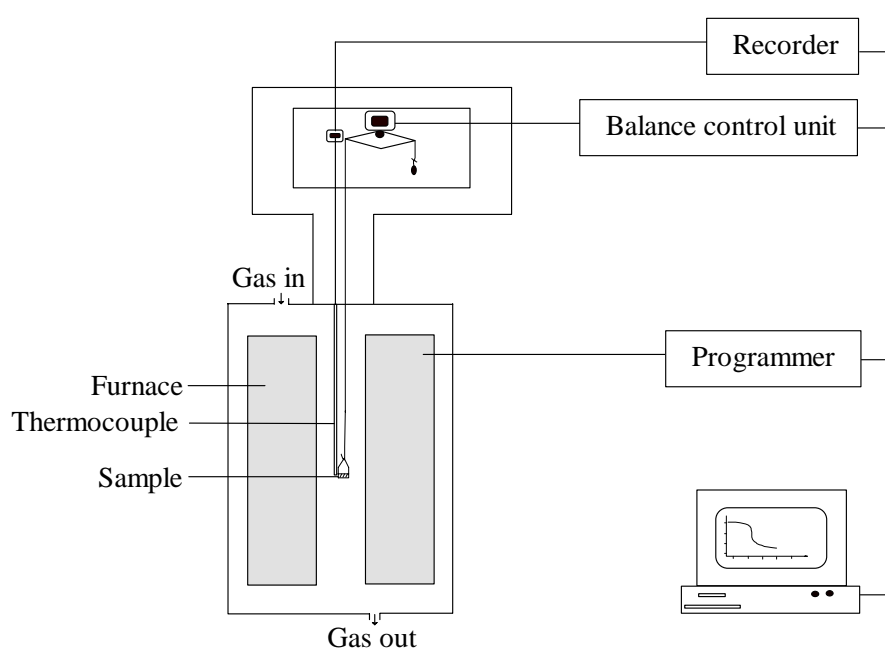


**Figure 3.2** Schematic diagram of a thermogravimetric system.

### 3.2.1 Biomass Pyrolysis Kinetic Model

The mechanism of biomass pyrolysis is very complicated involving many thermal reactions with simultaneous heat and mass transfer. There has been

considerable research effort to better understand the biomass pyrolysis by proposing some simplified models to predict the residual weight, decomposition rate and also the kinetic parameters. Normally in many of the kinetic formulations of thermal decomposition reaction, it has been assumed that the isothermal homogeneous gas or liquid phase kinetic equation can be applied (Baker, 1978). The proposed models were categorized with models containing only one differential equation, models of parallel reactions, models involving more than one fraction, and models involving a continuous distribution of fractions (Conesa, Marcilla, Caballero and Font, 2001).

Several investigations of biomass pyrolysis kinetics have been reported in literature. For example, the pyrolysis kinetic of olive stones and almond shells was studied by using the TGA technique (Caballero et al., 1997). The different kinetic schemes were grouped into two or three overall processes corresponding to the decomposition of hemicellulose, cellulose and lignin. The best results were found for the model describing the biomass decomposition via three independent reactions. Teng, Lin and Ho (1997) studied the kinetics of rice hull pyrolysis by a combined model of volatile evolutions of four independent parallel reactions. These reactions are associated with the moisture evolution, and the decomposition of hemicellulose, cellulose and lignin. The kinetic study on the pyrolysis of oil-palm solid waste was modeled using one-step global model and two-step consecutive reaction model by Guo and Lua (2001). They found that the two-step model could describe well their experimental data. They also suggested that these two reactions account for the softening effect and formation of an intermediate during the pyrolysis process. Font, Marcilla, Verdu and Devesa (1991) investigated the kinetic pyrolysis of almond shell by using the two-parallel reactions model. This model assumes that the biomass

consists of two main fractions having independent pathway of decomposition based on the first order reaction.

In this work, the preliminary result indicated that the DTG diagram of longan seed pyrolysis exhibited only one major peak. Therefore, it is likely that the decomposition reaction of longan seed involves only one global reaction. The one-step global model is thus selected to test with the experimental data. However, it is well known that the pyrolysis of lignocellulosic materials is a complex process. Therefore, the two-parallel reactions model is also tried to describe the pyrolysis of longan seed. This model is based on the model used in the work of Font et al. (1991). However, in order to increase the model flexibility, we further assumed that the reaction order of the first fraction is first order while that of the second fraction is optimally searched (Luangkiattikhun, Tangsathitkulchai and Tangsathitkulchai, 2006).

### 3.2.1.1 One-Step Global Model

The one-step global model is the model containing only one differential equation based on the reaction order. It is the simplest kinetic model to describe the decomposition of a pyrolyzed material. The kinetic equation of this model can be represented as



where  $k$  is the rate constant and obeys the Arrhenius law. Therefore, the rate of decomposition can be expressed as the following:

$$\frac{d\alpha}{dt} = k(1-\alpha)^n = A \exp\left(\frac{-E}{R_g T}\right) (1-\alpha)^n \quad (3.2)$$

where  $\alpha$  is the conversion defined in terms of the reacted mass fraction,

$$\alpha = \frac{w_0 - w}{w_0 - w_f} \quad (3.3)$$

with  $w_0$ ,  $w$  and  $w_f$  being the initial, actual and final mass of the sample, respectively.  $A$  is the frequency or pre-exponential factor,  $E$  is the activation energy,  $R_g$  is the universal gas constant,  $T$  is the absolute temperature,  $n$  is the order of reaction and  $t$  is the time. For a constant heating rate,  $\beta$ , the correlation between the temperature  $T$  and the time  $t$  is

$$\frac{dT}{dt} = \beta \quad (3.4)$$

Dividing Equation 3.2 by Equation 3.4, the rate of decomposition reaction can be expressed as a function of temperature i.e.,

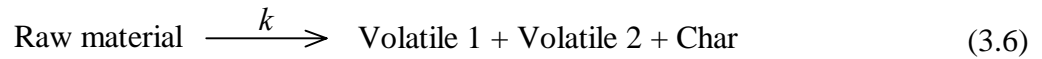
$$\frac{d\alpha}{dT} = -\frac{A}{\beta} \exp\left(\frac{-E}{R_g T}\right) (1 - \alpha)^n \quad (3.5)$$

This ordinary differential equation was used to fit the experimental data to obtain the parameters  $A$ ,  $E$  and  $n$ .

### 3.2.1.2 Two-Parallel Reactions Model

The two-parallel reactions model basically assumes that the reaction is controlled by kinetics regime and the secondary reactions are neglected. This model proposes that the raw material consists of two homogeneous fractions namely  $M_1$  and  $M_2$  and each fraction decomposes simultaneously at different rates at a

given temperature, generating the volatile matters and solid char. The scheme of overall reaction is given as



Equation 3.6 can be represented in the form of two individual parallel reactions as Equation 3.7–a, and 3.7–b, respectively,



where  $k_1$  and  $k_2$  are the rate constants of each reaction. The residual weight fractions of solid product are defined as follows,

$$\alpha = \frac{M - m_f}{1 - m_f}; \quad \alpha_1 = \frac{M_1 - m_{f1}}{1 - m_f}; \quad \alpha_2 = \frac{M_2 - m_{f2}}{1 - m_f} \quad (3.8)$$

where  $m_f$  is the final mass fraction of solid char,  $m_{f1}$  and  $m_{f2}$  are the final mass fractions of the first and second components, respectively.  $M$ ,  $M_1$  and  $M_2$  are mass fractions of total residual weight, residual weight of component 1 and 2 present at time  $t$ , respectively. Obviously,

$$M = M_1 + M_2 \quad (3.9\text{--a})$$

$$m_f = m_{f1} + m_{f2} \quad (3.9\text{--b})$$

The rate of decomposition reaction in Equation 3.7–a and 3.7–b can be expressed as follows;

$$\frac{d\alpha_1}{dt} = -A_1 \exp\left(\frac{-E_1}{R_g T}\right) \alpha_1 \quad (3.10\text{--a})$$

$$\frac{d\alpha_2}{dt} = -A_2 \exp\left(\frac{-E_2}{R_g T}\right) \alpha_2^n \quad (3.10\text{--b})$$

For a constant heating rate,  $\beta$ , Equation 3.10–a and 3.10–b are in the

$$\frac{d\alpha_1}{dT} = -\frac{A_1}{\beta} \exp\left(\frac{-E_1}{R_g T}\right) \alpha_1 \quad (3.11\text{--a})$$

$$\frac{d\alpha_2}{dT} = -\frac{A_2}{\beta} \exp\left(\frac{-E_2}{R_g T}\right) \alpha_2^n \quad (3.11\text{--b})$$

Rearranging Equation 3.11 and integrating to obtain

$$\int_a^{\alpha_1} \frac{d\alpha_1}{\alpha_1} = -\frac{A_1}{\beta} \int_0^T \exp\left(\frac{-E_1}{R_g T}\right) dT \quad (3.12\text{--a})$$

$$\int_b^{\alpha_2} \frac{d\alpha_2}{\alpha_2^n} = -\frac{A_2}{\beta} \int_0^T \exp\left(\frac{-E_2}{R_g T}\right) dT \quad (3.12\text{--b})$$

where  $a$  and  $b$  are the initial values of  $\alpha_1$  and  $\alpha_2$ , respectively, and they represent the initial weight fractions of the component 1 and component 2 contained in the raw materials. They are assumed constant and depended only on the characteristics of the raw material. The relationship between  $a$  and  $b$  is;

$$a + b = 1 \quad (3.13)$$

The integration of Equation 3.12 can be achieved by expressing the exponential term in an asymptotic series and neglecting the higher order terms. The expressions for  $\alpha_1$  and  $\alpha_2$  can be derived as follows:

$$\alpha_1 = \exp \left[ \frac{-A_1 R_g T^2}{\beta E_1} \left( 1 - \frac{2R_g T}{E_1} \right) \exp \left( \frac{-E_1}{R_g T} \right) + \ln(a) \right] \quad (3.14-a)$$

$$\alpha_2 = \left[ \frac{(n-1)A_2 R_g T^2}{\beta E_2} \left( 1 - \frac{2R_g T}{E_2} \right) \exp \left( \frac{-E_2}{R_g T} \right) + b^{(1-n)} \right]^{\frac{1}{1-n}} \quad (3.14-b)$$

Finally, the total of remaining mass at any temperature is the sum of each residual fraction. That is

$$\alpha = \alpha_1 + \alpha_2 = \exp \left[ \frac{-A_1 R_g T^2}{\beta E_1} \left( 1 - \frac{2R_g T}{E_1} \right) \exp \left( \frac{-E_1}{R_g T} \right) + \ln(a) \right] + \left[ \frac{(n-1)A_2 R_g T^2}{\beta E_2} \left( 1 - \frac{2R_g T}{E_2} \right) \exp \left( \frac{-E_2}{R_g T} \right) + b^{(1-n)} \right]^{\frac{1}{1-n}} \quad (3.15)$$

Equation 3.15 was used to test against the experimental data and the six kinetic parameters ( $a$ ,  $A_1$ ,  $E_1$ ,  $A_2$ ,  $E_2$  and  $n$ ) were obtained by model fitting.

In all optimization, the kinetic parameters were estimated based on the minimization of sum of square of relative error. That is,

$$S = \sum_{i=1}^N \left[ \frac{(\alpha_{exp})_i - (\alpha_{cal})_i}{(\alpha_{exp})_i} \right]^2 \quad (3.16)$$

The subscript  $i$  refers to the data point in the total of  $N$  data points,  $\alpha_{exp}$  represents the experimental value and  $\alpha_{cal}$  represents the value calculated from a given set of estimated parameters.

### 3.2.2 Objectives of the Study

The purpose of this research part was to investigate the non-isothermal pyrolysis behavior of longan seed in a thermogravimetric analyzer. The effects of particle size and heating rate on the thermograms and kinetic parameters were studied. The one-step global model was tested against the experimental data to obtain the pyrolysis kinetic parameters. In addition, the two-parallel reactions model was also tested to check its validity in comparison with that predicted by the one-step model.

## 3.3 Materials and Methods

### 3.3.1 Pyrolysis of Longan Seed

The longan seed was collected from the fruit cannery plant of Malee Sampran Public Company Limited in Nakhon Pathom, Thailand. This fresh-longan seed was cleaned by water and dried in an oven at 110°C for 24 h. The pre-dried

longan seed was then crushed and sieved to obtain the average particle sizes of 0.05, 0.1, 1.0 and 2.1 mm.

The pyrolysis of longan seed was carried out by using a thermogravimetric analyzer (TGA7 series, Perkin Elmer, USA). The experiment was performed in the non-isothermal pyrolysis mode under the constant flow of nitrogen (Nitrogen purity of 99.999%, supplied by TIG, Thailand). The final temperature was fixed at 650°C, and the heating rates studied were of 5, 10, 20, 30, 50 and 100°C/min.

### **3.3.2 Proximate Analysis**

Proximate analysis was conducted by a thermogravimetric analyzer following the procedure reported by Lua and Guo (1998). The sample of about 15 mg was placed in a platinum pan that suspended to the balance of TGA. The heating program commenced from the room temperature to 110°C under the inert atmosphere of nitrogen, the system was held at this temperature until the sample weight remained unchanged approximately for 30 min to complete the dehydration step. The moisture content was recorded from the weight loss at this stage. The temperature was then heated to 850°C and held at this temperature for 7 min to determine the volatile matters fraction. After this the inert gas was changed to air to provide the oxidizing atmosphere. The sample was allowed to cool to 800°C and held at this temperature until the constant of residual weight was established. The weight loss during this period was due to the combustion of the fixed carbon. The ash content was readily obtained from this final mass of residual solid.

### 3.4 Results and Discussion

#### 3.4.1 Proximate and Ultimate Analyses of Longan Seed

The proximate and ultimate analyses of longan seed and other biomasses are shown in Table 3.1 and Table 3.2, respectively. The fixed carbon content of longan seed is 19.6% with relatively low ash content of 1.7% and the sulfur content is also low at 0.1%. These values of analyses are comparable with the other carbonaceous materials reported in the literature. Therefore, the longan seed used in this study could be used as a potential precursor for activated carbon production.

**Table 3.1** Proximate analyses of longan seed and some biomasses used for activated carbon preparation.

Material	Proximate analysis (dry basis) [wt%]		
	Fixed carbon	Volatile matters	Ash
Longan seed	19.6	78.7	1.7
Oil palm shell <sup>1</sup>	19.8	77.6	2.6
Apricot stone <sup>2</sup>	13.7	86.1	0.2
Almond shell <sup>2</sup>	11.8	87.2	1.0
Cherry stone <sup>2</sup>	10.0	89.4	0.6
Grape seed <sup>2</sup>	19.0	78.2	2.8

Sources: <sup>1</sup>Guo and Lua (2001); <sup>2</sup>Gergova, Petrov and Eser (1994)

**Table 3.2** Ultimate analyses of longan seed and some biomasses.

Material	Ultimate analysis [wt%]				
	C	H	N	S	O (by diff.)
Longan seed	46.5	6.3	1.4	0.1	45.4
Apricot stone <sup>1</sup>	55.6	6.8	0.2	0.1	37.3
Almond shell <sup>1</sup>	51.0	6.3	0.5	0.2	42.0
Cherry stone <sup>1</sup>	53.9	7.1	0.3	0.3	38.4
Grape seed <sup>1</sup>	62.2	7.8	1.6	0.2	28.2

Source: <sup>1</sup>Gergova et. al. (1994)

### 3.4.2 Typical Results of Non-Isothermal Pyrolysis of Longan Seed

Results of the non-isothermal pyrolysis of crushed longan seed under nitrogen atmosphere is presented in Figure 3.3. Three regions of weight loss behavior upon increasing pyrolysis temperature can be observed. The first region from ambient temperature up to 100°C corresponds to the loss of contained water. The main second region covers the temperature from 100-500°C. The maximum weight loss rate occurs at 260°C with the main pyrolysis decomposition of longan seed proceeding through this temperature range. This pyrolysis process involves the evolution of gases and tar from the solid with the formation of residue char. The final region for temperature above 500°C corresponds to the consolidation of char structure as reflected by a small weight change on increasing pyrolysis temperature.

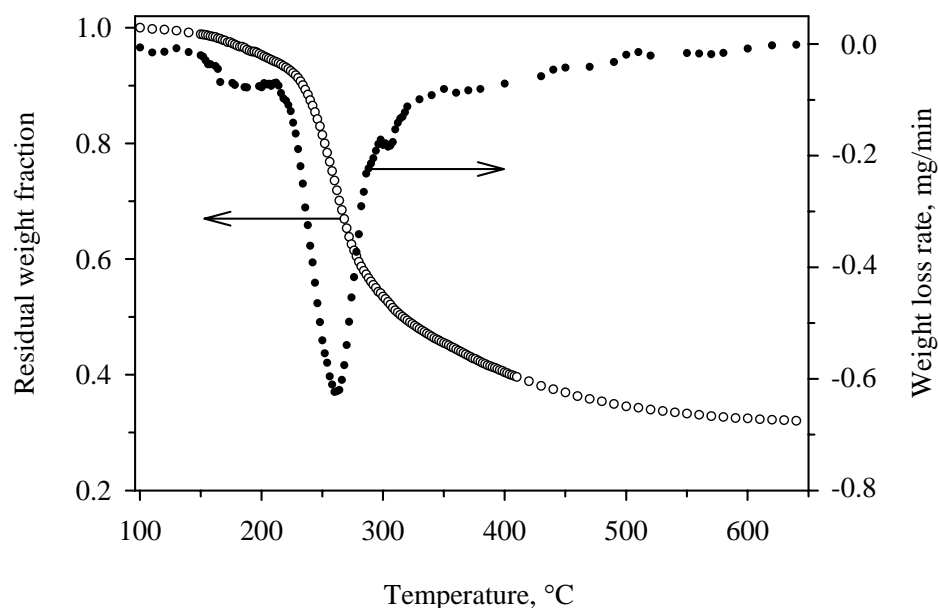


**Figure 3.3** The typical residual weight fraction (TG) and weight loss rate (DTG) for the non-isothermal pyrolysis of longan seed, particle size 2.1 mm and a heating rate 5°C/min.

The comparison of DTG for the non-isothermal pyrolysis under the inert (nitrogen) and the oxidizing (air) atmosphere are displayed in Figure 3.4. It is found that the decomposition rate curves for pyrolysis in nitrogen and in air coincide over the pyrolysis temperature up to 320°C. At higher temperatures, the presence of oxygen in air shows the second peak of DTG curve due to combustion reaction over the temperature range from 320 to 500°C, with a maximum rate occurring at 450°C. This result shows that there are two consecutive stages proceeded in air environment consisting of the evolution of volatile matters followed by the burning of combustible components.

There has been some indication that the overall weight loss of a biomass results from the contributing effect of each cellulosic component of the biomass,

weighting by its composition. Orfao et al. (1999) studied the pyrolysis behavior of biomass components separately (cellulose, xylan (monomer of hemicellulose) and lignin) under the atmosphere of air and nitrogen. In air condition, they found the peaks of maximum weight loss rate of cellulose to occur at 294°C and 467°C, for xylan at 251°C and 401°C and for lignin only one single peak at 389°C was observed. Comparing their results with that of the longan seed, the peaks seen in Figure 3.4 nearly match the peaks found in xylan and cellulose. Therefore, it could be approximately inferred that the longan seed composition consists mainly of hemicellulose and cellulose components.

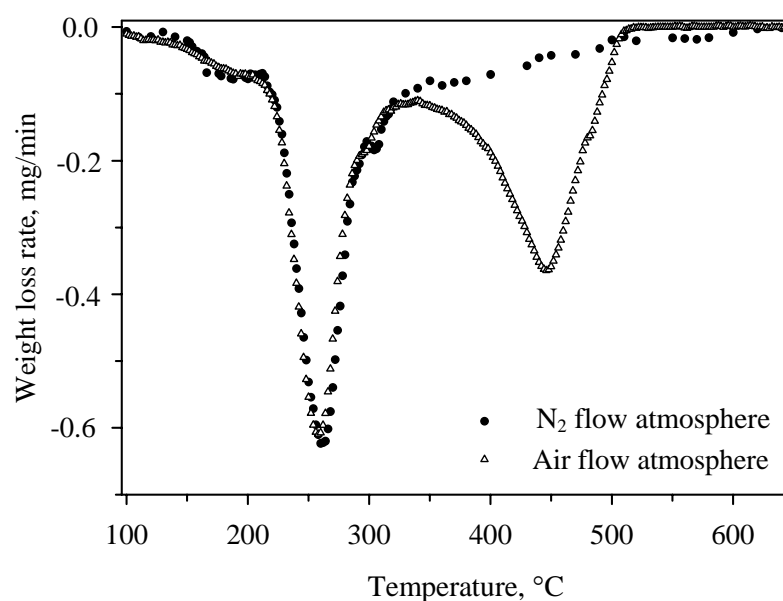


**Figure 3.4** The weight loss rate curves (DTG) for the non-isothermal pyrolysis of longan seed under the inert (nitrogen) and the oxidizing (air) atmosphere, particle size 2.1 mm and a heating rate 5°C/min.

### 3.4.3 Initial Sample Weight Effect

Figure 3.5 shows the influence of initial sample weight on the residual weight versus temperature for the weights of 15 and 30 mg run at heating rates of 5 and 100°C/min. It is seen that there is a measurable influence of the initial weight for the condition of heating rate at 100°C/min, showing a shift to a higher pyrolyzed temperature in the range of 240-320°C as the weight is increased. This behavior may arise from the interparticle transport resistance leading to the heat transfer limitation at a high heating rate condition. It is also interesting to observe that the final solid yield is not affected by this effect. Thus, it is inferred that the initial sample weight in this study range only affect the increasing of heat transfer resistance under high heating rate condition. In further analysis of pyrolysis kinetics of TGA of longan seed it is assumed that the process is controlled by the chemical reaction. Therefore the initial sample weight for 15 mg was chosen for a series of experiments in this work and was considered to be appropriate since the heat and mass transfer resistance were minimized.

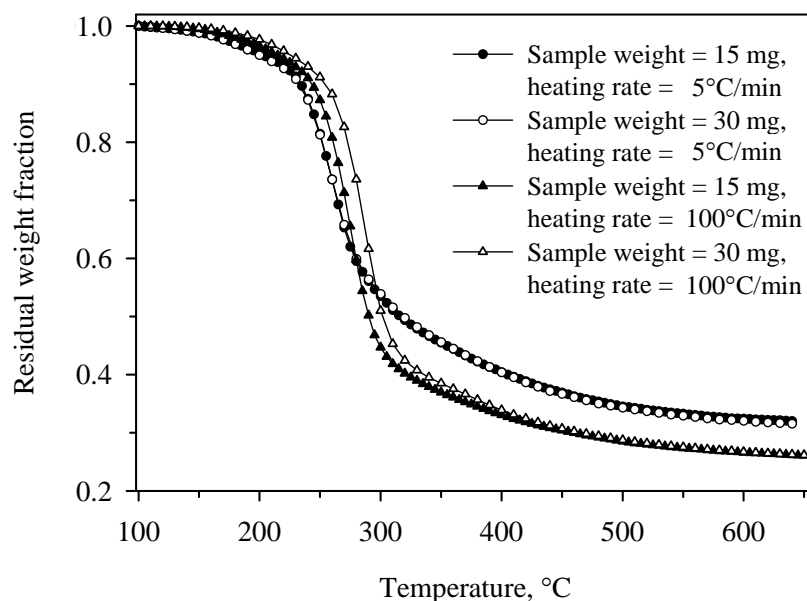


**Figure 3.5** The TG for the non-isothermal pyrolysis of longan seed with different of the sample weight, at heating rate of 5 and 100°C/min for a particle size of 1.0 mm.

#### 3.4.4 Particle Size Effect

The TG and DTG results of the longan seed with different particle sizes at the heating rate 5°C/min are shown in Figure 3.6 and 3.7, respectively. The TG and DTG for all particle sizes show a similar trend. However, it is found that the final yield depends on the particle size, with larger particle size giving the higher char yield. It is observed that the particle size starts to have an effect at around 270°C, separating the TG to different final yield values. For the DTG data, the temperature range of the main devolatilization appears to start and end at approximately the same temperature for all particle sizes (210-350°C). However, the magnitude of the maximum rate of weight loss for a smallest particle size (0.05 mm) is higher than the other larger sizes.

According to the obtained results, decreasing particle size resulted in the decrease of char yield. This can be explained by the fact that temperature gradient in small particles is less than that in the larger particle sizes, indicating the decreasing in heat transfer resistance in the smaller size particle. For this reason, the pyrolysis should be controlled by pure reaction kinetics, giving the conversion in the smaller particle higher than that in the larger particles. This result also agrees with the work reported by other investigators (Guo and Lua, 2001; Haykiri-Acma, 2006).

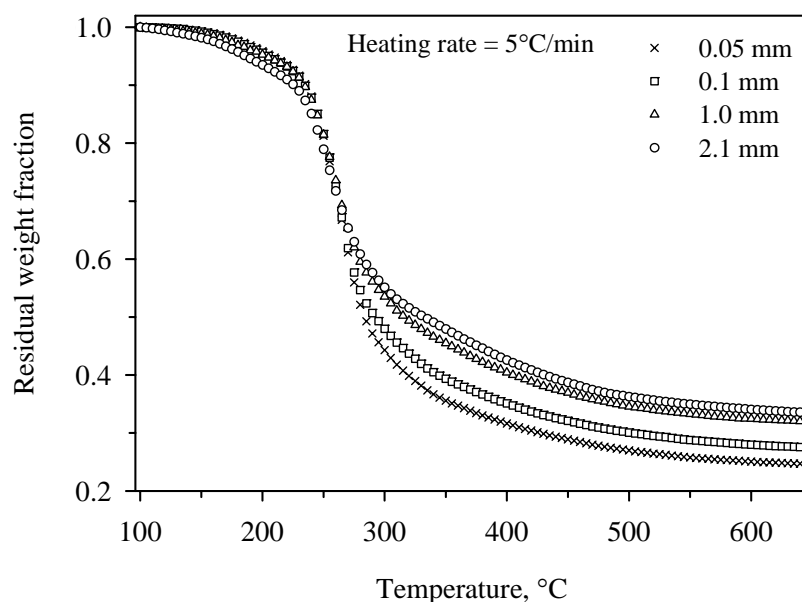


**Figure 3.6** The TG curves for the non-isothermal pyrolysis of longan seed with different particle sizes under the nitrogen atmosphere and a heating rate at 5°C/min.

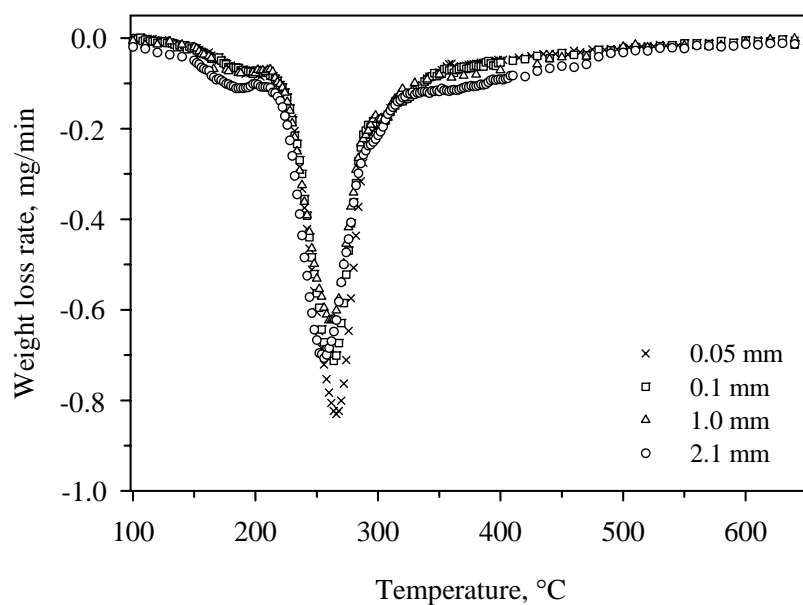


**Figure 3.7** The DTG for the non-isothermal pyrolysis of longan seed with different particle sizes under the nitrogen atmosphere and a heating rate 5°C/min.

In addition, the appearance of the particle size influence is also strongly depended on the heating rate. Figure 3.8 shows the effect of particle size on the TG results obtained at a high heating rate of 100°C/min. It is observed that the difference in solid yields diminishes at the high heating rate. This is probably attributed to the lowering of heat transfer resistance caused by the increasing in heating rate. This heating rate effect will be further discussed in the next section.

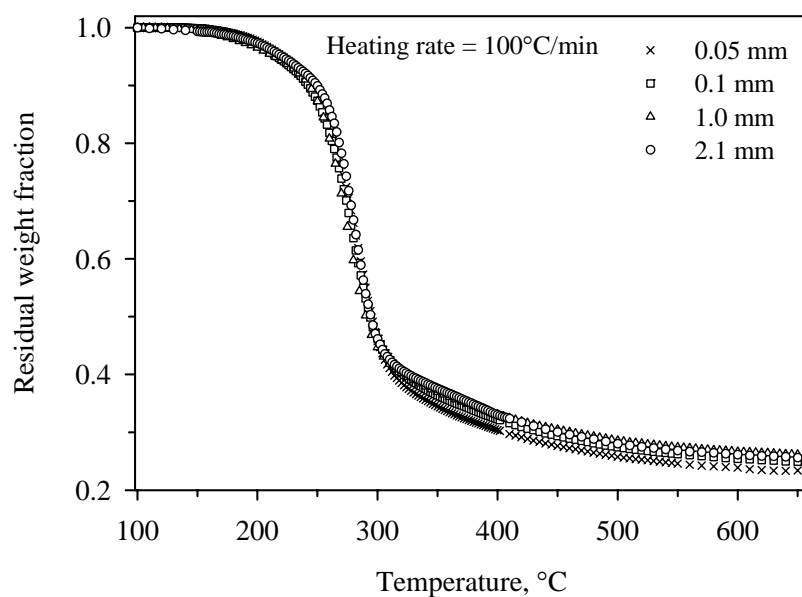


**Figure 3.8** The TG for the non-isothermal pyrolysis of longan seed with different particle sizes under the nitrogen atmosphere and a high heating rate 100°C/min.

### 3.4.5 Heating Rate Effect

The effect of heating rate on the TG and DTG curves for longan seed particle size of 1.0 mm are shown in Figure 3.9 and 3.10, respectively. It is observed that there is a lateral shift in TG curves in the main devolatilization range around 200-300°C as the heating rate is increased. This indicates that over this temperature range the longan seed decomposed at a higher temperature when the higher heating rate was applied. The heating rate significantly affects the maximum weight loss rate of DTG curves, showing that the maximum weight loss rate increases with an increase in heating rate.

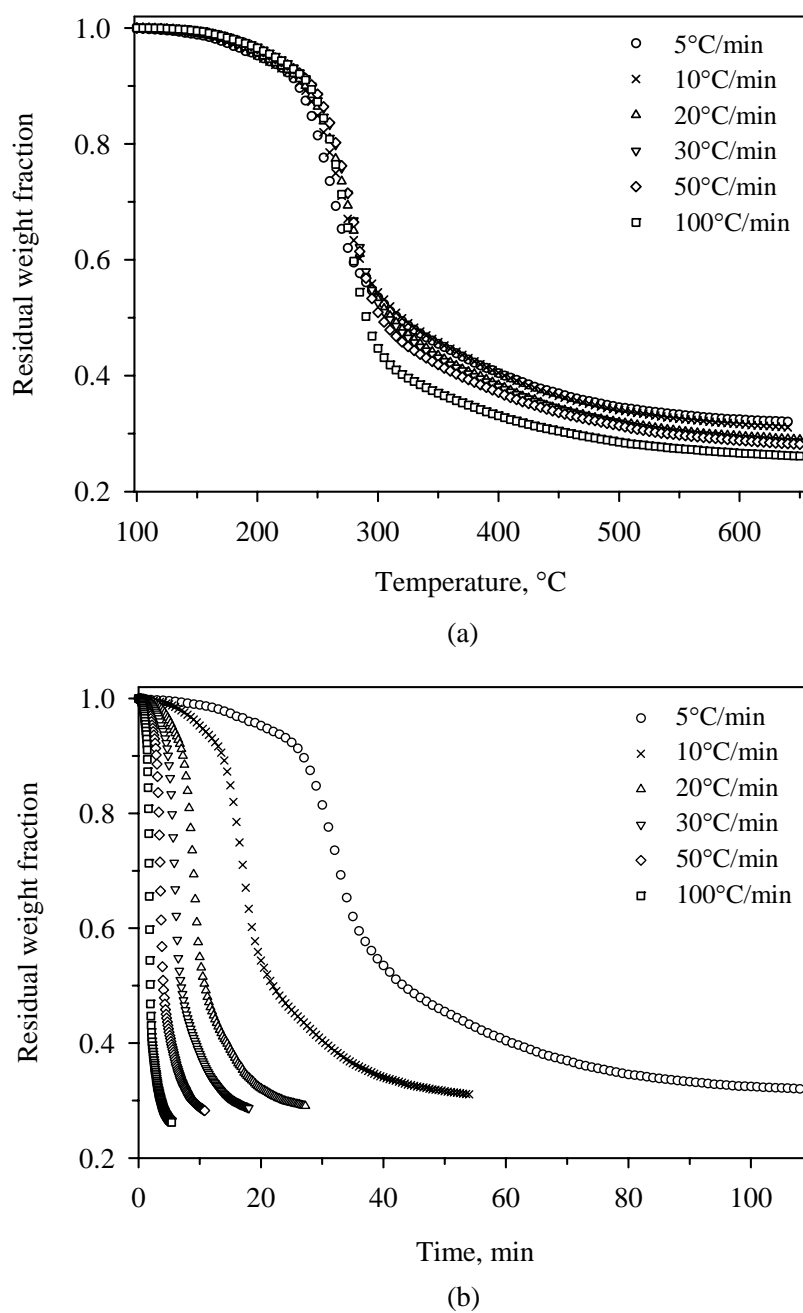


**Figure 3.9** TG curves for the non-isothermal pyrolysis of longan seed at different heating rates of a particle size 1.0 mm, (a) versus the temperature and (b) versus the time.

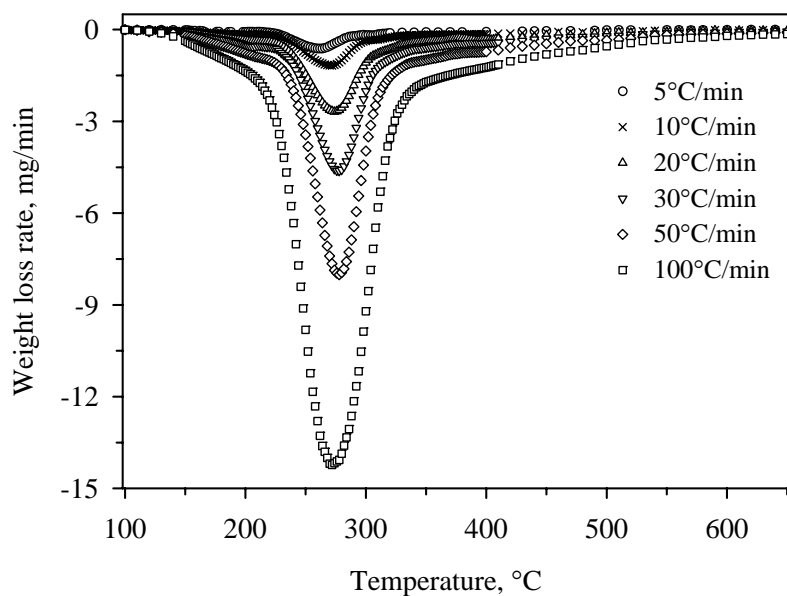


**Figure 3.10** The DTG for the non-isothermal pyrolysis of longan seed at different heating rates of a particle size 1.0 mm.

The yield of solid char is also significantly affected by the heating rate in that the yield tends to decrease with increasing in the heating rate. This effect of heating rate on the char yield was also found by previous investigators (Gonzalez et al., 2003; Guo and Lua, 2001). The solid yield decreases at a high heating rate signifies a decreasing of heat transfer resistance due to an abrupt increase of particle temperature. This heating rate effect should become less for the smaller size particle, because of its lesser heat transfer resistance. The evidence of this postulation is seen from the comparison of the heating rate effect at 5 and 100°C/min for various particle sizes, as displayed in Figure 3.11. It is seen that the final yield obtained from heating rate of 5 and 100°C/min in a particle size of 0.05 mm is approximately the same, but the difference of this two yields in the larger particle size tends to increase as the particle size is increased.

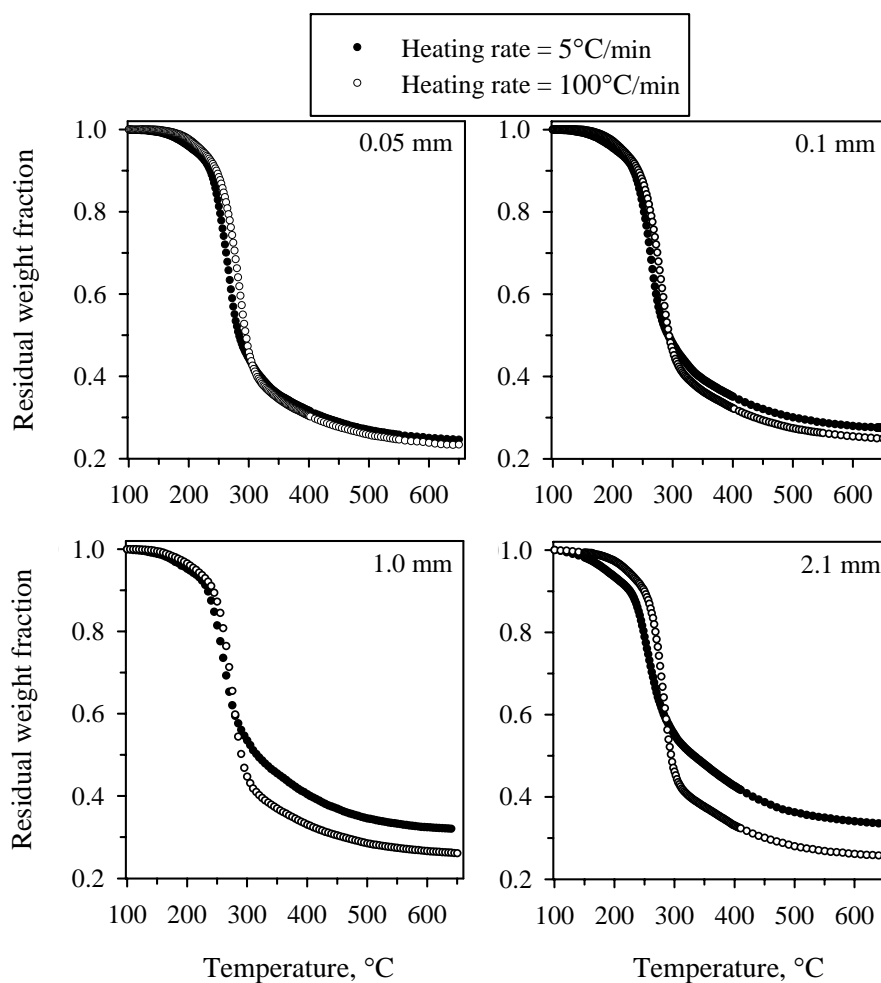
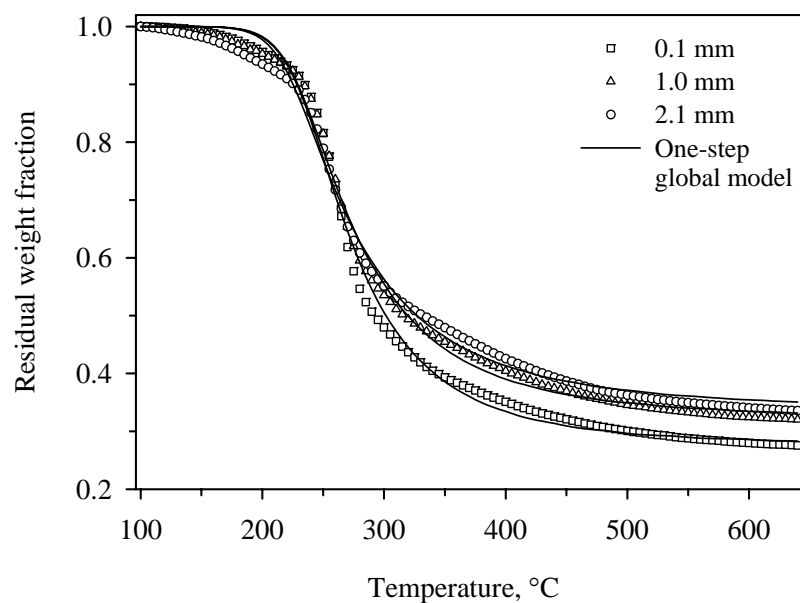


**Figure 3.11** The comparison of the TG for the non-isothermal pyrolysis of longan seed at heating rate 5 and 100°C/min for different particle sizes.

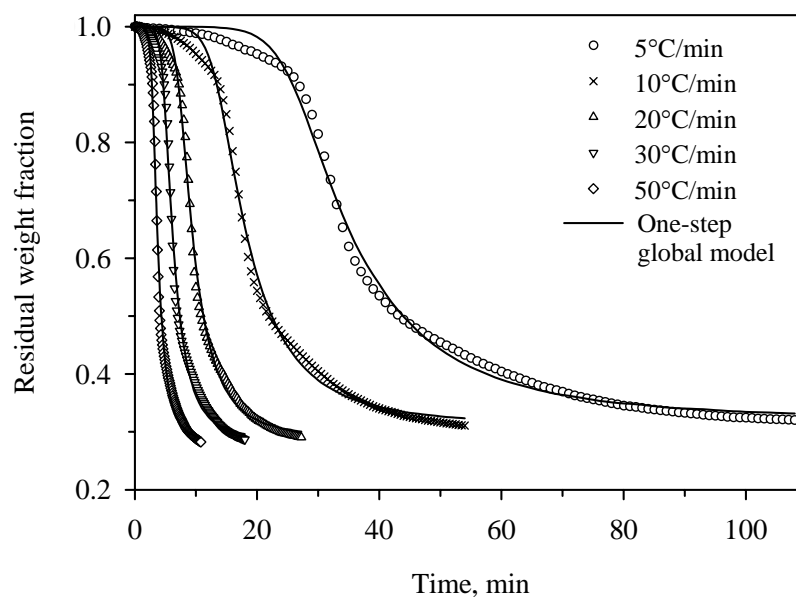
### 3.4.6 Model Fitting of Pyrolysis Data

With the appearance of only one peak in the DTG, it is reasonable that the experimental data could be described by the one-step global model. The fitting of the experimental data for different particle sizes and heating rates to the one-step global model are shown in Figure 3.12 (a) and (b), respectively. Overall, it is found that the optimized results from one-step global model agree reasonably with the experimental data. The major mismatch is found in the temperature range of 150-220°C,

with the model over-predicting the slight decreasing in mass fraction seen in the experimental data.



(a) Particle size effect



(b) Heating rate effect

**Figure 3.12** The TG curves for the effects of (a) particle size and (b) heating rate; from the experiment (symbols) and the one-step global model fitting (lines).

Next, the two-parallel reactions model was employed to test against the experimental data. The comparison between the experimental data and the model prediction for the effect of particle size is shown in Figure 3.13 and the kinetic parameters are listed in Table 3.3, while the results on heating rate dependence are shown in Figure 3.14 and Table 3.4, respectively. It is seen that the two-parallel reactions model can describe the experimental data extremely well for all particle sizes and heating rates studied, with the maximum deviation being in the range of 1.63-3.08%. The two-parallel reactions model can account for the mismatch previously observed in the one-step global model in the temperature range of 150-220°C. Therefore, the assumption of two parallel decomposition scheme proposed by the model seems to be reasonably sound. The model optimization gave the values of the fraction parameters  $a$  and  $b$  as 0.56 and 0.44, respectively.

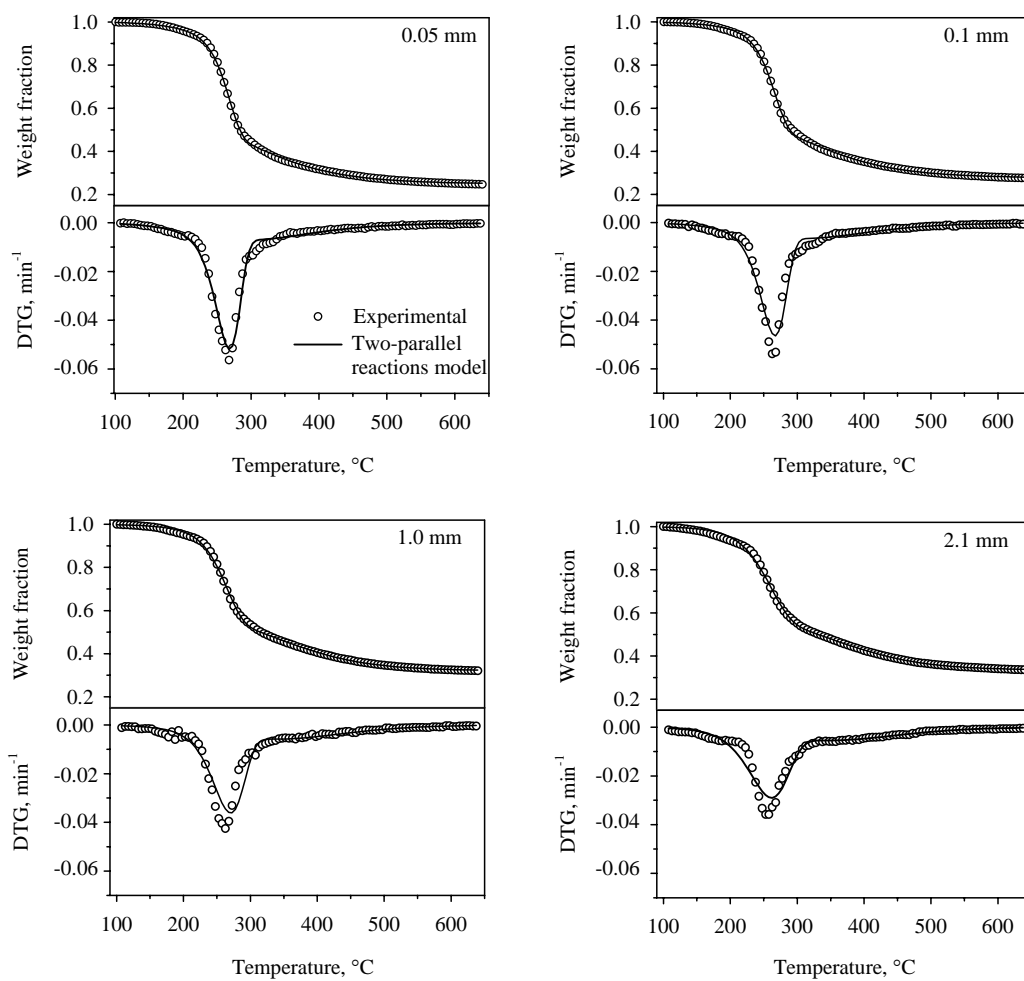


**Figure 3.13** The TG and DTG curves with different particle sizes at a heating rate 5°C/min for experimental data, the lines denote for the fitted data from two-parallel reactions model.

**Table 3.3** The kinetic parameters obtained from the two-parallel reactions model of longan seed with different particle sizes under the nitrogen atmosphere and a heating rate 5°C/min.

Parameter	Particle size [mm]			
	0.05	0.1	1.0	2.1
<i>a</i>	0.56			
<i>b</i>	0.44			
$A_1$ [min <sup>-1</sup> ]	4.35×10 <sup>10</sup>	4.65×10 <sup>9</sup>	2.24×10 <sup>7</sup>	1.52×10 <sup>5</sup>
$E_1$ [kJ/mol]	134.43	124.31	100.96	79.00
$A_2$ [min <sup>-1</sup> ]	2.92	1.52	0.56	0.30
$E_2$ [kJ/mol]	35.12	33.47	31.26	29.42
<i>n</i>	1.66	1.55	1.31	1.18
Max. Error [%]	2.89	3.08	2.32	2.26

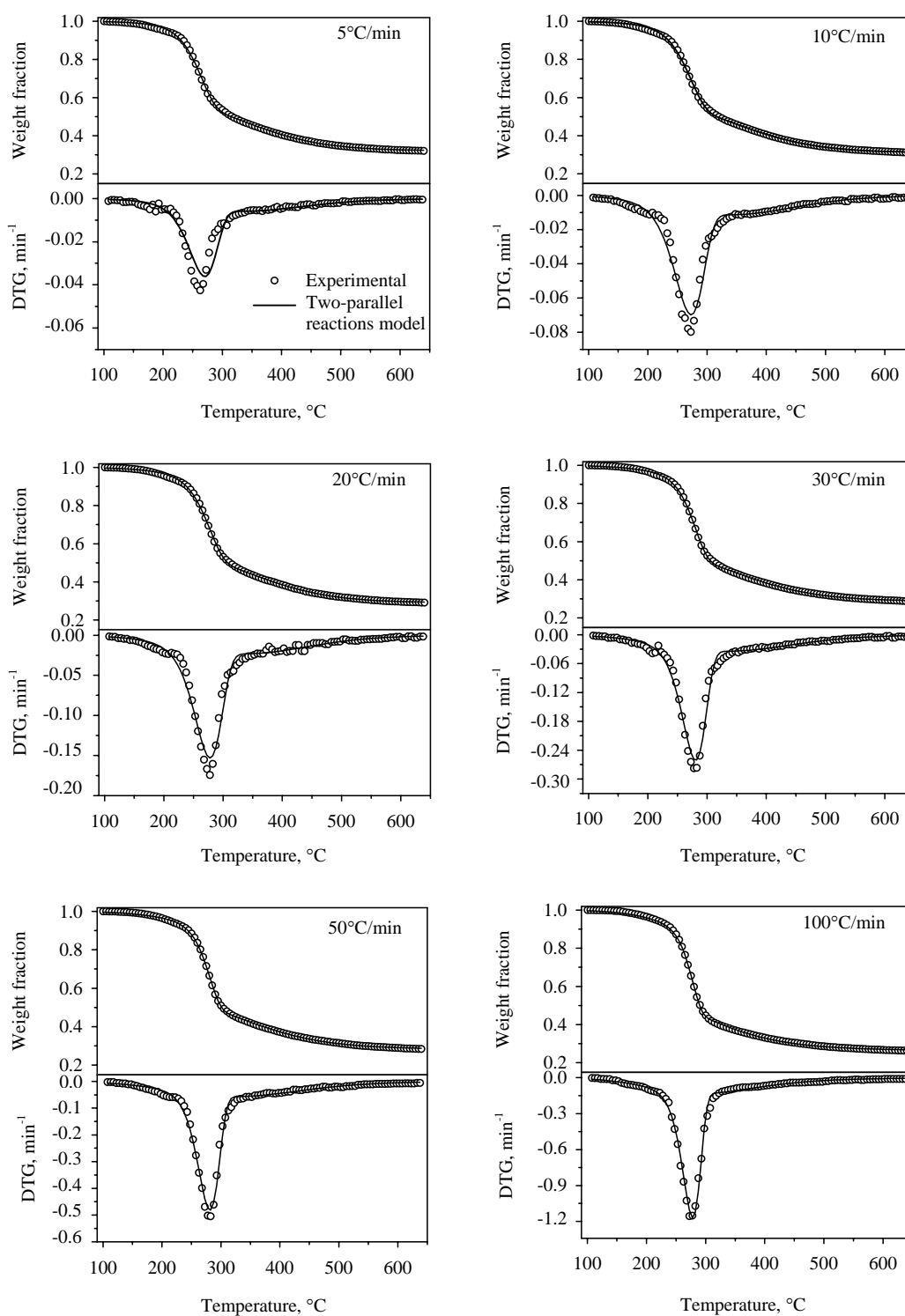


**Figure 3.14** The TG and DTG curves for different heating rates with a particle size of 1.0 mm from the experiment and the two-parallel reactions model fitting.

**Table 3.4** The kinetic parameters obtained from the two-parallel reactions model of longan seed at different heating rates with a particle size of 1.0 mm.

Parameter	Heating rate [°C/min]					
	5	10	20	30	50	100
$a$	0.56					
$b$	0.44					
$A_1$ [min <sup>-1</sup> ]	$2.23 \times 10^7$	$1.59 \times 10^7$	$2.04 \times 10^8$	$1.78 \times 10^{10}$	$8.62 \times 10^{11}$	$4.60 \times 10^{14}$
$E_1$ [kJ/mol]	100.96	97.93	107.04	125.62	140.81	164.87
$A_2$ [min <sup>-1</sup> ]	0.56	0.63	1.07	1.54	2.27	31.46
$E_2$ [kJ/mol]	31.26	29.41	28.52	28.14	27.08	32.30
$n$	1.31	1.22	1.19	1.22	1.23	1.62
Max. Error [%]	2.32	1.72	1.96	2.05	1.63	2.14

The effects of heating rate and particle size on the kinetic parameters are shown in Figure 3.15 (a) and 3.15 (b) for clearer observation. Figure 3.15 (a) shows a continued decreasing in the parameter values as the particle size is increased. The order of reaction 2 ( $n$ ) decrease from 1.66 to 1.18 as the particle size is increased from 0.05 to 2.1 mm. On the other hand, the kinetic parameters as affected by the variation in heating rate do not display a definite trend, as seen in Figure 3.15 (b). However, the  $A_1$  and  $E_1$  tend to increase with increasing heating rate, except at the heating rate of 10°C/min.

$A_2$  shows an increase with heating rate, although the effect is not pronounced for heating rate less than 50°C/min.  $E_2$  and  $n$  initially decrease in values before increasing markedly at heating rates larger than 50°C/min. It should be noted

that the model reaction is based on the assumption of purely kinetic control, without the effect of heat and mass transfer resistance. Under this assumption, the kinetic parameters should be independent of particle size and heating rate. However, the variation of kinetic parameters found here could be ascribed to the complex scheme of pyrolysis reaction and also the influence of some heat and mass transfer resistance existing in the real process.

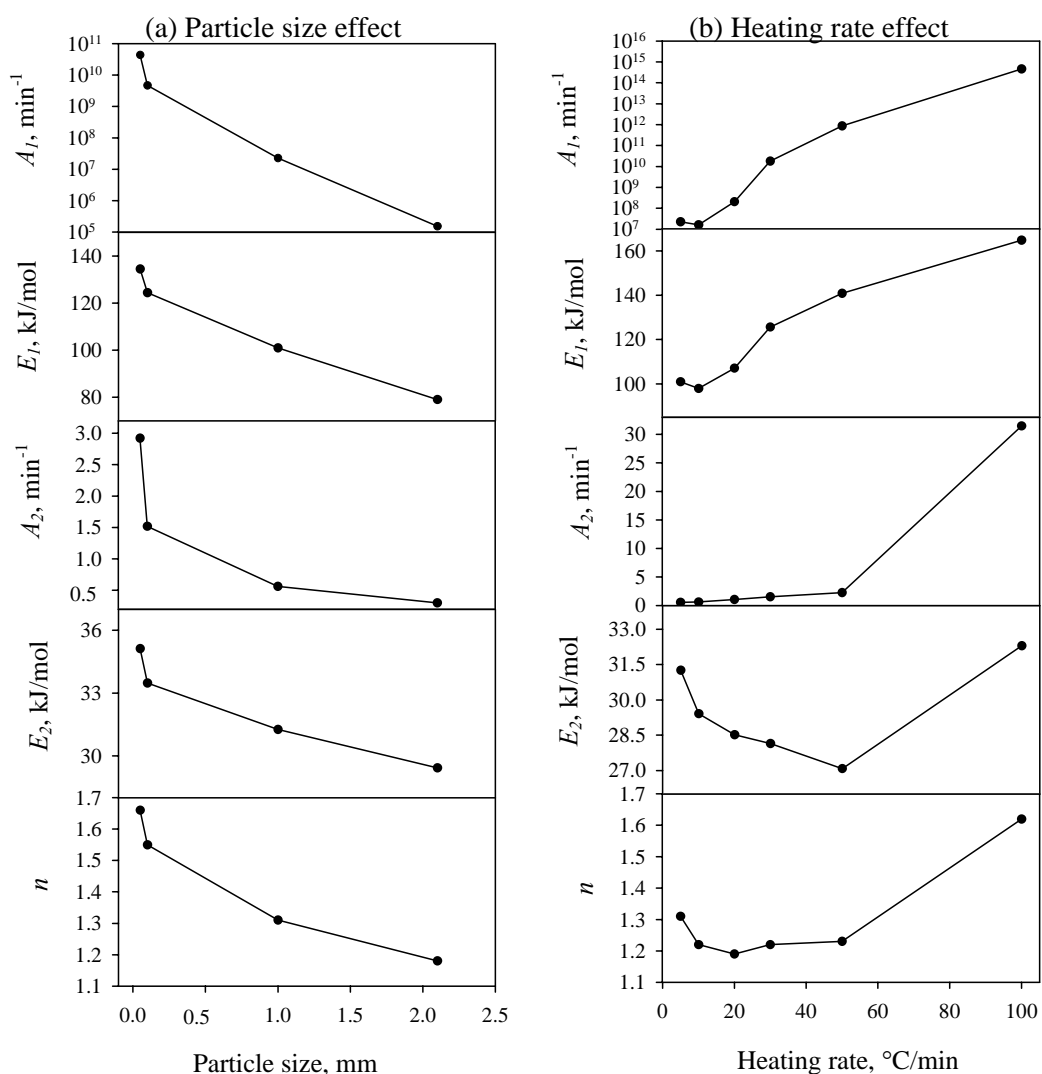


**Figure 3.15** The variation of kinetic parameters depend on the effects of

(a) particle size and (b) heating rate.

All results from the model fitting show that the pre-exponential factor and activation energy in the first fraction are higher than that in the second fraction. These  $A_1$  and  $E_1$  parameters values are  $1.52 \times 10^5$ - $4.60 \times 10^{14} \text{ min}^{-1}$  and 79.00-164.87 kJ/mol and  $A_2$  and  $E_2$  are 0.30-31.46  $\text{min}^{-1}$  and 27.08-35.12 kJ/mol, respectively. It is clearly seen that the parameters in reaction 2 ( $A_2$  and  $E_2$ ) are normally much lower than that in reaction 1 ( $A_1$  and  $E_1$ ). This behavior could be further examined from the contribution of each reaction as shown in Figure 3.16. The  $\alpha_1$  and  $\alpha_2$  are referred to the decomposition of the biomass composition in fraction  $a$  and  $b$ , respectively. The results indicate that the composition in the fraction  $\alpha_1$  sharply decreases at 220°C and reaches a final fractional value at 300°C. However, the  $\alpha_2$  decreases continuously from the initial temperature of 100°C down to the final temperature. These decomposition behaviors suggest that reaction 1 proceeds faster than reaction 2, showing by the higher values of  $A$  and  $E$ . Tsamba, Yang and Blasiak (2006) summarized the kinetic parameters values of biomass components from the literatures and their studies as follows:  $E_{\min}(\text{hemicellulose}) = 147.24 \pm 38.52 \text{ kJ/mol}$ ,  $E_{\max}(\text{hemicellulose}) = 172.75 \pm 39.44 \text{ kJ/mol}$ ,  $E_{\min}(\text{cellulose}) = 176.92 \pm 42.41 \text{ kJ/mol}$  and  $E_{\max}(\text{cellulose}) = 248.64 \pm 25.75 \text{ kJ/mol}$ . Comparing with these results, the values of activation energy obtained from reaction 1 in the present study (79.00-164.87 kJ/mol) could be attributed to the hemicellulose decomposition. The reaction 2 should correspond to the decomposition of lignin since the activation energy obtained in this work (27.08-35.12 kJ/mol) is in the range of 34-65 kJ/mol, which was reported by Varhegyi, Antal, Jakab and Szabo (1997).

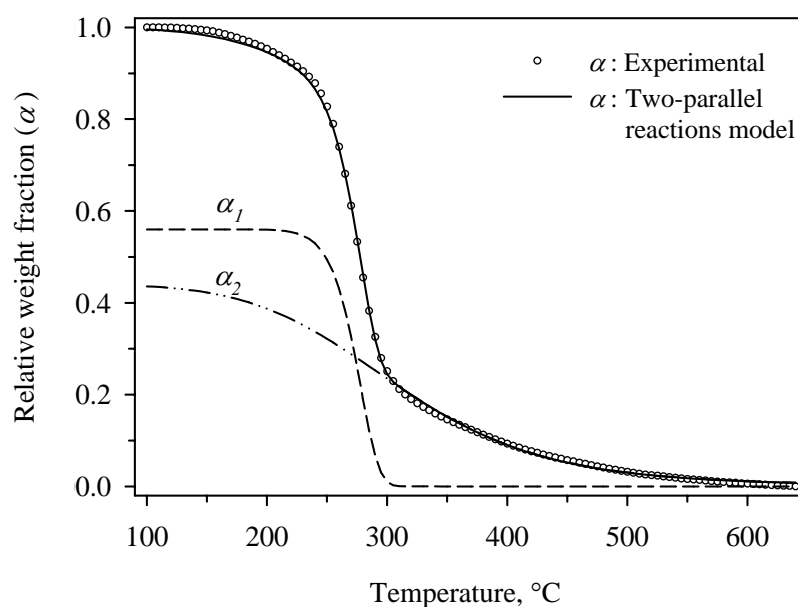


**Figure 3.16** The relative weight fraction ( $\alpha$ ) derived from the reaction schemes for a particle size of 1.0 mm at heating rate of 100°C/min.

### 3.4.7 Sensitivity Analysis of the Two-Parallel Reactions Model

The two-parallel reactions model contains six kinetic parameters, thus making it difficult to assess the accuracy of the model with respect to the variation of model parameters. So the analysis of the sensitivity of each parameter on the model result was performed by changing each parameter  $\pm 25\%$  while keeping the other parameters constant. The analysis was performed using the data of the 1.0 mm longan seed particle at the heating rate of 100°C/min. The resulting change in TG curves are compared to the standard data computed from the optimized parameters, and are displayed in Figure 3.17. The maximum deviation (%Max. Error) derived from this sensitivity analysis are also listed in Table 3.5.

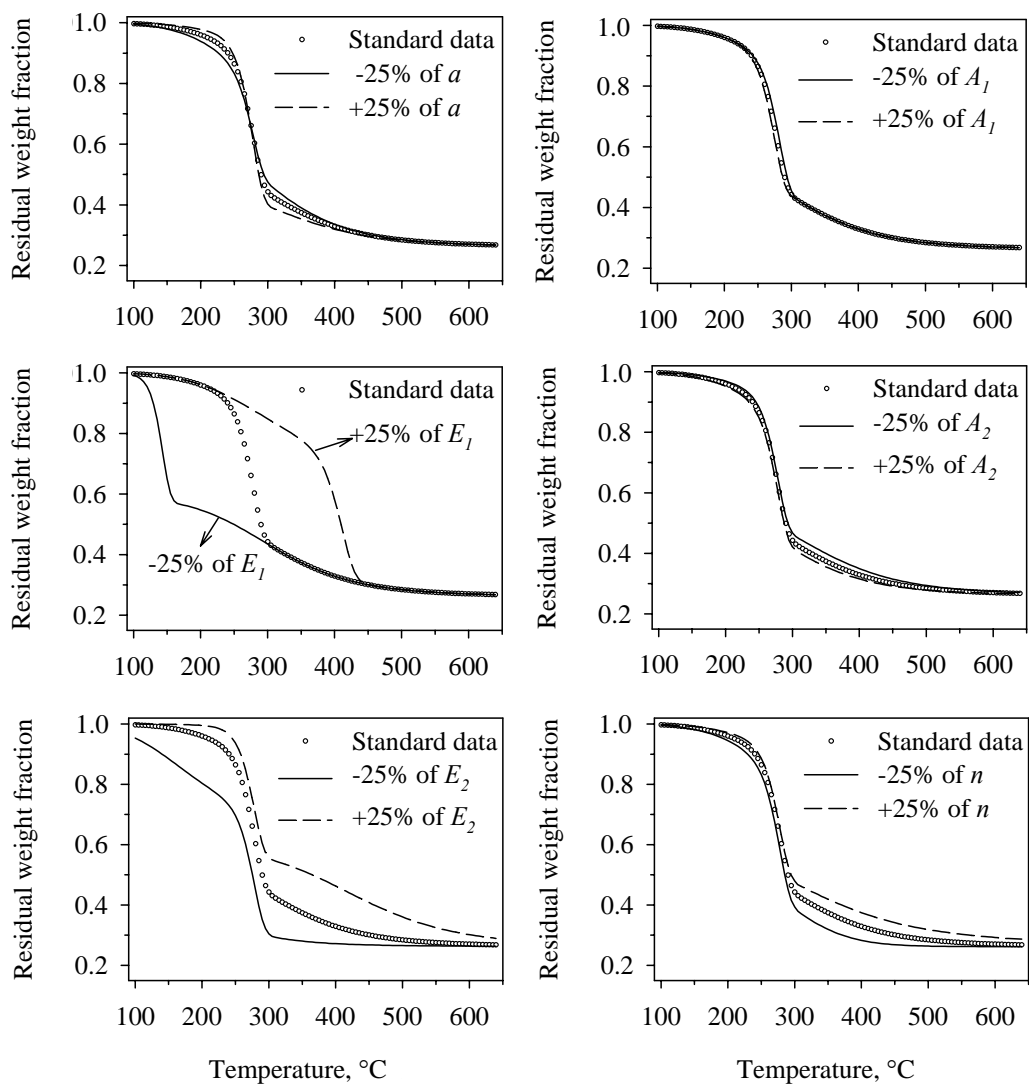


**Figure 3.17** The sensitivity analysis of kinetic parameters on the weight fraction.

The parameter  $a$  reflects the fractional composition in reaction 1, showing that increasing in  $a$  leads to an increase in the fraction to decompose in reaction 1. It is observed that the +25% of  $a$  make a weight fraction higher than the standard data in the temperature range of 200-275°C and a lower in the temperature range of 275-400°C, while for the -25% changes the behaviors show the opposite direction. The change of pre-exponential factors,  $A_1$  and  $A_2$ , describe how fast of the

decomposition rate, the higher  $A$  values the faster of reaction. An increasing in  $A_1$  is observed to decrease the weight fraction in the temperature range of 250-300°C. The increasing of  $A_2$  also makes a decreasing of weight fraction through the entire range of temperature corresponding to reaction 2. The highest sensitivity is found for the activation energies in both reactions (see the %Max. Error in Table 3.5), it seems that this parameter effect is more pronounced for reaction 1. The activation energy corresponds to the energy barrier of the reaction as the higher value means the slower the reaction rate. Therefore, the increasing in the activation energy should prolong the decomposing reaction to the higher temperature or longer time. The behaviors seen in the sensitivity analysis support this result, e.g. the main devolatilization of reaction 1 is prolonged to the temperature range 350-450°C by +25% of  $E_1$  and the +25% of  $E_2$  also retards the reaction 2 to decompose at the higher temperature. The increasing of reaction order  $n$  also retards the decomposition, yielding the higher residual weight fraction than the lesser order reaction does.

**Table 3.5** The values of %Max. Error derived from the changing of kinetic parameters for sensitivity analysis, for a particle size of 1.0 mm at heating rate of 100°C/min.

Sensitivity analysis	Max. Error [%]					
	$a$	$A_1$	$E_1$	$A_2$	$E_2$	$n$
+25%	9.72	4.85	110.68	5.56	40.19	13.32
-25%	8.29	8.12	43.96	8.60	31.90	14.85

### 3.5 Conclusions

The non-isothermal pyrolysis of longan seed exhibited a TG curve in sigmoid shape and showed only one major peak in DTG curve. The condition of a particle size 1.0 mm and at the heating rate of 5°C for the final temperature at 650°C produced the char yield of 30% and the main devolatilization is in the temperature range of 210-330°C. The heat transfer resistance increased by both the increasing in particle size and the decreasing in heating rate, giving an increasing in the char yield. The kinetics of the decomposition of longan seed could be well described by the two-parallel reactions model. The initial fraction of the biomass components derived from this model was 0.56 and 0.44 for reaction 1 and reaction 2, respectively. The pre-exponential factors in the range  $1.52 \times 10^5$ - $4.60 \times 10^{14} \text{ min}^{-1}$  and activation energy range of 79.00-164.87 kJ/mol were obtained for the reaction 1 depending on the particle size and applied heating rates. The reaction 2 was fitted well with the reaction order of 1.18-1.62, the pre-exponential factors of 0.30-31.46  $\text{min}^{-1}$  and activation energy of 27.08-35.12 kJ/mol. These values of activation energy suggested that the reaction 1 and 2 could be represented by the decomposition of hemicellulose and lignin, respectively. The sensitivity analysis on the predicted TG curve for a particle size 1.0 mm at heating rate 100°C/min revealed that the predictions showed high sensitivity towards the changes in the activation energies in reaction 1 and 2.

### 3.6 References

- Baker, R. R. (1978). Kinetic parameters from the non-isothermal decomposition of a multi-component solid. **Thermochim. Acta** 23: 201-212.

- Balci, S., Dogu, T. and Yucel, H. (1993). Pyrolysis kinetics of lignocellulosic materials. **Ind. Eng. Chem. Res.** 32: 2573-2579.
- Caballero, J. A., Conesa, J. A., Font, R. and Marcilla, A. (1997). Pyrolysis kinetics of almond shells and olive stones considering their organic fractions. **J. Anal. Appl. Pyrolysis** 42: 159-175.
- Conesa, J. A., Marcilla, A., Caballero, J. A. and Font, R. (2001). Comments on the validity and utility of the different methods for kinetic analysis of thermogravimetric data. **J. Anal. Appl. Pyrolysis** 58-59: 617-633.
- Encinar, J. M., Beltran, F. J., Bernalte, A., Ramiro, A. and Gonzalez, J. F. (1996). Pyrolysis of two agricultural residues: olive and grape bagasse. Influence of particle size and temperature. **Biomass and Bioenergy** 11: 397-409.
- Freeman, E. S. and Carroll, B. (1958). The application of thermoanalytical techniques to reaction kinetics. The thermogravimetric evaluation of the kinetics of the decomposition of calcium oxalate monohydrate. **J. Phys. Chem.** 62: 394-397.
- Font, R., Marcilla, A., Verdu, E. and Devesa, J. (1991). Thermogravimetric kinetic study of the pyrolysis of almond shells and almond shells impregnated with  $\text{CoCl}_2$ . **J. Anal. Appl. Pyrolysis** 21: 249-264.
- Garcia-Ibanez, P., Sanchez, M. and Cabanillas, A. (2006). Thermogravimetric analysis of olive-oil residue in air atmosphere. **Fuel Process. Technol.** 87: 103-107.
- Gergova, K., Petrov, N. and Eser, S. (1994). Adsorption properties and microstructure of activated carbons produced from agricultural by-products by steam pyrolysis. **Carbon** 32: 693-702.

- Gonzalez, J. F., Encinar, J. M., Canito, J. L., Sabio, E. and Chacon, M. (2003). Pyrolysis of cherry stones: energy uses of the different fractions and kinetic study. **J. Anal. Appl. Pyrolysis** 67: 165-190.
- Guo, J. and Lua, A.C. (2001). Kinetic study on pyrolytic process of oil-palm solid waste using two-step consecutive reaction model. **Biomass and Bioenergy** 20: 223-233.
- Haines, P. J. (1995). **Thermal methods of analysis principles, applications and problems**. Glasgow, UK: Chapman & Hall.
- Haykiri-Acma, H. (2006). The role of particle size in the non-isothermal pyrolysis of hazelnut shell. **J. Anal. Appl. Pyrolysis** 75: 211-216.
- Karaosmanoglu, F., Isigigur-Ergudenler, A. and Sever, A. (2000). Biochar from the straw-stalk of rapeseed plant. **Energy Fuels** 14: 336-339.
- Lua, A. C. and Guo, J. (1998). Preparation and characterization of chars from oil palm waste. **Carbon** 36: 1663-1670.
- Luangkiattikhun, P., Tangsathitkulchai, C. and Tangsathitkulchai, M. (2006). Non-isothermal thermogravimetric analysis of oil-palm solid wastes. **Bioresour. Technol.**: In press.
- Mackay, D. M. and Roberts, P. V. (1982). The influence of pyrolysis conditions on yield and microporosity of lignocellulosic chars. **Carbon** 20: 95-104.
- Mangut, V., et al. (2006). Thermogravimetric study of the pyrolysis of biomass residues from tomato processing industry. **Fuel Process. Technol.** 87: 109-115.
- Nugranad, N. (1997). **Pyrolysis of biomass**. Ph.D. Dissertation, University of Leeds, United Kingdom.

- Oasmaa, A. and Czernik, S. (1999). Fuel oil quality of biomass pyrolysis oils-state of the art for the end users. **Energy Fuels** 13: 914-921.
- Orfao, J. J. M., Antunes, F. J. A. and Figueiredo, J. L. (1999). Pyrolysis kinetics of lignocellulosic materials—three independent reactions model. **Fuel** 78: 349-358.
- Teng, H., Lin, H-C. and Ho, J-A. (1997). Thermogravimetric analysis on global mass loss kinetics of rice hull pyrolysis. **Ind. Eng. Chem. Res.** 36: 3974-3977.
- Tsamba, A. J., Yang, W. and Blasiak, W. (2006). Pyrolysis characteristics and global kinetics of coconut and cashew nut shells. **Fuel Process. Technol.** 87: 523-530.
- Varhegyi, G., Antal, M. J. Jr., Jakab, E. and Szabo, P. (1997). Kinetic modeling of biomass pyrolysis. **J. Anal. Appl. Pyrolysis** 42: 73-87.

# CHAPTER IV

## ACTIVATED CARBON FROM LONGAN SEED

### 4.1 Abstract

This chapter is concerned with the preparation of activated carbons from longan seed by several methods including the conventional two-step CO<sub>2</sub> activation, one-step CO<sub>2</sub> activation and chemical activation with H<sub>3</sub>PO<sub>4</sub>. The study of carbonization temperature effect in the two-step CO<sub>2</sub> activation was also investigated. In addition, the structural model was proposed to predict the pore development of activated carbon during char gasification with CO<sub>2</sub>. The porous properties of the prepared activated carbons were measured by using a volumetric method of the nitrogen adsorption at -196°C. The optimum conditions that gave the activated carbon with maximum surface area and pore volumes by each activation method were identified. The observed results from the conventional two-step and the proposed carbon activation model suggested the mechanisms for pore evolution during gasification process to consist of three-stage development, from which pore creation, pore coalescence and pore collapse contributing to different extent in each of these three stages. The study on carbonization temperature effect showed that the carbonized char at 350°C is the most reactive char that produced activated carbon with the highest porous properties. Comparing the results of one-step CO<sub>2</sub> activation with those of two-step operation indicated that both methods showed similar mechanism of pore development. Chemical activation by H<sub>3</sub>PO<sub>4</sub> suggested that the added chemical produced the phosphate compounds within the structure of

chemically activated carbon which was thermally stable in the temperature range 400-800°C.

## **4.2 Introduction**

Activated carbon is categorized as one of the most versatile adsorbent. It is widely used in many applications of separation and purification, including gas phase and liquid phase. Activated carbon is highly porous with very high specific surface area and is non-polar in nature but having slight polar property resulting from the existence of surface functional groups. There are generally two methods of manufacturing activated carbon, physical activation and chemical activation. Physical activation involves two basic steps of carbonization and activation with the mild oxidizing gas. Chemical activation involves only one carbonization step of a precursor impregnated with an inorganic salt or acids. The preparation conditions are carefully controlled to achieve the desired properties in pore structure and mechanical strength. However, there are other techniques that have been employed to produce activated carbon that meets the specific application requirement. For example, the one-step physical activation (Alaya, Girgis and Mourad, 2000; Gergova and Eser, 1996; Lua and Guo, 2000), and the combination of chemical and physical activation (Molina-Sabio, Rodriguez-Reinoso, Caturla and Selles, 1996). Activated carbon can be produced from a variety of carbonaceous materials. Coconut shell, coal, lignite, wood and some polymers are typically employed as the precursors for commercial production.

The preparation of activated carbon from agricultural and industrial solid wastes has also been the subject of numerous investigations. Examples are macadamia

nut shell (Ahmadpour and Do, 1997), rice husk (Yalcm and Sevinc, 2000), corn-cob (Chang, Chang and Tsai, 2000), apricot stone (Gergova, Petrov and Eser, 1994), grape seed (Gergova et al.), almond shell (Gergova et al.; Rodriguez-Reinoso and Molina-Sabio, 1992), olive stone (Al-Khalid, Haimour, Sayed and Akash, 1998; Rodriguez-Reinoso and Molina-Sabio), peach stone (Rodriguez-Reinoso and Molina-Sabio), cherry stone (Gergova et al.; Lussier, Shull and Miller, 1994), oil-palm wastes in the forms of shell (Lua and Guo, 2000), fiber (Lua and Guo, 1998), oil-extracted kernel (Guo and Lua, 2000), etc. The aim of this work is to convert longan seed, an abundantly available waste produced from the fruit cannery, into the activated carbon adsorbent. This process of activated carbon production help mitigating the disposal problem of longan seed and yet making a value added and useful product from the discarded solid waste.

The topics studied in this chapter involve the preparation of activated carbon by different methods, including the conventional two-step physical activation by  $\text{CO}_2$ , the one-step physical activation by  $\text{CO}_2$  and the chemical activation with  $\text{H}_3\text{PO}_4$ . In addition, a new structural model was proposed to simulate the pore evolution of gasified char during the activation step of the conventional two-step preparation method. An investigation into the effect of carbonization temperature on the porous properties of activated carbon in the two-step physical activation was further reported. The aim was to examine the effect of char properties on the quality of the prepared activated carbon. A one-step physical activation by  $\text{CO}_2$  was additionally studied to see any significant difference in the properties of activated carbon in comparison with that derived by the two-step method. The last topic involves the chemical activation with  $\text{H}_3\text{PO}_4$  to compare the results with the physical activation. Experimental results generated from this study should be valuable in understanding the pore development

and the variables involved during the preparation of activated carbon from longan seed precursor.

#### **4.2.1 Carbon Activation Model**

Characterization of resulting activated carbon is commonly carried out by studying adsorption isotherms of some common probe molecules. Adsorption equilibria in carbonaceous materials have been studied fairly intensively both experimentally and theoretically in the past few decades. This is mostly due to the advances in experimental techniques and the availability of high speed computer that make advanced theoretical tools such as Density Functional Theory (DFT) (El-Merraoui, Aoshima and Kaneko, 2000) and Monte Carlo simulations (Gavalda, Gubbins, Hanzawa, Kaneko and Thomson, 2002; Gavalda, Kaneko, Thomson and Gubbins, 2001; Suzuki, Iiyama, Gubbins and Kaneko, 1999) being applied more readily to solve numerous adsorption problems in carbon materials. As a result of these studies, it is increasingly recognized that the pore size distribution (El-Merraoui et al., 1998; Jaroniec, Gilpin and Choma, 1993; Jaroniec, Madey, Choma, McEnaney and Mays, 1989; Kaneko, 1998; Kruk, Jaroniec and Choma, 1998; Li, Kruk, Jaroniec and Ryu, 1998; Ohba, Suzuki and Kaneko, 2000; Setoyama, Suzuki and Kaneko, 1998; Wang and Kaneko, 1998) and the surface topology (including chemistry) (Abe, Kawashima, Kozawa, Sakai and Kaneko, 2000) all affect the adsorption equilibria. Among these two factors, pore size distribution is the prime factor when dealing with non-polar adsorbates or weakly polar adsorbates. Attempts to characterize the pore size distribution have been made by many workers in this field, mostly by using the measured adsorption isotherm and solving the integral equation of which the pore size distribution function is the kernel (Do, 1998). Such a derivation of pore size

distribution depends on how valid is the local isotherm which appears as the integrand of the above mentioned integral equation. In this proposed model, this problem will be addressed from the opposite direction, that is the process of char physical activation with either steam or carbon dioxide is modeled in an attempt to derive information on the evolution of geometrical surface area, pore volume and pore size distribution.

There are several models that have been developed in the literature to predict the porosity evolution of reacting solid. The modeling by treating the diffusion and reaction in a single cylindrical capillary and also in a random assembly of capillaries of the same radius was investigated by Petersen (1957). Szekely and Evans (1970) used two structural models, pore model and grain model to explore the gas-solid reactions. Another approach employing population balance equations to describe the change in the pore structure during gasification process was proposed by Hashimoto and Silveston (1973). Gavalas (1980) used a random capillary model to model char gasification. A random pore model for interpreting of fluid-solid reaction was developed by Bhatia and Perlmutter (1980). The discrete model was also used to illustrate the evolution of pore structure by Sandmann and Zygorakis (1986).

These models are mostly focused on the macroscopic properties of the solid. Such a picture does not properly describe the microscopic structure of char and the final product of activated carbon. It is the objective of this research to develop a structural model that properly does so. In this proposed model, it is simply assumed that char is composed of bundles of graphite layers and the porosity is created via a consumption of carbon by the gasification reaction. The model results are validated with the experimental data of longan seed-derived char gasification by  $\text{CO}_2$ .

#### 4.2.1.1 Algorithm of Carbon Activation Model

It is well known that char produced from the carbonization process consists of amorphous carbon and the graphitic crystallites (Bansal, Donnet and Stoeckli, 1988; Byrne and Marsh, 1995). The amorphous part is gasified during the initial stage of activation (burn-off < 10%), giving rise to some pore creation by the opening of the original blocked pores. The next stage involves the gasification of graphitic crystallites, which further creates new pores as well as the widening of existing pores. Since the gasification of amorphous carbon is too complex to model due to its highly disorganized structure, the model of char gasification proposed in this work will be limited to the gasification of the graphitic crystallites. The contribution of pore creation by the amorphous carbon during the initial part of activation, as compared to that at higher burn-offs, is considered to be relatively small and this contribution can be well incorporated into the crystallite model without appreciable error.

The carbon char is assumed to consist of bundles of parallel graphitic crystallites. Each of these crystallites contains equal-sized basal planes of hexagonal ring of carbon, but each of these planes (hereafter called layers) possesses different reactivity towards the gasifying agent as it is logical to expect physically that those layers are not energetically homogeneous with respect to chemical reaction. We use a random generator of MATLAB to generate randomly a number between zero and one to represent a reactivity for each of those layers or a group of layers. Such an assignment of random reactivity is consistent with the expectation of randomness in a realistic char particle. In our model, each crystallite contains fifteen carbon layers in accord with the experimental finding of Franklin (1951), and to ensure a good

statistical averaging we use one hundred crystallites in the model system. A schematic diagram of one crystallite is shown in Figure 4.1 (a).

The extent of gasification reaction for each carbon layer follows the reaction equation,

$$L_t = L_i - (a \times t), \quad (4.1)$$

where  $L_t$  is the length of carbon layer at a theoretical time  $t$ ,  $L_i$  is the initial length of carbon layer, and  $a$  is the carbon layer reactivity, with the reaction progressing along the carbon plane in a lengthwise direction. In this model, the theoretical time is defined as an incremental integer starting from zero. The simulation is performed for each loop of a theoretical time to arrive at a certain value of burn-off along with the evaluated porous properties of the carbon, as follows.

First, reactivity number is randomly assigned to the carbon layer in each crystallite as a “layer group”. The layer group designated as “1- $n$ ” group means that the adjacent layers of carbon can be grouped up to  $n$  layers, with these layers having the same reactivity. For example, 1-1 group indicates that every carbon layer in a crystallite will have its own reactivity, 1-2 group means that some crystallites can have individual reactivity or two adjacent layers with the same reactivity, etc. The application of a layer group concept adds flexibility in controlling the micropore size distribution generated in the early stage of the gasification reaction. In this work, two types of layer group, 1-2 and 1-5 group, are selected for the simulation scheme. This would give the largest created pore width of 10 and 20 Å (based on interlayer spacing of 3.35 Å of graphite), which constitute the micropore size range. Table 4.1 shows typical reactivity values for crystallite number 1 to 5 and

number 96 to 100, showing layer groups of 1-2 and 1-5, respectively. To obtain good simulation results, it is also necessary to assign a zero reactivity to some of the crystallites to account for the diffusional resistance inside the char at the early stage of gasification where the degree of burn-off is still low. Obviously, the number of these zero-reactivity crystallites decreases as the extent of reaction increases. For burn-off higher than 30%, the non-reactive crystallites are reassigned with reactivity numbers for the pore evolution is now completely controlled by the rate of chemical reaction. The number of non-reactive crystallites used in the calculation and their relative importance up to 30% burn-off are arbitrarily selected and adjusted so that a good match between the experimental and computed porous properties of the char is obtained.

Next, from the theoretical time and the assigned reactivities, the linear length ( $L_t$ ) of each carbon layer is calculated via Equation 4.1. Using the interlayer spacing of 3.35 Å for graphite as the layer thickness, the initial volume ( $V_0$ ) and the volume of char at a theoretical time  $t$  ( $V$ ) are calculated. The percentage burn-off of char is then calculated from the relation,

$$(\% \text{Burn-off})_{\text{cal}} = [(V_0 - V)/V_0] \times 100 \quad (4.2)$$

The pore size and pore volume are estimated from the layer width and the void volume existing between at least two adjacent layers, respectively. The pore surface area for each pore size is then calculated from the area of the two opposite carbon planes. Pore volume distribution is readily obtained from the knowledge of pore volumes of different pore sizes. Figure 4.1 (b) illustrates the typical porous structure of the crystallite containing a number of slit pores at a given burn-off. The

computation is repeated for different larger values of theoretical time to give different degrees of burn-off and the corresponding porous properties of the gasified char. It should be noted that the forward computation of the model to obtain a good fit between simulated and experimental results is based largely on the sensible selection of layer group pattern and the number of non-reactive carbon layers as previously described. The sum of square of relative error was used to decide the best fitting of the model to the experimental results.

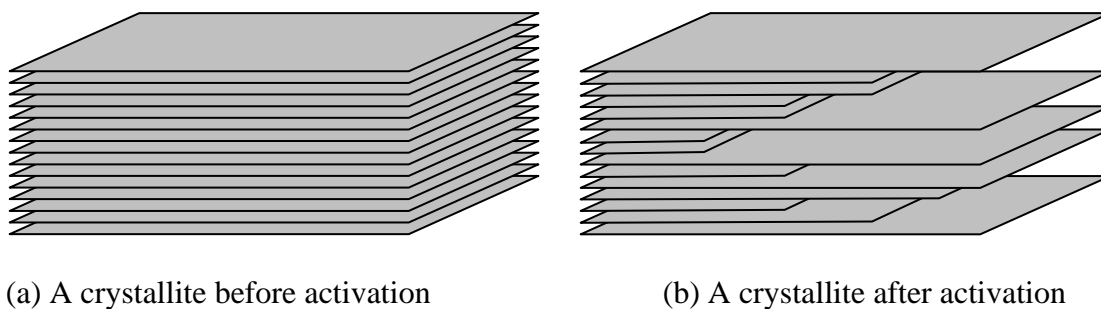


**Figure 4.1** Schematic diagram of a graphitic crystallite (a) before activation  
(b) after activation.

**Table 4.1** Typical generated reactivities of carbon layers of some graphitic crystallites.

Layer number	Crystallite number									
	1	2	3	4	5	96	97	98	99	100
1	0.034	0.704	0.333	0.092	0.967	0.937	0.772	0.126	0.499	0.926
2	0.100	0.704	0.333	0.092	0.654	0.012	0.772	0.126	0.499	0.926
3	0.528	0.149	0.117	0.393	0.111	0.694	0.772	0.126	0.499	0.926
4	0.356	0.149	0.117	0.393	0.657	0.795	0.772	0.126	0.755	0.926
5	0.823	0.718	0.138	0.035	0.386	0.339	0.772	0.228	0.755	0.926
6	0.240	0.718	0.138	0.035	0.004	0.956	0.024	0.228	0.755	0.137
7	0.979	0.130	0.420	0.458	0.685	0.346	0.024	0.228	0.526	0.137
8	0.797	0.130	0.420	0.458	0.855	0.532	0.024	0.228	0.526	0.137
9	0.828	0.680	0.917	0.930	0.396	0.184	0.024	0.117	0.526	0.137
10	0.560	0.680	0.917	0.930	0.317	0.640	0.024	0.117	0.332	0.137
11	0.369	0.779	0.784	0.071	0.198	0.855	0.385	0.117	0.332	0.218
12	0.853	0.779	0.784	0.071	0.756	0.199	0.385	0.117	0.332	0.218
13	0.229	0.764	0.486	0.724	0.162	0.434	0.385	0.907	0.750	0.218
14	0.119	0.764	0.486	0.724	0.136	0.435	0.385	0.907	0.750	0.218
15	0.965	0.231	0.513	0.980	0.131	0.272	0.385	0.907	0.750	0.218

### **4.2.2 Objectives of the Study**

The main purpose was to investigate the porous properties of activated carbon prepared from longan fruit seed and its dependence on the preparation conditions and methods. The preparation methods studied include the conventional two-step and one-step CO<sub>2</sub> activation, and the chemical activation with H<sub>3</sub>PO<sub>4</sub>. The effect of carbonization temperature on carbon porous properties in the subsequent CO<sub>2</sub> activation was also investigated. The structural model of carbon activation has been proposed and was tested against the experimental data of gasification data of longan seed-derived char with CO<sub>2</sub>. Better insight into the porous development of carbon during the gasification of char was explored from this model.

## **4.3 Materials and Methods**

### **4.3.1 Conventional Two-Step Physical Activation by CO<sub>2</sub>**

#### **4.3.1.1 Carbonization**

A batch of fresh longan seed was first pre-dried in an oven at 110°C for overnight, crushed, and sieved to obtain an average particle size of 2.1 mm. About 20 g of the prepared longan seed was carbonized in a horizontal tube furnace (Carbolite, UK) under the flow of N<sub>2</sub> at the rate of 100 cc/min. In all runs carbonization temperature was programmed to increase from room temperature to 650°C at a heating rate of 5°C/min and then held at this temperature for 2 h. Then the char was cooled down in the tube furnace to room temperature under the flow of N<sub>2</sub>. The char product was kept for further activation step.

#### 4.3.1.2 Activation

Activation of the derived char was carried out in the same horizontal tube furnace (Carbolite, UK). About 10 g of char were put in a ceramic boat and placed at the middle of the furnace. The temperature was increased from room temperature to the desired activation temperature at a heating rate of 5°C/min under the flow of N<sub>2</sub> (100 cc/min). Next, the flow of N<sub>2</sub> was stopped and CO<sub>2</sub> (Linde Gas, 99.95%) was admitted into the furnace at a constant flow rate of 100 cc/min. After holding for the required activation time, the furnace was switched off and cooled to the ambient temperature under the flow of N<sub>2</sub>. The activated carbon product was kept for further analysis. The activation temperatures studied were 800, 850 and 900°C and the holding times were 30, 60, 120 and 180 min for each activation temperature. For the 900°C series, the holding time of 180 min was not performed since the char was completely gasified. The activation runs gave char burn-off up to 90%. The burn-off expresses the weight loss of char during activation step and is defined as

$$\% \text{Burn-off} = [(M_c - M_{ac}) / M_c] \times 100 \quad (4.3)$$

where  $M_c$  is the initial weight of the raw char and  $M_{ac}$  is the weight of the obtained activated carbon.

#### 4.3.2 Carbonization Temperature Effect

The dried longan seed was crushed and sieved to obtain an average particle size of 2.1 mm. Carbonization was performed in a horizontal tube furnace under the flow 100 cc/min of N<sub>2</sub>. The carbonization temperatures were varied in the

range of 250-750°C and the heating rate and holding time were kept constant for all runs at 5°C/min and 2 h, respectively. The derived chars were characterized for porosity by the adsorption of CO<sub>2</sub> at 0°C using an Intelligent Gravimetric Analyzer (IGA002, Hiden analytical, UK). The chars also were measured for the true density by a pycnometer (AccuPyc1330, Micromeritics, USA), using helium at 27°C as the displacement fluid. These chars were further activated with CO<sub>2</sub> as an oxidizing gas in the tube furnace. Activation condition was fixed at 850°C and activation time of 2 h.

### 4.3.3 One-Step Activation

A batch of pre-dried longan seed was crushed to obtain an average particle size of 2.1 mm. The crushed longan seed weighing about 20 g was placed in the horizontal tube furnace (Carbolite, UK) and N<sub>2</sub> was allowed to flow through at the rate of 100 cc/min. The temperature was programmed for heating up from room temperature to the desired final temperature at the rate 10°C/min. Next, the N<sub>2</sub> flow was replaced by CO<sub>2</sub> using flow rate of 100 cc/min. The activation temperatures studied were 850°C and 900°C and the activation time from 30-120 min. After the activation step was completed, the CO<sub>2</sub> was stopped and the N<sub>2</sub> was admitted as inert atmosphere during the cooling period. The total weight loss of the one-step activation process is defined as

$$\% \text{Total weight loss} = [(M_i - M_{ac}) / M_i] \times 100 \quad (4.4)$$

where  $M_i$  is the initial weight of the raw material and  $M_{ac}$  is the weight of the obtained activated carbon.

#### 4.3.4 Chemical Activation by H<sub>3</sub>PO<sub>4</sub>

A batch of 20 g of crushed longan seed with an average size of 2.1 mm was impregnated in a 20 ml of 50 wt% H<sub>3</sub>PO<sub>4</sub> solution for 1 h. The impregnated longan seed was then dried in oven at 110°C for 12 h. This sample was then carbonized in the tube furnace under N<sub>2</sub> flow of 100 cc/min. The effect of carbonization temperature was studied in the range 400-900°C and for a fixed holding time of 1 h. The obtained products were leached with distilled water until the pH around 7 was achieved, and dried at 110°C for 48 h. The dried activated carbon samples were further characterized for the porous properties by N<sub>2</sub> adsorption.

#### 4.3.5 Activated Carbon Characterization

The porous structures of the derived activated carbons were determined from the isotherm data of N<sub>2</sub> at -196°C, using an Accelerated Surface Area and Porosimetry Analyzer (ASAP2010, Micromeritics, USA). Specific surface area was calculated from the N<sub>2</sub> adsorption isotherm by applying the Brunauer-Emmett-Teller (BET) equation (Do, 1998; Gregg and Sing, 1982), assuming the value of 0.162 nm<sup>2</sup> for the cross-sectional area of N<sub>2</sub> molecule. The total pore volume was determined from the volume of N<sub>2</sub> adsorbed at a relative pressure of 0.99 and converting it to the volume of N<sub>2</sub> in liquid state. Micropore volume was calculated from the N<sub>2</sub> adsorption data by using the Dubinin-Astakhov (DA) equation (Do; Gregg and Sing). Combined volume of mesopores and macropores was evaluated by subtracting the volume of micropores from the total pore volume. Typical pore size distributions covering the pore width from 5-1000 Å of the activated carbons were determined by applying the Density Functional Theory (DFT) (Olivier, 1995).

## 4.4 Results and Discussion

### 4.4.1 Conventional Two-Step Physical Activation by CO<sub>2</sub>

#### 4.4.1.1 Characterization of Char

It should be noted that the carbonization temperature of 650°C was chosen based on the thermal analysis results to ensure the complete devolatilization process, thus forming high carbon-content char. According to Table 4.2, it is seen that the fixed carbon content of the char is 86.4%, approximately fourfold increase in carbon content as compared to that of the original seed. The resulting char yield was 30% and the BET surface area and total pore volume of the char were 32.8 m<sup>2</sup>/g and 0.014 cm<sup>3</sup>/g, respectively. These porous properties values were obtained from the N<sub>2</sub> adsorption isotherm at -196°C. This should be kept in mind that these values might not represent the correct porous properties of the char. Since the char is dominated with very small pores, these pores become inaccessible to N<sub>2</sub> and also due to the large diffusional resistances of the gas at -196°C (Mackay and Roberts, 1982). This char was further activated by CO<sub>2</sub> at 850°C for 2 h, the fixed carbon content of activated carbon was 84.5%. The decreasing of carbon content is attributed to some carbon loss caused by the gasification reaction.

**Table 4.2** Proximate analyses of longan seed, char and activated carbon.

Sample	Proximate analyses in dry basis [wt%]		
	Volatile matters	Fixed carbon	Ash
Longan seed	78.7	19.6	1.7
Longan seed derived char carbonized at 650°C for 2 h	9.4	86.4	4.5
Longan seed derived activated carbon by CO <sub>2</sub> activation at 850°C for 2 h	6.8	84.5	8.7

#### 4.4.1.2 Activation of Char

The gasification process during the activation step is the most important process responsible for the production of activated carbon with high porosity. This process involves the reaction between carbon and CO<sub>2</sub> that gives rise to pore development. Figure 4.2 shows the dependence of char burn-off on activation temperature and activation time. The burn-off increases with an increase in both the temperature and time of activation, as expected. Relationship between the activation time and the burn-off for each temperature could be fitted as shown by the solid lines. The slope of these curves at a certain time also implies the gasification rate of carbon and CO<sub>2</sub> by equation,

$$-r_G = \frac{d(M_{ac}/M_c)}{dt} = \frac{-1}{100} \times \frac{d(\% \text{Burn-off})}{dt}, [\text{min}^{-1}] \quad (4.5)$$

The extent of gasification as reflected by the burn-off value increases with an increasing in activation temperature and time as seen in Figure 4.2. It is also observed that at each temperature the rate of gasification tends to decrease with the increasing in activation time. It is probable that during the initial period of gasification, the rate is higher because the reaction still proceeds in the vicinity of the carbon surface with minimal internal mass transfer resistance by pore diffusion. At longer times, CO<sub>2</sub> molecules need to diffuse deep into the internal pores, thus giving increased diffusional resistance with a consequent decrease in the rate of gasification reaction.

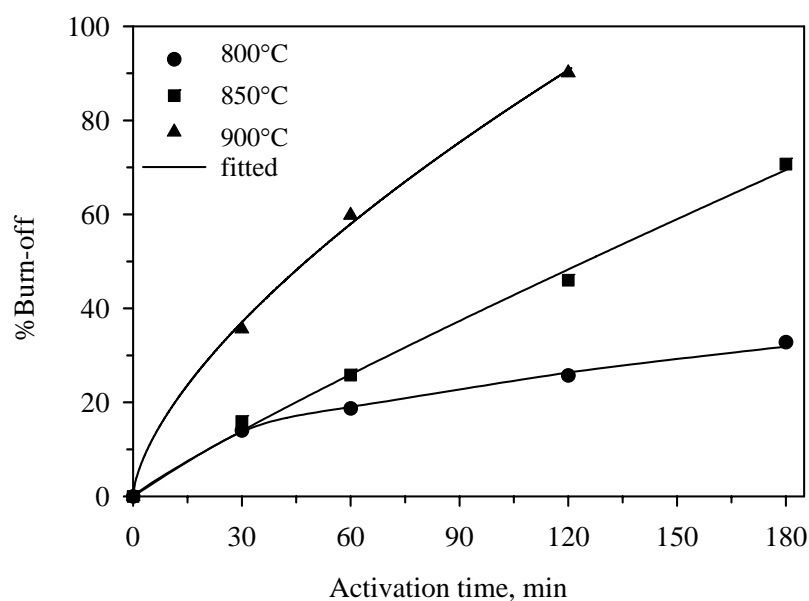


**Figure 4.2** The variation of char burn-off with activation condition.

#### 4.4.1.3 Porous Properties of Activated Carbons

The N<sub>2</sub> adsorption isotherms of the prepared activated carbons are shown in Figure 4.3. The isotherms show type I and type IV isotherms, according to Brunauer-Deming-Deming-Teller (BDDT) adsorption isotherm classification (Brunauer, Deming, Deming and Teller, 1940). For the 800°C and 850°C series at activation times longer than 30 min, there is a tendency for the isotherms to change from type I to type IV isotherm. However, all isotherms in the 900°C series are type IV. The N<sub>2</sub> uptake of the 800 and 850°C series increase with an increasing in activation time, but for the 900°C series the N<sub>2</sub> uptake decreases for longer activation time at 120 min. The existence of the hysteresis loop can be observed when the burn-off is higher than 25% (see the burn-off extent in Table 4.3). These hysteresis loops exist within the relative pressure range of 0.4-0.98. These results are indicative of the capillary condensation phenomena that results from the filling and emptying of mesopores by the sorbate liquid. At a given activation temperature or at a constant of activation time, the size of hysteresis loop appears to increase with increasing activation time or temperature. This reflects an increasing proportion of mesopore volume as can be seen from the drop in the percentage of micropore volume as the either activation time or temperature is increased (see Table 4.3).

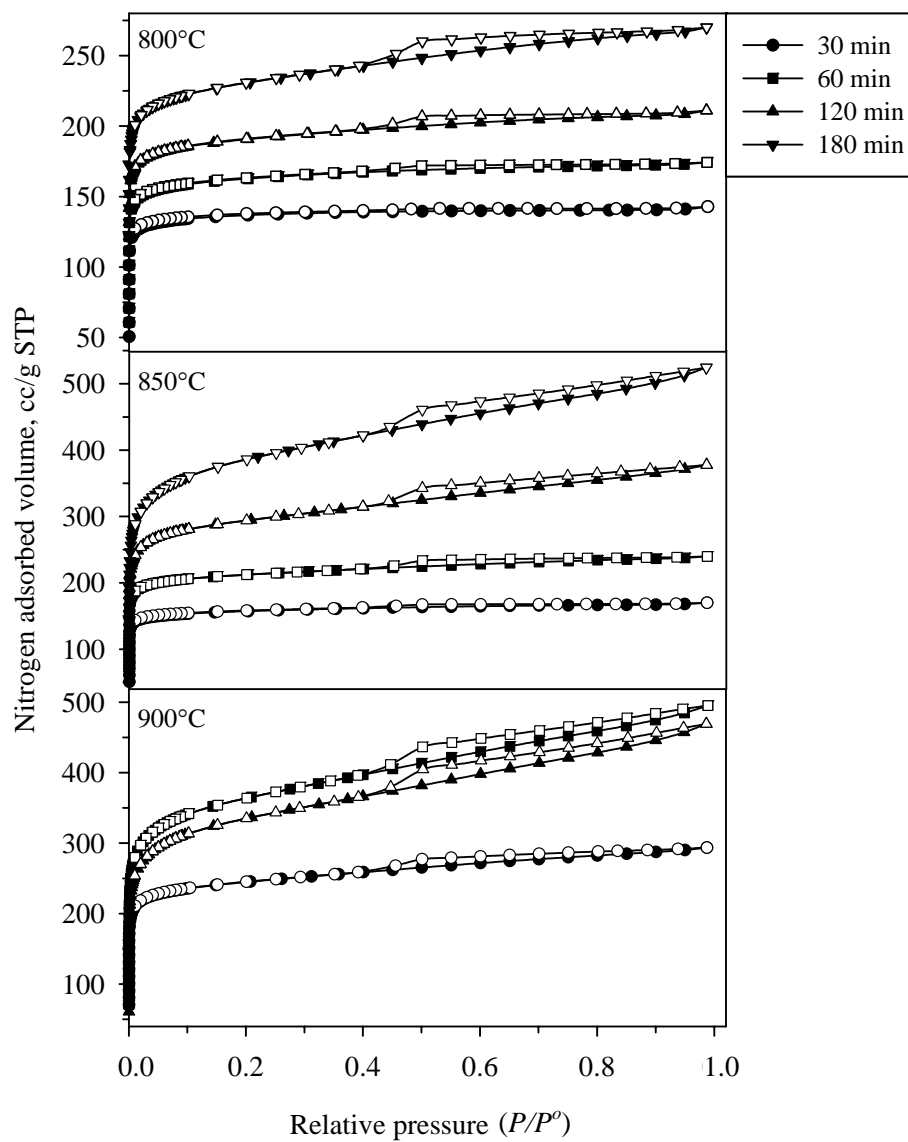


**Figure 4.3**  $N_2$  adsorption isotherms at  $-196^\circ\text{C}$  for activated carbons prepared at activation temperatures of 800, 850, and 900°C with different activation times.

The porous properties of activated carbons including BET surface area, micropore volume, and total pore volume are shown in Table 4.3. These properties were derived from N<sub>2</sub> adsorption data at -196°C. Depending on the preparation conditions, the BET surface area and total pore volume are in the range of 451-1278 m<sup>2</sup>/g and 0.22-0.81 cc/g, respectively. These prepared activated carbons are dominated with micropores, the volume of which is higher than 70%.

For activation temperature series of 800°C and 850°C, those porous properties increase with increasing in the activation time, except for the 900°C series. For this series, the porous properties increase for increasing activation time from 30 to 60 min but decrease at the longer time. This is probably due to the collapse of the pores which could result from the excessive gasification at this high activation temperature. Similarly, for the same activation time, the porous properties increase with increasing activation temperature. The best activation conditions that give the maximum in surface area (1278 m<sup>2</sup>/g) and pore volume (0.81 cm<sup>3</sup>/g) occur at 850°C and 180 min, corresponding to 70.7% burn-off and 8.7% of total yield of activated carbon.

**Table 4.3** Porous properties of activated carbons prepared from different activation conditions.

Activation condition (Temp.-Time)	Total yield [%]	BO [%]	S <sub>BET</sub> [m <sup>2</sup> /g]	V <sub>mic</sub> [cm <sup>3</sup> /g]	V <sub>me+ma</sub> [cm <sup>3</sup> /g]	V <sub>tot</sub> [cm <sup>3</sup> /g]
<b>800°C series</b>						
800–30	25.7	14.0	451	0.21 (95%)	0.01	0.22
800–60	24.3	18.7	538	0.25 (92%)	0.02	0.27
800–120	22.3	25.7	631	0.29 (88%)	0.04	0.33
800–180	20.1	32.8	766	0.35 (83%)	0.07	0.42
<b>850°C series</b>						
850–30	25.1	15.9	521	0.24 (92%)	0.02	0.26
850–60	22.2	25.8	705	0.32 (86%)	0.05	0.37
850–120	16.1	46.0	975	0.45 (82%)	0.10	0.55
850–180	8.7	70.7	1278	0.60 (74%)	0.21	0.81
<b>900°C series</b>						
900–30	19.2	35.6	813	0.38 (84%)	0.07	0.45
900–60	12.0	59.8	1204	0.56 (74%)	0.20	0.76
900–120	2.9	90.1	1108	0.52 (71%)	0.21	0.73

BO = Burn-off; S<sub>BET</sub> = BET surface area; V<sub>mic</sub> = Micropore volume;

V<sub>me+ma</sub> = Mesopore and macropore volume; V<sub>tot</sub> = Total pore volume

The following discussion explains the effect of activation conditions in terms of the burn-off. This parameter represents a combined effect of activation time and temperature on the degree of gasification. It appears from Table 4.3 that there is a direct relationship between % burn-off and the porous properties of activated carbon. Figure 4.4 shows plots of surface area and total pore volume as a function of % burn-off. These porous properties show a similar trend in that they increase with an increasing in burn-off extent up to about 70%, then decrease at higher value of burn-off. Figure 4.5 shows the pore volumes in each range of pore size including micropore, meso- and macropore and total pore with the evolved pores being almost micropores at low burn-off (less than 20%). When the burn-off is increased, the proportion of micropores decreases continually (see in Table 4.3). The changes of the pore evolution can be further examined by following the pore size distributions calculated by applying the DFT to the N<sub>2</sub> adsorption isotherms. Figure 4.6 presents the results of the dependence of pore size distribution on the char burn-off level. From these results, it could be inferred that the narrow pores or micropores are created at the initial stage of gasification. The subsequent pore development with increasing burn-off should involve the creation of new micropores and the widening of the existing micropores to produce mesopores. At burn-off higher than 70%, the decreasing of micropore and total pore volume as well as the surface area are probably caused by the decrease of new narrow pore formation combined with the collapse of the larger pores.

According to the result in Figure 4.6, the pore size distributions are bimodal with the first peak occurring at pore width around 7 Å and the second peak near 11 Å. Generally, the micropores can be divided into two types, ultramicropores

(pore width less than  $7\text{\AA}$ ) and supermicropores (pore width between  $7$  to  $20\text{\AA}$ ) (Gregg and Sing, 1982). As defined above, the peaks in pore size distribution correspond to the ultramicropores and the supermicropores, respectively.

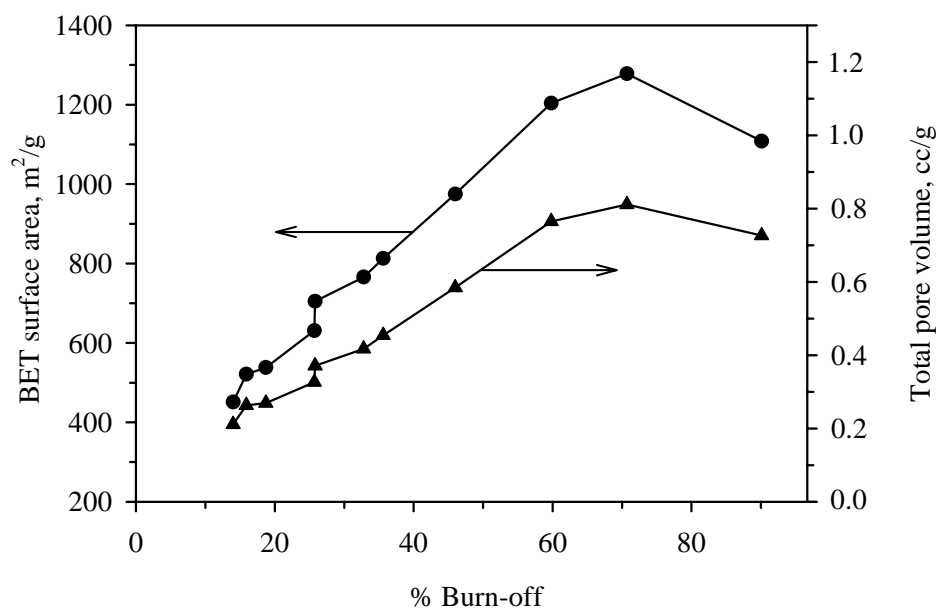


**Figure 4.4** BET surface area and total pore volume of longan seed activated carbons at different extent of burn-off.

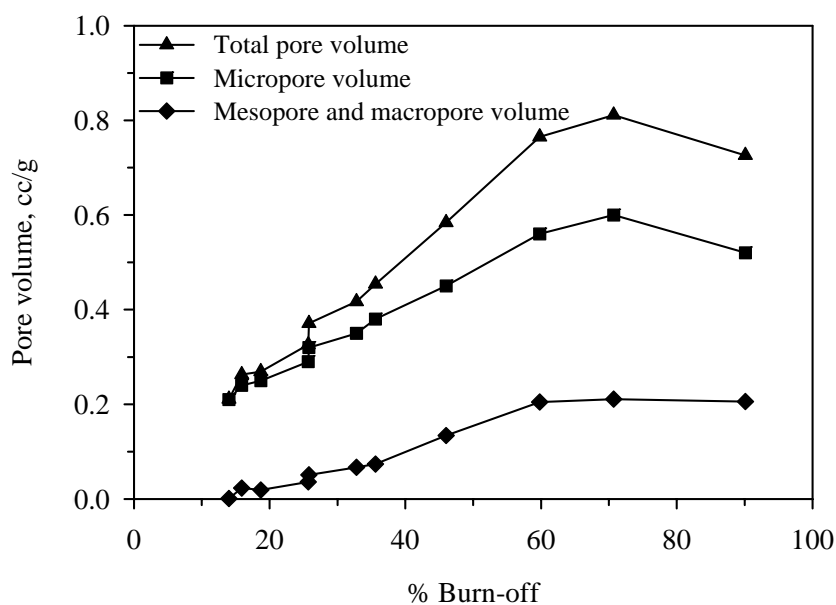


**Figure 4.5** Pore volume of activated carbons prepared with different char burn-offs.

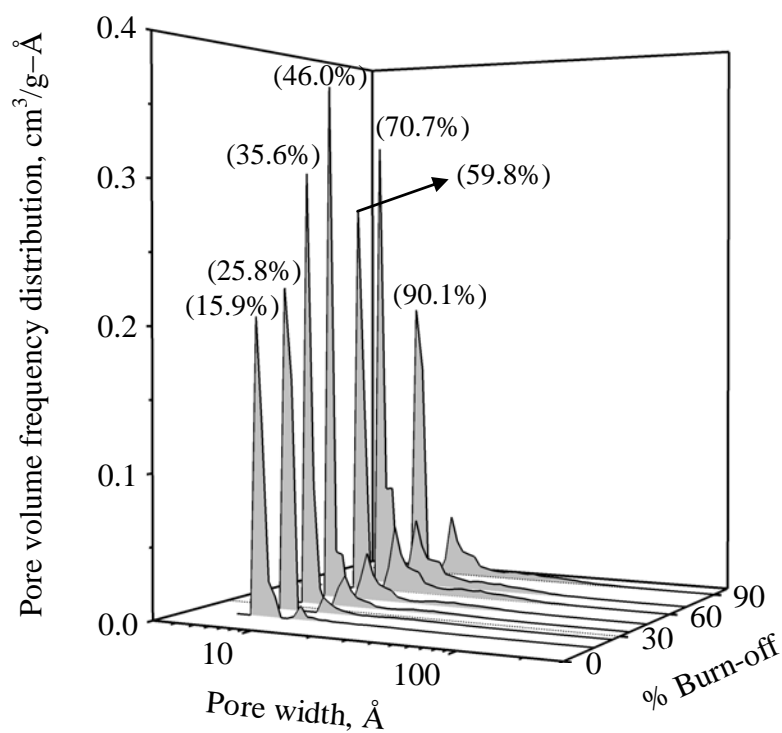


**Figure 4.6** Pore size distribution of activated carbons derived from different degrees of char burn-offs.

#### 4.4.2 Carbon Activation Model

The structural model proposed in this work is tested against the experimental gasification data of the longan seed-derived char by the conventional two-step CO<sub>2</sub> activation method. The BET surface area and total pore volume are used as the criteria to validate the model. As the model was constructed to describe only the gasification process, the physical properties of the raw char will provide the initial conditions for the model. These estimated initial parameters are surface area and total pore volume of char, and their values are 300 m<sup>2</sup>/g and 0.14 cm<sup>3</sup>/g, respectively.

From the characteristic of this structural model, the porosity is evolved due to the partial consumption of carbon layers, and the space between layers will constitute a pore, from which we can readily determine its pore volume and geometrical surface area. Since we assign only 15 layers initially in each graphitic crystallite, the largest possible pore width is 46.9 Å, in which we have assumed that the interlayer spacing between the two adjacent graphite layers is 3.35 Å. Thus, our model is restricted only to the description of micropores and lower end of the mesopore range. To facilitate the discussion later we shall define fine pores are those having widths smaller than 10 Å, large pores for widths greater than 20 Å and medium pores are those in between.

The evolution of surface area and total pore volume versus the extent of the gasification obtained from our structural model is shown in Figure 4.7 as solid lines with unfilled symbols. Experimental data are also shown in the same figure as solid symbols. The description of the surface area is regarded as excellent while that of pore volume is reasonably adequate despite the simplicity of our structural model. The model correctly describes the trend of the evolution of surface area and pore

volume, in that they both increase with burn-off and then decrease once a threshold burn-off has been reached. The agreement between the simulated pore volume and the data is good up to 25% burn-off, beyond which the model underpredicts the data. Furthermore, the maximum in the pore volume observed experimentally occurs at about 70% burn-off, while the model predicts a value of 85%. Nevertheless, the maximum value of the pore volume obtained by the model,  $0.86 \text{ cm}^3/\text{g}$ , agrees fairly well with the experimental data of  $0.81 \text{ cm}^3/\text{g}$ . Given the fact that the surface area is well described by the model and the pore volume only reasonably described, we can postulate that the spacing between the two initial adjacent graphite layers should be greater than  $3.35 \text{ \AA}$ . This is the possible reason why there is an underestimation of the total pore volume while the surface area is excellently described. This argument is physically justified as the interlayer spacing of  $3.35 \text{ \AA}$  is for perfect parallel graphite layers. For graphene layers in activated carbon, which are known to be turbostratic, the spacing between two layers would be expected to be greater than  $3.35 \text{ \AA}$ . As the burn-off is greater than 90%, the pore volume predicted by the model is higher than the experimental data and this is most likely due to the possible fact that the solid is readily disintegrated at this high burn-off and as a result the actual pore volume is lower than that predicted by the model.

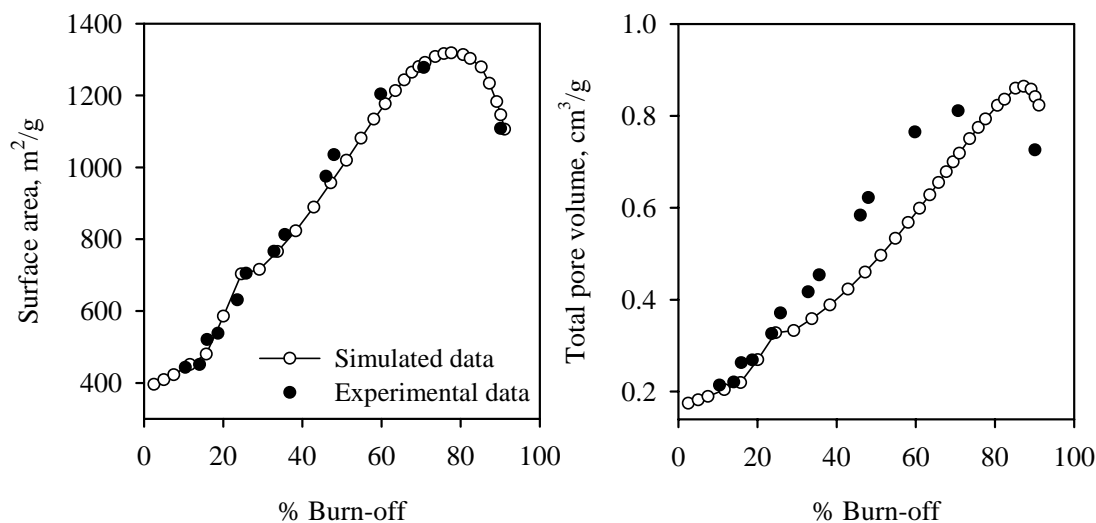


**Figure 4.7** Surface area and total pore volume of experimental and simulated data.

To check the effect of interlayer spacing, the simulation was also performed with two more interlayer spacings of 3.70 and 4.50 Å, respectively. The first value is the one suggested by Franklin (1950) for the interlayer spacing of a non-graphitizing carbon. Since the gasification was simulated with the same set of reactivities, the change would occur only for the pore volume but not with the surface area evolution. Figure 4.8 shows the simulated total pore volume and micropore volume for different interlayer spacings, as compared with the experimental values. The increasing of interlayer spacing shifts the pore volume curve upward closer to the experimental points. From the results, the interlayer spacing of 4.5 Å shows the best fitting up to 60% burn-off for the total pore volume and reasonable fitting for the micropore volume over the entire range of burn-off. Therefore, it could be inferred from the simulation that the interlayer spacing of the graphitic crystallite of longan seed derived char should probably have a value of 4.50 Å.

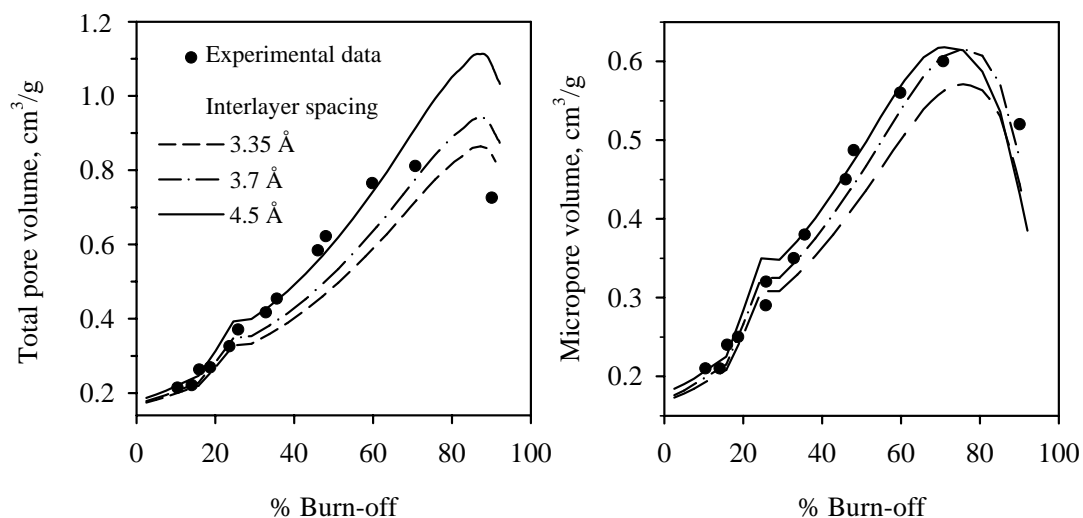


**Figure 4.8** Total pore and micropore volumes of experimental and simulated results with different interlayer spacing.

Apart from the surface area and the pore volume that can be obtained from the model, information about the pore size distribution of the gasified carbon can also be generated. This is shown in Figure 4.9 for a number of burn-off and this pore evolution data are also presented as pore volume for each pore size range (Table 4.4). The results show a deeper insight on how pores are generated and their pore size evolved with the degree of burn-off. There are three stages of pore development that can be observed in Figure 4.9. The first stage is for burn-off less than 5%, the second stage is for burn-off between 5% to 60% and finally the third stage for burn-off higher than 60%. During the first stage, only fine pores were evolved (creation stage), and the volume of these pores increases with burn-off as reflected in Figure 4.9 in that the volume increases while the pore width remains constant. These fine pores result from the increase in the number of these pores as well as the increase in the length of the existing fine pores. In the second stage, fine pores are still continually created, and

there is the onset of the medium pores. The main mechanism in this period is the increase in the length of each pore, which is due to the consumption of carbon layers, resulting in larger volume and surface area but the pore size remains fairly constant. In the last stage, the volume of fine pores decreases but the medium and large pores continue to evolve at the expense of fine pores. In this stage, two processes are possible. The first one is the coalescence of smaller pores to form larger pores and the collapse of pores due to the complete removal of the pore walls of some pores. The coalescence occurs in the early period of the third stage, and mechanistically this happens when one or two layers separating the two adjacent pores are completely consumed, resulting in the coalescence of these two pores into a larger one. Associated with this phenomenon is the loss of surface area but the volume and porosity increase. The collapse of pores occurs at the end of the third stage, and as a result pore volume, and surface area decrease with burn-off as seen experimentally in Figure 4.7 for burn-off greater than 80%. These results are in line with the results found by Dubinin and Zaverina (1949), from which it was reported that at burn-off less than 50% the porous structure of activated carbon is highly microporous, at burn-off lying between 50% and 75% the product carbon contains all types of pores, micro, meso and macropores, and at burn-off higher than 75% the porous structure is dominated with macropores.

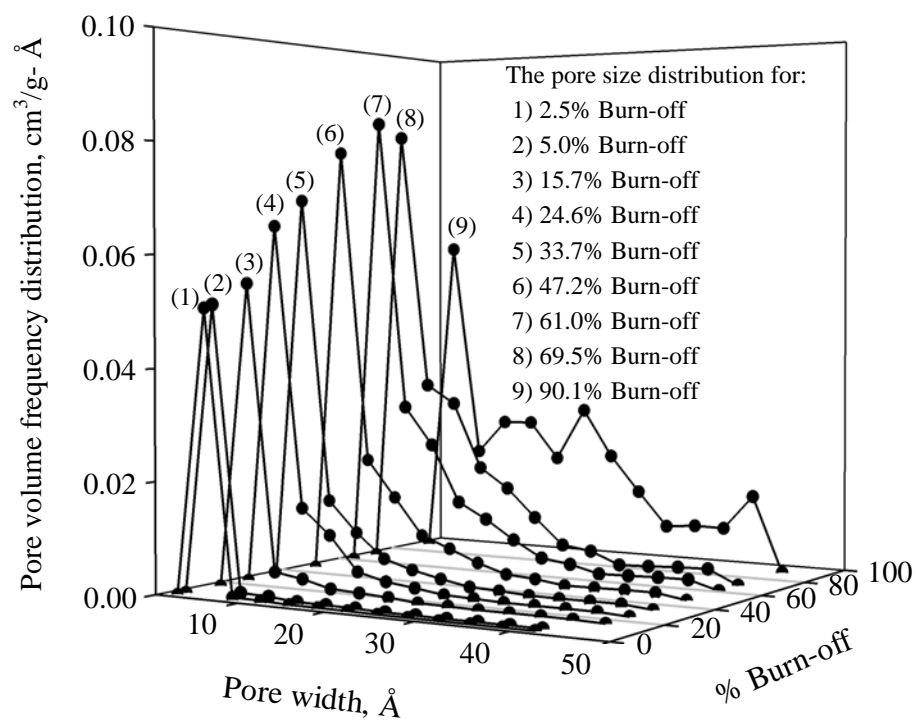


**Figure 4.9** The pore size distribution of simulated data at different degrees of char burn-offs.

**Table 4.4** Model-generated pore evolution data.

<b>BO</b> [%]	<b>V<sub>tot</sub></b> [cm <sup>3</sup> /g]	<b>Fine and medium pores</b> <b>(6.7-20 Å) volume</b> [cm <sup>3</sup> /g]	<b>Large pores</b> <b>(20-46.9 Å) volume</b> [cm <sup>3</sup> /g]
2.5	0.175	0.173	0.002
5.0	0.182	0.179	0.003
15.7	0.22	0.21	0.01
24.6	0.33	0.31	0.02
33.7	0.36	0.33	0.03
47.2	0.46	0.41	0.05
61.0	0.60	0.51	0.09
69.5	0.70	0.56	0.14
90.1	0.84	0.44	0.40

The experimental and simulated pore size distribution (PSD) of gasified carbon at two levels of char burn-offs are compared as shown in Figure 4.10. The experimental PSD results were calculated from N<sub>2</sub> adsorption isotherm data using the standard DFT method supplied by Micromeritics as DFT Plus software. There are two distinct peaks for the experimental PSD at pore width of 7 and 11 Å, respectively. The simulated PSD show a broader distribution into a smaller size range and give the second peak only at higher burn-off of 90.1%. The first possible reason for this is that smaller pores could not be probed by N<sub>2</sub> adsorption because these pores are either too small for nitrogen molecules to enter or the diffusional resistances at -196°C are too great to be probed within reasonable equilibration time. The other reason is the characteristic of the model that the basis for divisor is the value of one interlayer

spacing, leading to the less value of pore size distribution. The model is therefore needed to be refined in terms of the distribution of interlayer spacing values in the next stage of development. As shown in Figure 4.10, the maximum value of pore volume distribution occurs at about 5 and 7 Å for the simulated and experimental PSD, respectively, with the former giving the value about four times less than the latter. However, the experimental and simulated total pore volume compare fairly well, respectively, 0.59 versus 0.46 cm<sup>3</sup>/g (47.2% burn-off) and 0.73 versus 0.84 cm<sup>3</sup>/g (90.1% burn-off). Generally speaking, pore size distributions derived from the two techniques are within the same size range, although the simulation results give smaller average pore size as compared to the experimental estimation.

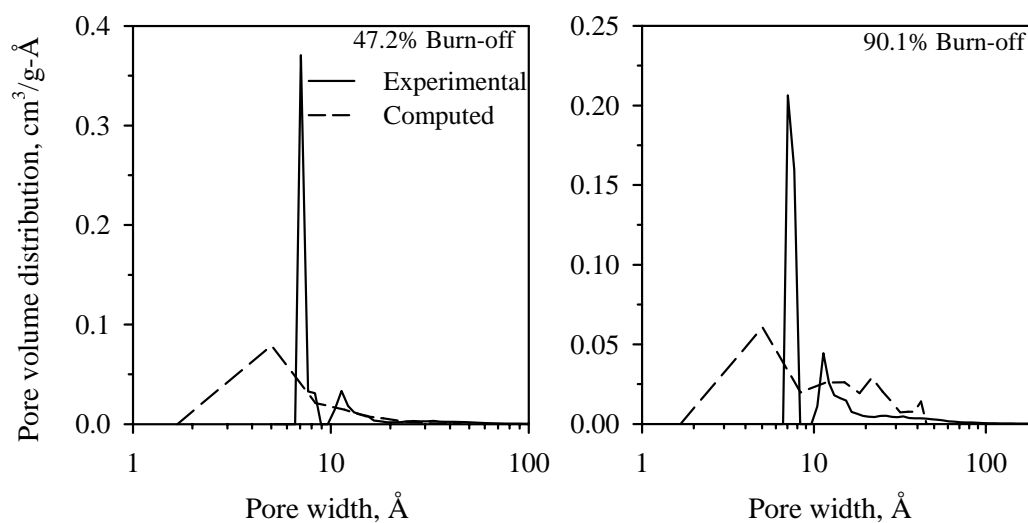


**Figure 4.10** Comparison of experimental and computed pore size distributions of activated carbon at two degrees of char burn-offs.

### 4.4.3 Carbonization Temperature Effect

#### 4.4.3.1 Char Properties

The yield of char obtained at different carbonization temperatures is shown in Figure 4.11. The char yield sharply decreased in the temperature range of 250-350°C from 67.3 to 41.1%, since this temperature range is in the main devolatilization stage of longan seed. The yield gradually decreased from 33.3 to 29% for further increasing of temperature in the range 450-650°C. This decreasing of char yield is ascribed to the releasing of volatile matters, hence giving the residual char with high carbon content. This is supported by the results shown in Figure 4.12 where the volatile matters content decreases and fixed carbon content increases with increasing in the carbonization temperature.

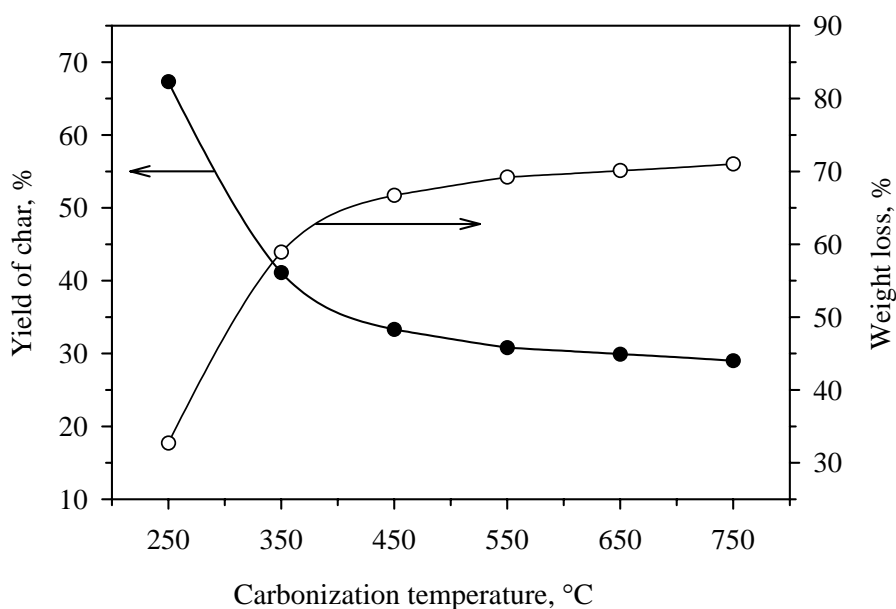


**Figure 4.11** Yield of chars and weight loss prepared at different carbonization temperatures.

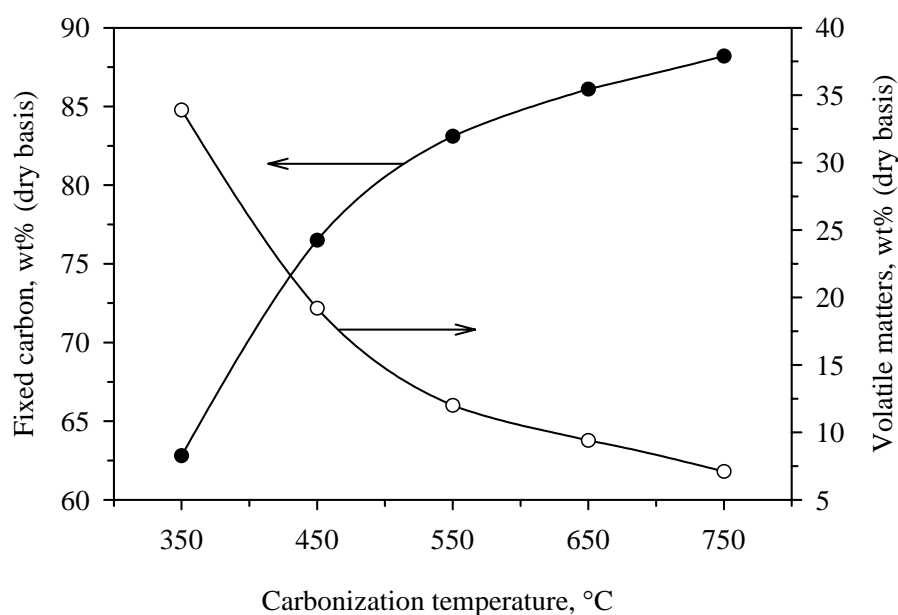


**Figure 4.12** Proximate analysis of chars prepared at different carbonization temperatures.

The true density of char increases with increasing in carbonization temperature as depicted in Figure 4.13. This result indicates the densification of char as the carbonization temperature is increased.  $\text{CO}_2$  isotherms were measured and analyzed to determine the pore volume of char, rather than using the standard  $\text{N}_2$  adsorption isotherms. This is due to the reason that the increased resistance for  $\text{N}_2$  diffusion at a low temperature of  $-196^\circ\text{C}$  and in pores of very small sizes and not well developed of char particles gave unnecessarily much longer time to reach the adsorption equilibrium. The  $\text{CO}_2$  isotherm in Figure 4.14 shows that the adsorbed amount increases with increasing in the carbonization temperature. Micropore volumes calculated by Dubinin-Rudushkevich (DR) equation (Gonzalez, Rodriguez-Reinoso, Garcia and Marcilla, 1997) using these isotherm data are shown in Figure 4.15. It is found that the micropore volume of char increases linearly with carbonization

temperature in the range from 350°C to 550°C and approaches a constant value at temperatures higher than 650°C. According to the results of true density and porosity, we may tentatively divide the effect of carbonization temperature into two ranges. These ranges are for the carbonization temperature of 350-550°C and 650-750°C.

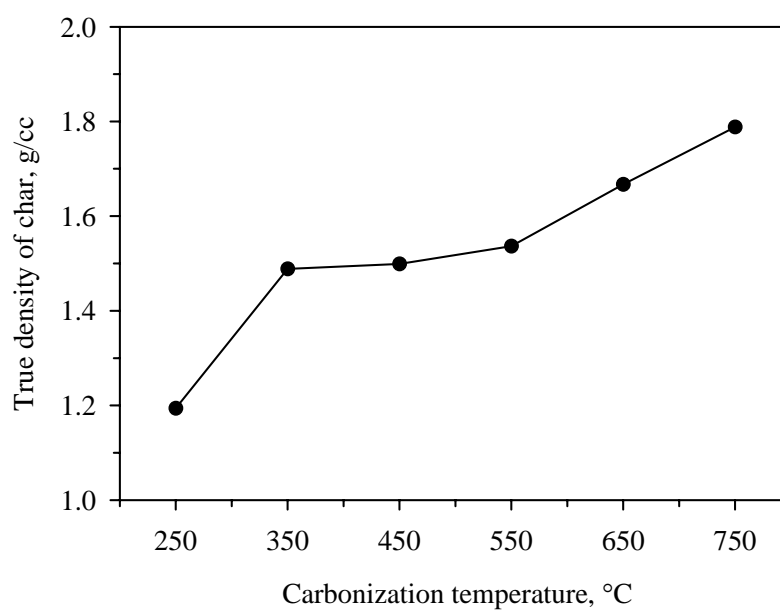


**Figure 4.13** True density of chars prepared at different carbonization temperatures.

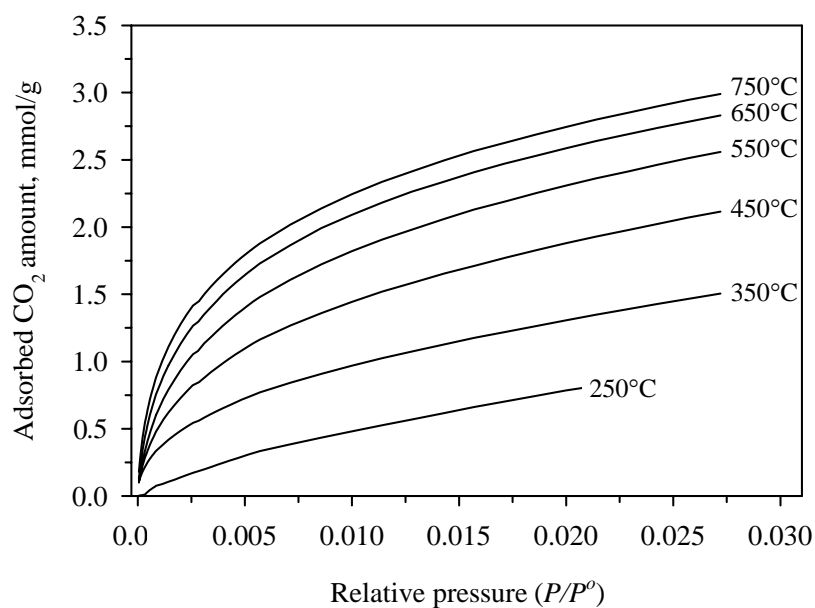


**Figure 4.14** CO<sub>2</sub> adsorption isotherms at 0°C of chars prepared at different carbonization temperatures.

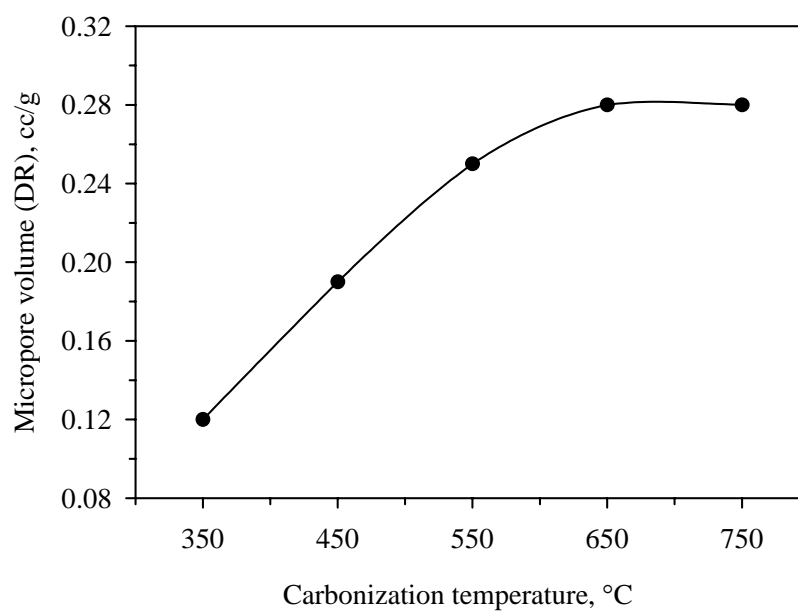


**Figure 4.15** Micropore volumes calculated from CO<sub>2</sub> adsorption isotherm at 0°C of chars prepared at different carbonization temperatures.

#### 4.4.3.2 Activation of Chars

The burn-off is defined as the fractional conversion of the char based on the initial mass of char used in the activation step, while the total weight loss is expressed as the total fractional conversion of the initial longan seed to the final product of activated carbon. Hence the total weight loss includes the conversion in both steps of carbonization and activation. Figure 4.16 shows the effect of carbonization temperature on the burn-off and total weight loss. The burn-off decreased with the increasing in the carbonization temperature but for the total weight loss it passed through a maximum at 350°C. It is known that the temperature range 250-550°C is in the devolatilization stage of longan seed. The remaining volatile in the char products would be furthered released during the heating up period to 850°C in the activation step with this effect becoming more pronounced for char carbonized at a low temperature. Therefore, the burn-off calculated from the weight loss during the activation did not come from the result of activation step alone. It might be logical to use the total weight loss to represent the degree of activation for each char because this conversion value is based on the same basis of the initial mass of longan seed. The activation process involves the consumption of carbon by partial gasification with oxidizing gas. Since the extent of activation is dependent on the char reactivity, the higher reactivity char would be gasified at a higher rate leading to the higher weight loss of char. Therefore, the total weight loss can be used as a measure for the reactivity of char, with the higher total weight loss indicating the higher char reactivity. Since the maximum total weight loss of 82% occurred with the char carbonized at 350°C (Figure 4.16), it can be argued that the carbonization temperature of 350°C produced char with the highest reactivity. It should be noted also that the

highest reactivity char is not the one with highest microporosity (see Figure 4.15), proving that there was no direct relationship between the char porosity and its reactivity. The decreasing of the char reactivity as carbonization temperature was increased could result from the denser and better development of ordered structure of the char produced at high temperatures, making it more difficult to be gasified.

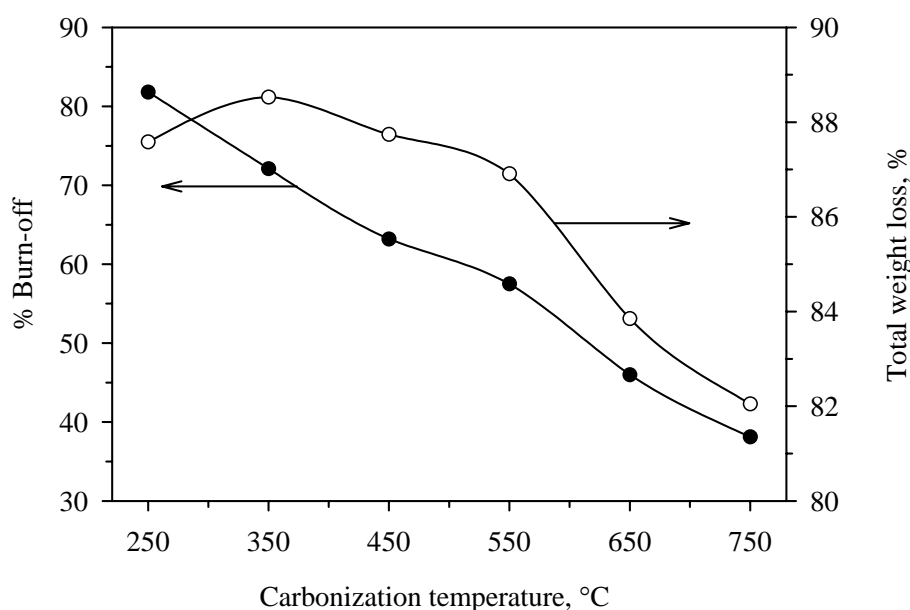


**Figure 4.16** Burn-off during activation process and the total weight loss of longan seed for the chars prepared at different carbonization temperatures, activation temperature of 850°C and for 2 h.

#### 4.4.3.3 Porous Properties of Activated Carbons

The derived-activated carbons prepared from different carbonization temperatures were measured for their porous properties by using the N<sub>2</sub> adsorption data at -196°C. The resulting adsorption isotherms are shown in Figure 4.17. The isotherms show type IV isotherm based on the BDDT classification. These

isotherms indicate that the activated carbon contains both the small and large pores i.e., having pore size distributions. Regarding to the closeness of  $N_2$  isotherms, the derived activated carbon can be separated into two groups. That is, the activated carbon prepared at 250-550°C and 650-750°C, respectively. This classification is the same as that mentioned earlier on the char density and porosity discussion. The first group has higher  $N_2$  adsorption capacity, showing the maximum for the 350°C char-derived activated carbon. The second group has a lower adsorption capacity with the activated carbon prepared from 750°C char giving the least amount of  $N_2$  adsorbed.

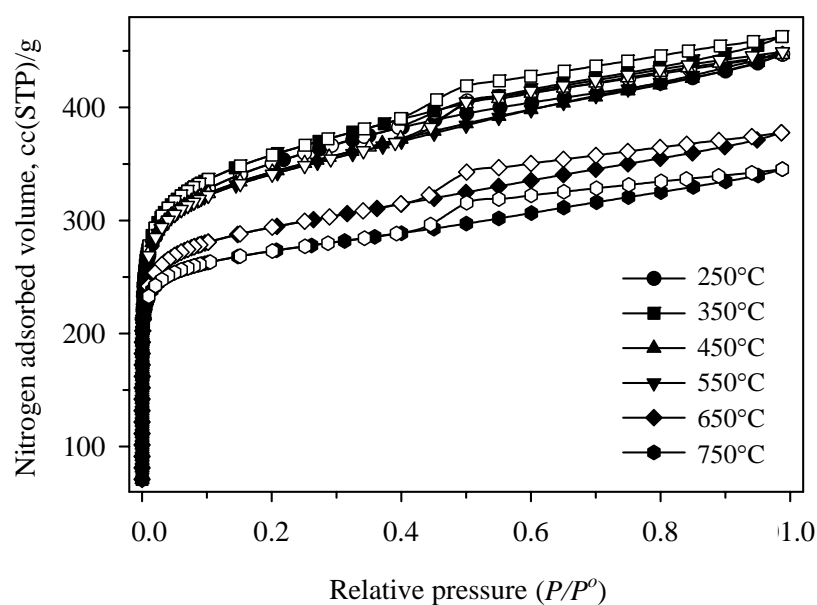


**Figure 4.17**  $N_2$  adsorption at  $-196^\circ\text{C}$  isotherms of activated carbons prepared from the chars derived at different carbonization temperature.

Table 4.5 summarizes the porous properties of chars and the char-derived activated carbons. The BET surface area, micropore volume and total pore volume are in the range of 906-1183  $\text{m}^2/\text{g}$ , 0.42-0.55  $\text{cm}^3/\text{g}$  and 0.53-0.72  $\text{cm}^3/\text{g}$ ,

respectively. These experimental data show that activated carbon produced from the char prepared at 350°C gave a maximum in porous properties including surface area and pore volume, as seen in Figure 4.18. It is also observed that the porous properties of activated carbon are directly related to the char reactivity during activation (total weight loss).

**Table 4.5** Porous properties of chars and the char-derived activated carbons.

Car. T [°C]	Total weight Loss [%]	Total yield [%]	Char properties		Activated carbon properties		
			True density [g/cm <sup>3</sup> ]	V <sub>mic, DR</sub> [cm <sup>3</sup> /g]	S <sub>BET</sub> [m <sup>2</sup> /g]	V <sub>mic</sub> [cm <sup>3</sup> /g]	V <sub>tot</sub> [cm <sup>3</sup> /g]
250	87.6	12.4	1.19	NA	1160	0.54 (78.2%)	0.69
350	88.5	11.5	1.49	0.12	1183	0.55 (76.4%)	0.72
450	87.7	12.3	1.50	0.19	1135	0.53 (76.8%)	0.69
550	86.9	13.1	1.54	0.25	1127	0.52 (75.3%)	0.69
650	83.9	16.1	1.67	0.28	975	0.46 (79.3%)	0.58
750	82.0	18.0	1.79	0.28	906	0.42 (79.2%)	0.53

Car. T = Carbonization temperature

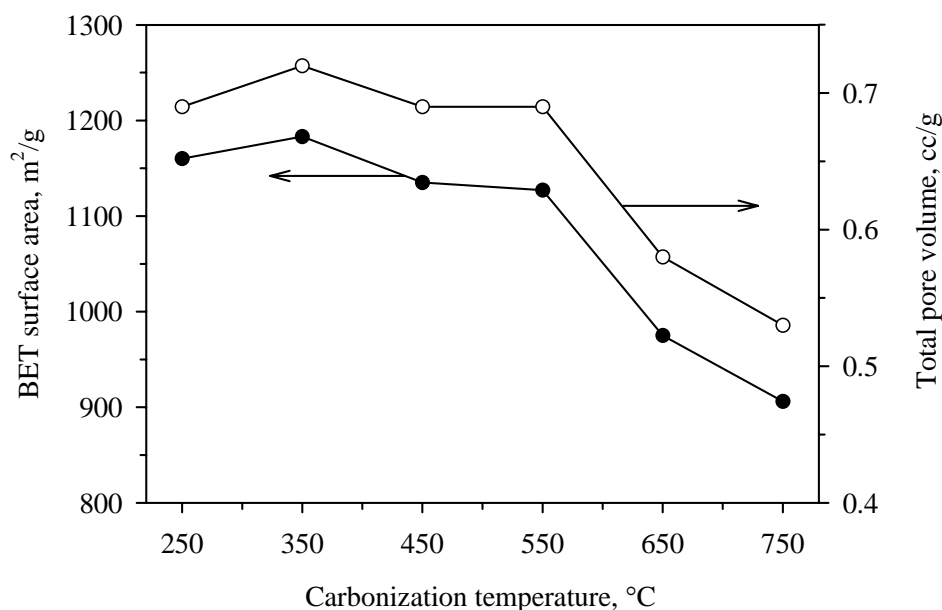


**Figure 4.18** BET surface area and total pore volume of activated carbons prepared from the chars derived at different carbonization temperatures.

#### 4.4.4 One-Step Activation

The comparison between the experimental results obtained from the one-step and the conventional two-step CO<sub>2</sub> activation is explored in this section. Since the separated carbonization step was not included in the one-step activation, the presentation of data from both preparation methods will be based on the total weight loss instead of % burn-off.

##### 4.4.4.1 Total Weight Loss in Activation

The total weight loss of longan seed obtained from the one-step and two-step activation as a function of activation time and at activation temperatures of 850°C and 900°C are shown in Figure 4.19. It is observed that the method of activation, the one-step or two-step, does not have a significant effect on the total weight loss of the resulting carbons, although it appears that the total weight loss from

the one-step activation are slightly higher than that of the two-step except at 60 min and 900°C. This small difference is probably due to the different heating rate used in these two methods which were 10°C/min and 5°C/min for one-step and two-step method, respectively. In addition, the similar trend of the total weight loss versus activation time obtained from these two methods should indicate that the gasification rate should also be similar.

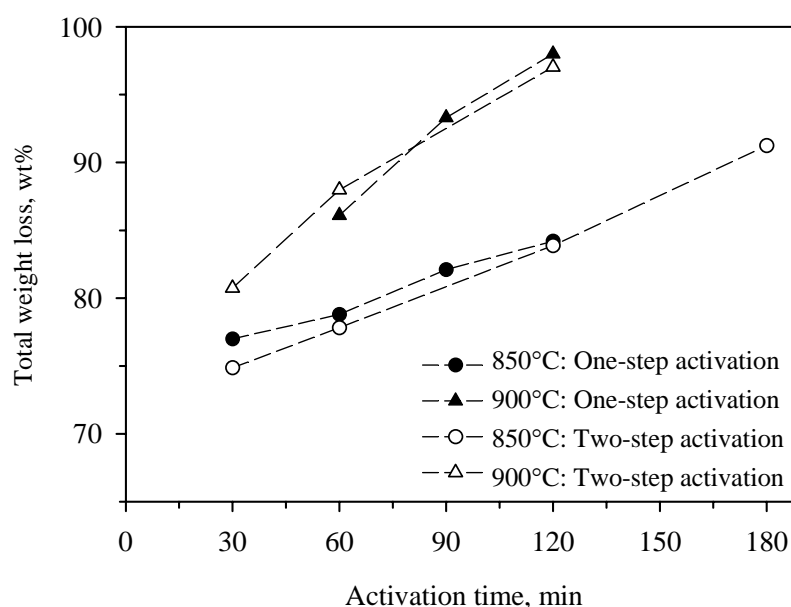


**Figure 4.19** The total weight loss in one-step and two-step activation versus the activation time at different activation temperatures.

#### 4.4.4.2 Porous Properties of Activated Carbon

The  $N_2$  adsorption isotherms at  $-196^\circ\text{C}$  of the one-step activated carbons can be considered to be the type IV as shown in Figure 4.20. The  $N_2$  adsorption capacity increases with increasing in the activation time from 30 to 120 min at the activation temperature at  $850^\circ\text{C}$  and for 60 to 90 min at  $900^\circ\text{C}$ . Increasing

activation time longer than 90 min at 900°C substantially decreases the amount of N<sub>2</sub> adsorbed.

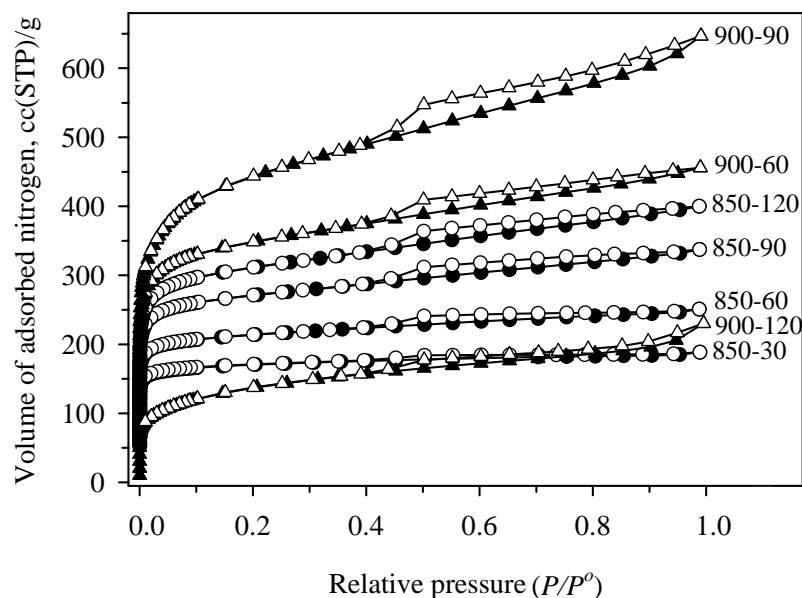


**Figure 4.20** N<sub>2</sub> adsorption at  $-196^{\circ}\text{C}$  isotherms on activated carbons prepared by one-step activation at different activation times and temperatures (the numbers in figure represent for activation condition of temperature-time).

Table 4.6 shows the porous properties of one-step activated carbon determined from the N<sub>2</sub> adsorption isotherms. Under the condition studied, BET surface area and total pore volume were found to be in range of 461-1471 m<sup>2</sup>/g and 0.29-1.00 cm<sup>3</sup>/g, respectively. The contribution of micropore volume lies between 55-89%.

**Table 4.6** Porous properties of activated carbons prepared from different activation conditions by one-step CO<sub>2</sub> activation.

Activation condition (Temp.-Time)	Total weight loss [%]	Total yield [%]	S <sub>BET</sub> [m <sup>2</sup> /g]	V <sub>mic</sub> [cm <sup>3</sup> /g]	V <sub>me+ma</sub> [cm <sup>3</sup> /g]	V <sub>tot</sub> [cm <sup>3</sup> /g]
<b>850°C series</b>						
850–30	77.3	22.7	570	0.26 (89%)	0.03	0.29
850–60	78.8	21.2	713	0.33 (84%)	0.06	0.39
850–90	82.1	17.9	901	0.43 (82%)	0.09	0.52
850–120	84.2	15.8	1032	0.48 (77%)	0.14	0.62
<b>900°C series</b>						
900–60	86.1	13.9	1154	0.55 (78%)	0.15	0.70
900–90	93.3	6.7	1471	0.71 (71%)	0.29	1.00
900–120	98.0	2.0	461	0.20 (55%)	0.16	0.36

Figure 4.21 compares the BET surface area and the volume of total pore, micropore and including the meso- and macropore as a function of total weight loss for one- and two-step activated carbons. The general behavior of these porous properties as a function of total weight loss for both methods is similar except in the region near the peak. These porous properties of the one-step activated carbons increase with increasing in the total weight loss up to 93.3%. Further increase in the total weight loss decreases these properties because of the excessive gasification at higher activation temperature and longer activation time. The highest porous properties for the one-step series was obtained for the carbon produced from the total weight loss

of 93.3%, corresponding to the activation at 900°C for 90 min, giving 1471 m<sup>2</sup>/g BET surface area, 1.00 cm<sup>3</sup>/g total pore volume, 0.71 cm<sup>3</sup>/g micropore volume and 0.29 cm<sup>3</sup>/g meso- and macropore volume. It is further noted that for the total weight loss up to 82.5%, these two methods produced the activated carbons having the same values of porous properties. At higher degree of activation up to the total weight loss around 82.5 to 93.3%, the porous properties including BET surface area, total pore volume and micropore volume from the one-step operation are slightly higher than those of the two-step method. The difference is also observed for the meso- and macropore volume for the total weight loss in the range of 82.5-88%, with the two-step activation tending to produce larger pore volume than those of the one-step. However, further increase in the total weight loss up to 93.3% the pore volume of larger pores obtained from the two-step method tends to give a constant value which is slightly lower than the one-step activation.

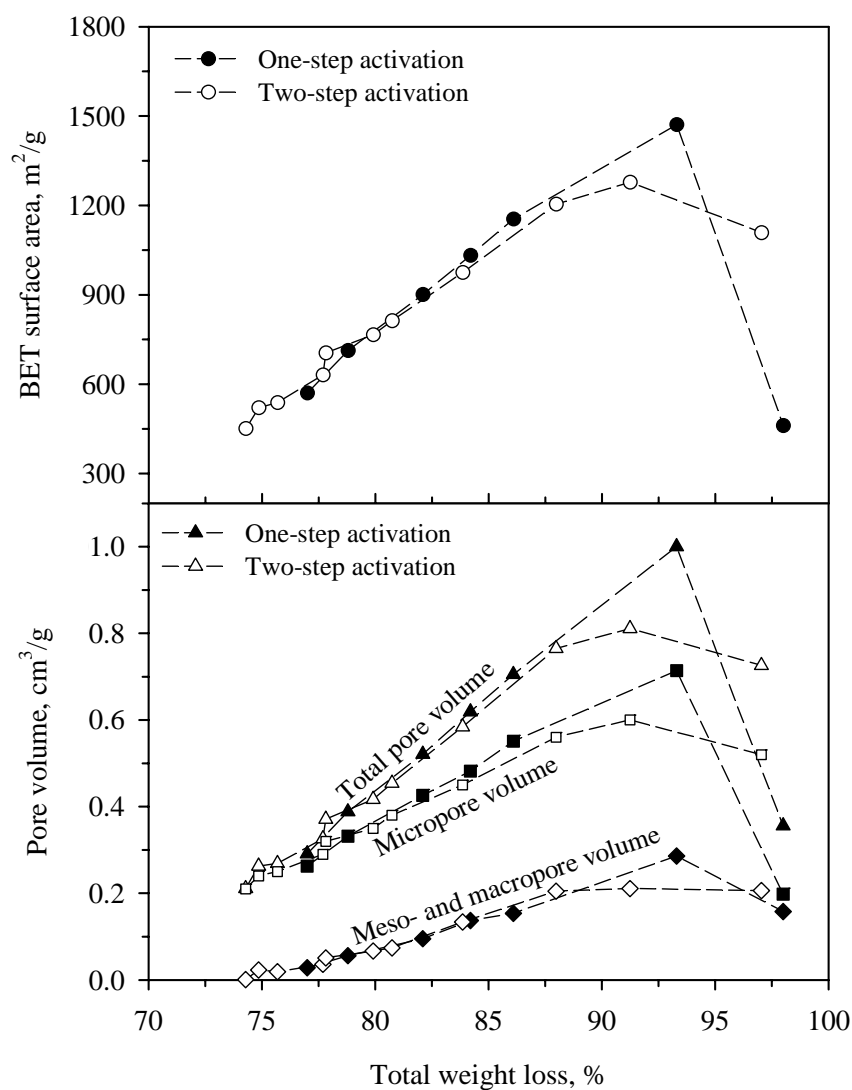


**Figure 4.21** BET surface area and pore volumes of one- and two-step activated carbons as a function of total weight loss.

#### 4.4.5 Chemical Activation by H<sub>3</sub>PO<sub>4</sub>

##### 4.4.5.1 Yield of Chemically Activated Carbon

The yields of chemically activated carbon by impregnation in a 50 wt% of H<sub>3</sub>PO<sub>4</sub> as compared with the char produced by carbonizing the longan seed without chemical addition as a function of the carbonization temperature are shown in

Figure 4.22. The yield of chemically activated carbon decreases in range of 41-28% with the increasing in carbonization temperature between 400-900°C. This decreasing in yield is due to the releasing of volatile matters from the chemical added-precursor. It is interesting to note that over the temperature range of 400-800°C, the yield of chemically activated carbon is higher than the yield of char. But at a high temperature of 900°C, the chemically activated carbon yield is the same as that of the char. This resulting behavior suggests that the added phosphoric retarded the evolution of volatiles. It is possible that the phosphoric acid could react with biomass structure to become the new structure that is thermally more heat resistant. These observations could be reasonably associated with the proposed mechanism that the chemical treatment initially causes cleavage of weaker bonds in biomass structure followed by the formation of the new stronger bonds (Girgis, and El-Hendawy, 2002; Jagtoyen, Thwaites, Stencel, McEnaney and Derbyshire, 1992).

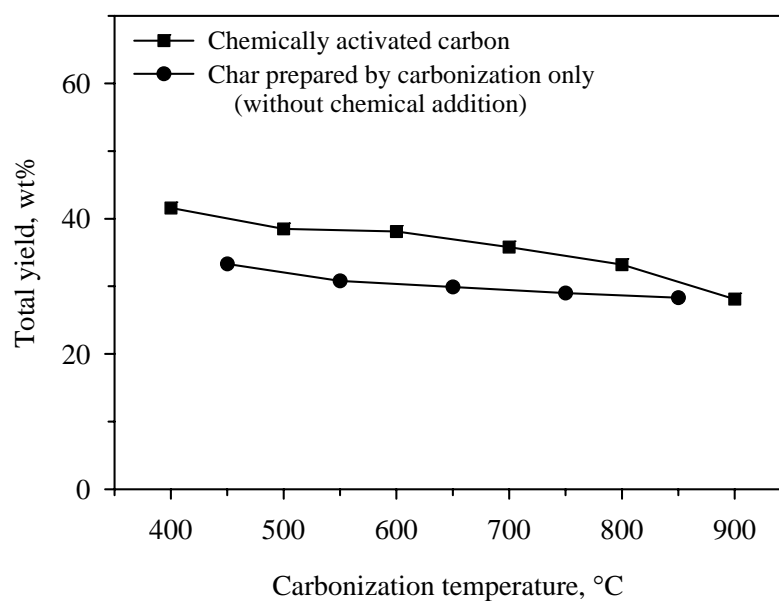


**Figure 4.22** The total yield of chemically activated carbons and the yield of char prepared without pre-impregnation.

#### 4.4.5.2 Porous Properties of Chemically Activated Carbon

The  $N_2$  adsorption isotherms at  $-196^\circ\text{C}$  of chemically activated carbon prepared at different carbonization temperatures are displayed in Figure 4.23. These isotherms are generally of Type I, indicating that the activated carbons are dominated by the microporosity, although a small hysteresis loop is seen for each isotherm. The order of  $N_2$  adsorption capacity from the lowest to highest in terms of the carbonization temperature is  $700^\circ\text{C} < 600^\circ\text{C} < 500^\circ\text{C} < 800^\circ\text{C} < 400^\circ\text{C} < 900^\circ\text{C}$ . This  $N_2$  adsorption capacity corresponds directly to the porosity of activated carbon.

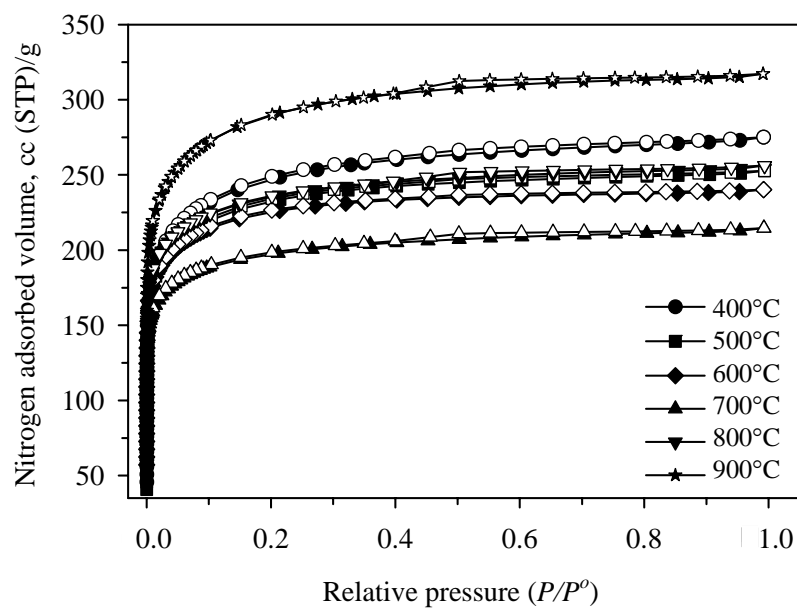


**Figure 4.23** N<sub>2</sub> adsorption isotherms at  $-196^{\circ}\text{C}$  of chemically activated carbon prepared at different carbonization temperatures.

The porous properties calculated from N<sub>2</sub> isotherms are listed in Table 4.7. The BET surface area and total pore volume of the obtained activated carbons are in the range of 651-946 m<sup>2</sup>/g and 0.33-0.49 cm<sup>3</sup>/g, respectively. These carbons contain mostly micropore of 90-95% of total pore volume, showing a small contribution of mesoporosity.

**Table 4.7** Porous properties of activated carbons prepared from different activation conditions by chemical activation.

Activation condition			Total yield [%]	$S_{\text{BET}}$ [m <sup>2</sup> /g]	$V_{\text{mic}}$ [cm <sup>3</sup> /g]	$V_{\text{me+ma}}$ [cm <sup>3</sup> /g]	$V_{\text{tot}}$ [cm <sup>3</sup> /g]
Temp. [°C]	Time [min]	H <sub>3</sub> PO <sub>4</sub> Concn. [wt%]					
400	60	50	41.6	808	0.38 (90%)	0.08	0.42
500	60	50	38.5	761	0.36 (92%)	0.03	0.39
600	60	50	38.1	739	0.35 (95%)	0.02	0.37
700	60	50	35.8	651	0.31 (94%)	0.02	0.33
800	60	50	33.2	774	0.36 (92%)	0.03	0.39
900	60	50	28.1	946	0.44 (90%)	0.05	0.49

The correlation between the porous properties such as BET surface area and total pore volume, including the pore volume in each pore size range, and the carbonization temperature are shown in Figure 4.24 and 4.25, respectively. The variation of these porous properties with carbonization temperature follows the same trend. The porous properties decrease with an increasing in the carbonization temperature up to 700°C, but at higher carbonization temperatures these porous properties start to increase with the maximum value occurring at 900°C. The decreasing of porosity in the range 400-700°C could result from the structural contraction of the phosphate linkages as found in the investigation of Jagtoyen and Derbyshire (1998). At carbonization temperature above 700°C, the phosphate linkages would be devolatilized. The evidence for supporting this hypothesis is seen in the

yield track that the chemically carbon yield decrease to that of the char at the high carbonization temperature (Figure 4.22). The porosity was created with the releasing of some phosphate groups at this high carbonization temperature. Therefore, the carbon porosity tends to increase for the carbonization temperature above 700°C.

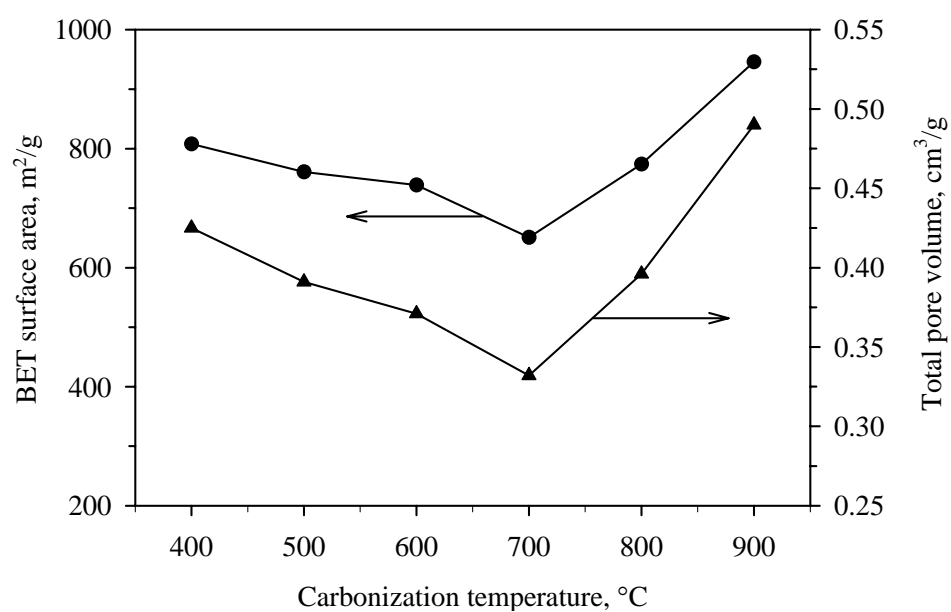


**Figure 4.24** BET surface area and total pore volume of chemically activated carbons prepared at different carbonization temperatures.

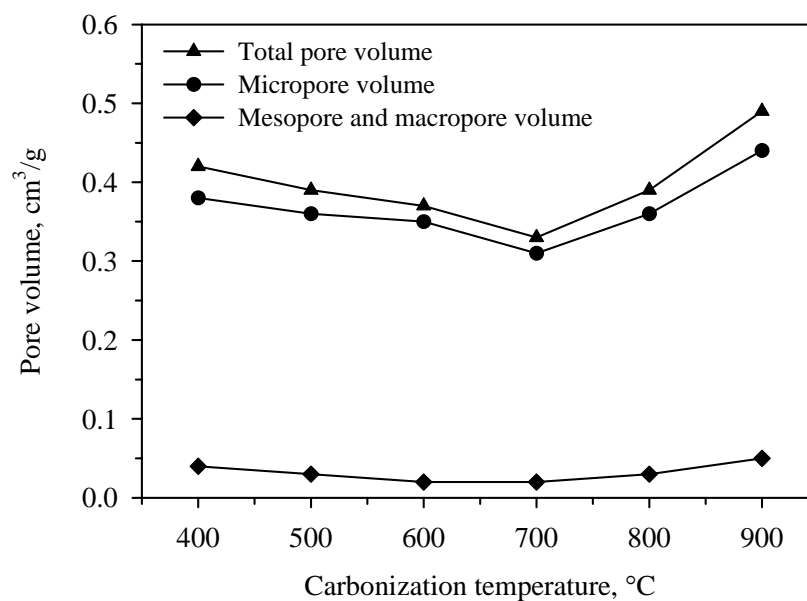


**Figure 4.25** The pore volumes of chemically activated carbons prepared at different carbonization temperatures.

## 4.5 Conclusions

Longan seed was used as a new precursor to produce the activated carbons. It was found that CO<sub>2</sub> activation as well as the H<sub>3</sub>PO<sub>4</sub> chemically activation of longan seed produced activated carbons with well-developed porosity and surface area. The conclusions for each topic from this research are listed as follows:

### Conventional Two-Step CO<sub>2</sub> Activation

- The activated carbon prepared by the conventional two-step activation at 850°C for 3 h had the highest porous properties of BET surface area of 1278 m<sup>2</sup>/g, total pore volume of 0.81 cm<sup>3</sup>/g and micropore volume of 0.60 cm<sup>3</sup>/g.
- The derived activated carbons were dominated with micropores of sizes smaller than 20 Å, with the percentages of micropore volume being higher than 70% of the total pore volume.

- The increasing in burn-off up to 70% resulted in an increase of the porous properties such as BET surface area, total pore volume and micropore volume. These properties, however, decreased at higher degree of activation.

#### **Carbon Activation Model**

- The model results were tested against the experimental data of longan seed char gasification with CO<sub>2</sub>. It was found that the description of surface area was regarded as excellent while that of pore volume was adequate in which the model calculation was based on the interlayer spacing of adjacent layer in a carbon crystallite being equal to 3.35 Å.

- The mechanism for pore evolution during gasification process was proposed as a three-stage development, from which pore creation, pore coalescence and pore collapse contribute to different extent in each of these three stages.

- From this model results, it was also found that the suitable interlayer spacing of adjacent layer in a carbon crystallite of a carbon char derived from longan seed should be 4.5 Å.

#### **Carbonization Temperature Effect on the Conventional Two-Step CO<sub>2</sub> Activation**

- The porous properties of activated carbons including BET surface area, micropore and total pore volumes increased with increasing carbonization temperature of char and passed through a maximum at 350°C.

- The porous properties directly correlated with the char reactivity during activation as measured by the percent of total weight loss.

### **One-Step CO<sub>2</sub> Activation**

- Using the same activation conditions the one-step and two-step CO<sub>2</sub> activation produced activated carbons with relatively the same values of total weight loss as well as the porous properties of the obtained carbons.

- The best condition for the production of high porous properties activated carbon from one-step CO<sub>2</sub> activation is at 900°C for 90 min, giving BET surface area 1471 m<sup>2</sup>/g, total pore volume of 1.00 cm<sup>3</sup>/g and micropore volume of 0.71 cm<sup>3</sup>/g.

### **Chemical Activation with H<sub>3</sub>PO<sub>4</sub>**

- The phosphoric added acted to produce the thermally stable of phosphate compounds, giving the yield of chemically activated carbon to be higher than the yield of char prepared by carbonization without added chemicals in the carbonization temperature range of 400-800°C.

- The porous properties decreased to the lowest values as the carbonization temperature was increased from 400°C to 700°C, then gradually increased at the higher temperature.

- The highest porous properties of activated carbon from chemical H<sub>3</sub>PO<sub>4</sub> activation was obtained from the condition of carbonization temperature at 900°C 1 h with the BET surface area of 946 m<sup>2</sup>/g, total pore volume of 0.49 cm<sup>3</sup>/g and micropore volume of 0.44 cm<sup>3</sup>/g.

## 4.6 References

- Abe, M., Kawashima, K., Kozawa, K., Sakai, H. and Kaneko, K. (2000). Amination of activated carbon and adsorption characteristics of its aminated surface. **Langmuir** 16: 5059-5063.
- Ahmadpour, A. and Do, D. D. (1997). The preparation of activated carbon from macadamia nutshell by chemical activation. **Carbon** 35: 1723-1732.
- Alaya, M. N., Girgis, B. S. and Mourad, W. E. (2000). Activated carbon from some agricultural wastes under action of one-step team pyrolysis. **J. Porous Mater.** 7: 509-517.
- Al-Khalid, T. T., Haimour, N. M., Sayed, S. A. and Akash, B. A. (1998). Activation of olive-seed waste residue using CO<sub>2</sub> in a fluidized-bed reactor. **Fuel Process. Technol.** 57: 55-64.
- Bansal, R. C., Donnet, J-B. and Stoeckli, F. (1988). **Active carbon**. New York: Marcel Dekker.
- Bhatia, S. K. and Perlmutter, D. D. (1980). A random pore model for fluid-solid reactions: I isothermal, kinetic control. **AIChE J.** 26: 379-385.
- Brunauer, S., Deming, L. S., Deming, W. E. and Teller, E. (1940). On a theory of the van der Waals adsorption of gases. **J. Amer. Chem. Soc.** 62: 1723-1732.
- Byrne, J. F. and Marsh, H. (1995). Introductory Overview. In J. W. Patrick (ed.). **Porosity in carbons: Characterization and applications**. London: Edward Arnold.
- Chang, C-F., Chang, C-Y. and Tsai, W-T. (2000). Effects of burn-off and activation temperature on preparation of activated carbon from corn cob agrowaste by CO<sub>2</sub> and steam. **J. Colloid Interface Sci.** 232: 45-49.

- Daud, W. M. A. W., Ali, W. S. W. and Sulaiman, M. Z. (2000). The effects of carbonization temperature on pore development in palm-shell-based activated carbon. **Carbon** 38: 1925-1932.
- Davis, K. A., Hurt, R. H., Yang, N. Y. C. and Headley, T. J. (1995). Evolution of char chemistry, crystallinity, and ultrafine structure during pulverized-coal combustion. **Combustion and Flame** 100: 31-40.
- Do, D. D. (1998). **Adsorption analysis: Equilibria and kinetics**. New Jersey: Imperial College Press.
- Dubinina, M. M. and Zaverina, E. D. (1949). **Dokl. Akad. Nauk. SSSR**. 68: 91-94.
- El-Merraoui, M., Aoshima, M. and Kaneko, K. (2000). Micropore size distribution of activated carbon fiber using the Density Functional Theory and other methods. **Langmuir** 16: 4300-4304.
- El-Merraoui, M., et al. (1998). Pore structures of activated carbon fibers from organometallics/pitch composites by nitrogen adsorption. **Carbon** 36: 1769-1776.
- Franklin, R. E. (1950). The interpretation of diffuse X-ray diagrams of carbon. **Acta Cryst.** 3: 107-121.
- Franklin, R. E. (1951). The structure of graphitic carbons. **Acta Cryst.** 4: 253-261.
- Gavalas, G. R. (1980). A random capillary model with application to char gasification at chemically controlled rates. **AIChE J.** 26: 577-585.
- Gavalda, S., Gubbins, K. E., Hanzawa, Y., Kaneko, K. and Thomson, K. T. (2002). Nitrogen adsorption in carbon aerogels: A molecular simulation study. **Langmuir** 18: 2141-2151.

- Gavalda, S., Kaneko, K., Thomson, K. T. and Gubbins, K. E. (2001). Molecular modeling of carbon aerogels. **Colloids Surf., A** 187-188: 531-538.
- Gergova, K. and Eser, S. (1996). Effects of activation method on the pore structure of activated carbons from apricot stones. **Carbon** 34: 879-888.
- Gergova, K., Petrov, N., and Eser, S. (1994). Adsorption properties and microstructure of activated carbons produced from agricultural by-products by steam pyrolysis. **Carbon** 32: 693-702.
- Girgis, B. S. and El-Hendawy, A-N. A. (2002). Porosity development in activated carbons obtained from date pits under chemical activation with phosphoric acid. **Microporous Mesoporous Mater.** 52: 105-117.
- Gonzalez, M. T., Rodriguez-Reinoso, F., Garcia, A. N. and Marcilla, A. (1997). CO<sub>2</sub> activation of olive stones carbonized under different experimental conditions. **Carbon** 35: 159-162.
- Gregg, S. J. and Sing, K. S. W. (1982). **Adsorption, surface area and porosity.** London: Academic Press.
- Guo, J. and Lua, A. C. (2000). Preparation of activated carbons from oil-palm-stone chars by microwave-induced carbon dioxide activation. **Carbon** 38: 1985-1993.
- Hashimoto, K. and Silveston, P. L. (1973). Gasification: part I. isothermal, kinetic control model for a solid with a pore size distribution. **AIChE J.** 19: 259-267.
- Jagtøyen, M. and Derbyshire, F. (1998). Activated carbons from yellow poplar and white oak by H<sub>3</sub>PO<sub>4</sub> activation. **Carbon** 36: 1085-1097.

- Jagtoyen, M., Thwaites, M., Stencel, J., McEnaney, B. and Derbyshire, F. (1992). Adsorbent carbon synthesis from coals by phosphoric acid activation. **Carbon** 30: 1089-1096.
- Jaroniec, M., Gilpin, R. K. and Choma, J. (1993). Correlation between microporosity and fractal dimension of active carbons. **Carbon** 31: 325-331.
- Jaroniec, M., Madey, R., Choma, J., McEnaney, B. and Mays, T. J. (1989). Comparison of adsorption methods for characterizing the microporosity of activated carbons. **Carbon** 27: 77-83.
- Kaneko, K. (1998). Nanospace geometry-sensitive molecular assembly. **Supramol. Sci.** 5: 267-273.
- Kruk, M., Jaroniec, M. and Choma, J. (1998). Comparative analysis of simple and advanced sorption methods for assessment of microporosity in activated carbons. **Carbon** 36: 1447-1458.
- Li, Z., Kruk, M., Jaroniec, M. and Ryu, S-K. (1998). Characterization of structural and surface properties of activated carbon fibers. **J. Colloid Interface Sci.** 204: 151-156.
- Lua, A. C. and Guo, J. (1998). Preparation and characterization of chars from oil palm waste. **Carbon** 36: 1663-1670.
- Lua, A. C. and Guo, J. (2000). Activated carbon prepared from oil palm stone by one step CO<sub>2</sub> activation for gaseous pollutant removal. **Carbon** 38: 1089-1097.
- Lussier, M. G., Shull J. C. and Miller, D. J. (1994). Activated carbon from cherry stones. **Carbon** 32: 1493-1498.
- Mackay, D. M. and Roberts, P. V. (1982). The influence of pyrolysis conditions on yield and microporosity of lignocellulosic chars. **Carbon** 20: 95-104.

- Marcilla, A., Garcia-Garcia, S., Asensio, M. and Conesa, J. A. (2000). Influence of thermal treatment regime on the density and reactivity of activated carbons from almond shells. **Carbon** 38: 429-440.
- Marsh, H. (2001). **Activated carbon compendium**. Amsterdam: Elsevier Science.
- Molina-Sabio, M., Rodriguez-Reinoso, F., Caturla, F. and Selles, M. J. (1996). Development of porosity in combined phosphoric acid-carbon dioxide activation. **Carbon** 34: 457-462.
- Ohba, T., Suzuki, T. and Kaneko, K. (2000). Relationship between DR-plot and micropore width distribution from GCMC simulation. **Carbon** 38: 1892-1896.
- Olivier, J. P. (1995). Modeling physical adsorption on porous and nonporous solids using Density Functional Theory. **J. Porous Mater.** 2: 9-17.
- Petersen, E. E. (1957). Reaction of porous solids. **AIChE J.** 3: 443-448.
- Rodriguez-Reinoso, F. and Molina-Sabio, M. (1992). Activated carbons from lignocellulosic materials by chemical and/or physical activation: An overview. **Carbon** 30: 1111-1118.
- Sandmann, C. W. Jr. and Zygorakis, K. (1986). Evolution of pore structure during gas-solid reactions: Discrete models. **Chem. Eng. Sci.** 41: 733-739.
- Setoyama, N., Suzuki, T. and Kaneko, K. (1998). Simulation study on the relationship between a high resolution  $\alpha_S$ -plot and the pore size distribution for activated carbon. **Carbon** 36: 1459-1467.
- Suzuki, T., Iiyama, T., Gubbins, K. E. and Kaneko, K. (1999). Quasi-symmetry structure of  $\text{CCl}_4$  molecular assemblies in a graphitic nanopore: a Grand Canonical Monte Carlo simulation. **Langmuir** 15: 5870-5875.

- Szekely, J. and Evans, J. W. (1970). A structural model for gas-solid reactions with a moving boundary. **Chem. Eng. Sci.** 25: 1091-1107.
- Wang, Z-M and Kaneko, K. (1998). Effect of pore width on micropore filling mechanism of SO<sub>2</sub> in carbon micropores. **J. Phys. Chem. B** 102: 2863-2868.
- Yalcin, N. and Sevinc, V. (2000). Studied of the surface area and porosity of activated carbon prepared from rice husks. **Carbon** 38: 1943-1945.

# **CHAPTER V**

## **EQUILIBRIA STUDY OF LONGAN SEED ACTIVATED CARBON**

### **5.1 Abstract**

This chapter reports on the equilibria study of water adsorption and ethanol adsorption. The longan seed based-activated carbons prepared from a series of different char burn-offs at 18.7%, 25.8% and 59.8% and a commercial coconut shell based-activated carbon were used to study water adsorption isotherms at temperatures from 20°C to 35°C. These tested carbons were different in terms of their pore size distribution and also the surface functional group properties by showing an increasing of total pore volume and the concentration of surface functional groups with increasing in the burn-off level. The water adsorption isotherms showed that the behavior and amount of water uptake could be divided into three consecutive ranges of relative pressure: 0.0-0.3, 0.3-0.7 and 0.7-0.94, corresponding to adsorption in ultramicropores, supermicropores, and mesopores, respectively. The isotherm data were simulated by the cluster model proposed by Do and Do. The correlation was found to be satisfactory over the entire range of relative pressure only with the lowest burn-off carbon which contained mainly micropores. For higher burn-off carbons, which showed increasing proportions of mesopores, the model needed to be modified by increasing the cluster size of the adsorbed water molecules from 5 to 20 for adsorption at relative pressure greater than about 0.7. The ethanol adsorption isotherms were studied using only two

carbons of the 59.8% burn-off and the commercial one. The ethanol isotherms were similar in shape to the nitrogen adsorption at  $-196^{\circ}\text{C}$ . The dual-Langmuir equation was found to fit well the ethanol isotherms. This equation describes the adsorption equilibrium occurring in micropores and in the large pores of meso- and macropores. The results showed that the micropores were completely filled at the relative pressure of approximately 0.1, with adsorption in the larger pores increasing with increased relative pressure over the entire range.

## **5.2 Introduction**

The study of the equilibrium adsorption of organic vapors in activated carbon has been investigated by many researchers. This has been achieved with a degree of success for non-polar molecules. However, the mechanisms of the polar molecules adsorption on the activated carbon are not fully satisfied. The difficulty arises from the nature of the heterogeneity in activated carbon surface, having interconnected pores of a variable shapes, sizes and surface characteristics. The other reason is associated with the affinity of the polar molecules among themselves being higher than the interaction between the molecules and pore wall. Among these polar adsorbates, water is possibly the least well understood. The major purpose of this chapter is to investigate the water adsorption behavior in a series of longan seed derived-activated carbons. Ethanol, the other type of polar molecule was also selected in this study to compare its adsorption behavior.

### **5.2.1 Water Adsorption**

Adsorption process by employing activated carbon as an adsorbent is widely applied in numerous industrial processes of separation and purification.

Basically, activated carbon surface is non-polar in nature. However, it can also adsorb several different polar molecules such as water with a significant adsorption capacity. This behavior sometimes creates a nuisance in practical adsorption processes, such as in the process of VOC removal from air since water is always present in air. Furthermore, it is also known that the efficiency of many industrial adsorbers can be largely affected even by the quite low humidity of the entering gases (Brennan, Bandosz, Thomson and Gubbins, 2001; Do and Do, 2000; Foley, Thomas, Forshaw, Stanton and Norman, 1997). However, to date the mechanism of water vapor adsorption on porous solid is not fully understood.

Water adsorption behavior on activated carbon is quite different from that of the other simple fluids such as nitrogen, carbon dioxide or hydrocarbons. There has been considerable research effort to better understand the water adsorption behavior including conducting experimental investigation, proposing isotherm equation models as well as molecular simulation study. Foley et al. (1997) studied the kinetics of water vapor adsorption on the coconut shell activated carbon. They found that the rate of adsorption and desorption depended on the relative pressure of isotherm and the slowest rate occurred in the region of relative humidities in the range 40-70%. Water adsorption experiments on a series of oxidized wood and coal based-activated carbons were studied by Salame and Bandosz (1999). Their results showed that the isosteric heat of water adsorption was affected by surface chemical heterogeneity only at low surface coverage and the limiting heat of adsorption was equal to the heat of water condensation of 45 kJ/mol. The water adsorption mechanism was also proposed by many research groups. The most plausible theory is the one proposed by Dubinin and Serpinsky (DS equation) (1981). Based on this DS

theory, water molecules are firstly adsorbed at the oxygenated groups on the carbon surface. Then these pre-adsorbed sites further act as the primary adsorption centers for more molecules to adsorb on. This model equation enabled some experimental data to be described, but it failed to explain the adsorption isotherms in some cases especially for carbons with a large number of surface functional groups (Do and Do, 2000).

Do and Do (2000) proposed a model which is more general in dealing with the different shapes of water isotherms for carbonaceous materials. The model assumptions were based on the growth of water clusters around the surface functional groups at the edges of the basal planes of the graphitic units, to form a pentamer cluster and subsequent adsorption of these clusters into the micropores. In addition, the molecular simulations have also been used to investigate the phenomena of water adsorption on activated carbons. McCallum, Bandosz, McGrother, Muller and Gubbins (1999), Muller and Gubbins (1998) and Muller, Rull, Vega and Gubbins (1996) used the grand canonical Monte Carlo simulation to find that the adsorption of water occurs via the formation of three-dimensional clusters on surface active sites. They found that the adsorption also depended strongly on the density and the strength of oxygen surface groups. Recently, Birkett and Do (2006) reported that water adsorption behavior was strongly influenced by both the pore width and the surface functional groups as found in their simulation study of water adsorption in finite carbon pores. Studies on the role of surface functional groups on water adsorption by using the oxidation treatment or modification of the carbon surface have also been reported (Salame and Bandosz, 1999). These methods produced the carbon with surface chemistry different from the original one. As a result of surface modification, the water adsorption mechanism is influenced more by the role of surface functional

group than by the effect of pore size distribution alone. However, Kaneko, Hanzawa, Iiyama, Kanda and Suzuki (1999) suggested that water can also be adsorbed via clusterization on hydrophobic carbon nanopores surface free of surface functional groups. The stabilization resulting from cluster developing reduces the hydrophilicity of water molecules, giving a less hydrophilic cluster that can be attracted to the hydrophobic surface of carbon (Ohba, Kanoh and Kaneko, 2004a; 2004b).

## 5.2.2 Model of Water Adsorption in Activated Carbon

### 5.2.2.1 Dubinin-Serpinsky (DS) Equation

The DS equation has been widely used for describing water adsorption isotherms. The model equation is presented as Equation 5.1 and can be rearranged to obtain the explicit form of adsorbed-phase concentration as shown in Equation 5.2 (Do, 1998):

$$x = \frac{C_{\mu}}{c(1 - kC_{\mu})(C_{\mu 0} + C_{\mu})} \quad (5.1)$$

$$C_{\mu} = \frac{-\frac{1}{k} \left( \frac{1}{cx} + kC_{\mu 0} - 1 \right) + \sqrt{\frac{1}{k^2} \left( \frac{1}{cx} + kC_{\mu 0} - 1 \right)^2 + \frac{4C_{\mu 0}}{k}}}{2} \quad (5.2)$$

where  $x$  is relative pressure ( $P/P^0$ ),  $C_{\mu}$  is the adsorbed water concentration,  $C_{\mu 0}$  is the concentration of the primary sites,  $k$  represents the rate of loss of the secondary sites due to the finiteness of the adsorption volume, and  $c$  is the ratio of the rate constants.

### 5.2.2.2 Do and Do Equation

Recently, Do and Do (2000) have proposed another model for water adsorption in activated carbon. The development of this model was based on the growth of a cluster of water molecules around the surface functional group to form a pentamer cluster and followed by the adsorption of this cluster into the micropore. This model is able to describe most of water adsorption behaviors of non-polar surface carbon as well as highly oxidized carbon. The final model equation reads

$$C_{\mu} = S_0 \frac{K_f \sum_{n=1}^{\infty} nx^n}{1 + K_f \sum_{n=1}^{\infty} x^n} + C_{\mu s} \frac{K_{\mu} \sum_{n=6}^{\infty} x^n}{K_{\mu} \sum_{n=6}^{\infty} x^n + \sum_{n=6}^{\infty} x^{n-5}} \quad (5.3)$$

where  $C_{\mu}$  is the water vapor adsorbed amount (mmol/g),  $x$  is the relative pressure,  $S_0$  is the functional group concentration (mmol/g),  $K_f$  is the chemisorption equilibrium constant,  $C_{\mu s}$  is the saturation concentration of water in micropore (mmol /g),  $K_{\mu}$  is the equilibrium constant of micropore adsorption, and  $n$  is the number of water molecules in a cluster usually taken as five.

### 5.2.3 Ethanol Adsorption

Ethanol shows a polar characteristic by the hydroxyl proton, however, it also presents the non-polar nature by the alkyl group. The association of these characteristics and the presence of both hydrophobic and hydrophilic on activated carbon surface seems to deliver the interesting phenomena of adsorption. In the work of Ohkubo, Iiyama, Nishikawa, Suzuki and Kaneko (1999) and Ohkubo and Kaneko (2001), it was found that the dispersion interaction between the alkyl chain in ethanol

molecules and the pore walls of activated carbon fibers is strong enough to give a representative type I isotherm. They also studied the adsorbed phase structure of ethanol in larger micropores and revealed that the ethanol molecules assembly occurred via the hydrogen bonds to form the ordered structure having the phase density close to that of bulk solid. Therefore, in this chapter the adsorption behavior of ethanol is studied and compared with the behavior of water adsorption. There have been no rigorous models to describe the adsorption mechanism of ethanol adsorption in activated carbon. In this work the dual-Langmuir model was chosen to fit the ethanol isotherm which generally shows the shape to be or close to type I.

### 5.2.3.1 Dual-Langmuir Equation

The dual-Langmuir consists of two basic Langmuir equations. The description of this equation involves the combined adsorption in micropore and in the larger pores of meso- and macropores which is accounted for by the first and second term in the RHS of equation 5.4, respectively.

$$C_{\mu} = C_{\mu 1} + C_{\mu 2} = C_{\mu m 1} \frac{b_1 P}{1 + b_1 P} + C_{\mu m 2} \frac{b_2 P}{1 + b_2 P} \quad (5.4)$$

where  $C_{\mu}$  is the total of adsorbed concentration.  $C_{\mu 1}$  and  $C_{\mu m 1}$ ,  $C_{\mu 2}$  and  $C_{\mu m 2}$  are the adsorbed concentration and maximum adsorbed concentration by the adsorption in micropore and larger pores, respectively. The  $b_1$  and  $b_2$  are the affinity constant for the adsorption in micropore and larger pores, respectively.

### 5.2.5 Objectives of the Study

The work in this chapter was aimed primarily to investigate the water adsorption behavior on activated carbons with different porous structure prepared by

varying the level of char burn-off during the activation step. It should be noted that this controlled changes of char burn-off not only affects the pore size distribution of the carbons but probably the types and concentration of surface functional groups as well. Therefore, the water adsorption behaviors were influenced by the simultaneous effect of these properties derived from the variation of physical activation condition. The series of activated carbon were produced from longan seed by CO<sub>2</sub> activation. In addition, a commercial coconut shell based-activated carbon was also tested for the purpose of comparison. Isotherm experiments were carried out by using a gravimetric adsorption technique. Due to the model simplicity and the ability to describe various water isotherms, the water isotherm model proposed by Do and Do (2000) was adopted in this work to simulate the water adsorption isotherms in the present study. In addition, ethanol was also studied for its adsorption behavior on the test activated carbons for comparison with the water adsorption. The experimental ethanol isotherms were tested against the dual-Langmuir isotherm equation.

## **5.3 Materials and Methods**

### **5.3.1 Materials**

Three activated carbons obtained from different char burn-offs of 18.7%, 25.8% and 59.8% were chosen for the adsorption study. This series of carbon samples were prepared by the conventional two-step CO<sub>2</sub> activation as previously outlined in Chapter IV. These selected carbons were referred to as LAC1, LAC2 and LAC3, respectively. A commercial activated carbon supplied by the Carbokarn Ltd. (Thailand) under the trade name of HR5 was also used for the experiment. It was

produced from coconut shell by steam activation and was designated in this work as CAC.

### **5.3.2 Material Characterization**

The carbon samples were characterized for the structural porous properties using the N<sub>2</sub> adsorption isotherms at -196°C, as described earlier in Chapter IV. These selected four activated carbons were further characterized for the surface functional groups using the Boehm titration method (Boehm, 2002). In this analysis, the total of the acidic and basic groups of surface functionality were determined. The analysis commenced by loading about 0.5 g of carbon samples into each of the 100 cc of 0.1 N solutions of HCl and NaOH, respectively. These mixtures were shaken for 24 h and thereafter the activated carbon suspensions were filtered. The remaining solutions were titrated with standard 0.1 N NaOH and 0.1 N HCl to determine the excess of acid and base remaining in the respective solution. The amount of acidic and basic neutralized by NaOH and HCl were then calculated and taken as the total concentration of acid and basic surface functional groups, respectively.

### **5.3.3 Water Adsorption Experiment**

The water vapor adsorption tests were performed by using an Intelligent Gravimetric Analyzer (IGA) supplied by Hiden Analytical, UK. This apparatus allows the measurement of adsorption and desorption isotherms of vapor or gas sorbates via the gravimetric system. Initially, the sample weighing about 0.2 g was outgassed at 300°C for 10 h. The numbers of pressure points were specified and the measurement of the adsorbed amount at equilibrium performed for each scan of adsorption and

desorption. Water adsorption isotherms for all samples were conducted at four different temperatures of 20, 25, 30 and 35°C.

#### **5.3.4 Ethanol Adsorption Experiment**

The ethanol adsorption was performed in order to compare its adsorption behavior with the water adsorption. Only two carbon samples of LAC3 and CAC were selected for the tests. Experiments were carried out by the IGA. The experimental steps procedure was the same as in the water adsorption tests. Ethanol adsorption isotherms for both samples were studied at four different temperatures of 20, 25, 30 and 35°C.

### **5.4 Results and Discussion**

#### **5.4.1 Water Vapor Adsorption**

##### **5.4.1.1 Porous Characteristics of Activated Carbons**

Figure 5.1 shows the N<sub>2</sub> adsorption isotherms of the test activated carbons. It is seen that the longan seed carbon series with low burn-off (< 25.8%) as well as the commercial carbon show type I adsorption isotherm. However, at the highest burn-off of 59.8%, the type IV isotherm is observed. The type I isotherm indicates that the activated carbons are dominated by microporosity and the increase in the size of hystereses loop with increased char burn-off is indicative of an increase in the proportion of mesopore volume. The small figure at the right-hand side is shown for clearer observation of the isotherms in the low pressure range.

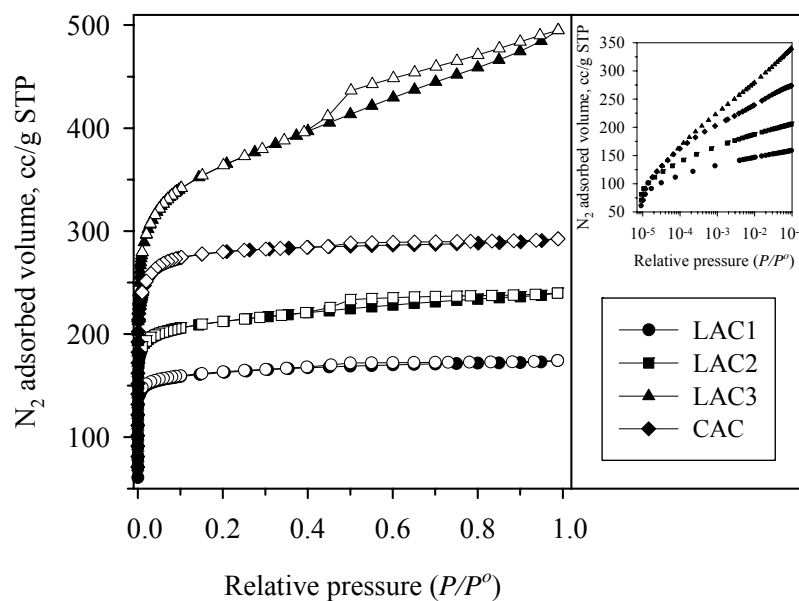


**Figure 5.1** Typical  $N_2$  adsorption isotherms at  $-196^\circ\text{C}$  of test activated carbons; solid symbols denote adsorption, open symbols denote desorption.

The porous structural properties of the test activated carbons such as BET surface area, micropore volume and total pore volume were calculated from  $N_2$  adsorption isotherms at  $-196^\circ\text{C}$  and are shown in Table 5.1. For the longan seed activated carbons, it is observed that these porous properties increase with increasing in the burn-off level as expected. However, the percent of micropore volume decreases with increasing in burn-off (74% to 54%). This means that the mesopore and macropore volumes increase with increasing in the degree of burn-off at the expense of micropores. It is also interesting to observe that the commercial activated carbon is mostly microporous, containing about 82% of micropore volume.

**Table 5.1** Porous properties derived from nitrogen adsorption of activated carbons.

Sample	BO [%]	$S_{\text{BET}}$ [m <sup>2</sup> /g]	$V_{\text{mic(DFT)}}$ [cm <sup>3</sup> /g]	$V_{\text{me+ma}}$ [cm <sup>3</sup> /g]	$V_{\text{tot}}$ [cm <sup>3</sup> /g]
LAC1	18.7	538	0.20 (74%)	0.07	0.27
LAC2	25.8	705	0.26 (70%)	0.11	0.37
LAC3	59.8	1204	0.41 (54%)	0.35	0.76
CAC	NA	923	0.37 (82%)	0.08	0.45

Figure 5.2 shows the pore size distributions (PSD) of activated carbon samples derived by using the density functional theory (DFT). This method assumes the slit-like pore geometry with the pore width being defined by the distance between the centers of carbon atoms of the two parallel graphitic layers. It is noted that there are two main peaks of PSD at pore width of 7.3 Å and 11.8 Å which are within the micropore limit (less than 20 Å). It is also seen that all the activated carbon samples contain mostly of pores with less than 100 Å in width. The PSD curves also show that the micropore and mesopore volume (area under the curves) of longan seed activated carbon series increase with the increasing in the burn-off level.

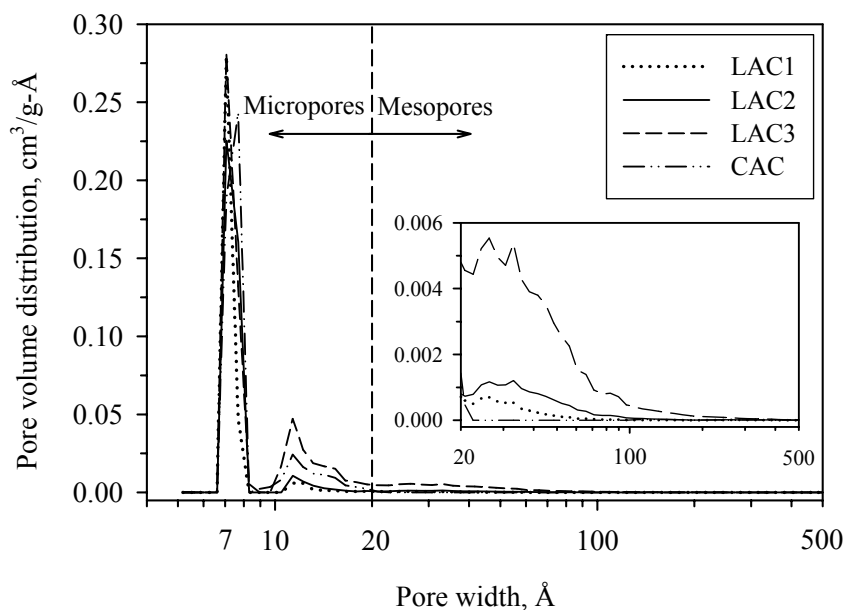


**Figure 5.2** Pore size distribution of activated carbons derived from DFT model.

The volume-surface average pore width calculated from the DFT discrete data of pore volume are listed in Table 5.2. For the range of pore width less than 10 Å and between 10 to 20 Å, the average pore width for all carbon samples are approximately equal. In the mesopore size range of 20 to 500 Å, the average pore width of the LACs series increase with the increasing in burn-off level in a narrow range (38.1-44.6 Å). The relatively constant pore width observed in micropores for each carbon with burn-off less than 60% agrees qualitatively with the simulation results of the carbon activation model recently proposed by Junpirom, Do, Tangsathitkulchai and Tangsathitkulchai (2005). They found that the basic mechanism of pore development in this regime is by the increase in the length of each pore due to the consumption of graphitic carbon layers, resulting in larger pore volume and surface area but with the average pore size remaining fairly constant. The CAC sample

also contained micropore with comparable average pore width but gave much larger mesopore size.

**Table 5.2** The average pore width in each pore size range from DFT calculation.

Sample	Average pore width [Å]		
	Pore width $\leq 10$ Å	10 Å < Pore width $\leq 20$ Å	20 Å < Pore width $\leq 500$ Å
LAC1	7.4	13.5	38.1
LAC2	7.6	13.4	43.9
LAC3	7.6	13.5	44.6
CAC	7.8	13.6	92.6

The surface chemistry properties were also measured for the total amount of acidic and basic groups by Boehm titration as previously outlined and the results are shown in Table 5.3. It is seen that the amounts of surface functional groups of LACs increase with increasing in the burn-off level. The amount of surface functional group of CAC lies between those of the LAC1 and LAC2. Since all samples were prepared by physical activation and these surface functional groups were introduced during the preparation step by the forming of the heteroatoms bonded with the basal plane of the aromatic sheets (Bansal, Donnet and Stoeckli, 1988), the increasing of surface functional groups with increasing burn-off can be simply explained by the consequent increase of surface area and porosity of the prepared carbons.

**Table 5.3** Surface chemistry property obtained from Boehm titration.

Sample	Acidic [mmol/g]	Basic [mmol/g]	Total [mmol/g]
LAC1	1.00	0.92	1.92
LAC2	1.97	1.30	3.27
LAC3	2.08	1.71	3.79
CAC	1.51	1.30	2.81

#### 5.4.1.2 Water Adsorption Isotherms

Typical water adsorption isotherms for all carbon samples at 30°C are presented in Figure 5.3 and can be approximated by the type V isotherm. It is obvious that the shapes of water isotherms are different from those of the N<sub>2</sub> isotherms and all of them show significant hystereses. The size of hysteresis loop of the LACs carbon increases with increasing in the char burn-off. This trend agrees with that of the pore width in that the average pore width in the mesopore range also increases with increasing in the burn-off level (see Table 5.1). Thus, it is inferred that the size of hysteresis loop correlates directly with the average pore width of the large pores. This result is also in accord with the work of Miyawaki, Kanda and Kaneko (2001) for the case of activated carbon fibers (ACF) series. It is also observed that the hystereses do not close the loops until they reach a relatively low pressure. This may arise from the difficulty in breaking the hydrogen bonds which give strong adsorption between water molecules and the functional groups on the carbon surface. These hystereses of water isotherms were reported to result from the difference between the steps involved in pore filling and pore emptying. The pore emptying involves the removal of adsorbed molecules that formed a stable phase in pores which would be a

more liquid-like phase in the central layer as the pore width is increased. Therefore, desorption process in large pores is difficult to remove from the adsorbed phase (Rouquerol, Rouquerol and Sing, 1999).

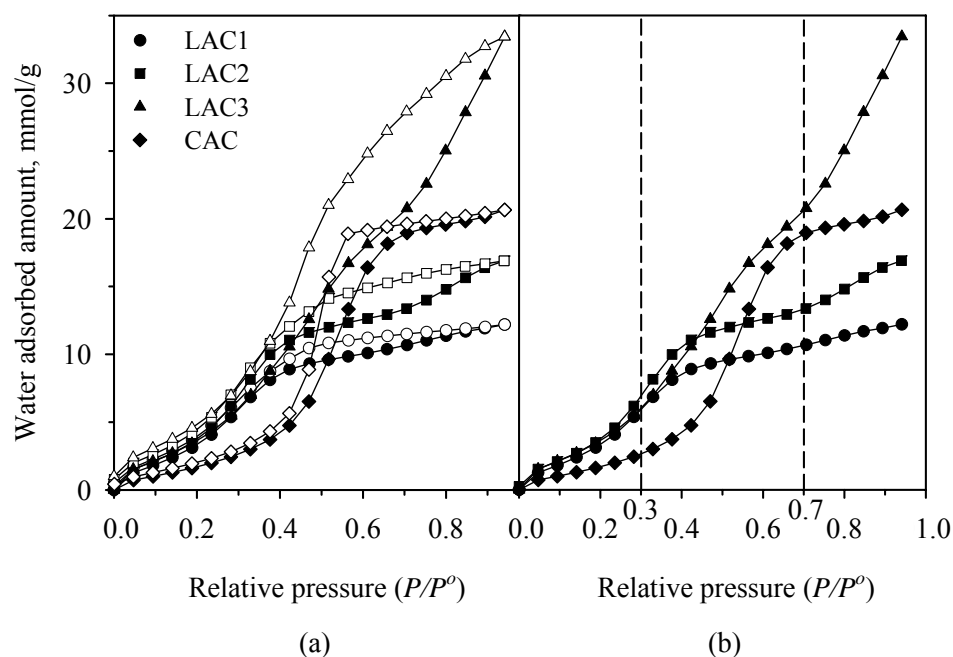


**Figure 5.3** Typical water adsorption isotherms at 30°C for different activated carbons; (a) adsorption–desorption branches, (b) adsorption branch.

Considering the difference in the shape of isotherms displayed by each activated carbon appears to suggest that the underlying adsorption mechanisms could be different. This postulation can be partly examined from Figure 5.4 which shows plots of the incremental of water adsorbed amount versus the relative pressure. All carbons show roughly three main peaks of curves. For relative pressures lower than 0.7, the curves give a narrow initial peak exhibited by all carbon samples, followed by the main peak at 0.3 for LAC1 and LAC2, 0.5 for LAC3 and 0.6 for

CAC, respectively. At higher relative pressures, LAC2 and LAC3 show a significant peak at the relative pressure of 0.85. It is seen that different carbon samples show similar pattern of changes except the differences in the peak position.

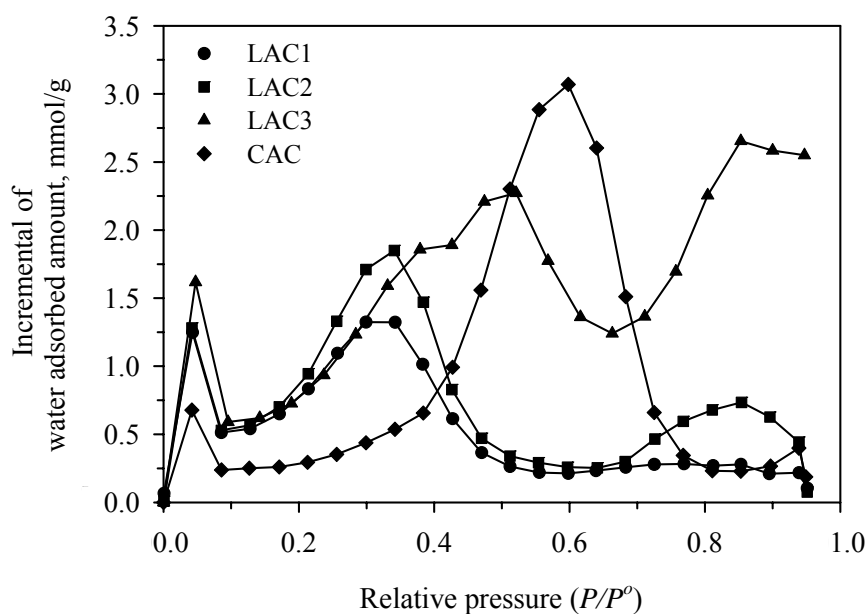


**Figure 5.4** The incremental of water adsorbed amount versus relative pressure.

Therefore, it could be hypothesized that the mechanisms involved in water adsorption by the various carbons with respect to pressure change may be fundamentally similar. With reference to this adsorption behavior and the shapes of the isotherm curves in Figure 5.3, it might be reasonable to divide the adsorption into three ranges of relative pressure, namely 0.0-0.3, 0.3-0.7 and 0.7-0.94, as illustrated in Figure 5.3 (b). At the low relative pressure of 0.0-0.3, the adsorbed amount increased continuously with increasing pressure. The adsorbed amounts of the LACs are relatively the same and greater than that of the CAC. In the range of relative pressure from 0.3-0.7, the steep increasing of the amount adsorbed occurs for the LAC3 and

CAC, while the LAC1 and LAC2 still show an increase but with a much lesser extent. The LAC3 continue to show a further sharp increase in the adsorbed amount for relative pressure greater than 0.7, while the rest of LAC series give marginal increasing with LAC2 showing a slight inflection at the relative pressure of 0.7. The CAC shows similar behavior to LAC1 and LAC2 in the last pressure range but with higher adsorption capacity.

Table 5.4 shows the micropore volume derived from the DFT calculation and the pore volume computed from water adsorption isotherms estimated up to the relative pressure of 0.7. It is observed that these two values are surprisingly agreeable. This indicates that the water adsorption mechanism for the relative pressure up to 0.7 should involve the adsorption in micropores. This number is comparable to that reported by Alcaniz-Monge, Linares-Solano and Rand (2001; 2002) who found the water adsorption up to the relative pressure of about 0.8 to result from micropore filling. It is also interesting to observe the adsorption behavior in the low pressure range up to around 0.3, as appeared in Figure 5.3. The water uptake is quite different between the LACs series and the CAC, with the latter giving a lesser adsorbed amount. This difference could be ascribed to the different characteristics of porous structure, surface structure and surface functional group properties of each type of carbon material.

**Table 5.4** Pore volume derived from the DFT analysis of N<sub>2</sub> (−196°C) data and the adsorbed water amount.

Sample	V <sub>mic(DFT)</sub> (Pore width ≤ 20 Å) [cm <sup>3</sup> /g]	Pore volume estimated from adsorbed water (0.0 ≤ P/P <sup>0</sup> ≤ 0.7) [cm <sup>3</sup> /g]
LAC1	0.202	0.209
LAC2	0.264	0.262
LAC3	0.410	0.407
CAC	0.370	0.371

In addition, the similarity of water isotherms in this low pressure range for the LACs series deserves further examination. The information in Table 5.5 shows the values of the ultramicropore volume (pore width less than 7 Å) and the corresponding relative pressure of the water isotherms that the water accessed this volume. From these results, it can be said that the calculated relative pressures of the LACs series in Table 5.5 are comparable and close to the value of 0.3 at which their isotherms start to separate from each other (see Figure 5.3). This indicates that at the relative pressure less than 0.3 the water adsorption is controlled to a greater extent by the adsorption in ultramicropores. For relative pressures higher than 0.7, water uptake increases with increasing in the char burn-off mainly due to the corresponding increase of the mesopore and macropore volume. It can thus be inferred that pore size distribution of activated carbon plays a significant role in the adsorption behavior of water inside the pores with water being adsorbed in all sizes of pores with respect to the pressure change. It is generally accepted that water adsorption in activated carbon

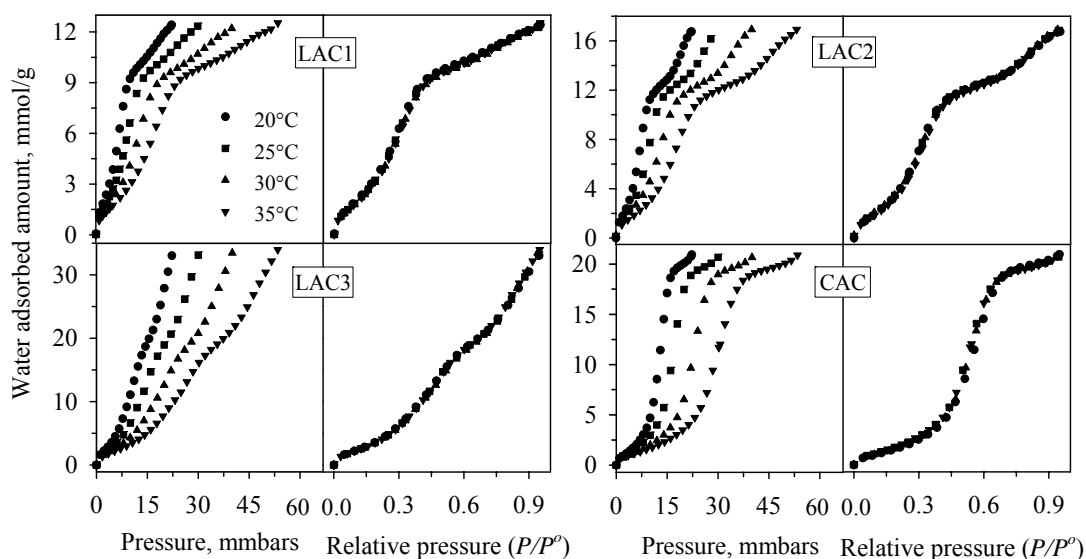
involves the adsorption of the first water molecule onto acidic surface groups followed by further adsorption via hydrogen bonding between water molecules. Therefore, the effect of pore size distribution on water adsorption behavior of the non-oxidized activated carbon could be viewed as the role and effect of surface functional groups which distribute in various pore sizes.

**Table 5.5** Estimated relative pressure from water isotherms for volume adsorbed corresponding to ultramicropore volume.

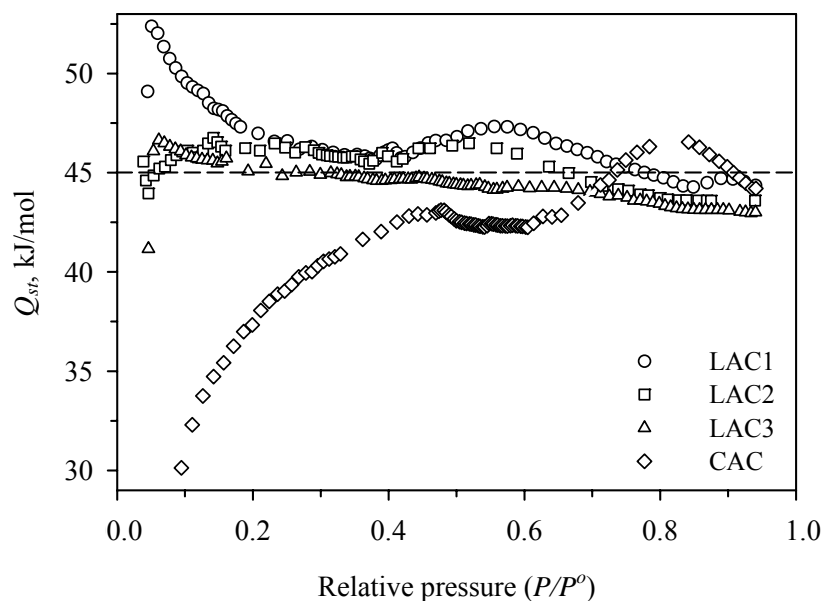
Sample	$V_{\text{DFT}}$ (Pore width $\leq 7.33 \text{ \AA}$ ) [cm <sup>3</sup> /g]	$P/P^0$ of H <sub>2</sub> O isotherms
LAC1	0.150	0.361
LAC2	0.122	0.289
LAC3	0.152	0.347
CAC	0.101	0.433

Figure 5.5 shows additional isotherm data for water adsorption at various temperatures including 20, 25, 30 and 35°C. Regarding the adsorption isotherms that are plotted versus pressure, it is clear that the water uptake decreases when the adsorption temperature is increased, indicating that water adsorption involves the liberation of heat. It is also interesting to observe that the temperature has no distinct effect on the shape of water isotherms in that all the isotherm curves fall into one single curve when the isotherms are plotted against the relative pressure, as shown in Figure 5.5. The isosteric heat of adsorption ( $Q_{st}$ ) was calculated from these isotherms data by employing the van't Hoff equation (Gregg and Sing, 1982), giving

results as shown in Figure 5.6. The  $Q_{st}$  of LACs appear to vary, over almost the entire range of relative pressure, in the vicinity of 45 kJ/mol which is the latent heat of bulk water condensation (Brennan et al., 2001; Salame and Bandosz, 1999). However, the different trend occurs for the CAC such that the  $Q_{st}$  increases first with pressure and reaches a maximum around 42.9 kJ/mol at the relative pressure of 0.5 before approaching the value closer to 45 kJ/mol at relative pressures higher than 0.7.



**Figure 5.5** Water adsorption isotherms for different activated carbons at various temperatures.



**Figure 5.6** Isosteric heat of water adsorption for different activated carbons.

#### 5.4.1.3 Simulation of Water Adsorption Isotherms

The fitted results to the isotherm data by DS equation are displayed in Figure 5.7. The results show that the DS model can describe the CAC isotherm reasonably correct up to the relative pressure of about 0.45 but fails completely at higher relative pressure values. For the LAC series, the DS model can fit the lowest burn-off carbon (LAC1) well except over the intermediate pressure range (relative pressure: 0.35-0.50) where the model underpredicts the experimental data. For higher burn-off samples (LAC2 and LAC3), the model can predict the correct trend of isotherm data but cannot account for the inflection characteristics of the isotherm curves.

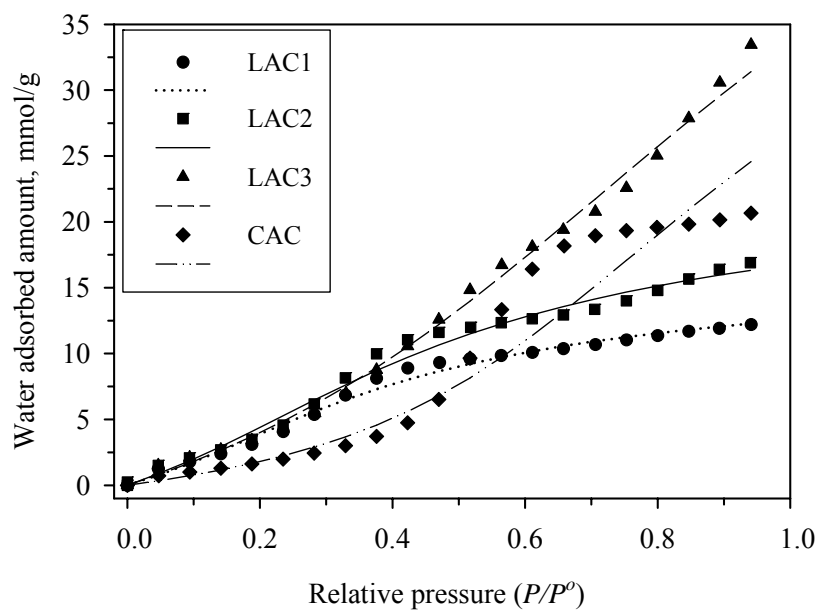


**Figure 5.7** Fitting of the Dubinin–Serpinsky (DS) model to the experimental water isotherms of activated carbon series: symbols denote experimental data, lines denote fitted results.

The Do and Do model was tested against the experimental data and the results are shown in Figure 5.8 and Table 5.6 shows the model parameters obtained from the data fitting. It is seen that the model can describe only the data of LAC1 carbon very well over the entire range of relative pressure. However, the isotherms of other carbons can be fitted with reasonable accuracy more or less up to the relative pressure around 0.5.

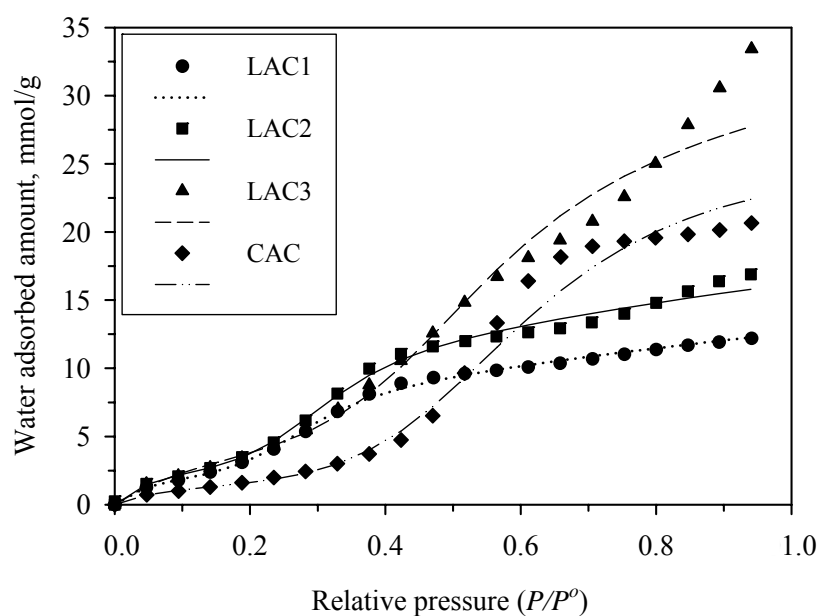


**Figure 5.8** Fitting of the original Do and Do model to the experimental water isotherms of activated carbon series; symbols denote experimental data, lines denote fitted result.

**Table 5.6** The optimized parameters derived from the water adsorption model of Do and Do.

Sample	Simulated parameter					
	$S_0$ [mmol/g]	$K_f$	$C_{\mu s}$ [mmol/g]	$K_{\mu}$	$n$	$r^2$
LAC1	2.38	20.84	5.49	504.5	5	0.998
LAC2	2.93	18.69	7.49	316.8	5	0.992
LAC3	4.36	8.28	16.45	22.7	5	0.971
CAC	1.54	15.30	19.85	13.3	5	0.979

The mismatch of the simulated results with experimental isotherms at higher pressures, corresponding to adsorption in large pores, suggesting that the adsorption behavior of water should depend on the pore size. Therefore, we propose to modify this model to account for the effect of pore size on adsorption by dividing the pressure into two ranges, i.e. adsorption at low and high pressure ranges. In the low pressure range, the experimental data were fitted directly by the model equation with five water molecules in a cluster (a pentamer) while the cluster size can be changed for simulation at the high pressure range. The exact relative pressure at which the change in the cluster size occurred was determined for each activated carbon by a trial-and-error search procedure to give the best fit between the simulated and experimental isotherms.

Figure 5.9 shows the calculated results and Table 5.7 lists the optimum parameters derived by the modified model outlined earlier. It is observed that the model can describe the data extremely well for all samples investigated in this work, except for the LAC3 sample at relative pressures greater than 0.9 where the effect of capillary condensation could occur (Do and Do, 2000). The LAC2 and LAC3 show the inflection points at the relative pressure of 0.7 with 5 and 20 water molecules in a cluster for adsorption at relative pressures lower and higher than 0.7, respectively. The inflection point of CAC was found to be 0.66 with the cluster size being 7 and 20 for the lower and higher relative pressure range, respectively. The cluster size obtained in this work for adsorption in micropores (5 and 7) is comparable to the values of 8-10 for the optimum cluster size for adsorption in graphite nanopore (pore width 1.1 nm) as reported by Ohba et al. (2004b) and Kimura et al. (2004).

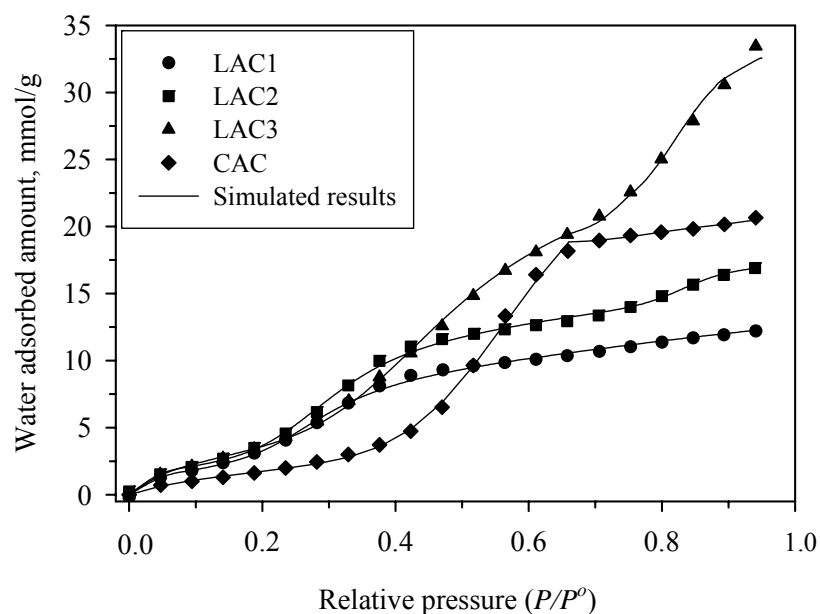


**Figure 5.9** Fitting of the modified isotherm model of Do and Do to the experimental water isotherms of carbon series.

**Table 5.7** The optimized parameters derived from the modified isotherm model of Do and Do.

Sample	Relative pressure	Simulated parameters				
		$S_0$ [mmol/g]	$K_f$	$C_{\mu s}$ [mmol/g]	$K_{\mu}$	$n$
LAC1	$(0.0 < P/P^0 \leq 0.94)$	2.38	20.84	5.49	504.5	5
LAC2	$(0.0 < P/P^0 \leq 0.70)$	2.56	27.06	7.80	387.4	5
	$(0.70 < P/P^0 \leq 0.94)$	0.004	100.07	3.58	38.8	20
LAC3	$(0.0 < P/P^0 \leq 0.70)$	3.59	12.42	13.80	47.2	5
	$(0.70 < P/P^0 \leq 0.94)$	0.089	12.20	12.05	46.6	20
CAC	$(0.0 < P/P^0 \leq 0.66)$	2.02	8.80	19.97	42.9	7
	$(0.66 < P/P^0 \leq 0.94)$	0.614	0.013	1.06	157.5	20

The model parameters shown in Table 5.7 reflect the chemical nature of the carbon surface. For example,  $S_0$  and  $C_{\mu s}$  are two relevant parameters which involve the surface functional group concentration and the saturation concentration in the micropore, respectively. For the LAC series the  $S_0$  and  $C_{\mu s}$  of micropores ( $P/P^o < 0.7$ ) show an increase with increasing in the burn-off with the values of 2.38, 2.56 and 3.59 mmol/g and of 5.49, 7.80 and 13.80 mmol/g for the burn-off of 18.7%, 25.8% and 59.8%, respectively. For adsorption in mesopores ( $P/P^o > 0.7$ ) the  $S_0$  and  $C_{\mu s}$  of LAC2 and LAC3 also increase with increasing in the burn-off. This increase is consistent with the higher specific surface area and pore volume of the carbons as the burn-off is increased. It is observed that the total of  $S_0$  and the concentration of acidic surface group from Boehm titration of the LACs carbons follow the same trend. Those  $S_0$  are 2.38, 2.56 and 3.68 mmol/g while the Boehm's results are 1.00, 1.97 and 2.08 mmol/g, for the activated carbons LAC1, LAC2, and LAC3, respectively. The  $K_f$  and  $K_\mu$  involve the equilibrium constant for the chemisorption and micropore adsorption, respectively. These parameters represent the influences of the functional groups and the microporosity on the adsorption behavior, respectively, giving a different curvature of the adsorption isotherm. Therefore, they change with the different type of carbon samples having different shape of water isotherms. It is found that these two parameters can change in values when the pressure range is varied but with no definite effect of pressure (Table 5.7).

The two-step simulation scheme clearly indicates the different adsorption mechanism in the low and high pressure ranges corresponding to adsorption in micropores and larger meso- and macropores, respectively. At low

pressures up to the relative pressure of 0.7 the adsorption involves micropore filling with the pentamer clusters of water for the LACs series and a cluster of 7 molecules for the coconut shell-based activated carbon. The difference in cluster size between these two raw materials is possibly ascribed to the differences in porous structure and surface functionalities of each carbon sample. For the relative pressures greater than 0.7 the adsorption occurs in the mesopores and macropores with the increase in cluster size. The increased cluster size in mesopore adsorption is the result of the lower interaction energy of solid surface and adsorbate molecules in mesopores as compared to that in micropores.

#### **5.4.2 Ethanol Adsorption**

Typical isotherms of ethanol adsorption at 30°C by the test activated carbons are shown in Figure 5.10. The isotherm shapes are different, showing type I and IV for CAC and LAC3, respectively. The adsorption capacity of LAC3 is higher than that of CAC, due principally to the higher porosity of LAC3. The ethanol isotherm of each carbon is similar in shape to its corresponding N<sub>2</sub> isotherms. There is the presence of the hysteresis loop in the LAC3's isotherm starting at the relative pressure of approximately 0.5. A relatively small hysteresis loop is also detected for the isotherm of CAC over the same relative pressure range as found in LAC3. The initially sharp rising in the isotherm shape indicates the strong influence of the interaction between the ethanol molecule and carbon surface. This interaction is the result of dispersive interaction between the alkyl chain and the carbon pore walls.

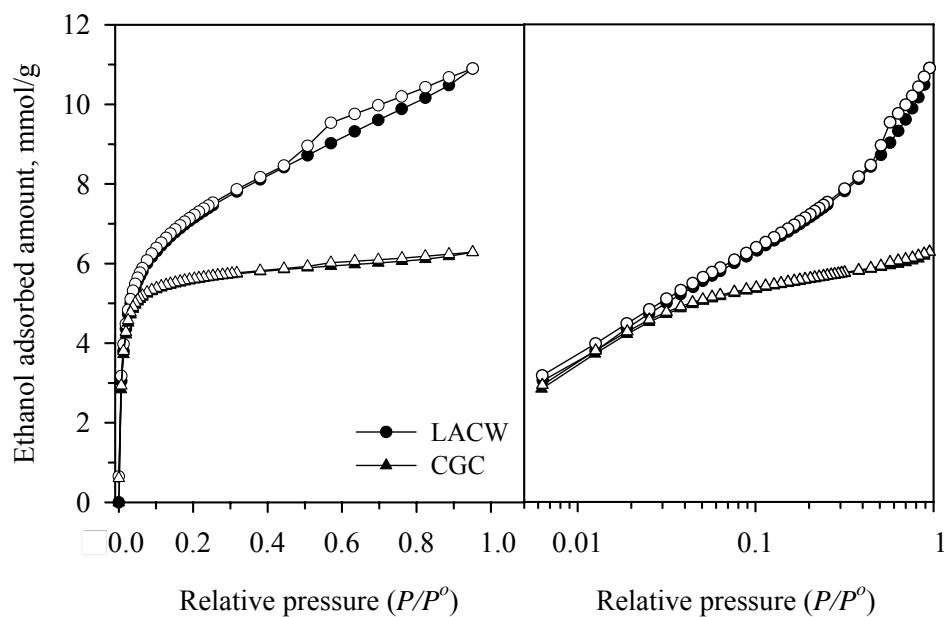


**Figure 5.10** Typical adsorption isotherm of ethanol at 30°C for test activated carbons. Filled symbols are for adsorption and empty symbols are for desorption.

The ethanol adsorption isotherms at different temperatures of 20-35°C on both carbon samples are shown in Figure 5.11. The adsorption is exothermic in nature, with the adsorption capacity decreasing with the increasing in the adsorption temperature. The adsorption temperature does not distinctly affect the isotherm when plotted on the basis of relative pressure.

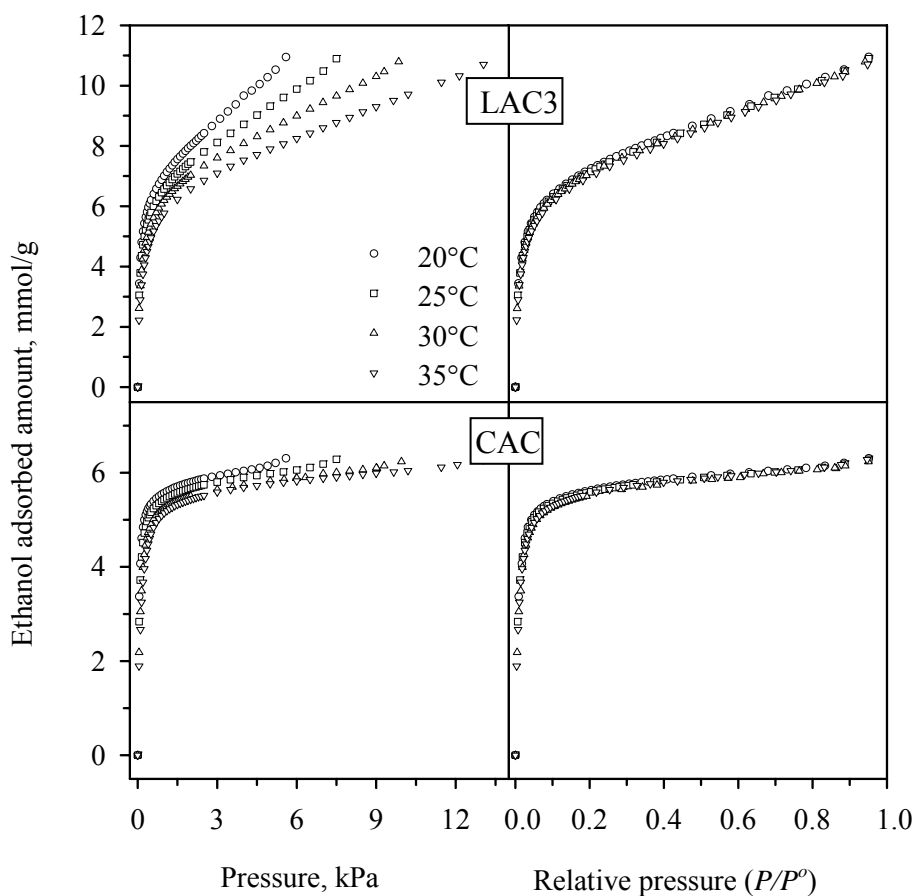


**Figure 5.11** Ethanol adsorption isotherms in test activated carbons at various temperatures.

The heat of adsorption ( $Q_{st}$ ) was calculated by van't Hoff equation, and the obtained results are shown in Figure 5.12. The  $Q_{st}$  initially decreases with an increasing in relative pressure up to 0.015, then tends to increase and has a trend to decrease again when the relative pressures greater than 0.07. The values of  $Q_{st}$  approximately lie between 56-44 kJ/mol and 60-44 kJ/mol for the LAC3 and CAC, respectively. These values are in accord with the value of 57.4 kJ/mol, 45.6 kJ/mol and 45.5 kJ/mol for the ethanol adsorption on activated carbon fibers (P5 and P20) and KOH-activated carbon (Max-31), respectively (Ohkubo et al., 1999). These

investigators reported that these values are greater than the ethanol adsorption on graphite from which they attributed this to the molecule-pore wall interaction.

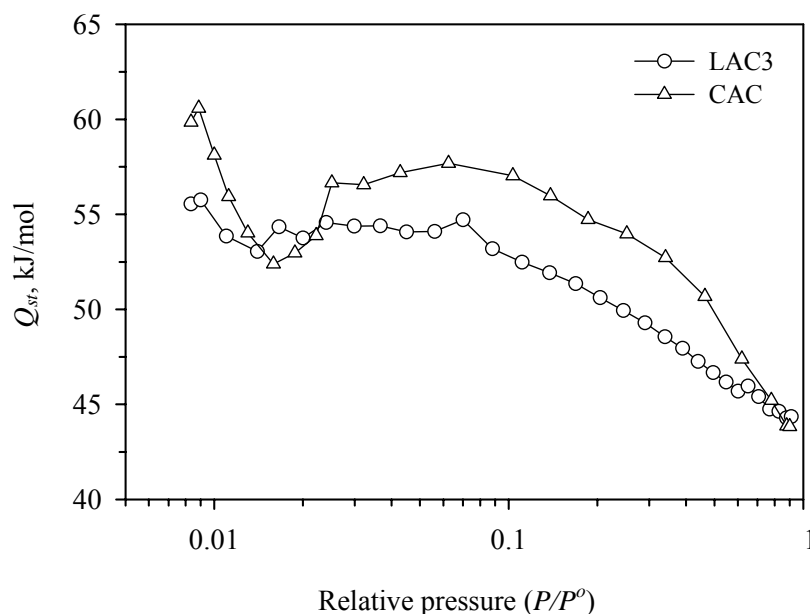


**Figure 5.12** Heat of adsorption of ethanol adsorption in LAC3 and CAC carbons.

The ethanol isotherms were fitted well with the dual-Langmuir equation, giving the results as shown in Figure 5.13 and the fitted parameters listed in Table 5.8. The dual-Langmuir is a combination of the two Langmuir equations that describe the adsorption in micropores ( $C_{\mu 1}$ ) and meso- and macropores ( $C_{\mu 2}$ ). It is seen that the adsorption in micropores occurred at the initial stage and approximately ends at the relative pressure of 0.1 and 0.15 for LAC3 and CAC, respectively. At greater relative pressures, the contribution of the mesopores filling gradually increases with the increasing in pressure.

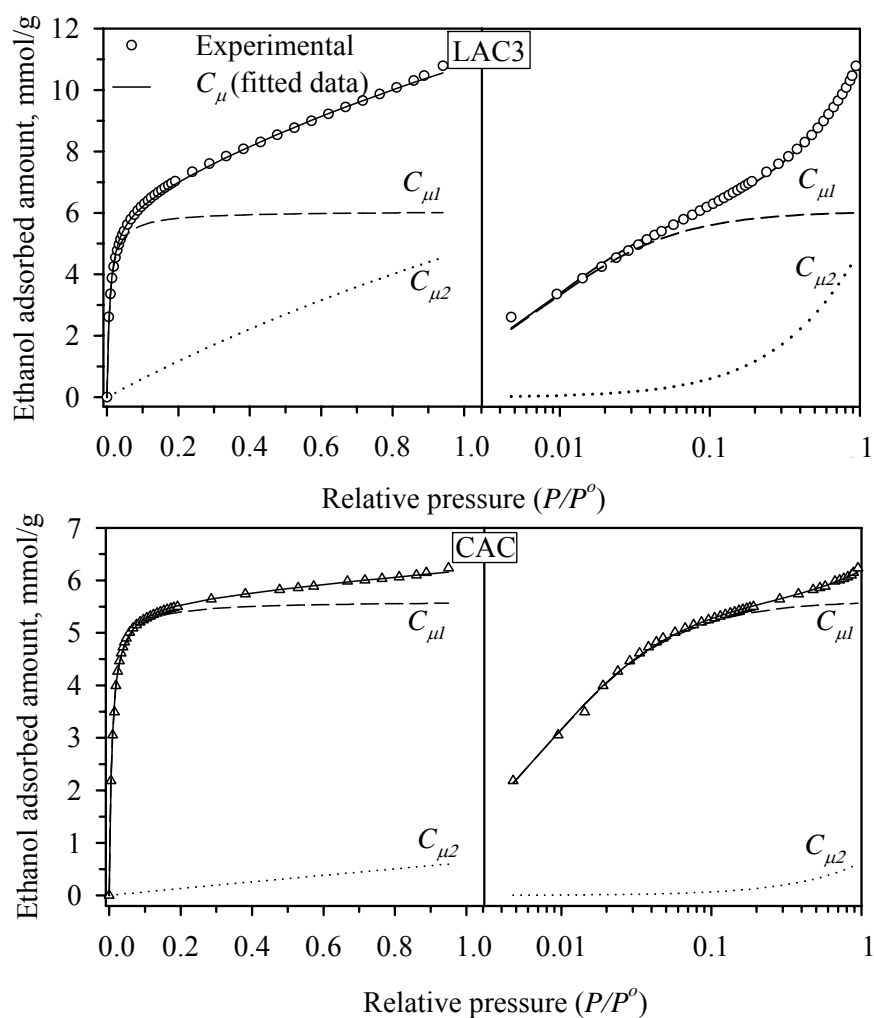


**Figure 5.13** Fitting of the dual-Langmuir model to the experimental ethanol isotherms at 30°C in carbon samples; symbols denote experimental data and lines denote fitted results.

The fitted parameter in Table 5.8 shows that the  $b_2$  is much less than  $b_1$  reflecting that the micropore has stronger affinity than the larger pores. There is a tendency that the model parameters decrease with increasing in the temperature, leading to a decreasing in the adsorption capacity at high temperature. This behavior is logical considering the exothermic nature of the adsorption process.

**Table 5.8** The optimized parameters from dual-Langmuir equation fitting with the ethanol adsorption isotherm at several temperatures.

Sample	$T$ [°C]	$C_{\mu m1}$ [mmol/g]	$C_{\mu m2}$ [mmol/g]	$b_1$ [kPa <sup>-1</sup> ]	$b_2$ [kPa <sup>-1</sup> ]
LAC3	20	6.26	22.46	20.83	0.045
	25	6.13	21.09	15.88	0.037
	30	6.06	20.46	11.62	0.029
	35	5.80	17.54	9.12	0.028
CAC	20	5.65	21.72	28.12	0.0053
	25	5.62	19.23	20.17	0.0045
	30	5.61	16.77	12.30	0.0037
	35	5.62	15.48	9.49	0.0032

## 5.5 Conclusions

Activated carbons with different pore size distribution were produced by controlling the burn-off level during carbon dioxide activation of longan seed char. The variation of char burn-off also affected the concentration of surface functional groups of the activated carbons. The resultant carbons were used to study the effect of combined influences of pore structure and surface properties on water adsorption behavior. The results obtained from this work showed that the water adsorption isotherm depended significantly on the pore size distribution through the role of acidic surface functional groups. It was found that water can adsorb into all pore sizes including, ultramicropores, supermicropores and larger pores (mesopores and macropores), corresponding to adsorption in the following range of relative pressure,

0.0-0.3, 0.3-0.7 and 0.7-0.94, respectively. The heat of adsorption calculated from the isotherms for activated carbon with different burn-offs had values comparable to the latent heat of water condensation of 45 kJ/mol, indicating the significance of water molecular interaction. Modification of water isotherm model of Do and Do by considering the adsorption in micropore and larger pores with different cluster sizes gave a full description of water adsorption in porous carbons. The cluster formation before being adsorbed into micropores and larger pores are different with regard to the size of the cluster. For adsorption in micropores the water cluster size are 5 and 7 molecules for the longan seed and coconut shell based carbon, respectively. The cluster size needed to be adjusted to 20 molecules for the adsorption into the meso- and macropores for both types of carbons.

The ethanol adsorption isotherms showed a significant difference from the water isotherms using the same activated carbons. The ethanol isotherms were similar to the nitrogen adsorption isotherm at  $-196^{\circ}\text{C}$ . Ethanol adsorption isotherms could be fitted extremely well with the dual-Langmuir equation. This isotherm equation describes the initial adsorption of ethanol in the micropores which completed at the relative pressure approximately 0.1. At higher pressures, adsorption in meso- and macropores became the dominant mechanism.

## 5.6 References

- Alcaniz-Monge, J., Linares-Solano, A. and Rand, B. (2001). Water adsorption on activated carbons: Study of water adsorption in micro- and mesopores. **J. Phys. Chem. B** 105: 7998-8006.

- Alcaniz-Monge, J., Linares-Solano, A. and Rand, B. (2002). Mechanism of adsorption of water in carbon micropores as revealed by a study of activated carbon fibers. **J. Phys. Chem. B** 106: 3209-3216.
- Bansal, R. C., Donnet, J-B. and Stoeckli, F. (1988). **Active carbon**. New York: Marcel Dekker.
- Birkett, G. R. and Do, D. D. (2006). The adsorption of water in finite carbon pores. **Mol. Phys.** 104: 623-637.
- Boehm, H. P. (2002). Surface oxides on carbon and their analysis: a critical assessment. **Carbon** 40: 145-149.
- Brennan, J. K., Bandosz, T. J., Thomson, K. T., Gubbins, K. E. (2001). Review: water in porous carbons. **Colloids Surf. A** 187-188: 539-568.
- Do, D. D. (1998). **Adsorption analysis: Equilibria and kinetics**. New Jersey: Imperial College Press.
- Do, D. D. and Do, H. D. (2000). A model for water adsorption in activated carbon. **Carbon** 38: 767-773.
- Dubinin, M. M. and Serpinsky, V. V. (1981). Isotherm equation for water vapor adsorption by microporous carbonaceous adsorbents. **Carbon** 19: 402-403.
- Foley, N. J., Thomas, K. M., Forshaw, P. L., Stanton, D. and Norman, P. R. (1997). Kinetics of water vapor adsorption on activated carbon. **Langmuir** 13: 2083-2089.
- Gregg, S. J. and Sing, K. S. W. (1982). **Adsorption, surface area and porosity**. London: Academic Press.

- Junpirom, S., Do, D. D., Tangsathitkulchai, C. and Tangsathitkulchai, M. (2005). A carbon activation model with application to longan seed char gasification. **Carbon** 43: 1936-1943.
- Kaneko, K., Hanzawa, Y., Iiyama, T., Kanda, T. and Suzuki, T. (1999). Cluster-mediated water adsorption on carbon nanopores. **Adsorption** 5: 7-13.
- Kimura, T., et al. (2004). Cluster-associated filling of water in hydrophobic carbon micropores. **J. Phys. Chem. B** 108: 14043-14048.
- McCallum, C. L., Bandosz, T. J., McGrother, S. C., Muller, E. A. and Gubbins, K. E. (1999). A molecular model for adsorption of water on activated carbon: comparison of simulation and experiment. **Langmuir** 15: 533-544.
- Miyawaki, J., Kanda, T. and Kaneko, K. (2001). Hysteresis-associated pressure-shift-induced water adsorption in carbon micropores. **Langmuir** 17: 664-669.
- Muller, E. A. and Gubbins, K. E. (1998). Molecular simulation study of hydrophilic and hydrophobic behavior of activated carbon surfaces. **Carbon** 36: 1433-1438.
- Muller, E. A., Rull, L. F., Vega, L. F. and Gubbins, K. E. (1996). Adsorption of water on activated carbons: a molecular simulation study. **J. Phys. Chem.** 100: 1189-1196.
- Ohba, T., Kanoh, H. and Kaneko, K. (2004a). Affinity transformation from hydrophilicity to hydrophobicity of water molecules on the basis of adsorption of water in graphitic nanopores. **J. Am. Chem. Soc.** 126: 1560-1562.
- Ohba, T., Kanoh, H. and Kaneko, K. (2004b). Cluster-growth-induced water adsorption in hydrophobic carbon nanopores. **J. Phys. Chem. B** 108: 14964-14969.

- Ohkubo, T., Iiyama, T., Nishikawa, K., Suzuki, T. and Kaneko, K. (1999). Pore-width-dependent ordering of C<sub>2</sub>H<sub>5</sub>OH molecules confined in graphite slit nanospaces. **J. Phys. Chem. B** 103: 1859-1863.
- Ohkubo, T. and Kaneko, K. (2001). Oriented structure of alcohol hidden in carbon micropores with ERDF analysis. **Colloids Surf. A** 187-188: 177-185.
- Rouquerol, F., Rouquerol, J. and Sing, K. (1999) **Adsorption by powder and porous solids: Principles, methodology and applications**. London: Academic Press.
- Salame, I. I. and Bandosz, T. J. (1999). Experimental study of water adsorption on activated carbons. **Langmuir** 15: 587-593.

# CHAPTER VI

## KINETICS OF BENZENE ADSORPTION

### IN ACTIVATED CARBON

#### 6.1 Abstract

The study of adsorption kinetics of benzene in activated carbon was reported in this chapter. The test activated carbons were the steam activated longan seed based-carbon and the coconut shell based-commercial activated carbon. Adsorption was studied at three different temperatures of 40, 50 and 70°C. The equilibrium isotherms were measured gravimetrically and they exhibited type I isotherm for the microporous carbon and type IV isotherm for carbon having the distribution of pore size. The isotherms were found to be reasonably well described by the model of dual-Langmuir. On the kinetic task, the pressure response in bulk phase was monitored as a function of time employing the constant molar flow rate technique. In this method, a very low and constant flow of adsorbate was introduced into a pre-evacuated adsorption cell, allowing the system to operate as a semi-batch adsorber. The mass balance equations were derived to extract the kinetic parameters, as represented by the surface diffusivity. This determined surface diffusivity was of the order of  $1 \times 10^{-10} \text{ m}^2/\text{s}$ . The relationship between the surface diffusivity and the temperature was found to follow the Arrhenius law, giving the activation energy for surface diffusion to be one third of the heat of adsorption at zero loading.

## 6.2 Introduction

In the design of an adsorption process, apart from the adsorption equilibrium data, the adsorption kinetics is also the necessary information. The requirement of kinetics involves how fast an adsorbate molecule could be adsorbed on the surface of porous solid. The overall adsorption rate in practical porous solids is generally controlled mainly by the diffusion ability of adsorbate molecules within the adsorbent particle. Normally, the adsorption kinetics in a porous solid involves the diffusion processes by different mechanisms including Knudsen diffusion, molecular diffusion, viscous flow and surface diffusion. The measurement of adsorption kinetics involving these mechanisms is not easy as compared to the equilibrium measurement. Therefore, it is necessary to develop methods for kinetic characterization that can provide reliable basis for estimation of the process performance and the key process design parameters.

There has been continued effort to investigate the diffusion phenomena in porous solids. Several measurement methods have been studied such as the chromatography method (Kawazoe, Suzuki and Chihara, 1974; Schneider and Smith, 1968), frequency response method (Yasuda, 1982), nuclear magnetic resonance spectroscopy (NMR) (Karger and Pfeifer, 1987), differential adsorption bed method (Mayfield and Do, 1991), and the microbalance method (Gray and Do, 1991). Another interesting technique that was proposed by Do (1995) is the constant molar flow in a semi-batch adsorber which was tested for its validity with several adsorbates (Prasetyo, 2000). This method gives some advantages, such as the test is simple to run, differential changes in conditions are almost ensured, heat effects can be minimized, the results can be obtained very quickly and the analysis of data is straightforward.

The constant molar flow (CMF) technique employs a precision low flow valve to control the continuous feed of a pure adsorbate into the adsorption chamber filled with an adsorbent. This system therefore operates in the semi-batch adsorption mode. The pressure response in the chamber is continually monitored as a function of time and subsequently analyzed by the formulated equations to give the corresponding kinetic parameters.

This work focuses on studying benzene vapor adsorption. Benzene is among the organic compounds designated as the priority pollutant by U.S. Environmental Protection Agency (EPA) because of its toxicity to man and the environment. Benzene is found in emissions from burning coal and oil, motor vehicle exhaust, and evaporation from gasoline service stations and in industrial solvents. These sources contribute to elevated levels of benzene in the ambient air, which may subsequently be breathed by the public. Regarding these problems the efficient treatment of benzene is required. The adsorption by porous solid is one of the efficient alternatives to control the benzene effluent. Therefore, this section aims to gain the information of benzene adsorption behavior for both equilibrium and kinetics. The kinetic experiments of benzene adsorption in activated carbons using the constant molar flow (CMF) technique were performed at Prof. Doung D. Do's laboratory, University of Queensland, Australia, under the collaboration of RGJ-Ph.D. scholarship.

### **6.2.1 The Formulation of Equations for CMF Analysis**

The diffusion mechanism in an activated carbon particle is generally controlled by the combination of pore and surface diffusion, as illustrated in Figure 6.1. The high surface area characteristic of activated carbon makes the surface diffusion flux comparable to the pore diffusion flux.

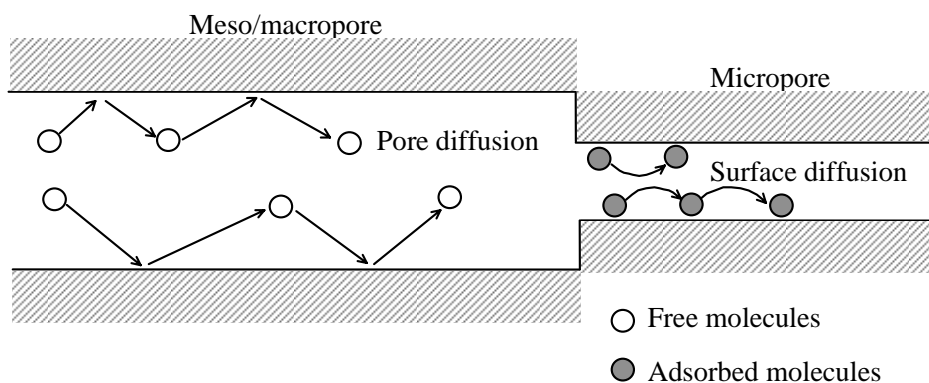


**Figure 6.1** Schematic diagram of diffusion mechanisms in activated carbon.

The following working equations for use with the CMF technique are obtained from the work of Do (1995). If the diffusion kinetics is controlled by the combination of the pore and surface diffusion, the mass balance equation of the adsorbate distribution in the particle is given by

$$\varepsilon \frac{\partial C}{\partial t} + (1 - \varepsilon) \frac{\partial C_{\mu}}{\partial t} = \varepsilon D_p \frac{1}{r^s} \frac{\partial}{\partial r} \left( r^s \frac{\partial C}{\partial r} \right) + (1 - \varepsilon) D_{\mu} \frac{1}{r^s} \frac{\partial}{\partial r} \left( r^s \frac{\partial C_{\mu}}{\partial r} \right) \quad (6.1)$$

where  $C$  is the concentration in the gas space inside the particle,  $C_{\mu}$  is the sorbate concentration in the adsorbed phase at any time  $t$ , the unit of these concentrations defined as moles per unit volume of solid particle.  $\varepsilon$  is the particle porosity.  $D_p$  and  $D_{\mu}$  are the pore diffusivity and surface diffusivity, respectively, which are assumed to be constant within the linear range of isotherm.  $r$  is the half width or radius of particle. The  $s$  is the particle shape factor corresponding to 0, 1 and 2 for slab, cylindrical and spherical shape, respectively.

To simplify the calculation procedure, a linear equilibrium isotherm is assumed. This means that the CMF method must be applied for adsorption in a

relatively low pressure region. The linear correlation of the concentration in the gas phase and the adsorbed phase inside the particle is thus

$$C_\mu = KC, \quad K = \text{Henry constant} \quad (6.2)$$

Substituting Equation 6.2 into Equation 6.1 gives the following diffusion equation

$$\frac{\partial C}{\partial t} = D_{app} \frac{1}{r^s} \frac{\partial}{\partial r} \left( r^s \frac{\partial C}{\partial r} \right), \quad D_{app} = \frac{\varepsilon D_p + (1-\varepsilon)KD_\mu}{\varepsilon + (1-\varepsilon)K} \quad (6.3)$$

There is a further assumption that the mass transfer resistance at the exterior surface of particle is negligible. The initial and boundary conditions to the mass balance equation (Equation 6.3) are

$$\begin{aligned} t = 0; C = 0 \\ r = 0; \frac{\partial C}{\partial r} = 0 \quad \text{and} \quad r = R; C = C_b \end{aligned} \quad (6.4)$$

where  $R$  is the particle radius and  $C_b$  is the adsorbate concentration in the vessel.

The mass balance equation of adsorbate in the whole vessel is

$$V \frac{dC_b}{dt} + \left( \frac{m_p}{\rho_p} \right) \left[ \varepsilon \frac{d\langle C \rangle}{dt} + (1-\varepsilon) \frac{d\langle C_\mu \rangle}{dt} \right] = \dot{N} \quad (6.5)$$

where  $\dot{N}$  is the molar supply rate of adsorbate with the unit being moles per unit of time.  $V$  is the vessel volume.  $m_p$  and  $\rho_p$  are the mass and density of solid particle,

respectively.  $\langle C_\mu \rangle$  and  $\langle C \rangle$  are the volumetric mean concentration in the particle and given by

$$\langle C_\mu \rangle = \frac{(s+1)}{R^{(s+1)}} \int_0^R r^s C_\mu dr \quad \text{and} \quad (6.6-a)$$

$$\langle C \rangle = \frac{(s+1)}{R^{(s+1)}} \int_0^R r^s C dr \quad (6.6-b)$$

The mass balance equation can be solved using the method of Laplace transform and the final solution for the pressure versus time is

$$P = \frac{\dot{N}(t)R_g T / V}{(1+\beta)} + \frac{\beta}{(1+\beta)^2} \frac{\dot{N} R_g T}{V} \frac{R^2}{(s+1)(s+3)D_{app}} - 2(1+s)\beta \left[ \left( \frac{\dot{N} R_g T}{V} \right) \left( \frac{R^2}{D_{app}} \right) \right] \times \sum_{n=0}^{\infty} \frac{\exp[-\lambda_n^2 (D_{app} t / R^2)]}{\lambda_n^2 [(1+s)^2 \beta^2 + (1+s)^2 \beta + \lambda_n^2]} \quad (6.7)$$

where

$$\beta = \left( \frac{m_p}{\rho_p} \right) \left[ \frac{\varepsilon + (1-\varepsilon)K}{V} \right] \quad (6.8)$$

The eigenvalues  $\lambda$  are obtained from the following transcendental equation:

$$\text{Slab } (s = 0); \quad \beta \tan(\lambda) + \lambda = 0 \quad (6.9-a)$$

$$\text{Cylinder } (s = 1); \quad 2\beta J_1(\lambda) + \lambda J_0(\lambda) = 0 \quad (6.9\text{--b})$$

$$\text{Sphere } (s = 2); \quad \lambda \cot(\lambda) - 1 = \lambda^2/3\beta \quad (6.9\text{--c})$$

In Equation 6.7, the plotting of pressure  $P$  versus time  $t$  will exhibit the straight line when the time is large. The asymptotic solution under this condition gives the slope and Y-intercept as follows

$$\text{Slope} = \frac{\dot{N} R_g T / V}{(1 + \beta)} \quad (6.10)$$

$$\text{Y - intercept} = \frac{\beta}{(1 + \beta)^2} \frac{\dot{N} R_g T}{V} \frac{R^2}{(s + 1)(s + 3)D_{app}} \quad (6.11)$$

So one can see that in Equation 6.10 the term  $\beta$  could be obtained and the  $K$  parameter involving the equilibrium partition between the gas-adsorbed phases in particle is derived from the correlation in Equation 6.8. When  $\beta$  is known,  $D_{app}$  follows from Equation 6.11. Finally, the surface diffusivity ( $D_\mu$ ) could be determined by substituting the pore diffusivity ( $D_p$ ) and  $D_{app}$  in Equation 6.3, where  $D_p$  is calculated from the following equation, which is derived from the Knudsen flux in the pore volume (Do, Do and Prasetyo, 2000; Prasetyo and Do, 1998):

$$D_p = \frac{D_K}{\tau} \quad (6.12)$$

where  $\tau$  is macropore tortuosity of the porous solid, for example, a typical value for activated carbon is 4.9 (Prasetyo and Do).  $D_K$  is the Knudsen diffusivity which can be calculated from the kinetic theory via the equation

$$D_K = \frac{4K_0}{3} \sqrt{\frac{8R_gT}{\pi M}} \quad (6.13)$$

where  $K_0$  is the Knudsen flow parameter, which is a function of solid characteristic only. For uniform cylindrical pore,  $K_0 = R/2$ , where  $R$  is the average pore radius. And  $M$  is the molecular weight of the adsorbate gas (Do et al.; Prasetyo and Do).

### 6.2.2 Objectives of the Study

In this chapter the adsorption of benzene in longan seed activated carbon are investigated covering the studied of equilibrium and kinetics. The dual-Langmuir equation is used to describe the adsorption equilibrium of benzene. The kinetic parameters of benzene adsorption in activated carbon are determined from the technique of a constant molar flow (CMF) at a constant of flow rate of  $6.6 \times 10^{-9}$  mol/s. Kinetics experiments were carried out to study the temperature effect at 40, 50 and 70°C.

## 6.3 Materials and Methods

### 6.3.1 Materials

The selected adsorbents for this study were longan seed activated carbon and a commercial activated carbon. The longan seed carbon designated as LACW was prepared by steam activation at 750°C for 1 h, while the commercial carbon was coconut shell based activated carbon supplied by C-Gigantic Ltd. (Thailand) and

named as CAC. For the dynamic adsorption measurement by the constant molar flow rate technique, these two carbon samples were cut to form a spherical shape particle of 3 mm in diameter. These test activated carbons were measured for the porous properties by the N<sub>2</sub> adsorption at -196°C.

### **6.3.2 Benzene Adsorption Isotherm**

The isotherms were measured gravimetrically by using an Intelligent Gravimetric Analyzer (IGA) supplied by Hiden Analytical Ltd., UK. The benzene adsorption isotherms were performed at three different temperatures of 40, 50 and 70°C. For each isotherm measurement, the loaded sample was outgassed at 300°C for 10 h at 10<sup>-4</sup> kPa. Isotherm data were automatically collected over the specified pressures in either adsorption or desorption scan.

### **6.3.3 Constant Molar Flow Rate Experiment**

The apparatus used to collect the adsorption kinetics data in a constant molar flow rate mode is shown in Figure 6.2. This rig consists of two separated sections of vapor reservoir and adsorption vessel and the two sections is separated by a variable leak valve (Varian model 951-5106). This valve is used as the admittance valve to control the very low flows of adsorbate with high accuracy from the reservoir to the adsorption section.

A sample particle in spherical shape was placed in the sample vessel. The sample was preliminary treated for each experiment by outgassing at 150°C for 24 h. The adsorbate was supplied into the sample vessel at a constant rate of 6.60×10<sup>-9</sup> mol/s. This flow rate was obtained from the preliminary runs to check a suitable flow rate. If the flow is either too slow or too fast the pressure response will be linear over a practical time span. The linearity corresponding to very low flow is the result of

quasi-equilibrium between the two phases and hence showing a linear pressure response. On the other hand, the linearity corresponding to very large flow is due to the physical filling of the volume space in the adsorption cell.

The measurement was performed for the LACW carbon at three different temperatures of 40, 50 and 70°C and the CGC was measured at one temperature of 50°C. In each run the pressure response against time was monitored and logged into a computer. The theory for CMF technique requires that the run be operated in the region where the equilibrium between the bulk and the adsorbed phase follows the linear isotherm relation. Therefore, the pressure should be kept within a very low range.

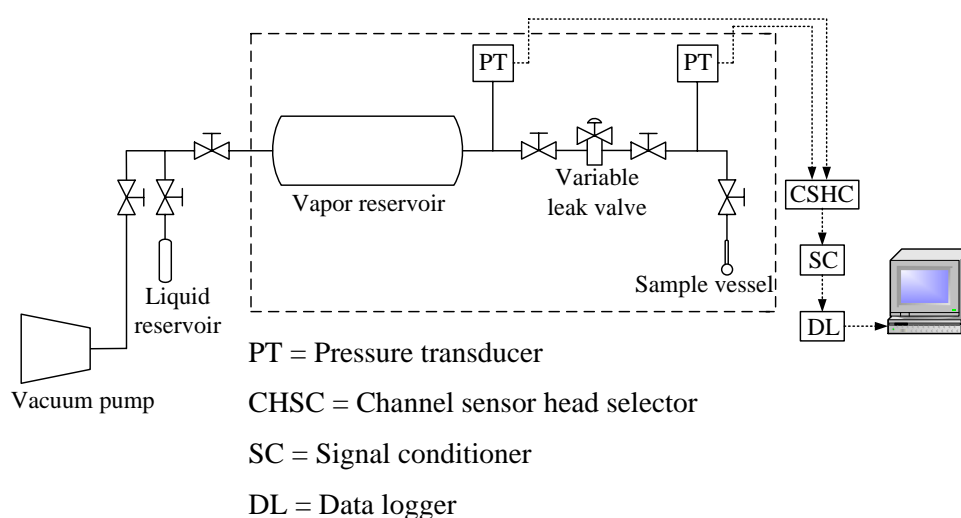


**Figure 6.2** Schematic diagram of a constant molar flow (CMF) adsorption test rig.

## 6.4 Results and Discussion

### 6.4.1 Porous Properties of Test Activated Carbons

The N<sub>2</sub> adsorption isotherms of the test activated carbons are shown in Figure 6.3. The longan seed based-activated carbon (LACW) shows type IV isotherm whereas the commercial carbon (CGC) is of type I. The isotherm shape implies that the CGC is predominantly dominated with the micropores as compared to the LACW. The observation of isotherms in the low pressure range up to the relative pressure of 0.30 on a semi-log plot shows a higher N<sub>2</sub> adsorption capacity of CGC than that of LACW. However, the opposite trend is observed at relative pressure greater than 0.30. This result indicates that the CGC contains higher micropore volume than that of LACW.

The physical properties of these two activated carbons are listed in Table 6.1. The BET surface area, total pore and micropore volume are determined from the N<sub>2</sub> adsorption isotherm. The true density was measured by the helium pycnometer technique (AccuPyc 1330, Micromeritics, USA) and the other two properties of the apparent density and median of macropore size were evaluated by using the mercury porosimetry (Poresizer 9320, Micromeritics, USA).

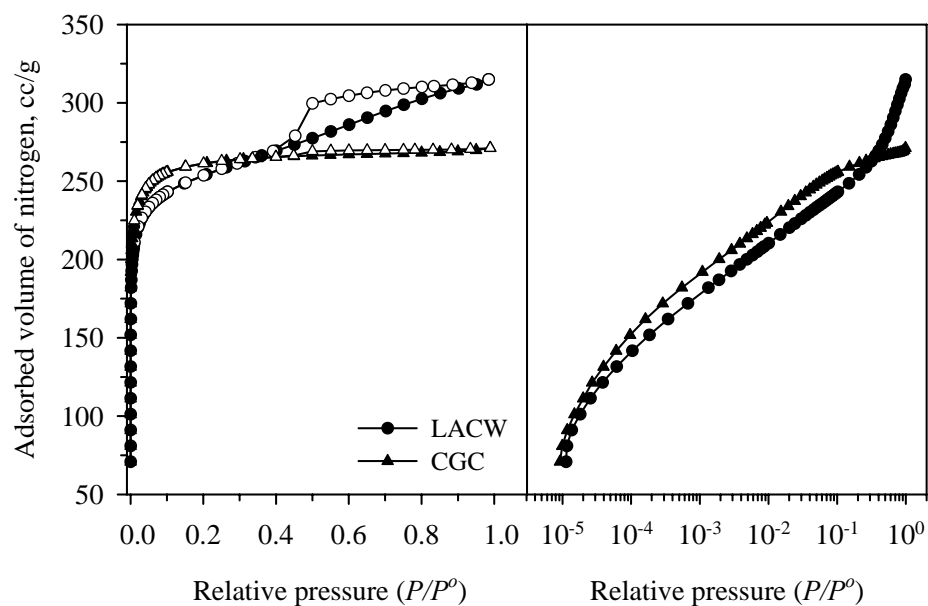


**Figure 6.3** N<sub>2</sub> adsorption isotherms at  $-196^{\circ}\text{C}$  for test activated carbons. Filled symbols are for adsorption and empty symbols are for desorption.

**Table 6.1** Porous and physical properties of test activated carbon.

Porous property	LACW	CGC
BET surface area [ $\text{m}^2/\text{g}$ ]	841	860
Total pore volume [ $\text{cm}^3/\text{g}$ ]	0.49	0.42
Micropore volume [ $\text{cm}^3/\text{g}$ ]	0.39	0.42
True density [ $\text{g}/\text{cm}^3$ ]	1.93	1.98
Apparent density [ $\text{g}/\text{cm}^3$ ]	1.17	1.10
Median of macropore size [ $\mu\text{m}$ ]	0.23	0.19

### 6.4.2 Benzene Adsorption Isotherm

The typical benzene adsorption isotherm at 50°C on the LACW and CGC carbons are shown in Figure 6.4. The isotherms exhibit type IV and type II for the LACW and CGC, respectively, similar to the N<sub>2</sub> isotherms. The benzene uptake sharply increases at initial relative pressures, indicating the predominant contribution of dispersion interaction between benzene molecules and solid surfaces. The maximum capacity of benzene adsorption in these two carbons is approximately the same which is different from that found in the N<sub>2</sub> adsorption. This behavior could be attributed to the existence of closely packed condition in the adsorbed phase of benzene in microporosity, which more pronounced in CAC than in LACW.

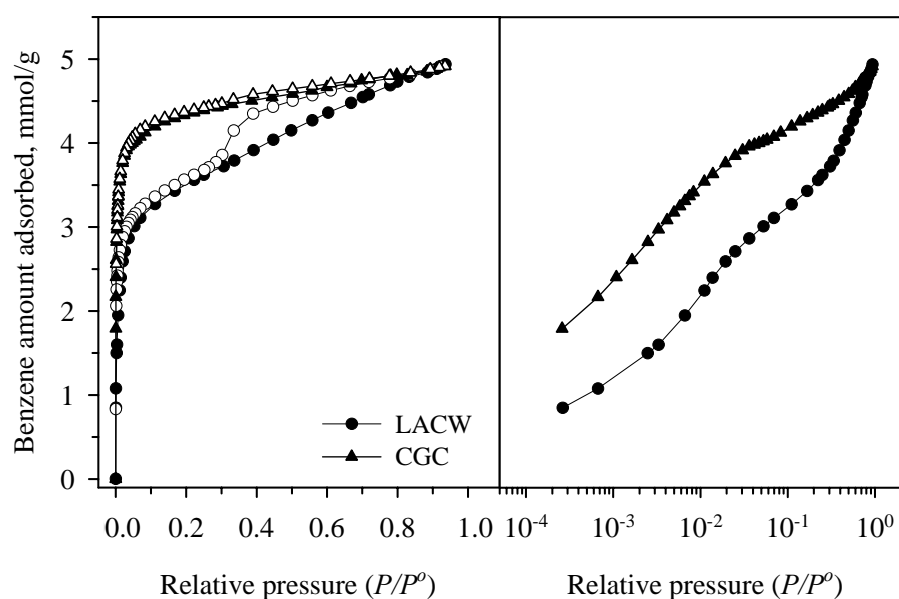


**Figure 6.4** Typical benzene adsorption isotherms at 50°C for test activated carbons.

Filled symbols are for adsorption and empty symbols are for desorption.

The results in Figure 6.5 display the benzene adsorption isotherms at different temperatures. Regarding the adsorption isotherms that are plotted versus pressure, it is clear that the adsorption of benzene decreases with the increasing in the adsorption temperature, indicating that the benzene adsorption is an exothermic process.

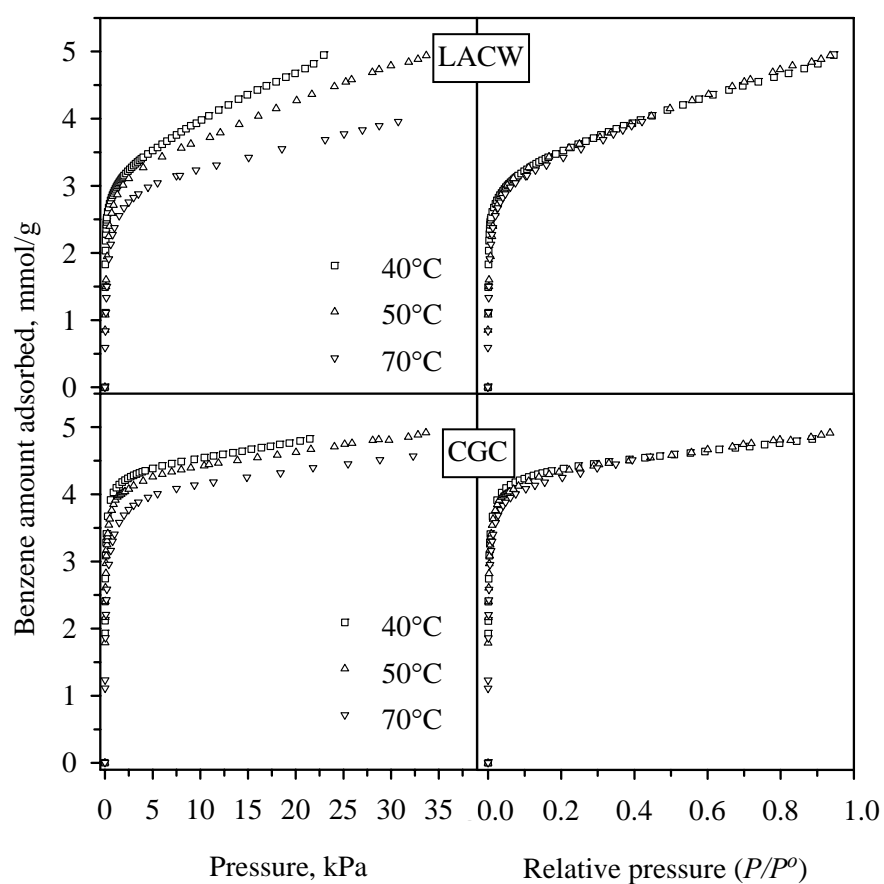


**Figure 6.5** Benzene adsorption isotherms in test activated carbons at different temperatures.

The isosteric heats of adsorption ( $Q_{st}$ ) were calculated from van't Hoff equation and presented in Figure 6.6. The  $Q_{st}$  values of both carbons varied in the range of 40-70 kJ/mol, but the track along the fractional uptake of each carbon seems to be different. The  $Q_{st}$  of LACW initially increases with fractional uptake and reaches the maximum value of 70 kJ/mol at the fractional uptake 0.2, then gradually decreases at higher uptake. However, the maximum  $Q_{st}$  of 70 kJ/mol in CGC is seen at the fractional uptake 0.4. Generally, the  $Q_{st}$  in CGC is observed to be higher than that in LACW at the fractional uptake above approximately 0.34. This result could support the hypothesis that adsorbed phase in CGC is more packed than that in the LACW.

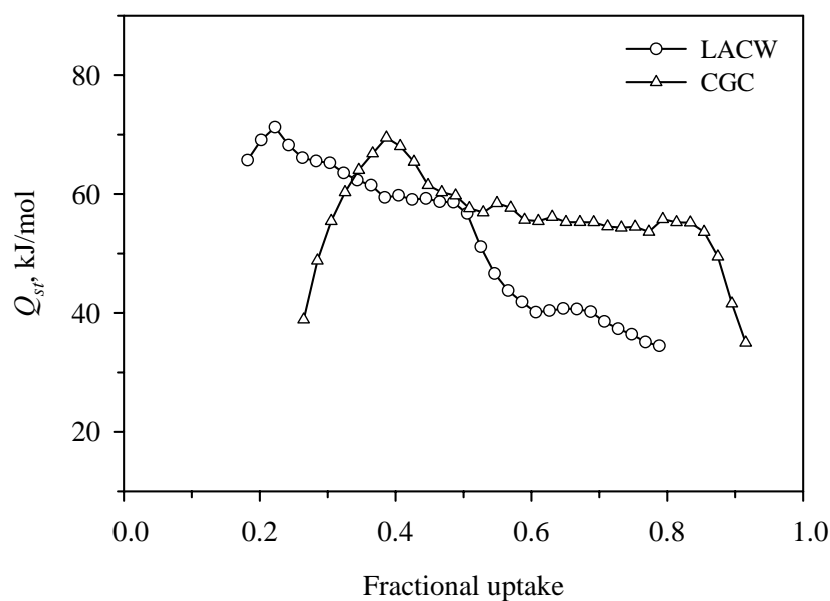


**Figure 6.6** The isosteric heat of adsorption for benzene adsorption in test activated carbons.

Accordingly, the adsorption of benzene is governed to a great extent by the dispersion force, showing a rapidly increasing isotherm at low pressure. Therefore, its adsorption could be described by the dual-Langmuir equation, shown as Equation 5.4:

$$C_{\mu} = C_{\mu 1} + C_{\mu 2} = C_{\mu m 1} \frac{b_1 P}{1 + b_1 P} + C_{\mu m 2} \frac{b_2 P}{1 + b_2 P} \quad (5.4)$$

It is found that the benzene isotherms could be well fitted by equation of dual-Langmuir equation as shown in Figure 6.7. In each isotherm, the dual-Langmuir is divided into adsorbed amount in micropore ( $C_{\mu 1}$ ) and in meso- and macropore ( $C_{\mu 2}$ ) and plotted with respect to pressure in Figure 6.8.

The optimal parameters,  $C_{\mu m 1}$ ,  $C_{\mu m 2}$ ,  $b_1$  and  $b_2$  derived by fitting the equation with the experimental isotherms at different temperatures are listed in Table 6.2. There is no consistent trend of these parameters as a function of temperature. However, the affinity  $b_1$  and  $b_2$  of CGC show higher values than those of LACW. These resulting parameters indicate that benzene is more attractive onto the CGC carbon surface than onto the LACW carbon.

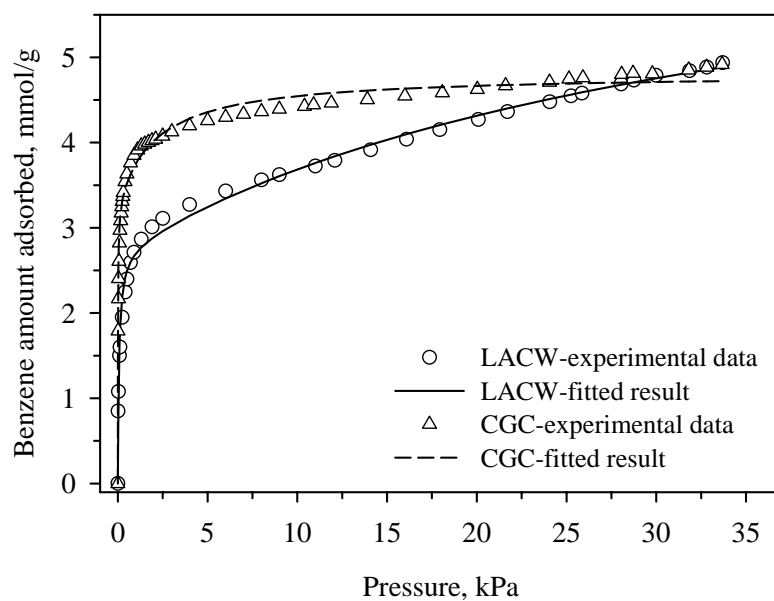


**Figure 6.7** Benzene adsorption isotherms at 50°C of test activated carbons obtained from experiment and dual-Langmuir fitting.

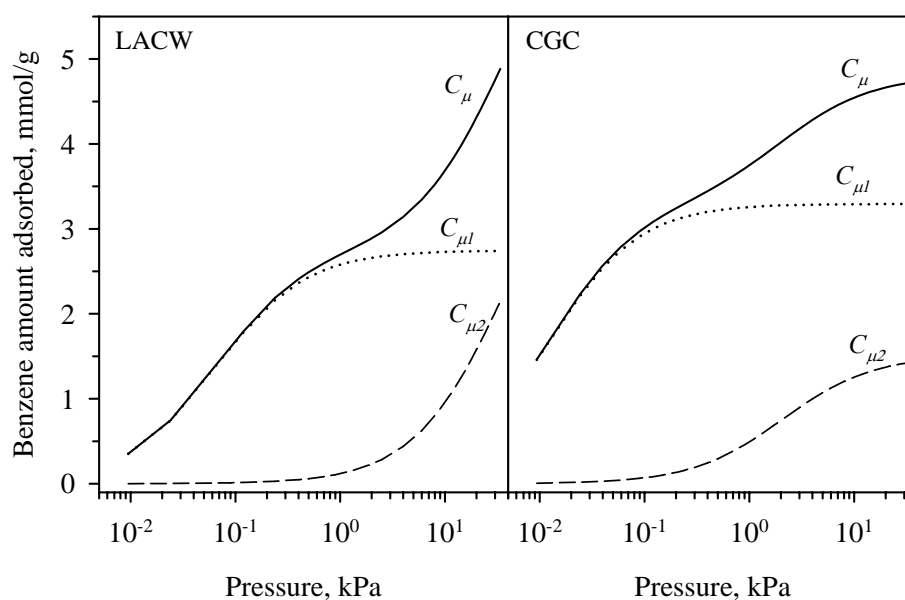


**Figure 6.8** The benzene amount adsorbed data from dual-Langmuir fitting at temperature 50°C of test activated carbons.

**Table 6.2** The optimized parameters from dual-Langmuir equation fitting with the benzene adsorption isotherms at different temperatures.

Sample	$T$ [°C]	$C_{\mu m1}$ [mmol/g]	$C_{\mu m2}$ [mmol/g]	$b_1$ [kPa <sup>-1</sup> ]	$b_2$ [kPa <sup>-1</sup> ]
LACW	40	2.79	3.94	52.20	0.04
	50	2.74	4.50	15.45	0.03
	70	2.61	2.16	7.42	0.05
CGC	40	3.17	1.54	223.43	1.09
	50	3.29	1.51	84.36	0.48
	70	2.16	2.26	158.25	1.15

### 6.4.3 Benzene Adsorption Kinetics

Accordingly, the current CMF method is assumed to apply with only the linear isotherm, so the measured pressure response was limited to approximately 0.004 kPa to ensure the Henry's law for linear adsorption isotherm. In principle, Henry constant can be directly estimated from the initial range of the experimental isotherm. However, there is a limitation of the experimental rig that prevents the measurement in a very low pressure range. For this reason, the Henry constant was derived directly from Equation 6.8 as explained earlier. Figure 6.9 demonstrates the measured benzene isotherm and the estimated linear isotherm at low pressure range. The completed isotherm can be obtained by extending the measured isotherm curve to intersect the linear isotherm. According to this result, the linear adsorption behavior can be roughly applied up to the pressure of 0.004 kPa, as illustrated in the figure.

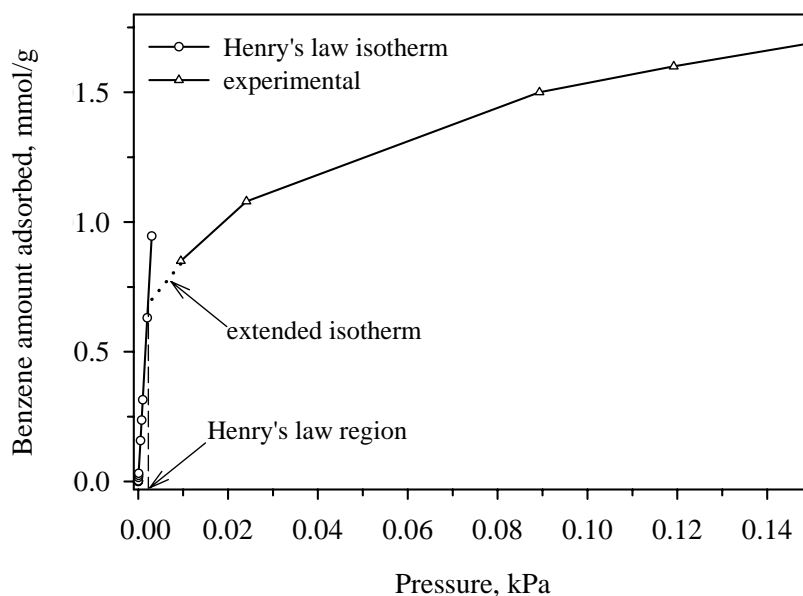


**Figure 6.9** Approximation of the Henry's law region of benzene adsorption isotherm.

The kinetic data of bulk pressure response during benzene adsorption of LACW at 40°C, 50°C and 70°C and of CGC at 50°C obtained from the constant molar flow rate technique (CMF) at the flow rate of  $6.6 \times 10^{-9}$  mol/s are shown in Figure 6.10 (a)-(d), respectively. The open circle symbols denote the experimental data and the straight line corresponds to the linear asymptote for the long time solution. It is observed that the relative increasing of pressure with respect to time in LACW at 70°C is faster than those at lower temperatures. This is due to the exothermic of adsorption process, showing a decrease in adsorption at a higher temperature. The parameter used to calculate the kinetic parameters are summarized in Table 6.3.

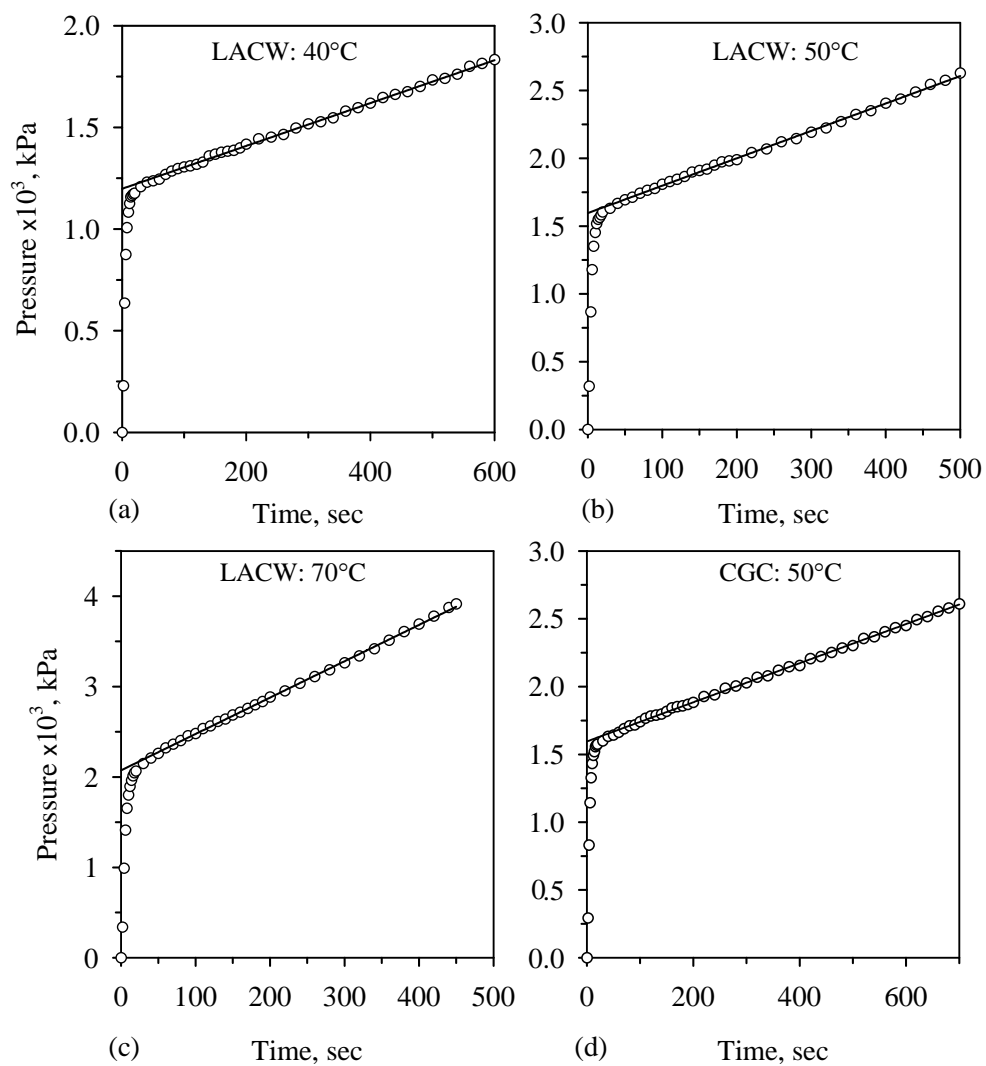


**Figure 6.10** The kinetic data of pressure responses of benzene adsorption in longan seed based-activated carbon (LACW) (a)-(c) at different temperatures and in a commercial activated carbon (CGC) (d) at 50°C, with the adsorbate flow rate of  $6.60 \times 10^{-9}$  mol/sec.

**Table 6.3** Parameters for CMF calculation.

Particle characteristic	Sample	
	LACW	CGC
$m_p$ [g]	0.014	0.021
$\rho_p$ [g/cm <sup>3</sup> ]	1.17	1.10
$\varepsilon$	0.39	0.44
$\tau$	4.9	4.9
$R_p$ [cm]	0.30	0.30
<b>Reservoir</b>		
$V$ [cm <sup>3</sup> ]	29.5	
<b>Adsorbate</b>		
$M$ [g/mol]	78.1	

Table 6.4 lists the values of Henry constant of benzene adsorption for various temperatures studied. This parameter indicates the affinity of adsorbate toward the adsorbent and as expected this parameter decreases with increasing in adsorption temperature as can be observed from the LACW data. At the same temperature, the Henry constants of LACW and CGC are almost comparable although that of LACW ( $1.22 \times 10^6$ ) is slightly higher than that of CGC ( $1.14 \times 10^6$ ).

**Table 6.4** Effect of temperature on Henry constant of benzene adsorption in test activated carbons.

Sample	$T$ [°C]	$K$
LACW	40	$2.28 \times 10^6$
	50	$1.22 \times 10^6$
	70	$6.52 \times 10^5$
CGC	50	$1.14 \times 10^6$

The Y-intercept of the fitted linear asymptote to the experimental data shown in Figure 6.10 also provides the kinetic parameters using Equation 6.11 to obtain the apparent diffusivity ( $D_{app}$ ). Then the pore diffusivity ( $D_p$ ) was calculated from Equation 6.12. The surface diffusivity ( $D_s$ ) is then determined from Equation 6.3 knowing  $D_{app}$  and  $D_p$ . All the calculated diffusivities are tabulated in Table 6.5. These all diffusivity values increase with the increasing in the temperature as expected. This results from the increasing of the kinetic energy leading to the higher degree of molecular mobility.

**Table 6.5** Kinetic parameters of benzene adsorption in test activated carbons for zero loading.

Sample	$T$ [°C]	$D_{app}$ [m <sup>2</sup> /s]	$D_p$ [m <sup>2</sup> /s]	$D_\mu$ [m <sup>2</sup> /s]	$E_{D\mu}$ [kJ/mol]
LACW	40	$1.32 \times 10^{-10}$	$4.81 \times 10^{-6}$	$1.30 \times 10^{-10}$	22.75
	50	$1.89 \times 10^{-10}$	$4.88 \times 10^{-6}$	$1.87 \times 10^{-10}$	
	70	$2.89 \times 10^{-10}$	$5.03 \times 10^{-6}$	$2.84 \times 10^{-10}$	
CGC	40	$1.35 \times 10^{-10}$	$4.05 \times 10^{-6}$	$1.32 \times 10^{-10}$	NA

The value of surface diffusivity for benzene adsorption in activated carbon found in this work is about two order of magnitude higher than that determined by Prasetyo, Do and Do (2002), who reported  $D_\mu$  to be in the range of  $5.30 \times 10^{-12}$ - $1.56 \times 10^{-11}$  m<sup>2</sup>/s for the adsorption temperature of 30-50°C. The difference of  $D_\mu$  is probably attributed to the different types of activated carbons used in the two studies.

Among the surface diffusivities of test activated carbons, it is found that the surface diffusivity of the CGC is lower than the LACW at the adsorption temperature of 50°C. This behavior could be due to the stronger affinity in CGC which is suggested by the higher value of the parameters of  $b_1$  and  $b_2$  of the dual-Langmuir equation. The surface diffusivity usually depends on the temperature on the basis of the Arrhenius equation (Miyabe and Guiochon, 2001). The activation energy of surface diffusion is therefore obtained from the Arrhenius plot of the surface diffusivity in logarithmic scale versus  $1/T$  as exhibited in Figure 6.11, giving the activation energy to be 22.75 kJ/mol (in Table 6.5). The least square regression for this correlation gives the regression coefficient of 0.98. It is found that the ratio of the

activation energy for surface diffusion to the heat of adsorption (at initial adsorption,  $Q_{st} = 65.7$  kJ/mol) is about 0.34. This ratio agrees with other experimental observations that the surface diffusion in the monolayer region generally has the activation energy to be one-third to one-half of the heat of adsorption (Do, 1998).

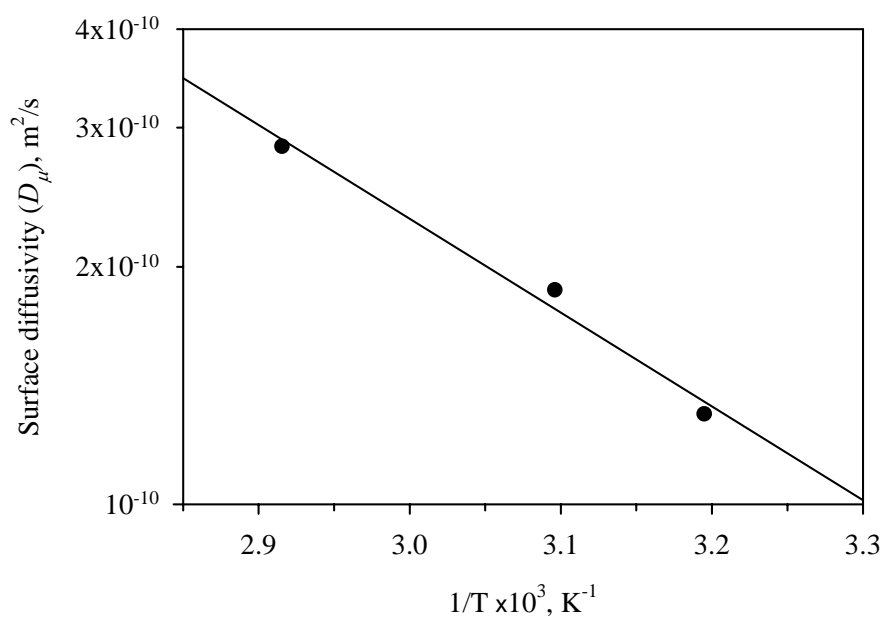


**Figure 6.11** Temperature dependence of surface diffusivity ( $D_\mu$ ) for benzene adsorption in longan seed activated carbon.

## 6.5 Conclusions

Benzene adsorption in commercial activated carbons basically exhibited the isotherm shape of type I, while the longan seed carbon which contained larger proportion of mesopores gave type IV isotherm. The benzene isotherms were described well by the dual-Langmuir equation. The kinetics of benzene adsorption in activated carbon was studied by using the technique of constant molar flow rate. This method was recently proposed and has proved to be a reasonably quick and reliable

method in determining diffusivities of gases in porous material such as activated carbon. The present study also found this technique to be quite useful in deriving the kinetic parameters of benzene adsorption. It was found that the surface diffusivity of benzene on the surface of longan seed based-carbon had the value in the range of  $1.30 \times 10^{-10}$ - $2.84 \times 10^{-10}$  m<sup>2</sup>/s. The obtained results obeyed the Arrhenius law which led to the determination of the activation energy for surface diffusion. This activation energy was found to be one third of the heat of adsorption at zero loading.

## 6.6 References

- Do, D. D. (1995). Dynamics of a semi-batch adsorber with constant molar supply rate: a method for studying adsorption rate of pure gases. **Chem. Eng. Sci.** 50: 549-553.
- Do, D. D. (1998). **Adsorption analysis: Equilibria and kinetics**. New Jersey: Imperial College Press.
- Do, D. D., Do, H. D. and Prasetyo, I. (2000). Constant molar flow semi-batch adsorber as a tool to study adsorption kinetics of pure gases and vapours. **Chem. Eng. Sci.** 55: 1717-1727.
- Gray, P. G. and Do, D. D. (1991). Dynamics of carbon dioxide sorption on activated carbon particles. **AIChE J.** 37: 1027-1034.
- Karger, J. and Pfeifer, H. (1987). N.m.r. self-diffusion studies in zeolite science and technology, **Zeolites** 7: 90-107.
- Kawazoe, K., Suzuki, M. and Chihara, K. (1974). Chromatographic study of diffusion in molecular-sieving carbon. **J. Chem. Eng. Japan** 7: 151-157.

- Mayfield, P. L. J. and Do, D. D. (1991). Measurement of the single-component adsorption kinetics of ethane, butane, and pentane onto activated carbon using a differential adsorption bed. **Ind. Eng. Chem. Res.** 30: 1262-1270.
- Miyabe, K. and Guiochon, G. (2001). Correlation between surface diffusion and molecular diffusion in reversed-phase liquid chromatography. **J. Phys. Chem. B** 105: 9202-9209.
- Prasetyo, I. (2000). **Kinetics characterization of hydrocarbons on activated carbon with new constant molar flow and differential permeation techniques.** Ph.D. Dissertation, University of Queensland, Australia.
- Prasetyo, I. and Do, D. D. (1998). Adsorption rate of methane and carbon dioxide on activated carbon by the semi-batch constant molar flow rate method. **Chem. Eng. Sci.** 53: 3459-3467.
- Prasetyo, I., Do, H. D. and Do, D. D. (2002). Surface diffusion of strong adsorbing vapours on porous carbon. **Chem. Eng. Sci.** 57: 133-141.
- Schneider, P. and Smith, J. M. (1968). Adsorption rate constants from chromatography. **AIChE J.** 14: 762-771.
- Yasuda, Y. (1982). Determination of vapor diffusion coefficient in zeolite by the frequency response method. **J. Phys. Chem.** 86: 1913-1917.

# **CHAPTER VII**

## **CONCLUSIONS AND RECOMMENDATIONS**

### **7.1 Conclusions**

This work is concerned with a systematic study of activated carbon from the new precursor, longan seed. It is the solid waste produced from the fruit cannery in Thailand. The project started with the thermal analysis of longan seed to investigate its decomposition behavior upon pyrolysis. The next task involved the preparation of activated carbons focusing mainly on using CO<sub>2</sub> as oxidizing gas in physical activation, and also a small section on chemical activation with phosphoric acid. A carbon activation model for describing the pore development during char gasification of physical activation was proposed and tested with experimental data. The following chapter presented the work on adsorption equilibrium of water and ethanol by the prepared carbons. The final part involved the kinetic study of benzene adsorption by using a constant molar flow rate technique.

On the thermal analysis, the longan seed with the average particle size of 1.0 mm was pyrolyzed in a thermogravimetric analyzer under the heating rate at 5°C/min for the final temperature of 650°C. The thermal decomposition covered the temperature range of 210-330°C and showed a major peak of main devolatilization around 260°C. The increasing in particle size and decreasing in heating rate gave an increase in the heat transfer resistance, leading to the increasing of char yield. The decomposition of longan seed was described well by the two-parallel reactions model. In this model,

it was assumed that biomass is composed of two main fractions and each fraction decomposed independently with its own reaction pathway. It was found that longan seed contained these two fractions with weight fraction of 0.56 and 0.44, respectively. It was also assumed that the reaction order of the first fraction was first order while that of the second fraction was optimally searched and found to vary from 1.8-1.62, depending on the pyrolysis conditions. Under the conditions investigated, the pre-exponential factor and activation energy for reaction 1 were  $1.52 \times 10^5$ - $4.6 \times 10^{14} \text{ min}^{-1}$  and 79.00-164.87 kJ/mol, respectively, and those for reaction 2 were 0.30-31.46  $\text{min}^{-1}$  and 27.08-35.12 kJ/mol, respectively. A sensitivity analysis revealed that the predicted TG curves showed high sensitivity towards the changes of activation energies for both reactions.

On the preparation of activated carbons, the purpose was to investigate the condition parameters affecting the porous properties of obtained activated carbon. A series of conditions investigated included the conventional two-step  $\text{CO}_2$  activation, effect of carbonization temperature, the one-step  $\text{CO}_2$  activation, and the  $\text{H}_3\text{PO}_4$  chemical activation. The model for describing the porous development during the char gasification in activation step is additionally proposed in this work. The conclusions from this work are as follows.

The conventional two-step  $\text{CO}_2$  activation was performed at activation temperatures of 800, 850 and 900°C, and at each temperature the activation times were varied from 30-180 min. The effects of activation time and temperature on the porous properties of prepared carbons could be combined into a single variable of char burn-off. The char burn-off was defined as the conversion of the char through the gasification by expressing it in terms of the percent of weight loss. Obviously, this

value increases with increasing in either the activation temperature or activation time. The porous properties such as BET surface area, total pore volume, and micropore volume increased with the increasing in the burn-off up to 70%, beyond which those properties tended to decrease. Activated carbon prepared at activation temperature 850°C for 3 h had the highest porous properties of BET surface area 1278 m<sup>2</sup>/g, total pore volume of 0.81 cm<sup>3</sup>/g and micropore volume of 0.60 cm<sup>3</sup>/g.

The carbon activation model was proposed to describe the evolution of char porosity during the gasification process. This structural model was formulated based on the assumption that the char structure is composed of the bundles of parallel graphite layers, and the reactivities of each layer with the gasification agent are assumed to be different to represent the different degree of heterogeneity of each layer (i.e. each layer will react with the gasification agent at different rate). The test of model against the experimental data of longan seed char gasification was based on the interlayer spacing of adjacent layer in a carbon crystallite of 3.35 Å. It was found that the model could describe well the surface area while the total pore volume was considered adequate. The model revealed that the pore evolution during the gasification process took place in a three-stage of development namely, pore creation, pore coalescence and pore collapse.

The effect of carbonization temperatures between 250°C to 750°C on the porous properties of activated carbon prepared at a fixed activation condition was investigated. The lower carbonization temperature produces char with higher reactivity than those prepared at the higher temperature, except the 250°C derived-char that had lower reactivity than the 350°C derived-char. This char reactivity was

represented by the total weight loss and it was found that the porous properties i.e. BET surface area and pore volumes were directly related to the value of reactivity.

The activated carbons were also prepared by the one-step CO<sub>2</sub> activation method. Surprisingly, the conventional two-step and one-step produced activated carbon with similar porous properties. The best condition for the production of highest porous properties of activated carbon was at 900°C for 90 min with maximum BET surface area 1471 m<sup>2</sup>/g, total pore volume of 1.00 cm<sup>3</sup>/g and micropore volume of 0.71 cm<sup>3</sup>/g.

For chemical activation with H<sub>3</sub>PO<sub>4</sub>, it was suggested that H<sub>3</sub>PO<sub>4</sub> produced the phosphate compounds within the structure of chemically activated carbon which was thermally stable in the temperature range 400°C-800°C. It was observed that the porous properties decreased to the lowest values as the carbonization temperature was increased from 400°C to 700°C but increased at a higher temperature. The highest porous properties found in chemically activated carbon are BET surface area of 946 m<sup>2</sup>/g, total pore volume of 0.49 cm<sup>3</sup>/g and micropore volume of 0.44 cm<sup>3</sup>/g, obtained from the carbonization temperature at 900°C for 1 h.

On the adsorption equilibrium study, water adsorption isotherms were found to depend significantly on the pore size distribution through the role of inherent acidic functional groups. Water can adsorb into all pore sizes including, ultramicropores, supermicropores and larger pores (mesopores and macropores), corresponding to adsorption in the following range of relative pressure, 0.0-0.3, 0.3-0.7 and 0.7-0.94, respectively. The similar value of heat of adsorption and the latent heat of water condensation indicated the significance contribution of water molecular interaction. The cluster model of Do and Do was used to describe the water adsorption isotherms

and further modification on the cluster size for adsorption in the large pores was required. That is the cluster size needed to be adjusted to 20 molecules for the adsorption in the large pores of meso- and macropores. The ethanol adsorption isotherms showed a significant difference from the water isotherms for the same test activated carbons. These ethanol isotherms could be described well with the dual-Langmuir equation. This model predicted the adsorption of ethanol to take place first in micropores up to the relative pressure of 0.1 and the adsorption in larger pores took on at higher pressures.

The last section of this research work was the investigation of benzene adsorption in activated carbon involving the equilibrium and the kinetic aspects. The benzene adsorption isotherms displayed the type I for the microporous carbon, but the carbon having a combination of all pore sizes showed type IV isotherm. As well, these isotherms could be well described by the dual-Langmuir equation. The kinetics of benzene adsorption was conducted by the technique of constant molar flow rate. The kinetic parameter in terms of surface diffusivity was determined to be in the order of  $1 \times 10^{-10} \text{ m}^2/\text{s}$ . The relationship between the surface diffusivity and the temperature was found to follow the Arrhenius law, giving the activation energy to be one third of the heat of adsorption at zero loading.

## **7.2 Recommendations**

### **7.2.1 Gasification Studying in a Thermogravimetric Analyzer**

The thermal analysis of the present study was focused only on the pyrolysis process which was related only to the carbonization step in the preparation of activated carbon by physical activation. To complete the kinetic study of activation

step, the gasification reaction of char should also be studied thermogravimetrically. The procedure is achieved by heating up the char under  $N_2$  atmosphere to the desired activation temperature and then replacing  $N_2$  with the oxidizing gas e.g.  $CO_2$ . The obtained results will provide the data of the weight loss against time during the course of gasification. The gasification rate of char could then be subsequently determined.

### **7.2.2 Refinement of a Carbon Activation Model**

The development of a carbon activation model has been proposed and was capable of predicting basic porous properties of activated carbon quite satisfactorily. However, it is interesting to improve the model that can be extended to other precursors and different activation conditions. In this respect, the use of distributed interlayer spacing of the char carbon should be tried. This consideration of interlayer spacing distribution could account for the heterogeneity and complexity of char structure from different types of precursor.

### **7.2.3 The Surface Functional Group Influence on Water Adsorption**

In this thesis work, the combined influences of the pore width and the surface functionality are not clearly separated in the analysis of water adsorption behavior. Further work should be directed toward studying the effects of concentration and density distribution of acidic functional groups on water adsorption. This may be achieved by the use of strong oxidizing agent e.g.  $HNO_3$  coupled with selective control of the type of acidic surface groups existing on the carbon surface by thermal treatment.

### **7.2.4 Kinetic Parameters at Loading Variation**

The adsorption kinetic experiments were performed for only the zero loading, based on the assumption of constant diffusivity. In practical operation, the

loading will be increased till the bulk pressure reaches the saturation state. It will be thus interesting to investigate the variation of the kinetic parameters as a function of the adsorption loading.

## **APPENDIX**

### **LIST OF PUBLICATIONS**

# LIST OF PUBLICATIONS

## 1. Referred Journals

Junpirom, S., Do, D. D., Tangsathitkulchai, C and Tangsathitkulchai, M. (2005). A carbon activation model with application to longan seed char gasification. **Carbon** 43: 1936-1943.

Wongkoblapp, A., Junpirom, S. and Do, D. D. (2005). Adsorption of Lennard-Jones fluids in carbon slit pores of a finite length. A computer simulation study. **Adsorpt. Sci. Technol.** 23: 1-18.

Junpirom, S., Tangsathitkulchai, C. and Tangsathitkulchai, M. (2006). Preparation of activated carbons from longan seed by physical and chemical methods (in Thai). **Suranaree J. Sci. Technol.**: Accepted for publication.

Junpirom, S., Tangsathitkulchai, C., Tangsathitkulchai, M. and Ngernyen, Y. (2007). Water adsorption in activated carbons with different burn offs and its analysis using the cluster model. **Korean J. Chem. Eng.**: Submitted.

## 2. Conference Proceeding

Junpirom, S., Tangsathitkulchai, C. and Tangsathitkulchai, M. (2004). Activated carbon from longan seed by carbon dioxide activation. **Regional Symposium on Chemical Engineering (RSCE2004)**.

### 3. Conference Abstracts

Junpirom, S., Tangsathitkulchai, C. and Tangsathitkulchai, M. (2005). Water adsorption equilibrium of longan seed activated carbons. **International Congress of Chemistry and Environment (ICCE2005)**.

Junpirom, S., Tangsathitkulchai, C. and Tangsathitkulchai, M. (2006). Carbonization temperature effect on the porous properties of physically activated carbon from longan seed. **International Carbon Conference (Carbon2006)**.

Luangkiattikul, P., Ngernyen, Y., Junpirom, S., Tangsathitkulchai, C. and Tangsathitkulchai, M. (2006). A char gasification model for predicting the porous properties of activated carbons. **Regional Symposium on Chemical Engineering (RSCE2006)**.

## **BIOGRAPHY**

Miss Supunnee Junpirom was born on the 20<sup>th</sup> of December 1977 in Kamphaeng Phet. She earned her Bachelor's degree in Chemical Engineering from Suranaree University of Technology (SUT), Nakhon Ratchasima, in 2000. She has received the Royal Golden Jubilee Ph.D. (RGJ-Ph.D.) scholarship from the Thailand Research Fund (TRF) to study the doctoral degree in Chemical Engineering at SUT since year 2000.